Unraveling property-performance relationships in CO_2 hydrogenation over iron-based catalysts

Dissertation

Zur Erlangung des akademischen Grades
Doctor rerum Naturalium (Dr. rer. nat.)
der Mathematisch-Naturwissenschaftlichen Fakultät
der Universität Rostock

vorgelegt von
Qingxin Yang

Geb. am 19. Juli 1993 in Shandong, China

Gutachter

Prof. Dr. Evgenii V. Kondratenko

Leibniz-Institut für Katalyse e.V., 18059 Rostock, Germany

Prof. Dr. Andrei Khodakov

Univ. Lille, CNRS, Centrale Lille, ENSCL, Univ. Artois, UMR 8181–UCCS–Unité de Catalyse et Chimie du Solide, 59000 Lille, France

Tag der Einreichung: 15 March 2022

Tag der mündlichen Prüfung: 21 June 2022

Eidesstattliche Versicherung

Hiermit versichere ich, Qingxin Yang, dass ich die vorliegende Dissertation selbständig verfasst habe. Die benutzten Hilfsmittel wurden in der Arbeit aufgeführt.

Acknowledgement

During this PhD journey, I received a lot of help form my supervisor, supporter, teammates, and helpers. Taking this opportunity, I would like to sincerely thank them all.

There is no doubt that this thesis would not be completed without the help, support, encourage, and guidance from my supervisor, Prof. Dr. Evgenii V. Kondratenko. Evgenii, thank you very much for giving me the opportunity to join your group as a PhD candidate and work on the topic of "CO_2 HYD" within the frame of SPP 2080 project. At this moment, my mind is full of scenes of countless discussions with you. Your deep insight into the scientific questions and your interest in scientific exploration have set me an example worthy of learning. To my surprise, you are familiar with all the details involved in the whole stages of research from catalyst preparation, reaction engineering, data analyses, modelling development to scientific writing. Therefore, I can always benefit from your suggestions. I want to say I am proud to be your student.

A lot of help was also provided by my colleagues from the department of "Catalyst Discovery and Reaction Engineering" led by Dr. David Linke in LIKAT. Some of them are familiar with the fundamentals of catalyst synthesis and taught me valuable experience. Some of them know a lot about reaction engineering and helped me solve problems during catalyst tests. Dr. Vita A. Kondratenko, thank you very much for performing TAP experiments and giving me valuable suggestions/comments for our joint work. Dr. Martin Holena, thank you for our collaboration in statistical analysis, which is an important part of this thesis. I will not forget the guidance in setup operation received from Dr. Martin Fait, Dr. Uwe Rodemerck, Dr. Mariana Armbruster. They always helped me to repair our reaction setup. In this regard, Mr. Axel Radtke who is responsible for the technical services in LIKAT is also acknowledged. Many thanks to Dr. Martin Fait, you have given numerous suggestions and guidance in my daily life and research since my first day in LIKAT. I would also like to acknowledge Andrey Skrypnik, Nils Ortner, Laura Kraußer for the effective cooperation on the topic of CO_2 hydrogenation in the past three years. We discussed our results, exchanged ideas, and overcame difficulties together. Dr. Dan Zhao, Dr. Shanlei Han, Karin Buchholz, Dr. Tatiana Otroshchenko, Dr. Yuming Li, Qiyang Zhang, Zeynep Aydin, Anna Zanina, Aleksandr Fedorov, many thanks for your help during my experimental research.

Part of characterization experiments for catalysts were performed by the colleagues from the Analytical Services Group in LIKAT. Their outstanding work and professional knowledge

Zusammenfassung

Die Emissionen des Treibhausgases Nummer eins, Kohlendioxid (CO_2), haben seit der industriellen Revolution stark zugenommen. Neben der Verringerung der CO_2-Emissionen bietet dessen Verwendung als Ausgangsstoff zur Herstellung von Chemikalien eine ergänzende Strategie zur Schließung des anthropogenen Kohlenstoffkreislaufs. Fe-basierte Katalysatoren werden in der Regel zur Herstellung von Chemikalien und Kraftstoffen durch CO_2-Hydrierung verwendet. Dieser Prozess wird auch als CO_2-Fischer-Tropsch-Synthese (CO_2-FTS) bezeichnet. Aus mechanistischer Sicht besteht dieser aus drei allgemeinen Reaktionen: (i) die Umwandlung von CO_2 in CO durch die umgekehrte Wassergas-Shift-Reaktion (RWGS), (ii) die anschließende CO-FTS-Synthese und (iii) die direkte CO_2-Methanisierung. Aufgrund des breiten Produktspektrums der CO_2-FTS an Fe-basierten Katalysatoren ist es äußerst wichtig, die selektivitätsbestimmenden Faktoren zu verstehen.

Um die dafür erforderlichen Grundlagen zu ermitteln, die oft in der Vielzahl an veröffentlichten Daten verborgen sind, wurde ein mathematischer Ansatz gewählt. Zu diesem Zweck wurden Literaturdaten gesammelt und anschließend mittels Regressionsbäumen, ANOVA und Mittelwertvergleichen analysiert. Die Elektronegativität des Dotierungsmittels für Katalysatoren auf Fe-Basis wurde als Deskriptor für den CO_2-Umsatz und die CH_4-Selektivität identifiziert. Darüber hinaus wurde festgestellt, dass die Kombination von Alkali- und Übergangsmetallen als Promotoren für Fe_2O_3 vielversprechend ist, um die Selektivität zu C_{2+}-Kohlenwasserstoffen und das Verhältnis von Olefinen zu Paraffinen zu verbessern. Der entwickelte 0.4Mn-K/Fe-Katalysator zeigte eine Selektivität zu C_2-C_4-Olefinen von 30,4 % bei einem CO_2-Umsatz von 42,3 % bei 300 °C. Die Selektivität zu C_{2+}-Kohlenwasserstoffen betrug 83,1 %.

Es ist bekannt, dass Alkalimetallpromotoren für Katalysatoren auf Fe-Basis die Produktverteilung der CO_2-FTS optimieren. Die Grundlagen ihrer Wirkung sind jedoch bisher ungeklärt. Die im Rahmen dieser Arbeit durchgeführte transiente kinetische Analyse ergab, dass der Alkalimetallpromotor eine entscheidende Rolle bei der Adsorption/Aktivierung von H_2 und CO/CO_2 spielt. Die Elektronegativität des Alkalimetallpromotors wurde erfolgreich mit der intrinsischen Aktivität von Eisencarbiden/Fe_3O_4, den Produktselektivitäten sowie den Geschwindigkeitskonstanten der Elementarschritte der CO- und CO_2-Aktivierung korreliert.

Diese Arbeit trug auch zum Verständnis des Zusammenspiels zwischen den physikochemischen Eigenschaften von promotorfreien Katalysatoren auf Fe-Basis und der

katalytischen Performance bei. Die Reduzierbarkeit von Fe_2O_3 wurde als Deskriptor für die Adsorptions- und Reaktivitätseigenschaften des *in situ* daraus gebildeten Fe_5C_2 in der CO_2-FTS vorgeschlagen. Die Ergebnisse der Anpassung von Mößbauer-Spektren deuten darauf hin, dass sich die Carbide im C/Fe-Verhältnis zueinander unterscheiden, welches durch die Reduzierbarkeit von Fe_2O_3 und die Reduktionstemperatur des Katalysators gesteuert werden kann. Dieses Verhältnis scheint die Lebensdauer und die Konzentration von Intermediaten zu beeinflussen, aus denen CO und CH_4 gebildet wird, was für die Produktselektivität von Bedeutung ist.

Abstract

The emissions of the number one greenhouse gas, carbon dioxide (CO_2), have strongly increased since the industrial revolution. Besides reducing CO_2 emissions, its usage as a feedstock to produce chemicals offers a complementary strategy to close the anthropogenic-carbon cycle. Fe-based catalysts are typically used to produce chemicals and fuels through CO_2 hydrogenation. This process is also known as CO_2 Fischer-Tropsch synthesis (CO_2-FTS). From a mechanistic viewpoint, it consists of three general reactions: (i) CO_2 conversion into CO through the reverse water gas shift (RWGS) reaction, (ii) the following CO-FTS synthesis and (iii) direct CO_2 methanation. Due to the broad product spectrum of CO_2-FTS over Fe-based catalysts, it is highly important to understand selectivity-determining factors.

To provide the required fundamentals often hidden in the vast body of reported data, a mathematical approach was applied. To this end, literature data were collected and then analyzed by regression trees, ANOVA, and comparison of mean values. The electronegativity of dopant for Fe-based catalysts was identified as a descriptor for CO_2 conversion and CH_4 selectivity. In addition, combining alkali and transition metals as promoters for Fe_2O_3 was concluded to be promising to enhance C_{2+}-hydrocarbons selectivity and the ratio of olefins to paraffins. The developed 0.4Mn-K/Fe catalyst displayed the selectivity to C_2-C_4 olefins of 30.4% at CO_2 conversion of 42.3% at 300 °C. The selectivity to C_{2+}-hydrocarbons was 83.1%.

Alkali metal promoters for Fe-based catalysts have been known to optimize the product distribution in CO_2-FTS. However, the fundamentals of their effects have not been clarified. The transient kinetic analysis carried out in this thesis identified that alkali promoter plays a crucial role in the adsorption/activation of H_2 and CO/CO_2. The electronegativity of alkali metal promoter was successfully correlated to the intrinsic activity of iron carbides/Fe_3O_4, product selectivity as well as the rate constants of elementary steps of CO and CO_2 activation.

This thesis also contributed to understanding of the interplay between physicochemical properties of promoter-free Fe-based catalyst and catalytic performance. The reducibility of Fe_2O_3 was suggested to be a descriptor for adsorptive and reactivity properties of therefrom *in situ* formed Fe_5C_2 in CO_2-FTS. The results of fitting of Mössbauer spectra suggest that the carbides differ in the C/Fe ratio, which can be controlled through the reducibility of Fe_2O_3 and catalyst reduction temperature. This ratio seems to affect the lifetime and the concentration of intermediates leading to CO and CH_4, which are relevant for product selectivity.

Table of Contents

List of Abbreviations

AM	Alkali metal
ANOVA	Analysis of variance
BET	Brunauer-Emmett-Teller method
BTX	Benzene, toluene and xylenes
DFT	Density functional theory
DRIFTS	Diffuse reflectance infrared Fourier transform spectroscopy
EXAFS	Extended X-ray absorption fine structure
FTIR	Fourier-transformed infrared spectroscopy
FTS	Fischer-Tropsch synthesis
GHSV	Gas hourly space velocity
HER	Hydrogen evolution reaction
ICDD	International center of diffraction data
ICP-OES	Inductively coupled plasma optical emission spectroscopy
IS	Isomer shift
MSI	Metal-support interaction
MTA	Methanol to aromatics
MTH	Methanol to hydrocarbons
MTO	Methanol to olefins
m-ZrO_2	Monoclinic ZrO_2
NAP-XPS	Near-ambient pressure X-ray photoelectron spectroscopy
NP	Nanoparticles
OBE	Oxygen binding energy
OCM	Oxidative coupling of methane
OXZEO	Oxide and zeolite
PX	P-xylene
RDS	Rate-determining step
RWGS	Reverse water gas shift reaction
SA	Single atom
SAED	Selected area electron diffraction patterns
SMSI	Strong metal-support interaction
SSITKA	Steady-state isotopic transient kinetic analysis
TAP	Temporal analysis of products
TEM	Transmission electron micrographs
TGA	Thermogravimetric analysis
TMC	Transition metal carbide
TOF	Turnover frequency
TOS	Time on stream
TPD	Temperature-programmed desorption
TPH	Temperature-programmed hydrogenation
TPR	Temperature-programmed reduction
t-ZrO_2	Tetragonal ZrO_2
WGS	Water gas shift reaction
XANES	X-ray absorption near edge structure
XPS	X-ray photoelectron spectroscopy
XRD	X-ray diffraction

1. Introduction

1.1. CO_2 emission and climate change

It is well documented that the emission of greenhouse gases is closely associated with the climate change evidenced by substantial harmful phenomena: the warming of the earth's atmosphere, sea-level rise, ocean acidification, more droughts and heat waves, etc.[1-4] Carbon dioxide accounts for about 76 % of total greenhouse emissions[5-6] and is primarily produced from fossil fuel and industrial process[7]. The global atmospheric CO_2 concentration increased strongly over the past 100 years (Figure 1-1), starting from the second industrial revolution, and reached 418 ppm[8] in January 2022. Driven by the increased CO_2 level, the global average surface temperature has risen about 1 °C since the beginning of industrial era (1850).[9]
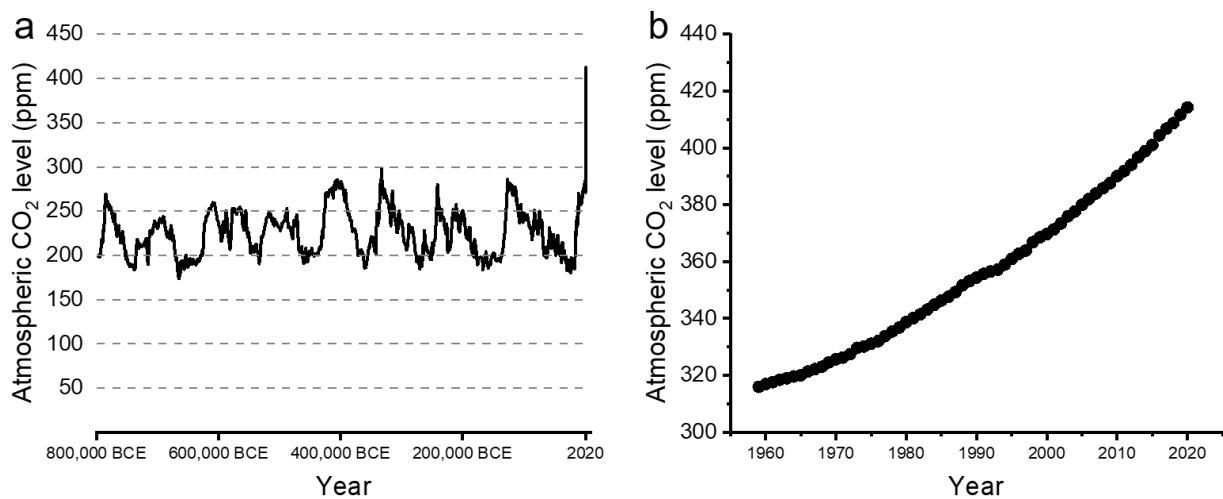
Figure 1-1 The global average carbon dioxide (CO_2) concentration in the atmosphere in parts per million (ppm) over (a) the past 800,000 years and (b) the past few decades (Data source: https://www.esrl.noaa.gov/gmd/ccgg/trends/data.html). BCE refers to before the common era.

To mitigate the growing climate changes and other global greenhouse effects, a consensus was achieved by all countries under the 2015 Paris agreement[10], that is to limit the planet´s temperature increase by the end of this century to 1.5-2 °C compared with the preindustrial level. Under such background, as of 2021 more than 100 countries have committed to reach carbon neutrality by 2050 or 2060.[11]

1.2. The heterogeneous hydrogenation of CO_2

Carbon dioxide utilization, a "one stone and two birds" approach, is appealing academic and industrial attentions to solve environmental and energy problems[12-15], especially in the last ten

years (Figure 1-2). Due to the inert chemical nature of CO_2 ($\Delta G^o_{298\ K}$ = -396 kJ mol^{-1}), a second co-reactant with higher Gibbs free energy, like H_2, is required.[16] Under this consideration, the electro-catalyzed water splitting with renewable energy (solar, wind, etc.) is the most ideal approach to produce hydrogen.[17-18] In this context, CO_2 hydrogenation with green H_2 is considered to be a promising method for the production of valuable chemicals and fuels[19-23], which does not need fossil raw materials and thus contributes to sustainable development. As shown in Figure 1-2, this topic, CO_2 hydrogenation, is gaining an increased interest as reflected by the growing number of publications in the past decade.
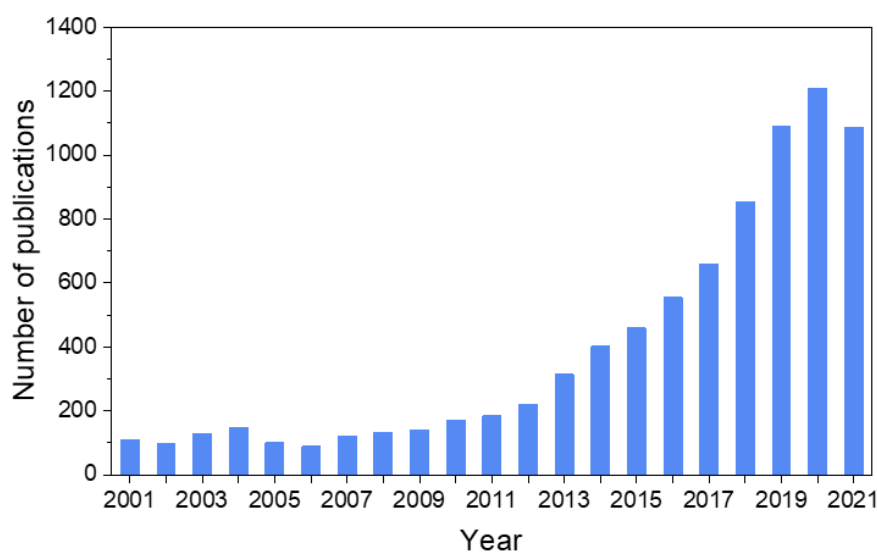
Figure 1-2 Number of publications on the topic of "CO_2 hydrogenation" searched on Web of Science until October of 2021.

It is indisputable that regulating product spectrum for industrially relevant reactions is of considerable research and economic values. However, various products can be formed from CO_2 hydrogenation due to the complex rection network involved in this chemical conversion process.[24-27] Therefore, design of active and particularly selective catalysts is still challenging. Depending on the desired products, catalysts based on transition metals[28-31], noble metals[32-35], metal oxides[36-39], transition metal carbides[40-43], as well as dual-functional catalysts[44-47] have been employed for thermo-catalytic hydrogenation of CO_2.

1.2.1. CO production-oriented CO_2 hydrogenation

CO_2 hydrogenation *via* the reverse water gas shift reaction (RWGS, Equation 1-1) is a crucial process for producing CO which is an important C_1 platform chemical and can be used in various industrial processes such as olefin hydroformylation, methanol synthesis and Fischer-Tropsch synthesis (FTS). Due to its endothermic feature, the RWGS reaction is favoured at

high reaction temperatures. The equilibrium CO_2 conversion increases with the increase in reaction temperature but is not affected by total pressure, because the number of molecules does not change.

$$CO_2 + H_2 \leftrightarrow CO + H_2O \quad \Delta H_{298K} = 41.2 \text{ kJ mol}^{-1} \qquad \text{Equation 1-1}$$
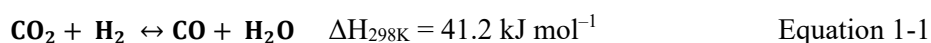
Based on the above considerations, a reaction temperature, usually higher than 700 °C, is needed to ensure high CO concentration.[48] Rational design of selective catalysts for the RWGS reaction is challenging due to the side reactions like Sabatier reaction.[49-50] On the other hand, a highly effective catalyst is needed to ensure that the reaction can be efficiently operated at low temperature and accordingly decrease energy consumption. Another advantage of low operation temperature is the possibility to avoid repaid catalyst deactivation due to coke deposition or/and metal sintering, which usually occur at high temperatures.

1.2.1.1. Transition metal/metal oxide catalysts

Fe-based catalysts have been extensively investigated for the RWGS reaction since the beginning of 1980s and Fe_3O_4 was regarded as main active phase in this reaction.[51-61] Weatherbee and Bartholomew established that CO was directly formed from CO_2 over Fe/SiO_2 catalyst with an ultrahigh feed space velocity, while the activity of this catalyst was quite low.[51] When a low feed space velocity and elevated pressure were employed, a higher activity of Fe/SiO_2 catalyst could be achieved at the expense of a decrease in CO selectivity. The introduction of promoter (e.g., Cu, Ni, Co, Mo, Cs) was reported as a useful strategy for tuning activity and selectivity of Fe-based catalysts.[58-59, 62-63] Sengupta et al. reported that Co and Ni promoters favored the reduction of Al_2O_3-supported iron oxide and therefore enhanced the reaction activity based on the redox mechanism of the RWGS reaction.[58] A similar effect of Ni promoter was observed by Yang et al.[59]. However, the authors found that the addition of Ni was detrimental to the reducibility of iron oxide and the enhancing effect was attributed to a strong interaction of Fe with Ni, which was claimed to influence CO_2 adsorption and activation. Additionally, Cu was identified as an effective secondary metal in Fe-based catalysts for improving both activity and CO selectivity even though the origins of such promotion effect is not clear so far.[55, 59, 63] Recently, the formation of $CuFe_2O_4$ and its redox properties were proposed to be important for improving catalyst performance in the RWGS reaction.[63]

As one of the most often used metal-based catalysts, supported Ni-based catalysts have been proved to be effective for CO_2 upgrading to CO.[64-68] The effect of Ni particle size on product selectivity was investigated by different groups.[67, 69-73] It was revealed that the different ability

of small Ni cluster (near to atomically dispersed Ni, 0.5 wt.% Ni/SiO_2) and large Ni particle (9 nm, 10 wt.% Ni/SiO_2) to activate H_2 results in distinct reaction behavior of monodentate formate which was identified by FTIR spectra as the key reaction intermediate.[69] Goncalves et al.[70] prepared a catalyst with highly dispersed Ni on silica (2.4 wt.% of Ni) using a magnetron sputtering deposition method, and the catalyst showed CO_2 conversions close to the thermodynamic equilibrium conversions under different H_2/CO_2 ratio and at various reaction temperatures. It was also reported that a Ni single-atom catalyst was highly active and stable in the RWGS reaction.[68] In this work, Ni^{2+} was incorporated into MgO structure by controlled substitution of Mg^{2+} to form a solid solution $Ni_xMg_{1-x}O$, where Ni loading could achieved up to 10 atom %, and the CO formation rate was linearly correlated to the concentration of surface isolated Ni. In addition to the nature of Ni species, the kind of support may play a crucial role in determining catalyst performance.[19, 74] Among many kinds of support materials, CeO_2 reveals a great potential as support due to its excellent oxygen storage capability[75-76]. The high activity in the RWGS reaction of $Ni-CeO_2$ catalyst system was attributed the synergy between oxygen vacancies in cerium oxide and highly dispersed Ni species, while CH_4 formation is favored over bulk NiO.[64, 77]

$Cu-ZnO/Al_2O_3$, which is known as a classical catalysts for the low-temperature CO shift reaction[78-81] and has been industrially employed for more than half a century, is also active and selective for the RWGS reaction[82-85] without any CH_4 formation. For Cu-ZnO or $Cu-ZnO/Al_2O_3$ catalyst systems, the ratio of Cu:ZnO has been examined as a crucial parameter for achieving desired catalytic performance.[86-87] Stone et al.[86] found that the highest CO_2 conversion was obtained over the Cu-ZnO catalyst with a Cu/Zn molar ratio of 30/70, while CO_2 conversion increased linearly with the content of Cu in the $Cu-ZnO/Al_2O_3$ catalysts. The activity from both two groups of catalysts could be correlated to the Cu surface area. A volcano-type relationship between CO formation rate and Cu content in Cu-ZnO catalyst was also established by Galvan and co-authors.[87] However, these authors did not find any relationship between the activity and the surface area of Cu. They proposed that the kind of interface between ZnO and Cu, which was influenced by the Cu:ZnO ratio, determines catalytic performance. As aforementioned, higher reaction temperatures are needed from a thermodynamic point of view to achieve industrially required level of CO_2 conversion. However, Cu species suffer from heavily sintering at high temperatures. On the other hand, reduced Cu is easily oxidized by CO_2 and H_2O[85]. These drawbacks of Cu-based catalysts lead to a rapid deactivation in the RWGS reaction and restricted their further implementation for industrial purpose. Numerous studies have been reported to resolve this problem and mainly

focused on adding promoter(s) or optimizing support.[88] Chen et al.[85, 89] improved the stability of Cu-based catalysts by adding 0.3 wt.% Fe as a promoter to 10 wt.% Cu/SiO_2. β-Mo_2C was employed as an efficient support to prepare highly dispersed surface Cu species catalyst without any other structural promoter.[90] Such catalyst displayed higher activity compared to traditional Cu-based or Pt-based catalysts due to an efficient Cu-Mo_2C interface. Moreover, the CO_2 conversion over 1 wt.% Cu/β-Mo_2C slightly decreased from 42% to 35% after 45h on stream at 600 °C, which was attributed to the high stability of dispersed Cu species.

Co-based catalysts were also proved to be active in CO_2 hydrogenation including the RWGS reaction.[29, 91-95] A 10 wt.% Co-CeO_2 catalyst prepared through a coprecipitation method was reported by Wang et al.[91], and this catalyst demonstrated high CO_2 conversion with CO selectivity > 90%. By adding small amounts of K, the CO_2 conversion increased further and was close to the equilibrium value, while the formation of CH_4 was completely inhibited as the active sites for methanation were poisoned by K. In a separate study,[96] these authors also optimized Co content in CeO_2 supported catalysts. The results indicate that the interaction between Co particle and Ce_2 is vital for catalytic performance. When the content of Co exceeded 5%, larger Co particles are formed and favor the CO_2 methanation reaction. Further, they prepared highly dispersed Co species on mesoporous CeO_2 support using a colloidal solution combustion method.[92] A strong interaction between Co species and CeO_2 endowed the 5%Co-CeO_2-M catalyst with high activity and excellent stability. The structure of support for Co-based catalyst has a strong influence in the product distribution of CO_2 hydrogenation. For example, two kinds of TiO_2, anatase and rutile, were employed to support Co and the obtained Co/TiO_2 catalysts were evaluated in CO_2 hydrogenation.[93] Interestingly Co/anatase-TiO_2 was selective for the RWGS reaction with CO selectivity of about 90%, while only CH_4 was formed over Co/rutile-TiO_2. Further mechanistic results pointed out that the reaction pathway of hydrogenation of formate, the key intermediate identified by DRIFT results, to CH_4 dominated for Co/rutile-TiO_2. On the contrary, the intermediate, CO, could desorb easily on Co/anatase-TiO_2.

1.2.1.2. Noble metal-based catalysts

Transition metal oxides, especially reducible metal oxides, supported noble metal catalysts were also extensively investigated due to their high activity towards RWGS reaction. In order to achieve desired CO selectivity and suppress its further hydrogenation to CH_4, a promising catalyst should favor desorption of adsorbed CO and hinder its dissociation. Huang et al. [97] studied the RWGS reaction over TiO_2-supported Ir-, Pt- or Au-containing catalysts. DFT calculations showed that stepped Au has a higher CO dissociation barrier compared with Ir

and Pt. Au/TiO$_2$ displayed the highest CO selectivity in catalytic tests. The authors proposed that the difference between CO dissociation barrier and CO desorption energy could be a descriptor for the selectivity to CO in the RWGS reaction.

Particle size of noble metals is an important parameter for their catalytic performance in the RWGS reaction.[35, 98] The effect of Ru particle size on product selectivity in CO$_2$ hydrogenation was investigated by Kwak and co-authors.[35] Both CO and CH$_4$ were produced over Ru/Al$_2$O$_3$ with atomically dispersed Ru, while CH$_4$ was the main product formed over supported 3D Ru clusters. The agglomeration of Ru small particles during the RWGS reaction was accompanied by an increase in the CH$_4$ selectivity. The catalytic performance of Pt single atoms was also influenced by their chemical environment. Fresh Pt single atoms with high Pt-O coordination displayed a low activity towards CO formation because the accessibility of Pt atom was limited.[99] Through a reduction-oxidation cycle, the Pt-O coordination was lowered, and more Pt atoms became available, which enhanced the activity by five times. As reported by Wang et al.[100], this strategy, tuning the micro-environment of active sites, was also successfully employed for Rh-containing catalysts which were generally regarded as methanation catalysts. In that study, Rh nanoclusters were enveloped in silica MFI zeolite (silicate-1) or HZSM-5. The former catalyst (Rh@S-1) displayed a CO selectivity of 79.8% at CO$_2$ conversion of 51.6%, whereas the latter mainly produced CH$_4$ with selectivity of 98.2% at CO$_2$ conversion of 68.2%. The amount of acidic site was identified as a critical role in hydrogen spillover and the formation of active hydrogen species.

The phenomenon of metal-support interaction (MSI) has been widely studied for tuning catalytic performance of supported noble metal catalysts in the RWGS reaction. Ma´s group proposed that the chemical state of metal species influenced by strong metal-support interaction (SMSI) played a dominant role in determining selectivity of CO$_2$ hydrogenation, while single-atom catalyst was not necessary.[101] CO was exclusively produced in CO$_2$ hydrogenation over Ir/CeO$_2$ catalyst with a decrease in the size of Ir nanocluster from 2.5 nm to 1 nm, while the former possessed CH$_4$ selectivity of 88%. The authors believed that more oxygen could be incorporated into Ir surface with a smaller size due to the SMSI effect. Thus, it was proved that the chemical sate of metal species was a crucial factor for their catalytic properties. A similar conclusion was also made by Zhang et al.[102] who used different reduction temperatures to induce SMSI effect. After catalyst reduction at high temperatures, Ir nanoparticles were overcoated by TiO$_x$. The catalyst with such structure preferred to form CO without the deep hydrogenation of CO/CO$_2$ to CH$_4$. It was recently reported that the electron state of Ru can influence the product selectivity of CO$_2$ hydrogenation.[103] When anatase-TiO$_2$

(a-TiO$_2$) was used as support, hydrogen spillover from Ru to a-TiO$_2$ was more pronounced accompanied by a charge transfer from Ru to the support, which reduced the ability of Ru to adsorb CO. However, hydrogen spillover was less favorable over Ru/rutile-TiO$_2$. The electron-rich Ru promoted CO adsorption, resulting in CO hydrogenation to CH$_4$.

1.2.1.3. Transition metal carbide catalysts

Transition metal carbides (TMCs), in particular molybdenum carbide, have been proved to be highly active and selective catalysts in CO$_2$ hydrogenation toward CO by numerous studies.[41-42, 104-109] On the basis of the pervious knowledge regarding the functionality of Mo$_2$C obtained from other reactions (water gas shift reaction, reforming reaction, and hydrogenation), Chen´s group[42] employed Mo$_2$C material for the RWGS reaction. A CO$_2$ conversion of 8.7 % with CO:CH$_4$ ratio of 14.5 was achieved over Mo$_2$C catalyst, which is comparable or superior to noble metal-based catalyst. The kind of crystal structures of molybdenum carbide may influence their performance in CO$_2$ hydrogenation.[104, 110] In this regard, Rodriguez et al. reported higher activity of β-MoC$_y$ with CO and CH$_4$ being the main products in comparison with α-MoC$_{1-x}$ catalyst which mainly produced CH$_3$OH.[104] C/Mo ratio was regarded as a crucial parameter in determining the product selectivity of molybdenum carbides.[109, 111] For example, Figueras et al. studied CO$_2$ adsorption and activation on two Au(111) supported MoCx catalysts which differed in the C/Mo ratio. Their catalytic performance in the RWGS reaction was also evaluated.[109] Direct CO$_2$ dissociation was established over carbon deficient MoC$_{0.6}$/Au(111) catalyst which mainly produced CO and CH$_4$. However, no CH$_4$ was detected over MoC$_{1.1}$/Au (111) because the CO$_2$ dissociation was not possible without H$_2$.

Various strategies, such as tuning morphology, changing the grain size and creating Mo$_2$C-containning heterostructures, have been developed to improve the efficiency of molybdenum carbide towards CO production from CO$_2$. Ma et al.[112] prepared dispersed Mo$_2$C clusters with sub-nano size (0.5 nm) on N-doped carbon/alumina support, which displayed an unexpected activity of 184.4 μmol g$_{Mo2C}^{-1}$ s^{-1} with 99.5 % CO$_2$ selectivity, and outperformed the bulk Mo$_2$C catalyst. A Mo$_2$C/Mo$_2$N nanowire composite was synthesized from two precursor components (Mo$_6$S$_2$I$_8$ and Mo$_3$O$_{10}$(C$_6$H$_8$N$_2$)·2H$_2$O).[113] Compared to individual Mo$_2$C and Mo$_2$N, the composite structure showed higher CO$_2$ conversion and CO selectivity. Recently, Zhou et al.[41] introduced a two-dimensional Mo$_2$C prepared from Mo$_2$CT$_x$ (T$_x$: O, OH and F) as a promising RWGS catalyst. Reductive treatments under different conditions of Mo$_2$CT$_x$ produced final catalysts with different termination groups (only Mo-terminated or abundant T$_x$ groups). The resulted T$_x$ free catalyst 2D-Mo$_2$C showed much higher CO chemisorption

capacity and superior activity for the RWGS reaction compared to β-MoC$_2$, Cu-ZnO-Al$_2$O$_3$ and Mo$_2$CT$_x$.

Besides molybdenum carbides, carbide materials based on other transition metals (Ti, Zr, Nb, Ta, W and V) were also evaluated in the RWGS reaction. Porosoff and co-workers[106] proposed a descriptor, oxygen binding energy (OBE) on transition metal carbide (TMC) surface, for CO$_2$ reduction with H$_2$. The TOF value of CO$_2$ conversion increased with a decrease in the OBE of TMC. Specially, Mo$_2$C has the highest activity among the studied carbide catalysts. Moreover, they found that the ability of catalyst to remove surface oxygen was also important for completing the whole catalytic cycle. Pajares et al.[114] studied the importance of carbon vacancies in vanadium carbide-based catalyst in the RWGS reaction. The adsorption and dissociation of H$_2$ and CO$_2$ are much more favorable over carbon vacancies enriched catalyst (V$_8$C$_7$) in comparison to stoichiometric sample (VC) as confirmed by DFT calculations. Such features of V$_8$C$_7$ sample resulted in a higher activity and CO selectivity (> 99 %). Moreover, this excellent performance was kept for 100 h at 723 K without obvious loss in CO$_2$ conversion.

1.2.1.4. Mechanistic concepts of the RWGS reaction

The mechanism of RWGS reaction has been extensively studied but is still controversial. Up to date, redox mechanism and associative mechanism, have been generally accepted. In their pioneering work, Fujita et al.[82] concluded that the RWGS reaction operates through a direct dissociation of CO$_2$ over Cu/ZnO catalyst because the initial rate of CO formation was independent on the presence or absence of H$_2$. Because of CO formation, metallic Cu was oxidized to Cu(I) oxide as confirmed by N$_2$O titration tests, XP and FTIR spectra. The formed Cu(I) oxide could react with hydrogen yielding H$_2$O. Accompanied with the reaction process, thus, surface oxidation and reduction were involved. This reaction pathway was called as redox mechanism[83, 115]. However, the redox mechanism cannot satisfactorily explain some experimental findings reported later. For example, a monolayer of formate was observed over Cu(110) single crystal and poly-crystalline Cu after CO$_2$ hydrogenation.[116] Moreover, Chen et al.[84, 117] showed that the CO formation rate of supported Cu catalyst using CO$_2$/H$_2$ feed was much higher in comparison with CO$_2$ alone, which indicated that the role of H$_2$ was not only to reduce oxidized Cu species. The RWGS reaction was studied over Pt/CeO$_2$ catalyst using temporal analysis of products (TAP) technique to distinguish the possible reaction mechanisms.[118] The highest CO yield was obtained when CO$_2$ and H$_2$ were consecutively pulsed with a H$_2$ delay time of 1s, indicating that this reaction followed according to an associative reaction pathway.

The development of advanced *in situ/operando* techniques is providing a chance to learn how the catalyst work under more realistic reaction conditions and enables researchers to investigate various reaction processes including the RWGS reaction. For example, formate species was observed directly during *in situ* DRIFTS experiments over molybdenum carbides catalysts.[119] However, the presence of formate cannot guarantee the dominant role of formate decomposition (associative pathway) in CO formation.[100, 103, 120-121] Recently, Su et al. investigated the RWGS reaction over Pt(111) model catalyst using ambient pressure X-ray photoelectron spectroscopy (AP-XPS).[122] CO adsorbates and adsorbed oxygen species were spectroscopically identified even in the absence of H_2, that is in a good agreement with the dissociation mechanism of CO_2 activation. The dominance of these two mechanisms was also strongly affected by the composition of catalysts. The reaction mechanism of the RWGS reaction was studied by Lobo et al. using gas-switching experiments over Fe/Al_2O_3 and Fe-K/Al_2O_3 catalysts.[54, 57] For the former material, CO was only formed after the switch from H_2 to CO_2, but not after switch from CO_2 to H_2. This indicated that the RWGS reaction proceeded through a redox pathway. However, CO could be observed both after switch from CO_2 to H_2 and after switch from H_2 to CO_2 over Fe-K/Al_2O_3 catalyst. Furthermore, carbon-containing species was observed in FTIR experiment with this catalyst. Thus, the authors concluded that the presence of K opened another reaction pathway, associative mechanism, in addition to redox mechanism.

1.2.2. CH_4 production-oriented CO_2 hydrogenation

CO_2 methanation, also known as the Sabatier reaction (Equation 1-2), is exothermic and accordingly favored at lower temperatures. Even though it is highly favorable thermodynamically, its kinetic barrier is high due to eight electrons being involved in this reaction. Therefore, it is of importance to develop active and selective catalysts for accelerating the reaction rate. Both non-noble metals and noble metals, particularly Ni, Co, Ru, and Rh, have been widely investigated as active species on the surface of reducible or irreducible metal oxide supports.

$$\mathbf{CO_2 + 4H_2 \rightarrow CH_4 + 2H_2O} \quad \Delta H_{298K} = \text{-165 kJ mol}^{-1} \quad\quad\quad \text{Equation 1-2}$$
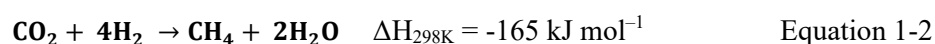
1.2.2.1. Non-noble metals-based catalysts

As an earth-abundant metal, Ni-containing catalysts have been extensively studied for CO_2 methanation due to its high activity towards this reaction. Falconer and co-authors studied the adsorption and reaction behavior of CO_2 over Ni/SiO_2 catalyst because silica support is inert for CO_2 adsorption.[123] It was revealed that CO_2 adsorbed on Ni in a dissociative manner with

the formation of CO and O. This is also the first step of CH_4 formation from CO_2 because CO_2 pre-adsorption and CO pre-adsorption resulted in the same CH_4 formation temperature and rate determined from temperature-programmed reaction experiments. However, the adsorption of CO_2 was much slower than the CO adsorption.

CO_2 hydrogenation over Ni-based catalysts is a structure-sensitive reaction.[73, 124-128] It was accepted that structure sensitivity could affect the reaction mechanism, and thus influence the activity and selectivity. Vogt et al.[73] prepared a series of silica-supported Ni nanoparticles with different sizes of 1-7 nm and studied the size effect on CO_2 hydrogenation using *operando* FTIR and quick-XAS technique. The RWGS reaction was determined to be primary reaction over Ni catalysts with the consecutive hydrogenation of adsorbed CO species that is the rate-determining step. As CO is an important intermediate in CO_2 hydrogenation, its adsorption strength plays a critical role for catalyst activity. The authors further established that the strength of CO adsorption decreased with a decrease in the Ni particle size, then the hydrogenation ability for adsorbed CO increased. Crystal engineering techniques were also employed to improve the performance of Ni-based catalysts in CO_2 hydrogenation. Liu et al.[126-127] prepared TiO_2- or ZrO_2-supported Ni catalysts (Ni(111)/TiO_2-P or Ni(111)/ZrO_2-P) with Ni (111) as the main exposing facet using plasma-assisted decomposition of Ni precursor. The obtained catalysts were compared with their counterparts (Ni/TiO_2-C or Ni/ZrO_2-C) with multi-facets in terms of activity. For example, Ni(111)/ZrO_2-P displayed a CO_2 conversion of as high as 74% at 300 °C, which was much higher than that of the latter catalyst Ni/ZrO_2-C (CO_2 conversion of 35%).[132]

In addition to the nature of active sites, the kind of support and the presence of promoters can strongly intervene the activity and product selectivity. Recently, Bao´s group found that Ni could be encapsulated by a thin layer of titania after a high-temperature (500 °C) reduction of Ni/t-TiO_2 due to the SMSI effect.[129] If the titania was treated in NH_3 or H_2, before used to support Ni, the obtained catalysts (Ni/t-TiO_2-NH_3 and Ni/t-TiO_2-H_2) did not undergo the SMSI phenomenon although after high temperature reduction. Therefore, CO_2 methanation exclusively proceeded probably because of the strong adsorption of CO and H_2 over these catalysts. It was revealed that the Ti^{3+} existed in the bulk of Ni/t-TiO_2-NH_3 and Ni/t-TiO_2-H_2 prohibited the occurring of any SMSI effect. Even though SiO_2[130-136] and Al_2O_3[137-141] have been widely used to support Ni as methanation catalysts, some other metal oxides, e.g., CeO_2, ZrO_2, TiO_2 and MgO, were also employed as support and even displayed more advantages.[126, 142-144] For example, catalytic activity of Ni/CeO_2 in terms of CO_2 methanation at low reaction temperature was proved to be higher than that of Ni/SiO_2 and Ni/Al_2O_3.[144-145] Stronger CO_2

chemisorption on Ni/CeO_2, induced by the presence of oxygen vacancies, was regarded as the main reason for the higher activity.[144]

Various transition metals/metal oxides were used to investigate their promotion effects for Ni-based catalysts on CO_2 methanation.[16, 27, 146] Fe[147], Co[148-149], La[150-151], and Mn[152-153] have been identified as promoters improving CH_4 yield because of higher Ni dispersion and enhanced CO_2 adsorption ability. For example, Vrijburg et al.[152-153] systematically investigated the promotion effect of Mn for Ni-based catalysts on CO_2 methanation using advanced spectroscopic characterization and DFT calculations. It was found that the decoration of metallic Ni by MnO improved CO_2 adsorption and activation, benefiting from the interfacial sites between MnO clusters and Ni species.

Besides working as promoters for Ni-based catalysts, Co and Fe were also reported to be active species in CO_2 methanation.[29, 154-155] Recently, Parastaev et al.[29] established that the activity of cobalt in CO_2 hydrogenation was strongly influenced by the particle size of support, ceria-zirconia. In this work, the authors found that metal-support interactions could be optimized *via* varying the particle size of ceria-zirconia. In detail, the ceria-zirconia supports with a middle size (20-30 nm) stabilized cobalt nanoparticles during reduction, facilitated the formation of oxygen vacancies in ceria, and promoted oxygen spillover from cobalt to the support. With above reasons, a high CO_2 methanation activity was obtained over optimized catalysts. CO_2 methanation over iron-based catalysts was reported by Kureti and coauthors.[154-157] Reactive surface carbon species and iron carbides phases could strongly influence the reaction activity.

1.2.2.2. Noble-metal-based catalysts

Due to their high activity and selectivity in CO_2 methanation, Rh- or Rh-based catalysts have been widely studied for many years. Numerous works revealed that the kind of support, the size of supported metal species, reduction and reaction conditions, as well as metal-support interactions are important factors influencing catalytic performance.

Forty years ago, Iizuka et al.[158] compared Rh-containing catalysts on the basis of different supports (ZrO_2, Al_2O_3, SiO_2 and MgO) in CO_2 hydrogenation. They found that Rh/ZrO_2 revealed the highest activity, while Rh/MgO was the least active catalyst. The activity order of $Rh/TiO_2 > Rh/Al_2O_3 > Rh/SiO_2$ was established by Solymosi er al.[159]. The observed effect of the kind of support was attributed to the extent of electronic interactions between the supported metal and the support. Scire et al.[160] found that the selectivity of CH_4 over Ru/ZSM-5 catalyst was higher than that over Ru/SiO_2. Based on FTIR spectra of adsorbed

CO species, more oxidized Ru species was found on the zeolite support compared with the SiO$_2$ support. Ru species with a higher positive polarization resulted in a weaker Ru-CO bond.

CO$_2$ methanation over precious metal-based catalysts was regarded as a structure-sensitive reaction. Thus, size, shape, composition, and distribution of metals could influence their catalytic performance. Guo et al.[161] prepared CeO$_2$-supported Ru single atoms (SA), Ru nanoclusters (NC, 1.2 nm) and Ru nanoparticles (NP, 4.0 nm). It was proved that the extent of SMSI effect, including the formation of Ru-O-Ce bond and the interfacial charge transfer, decreased from Ru(SA) to Ru (NP). The strong interfacial charge transfer hindered the reactivity of metal carbonyls which was regarded as the rate-determining step in CO$_2$ methanation. On the other hand, the effect of H$_2$ spillover was found to increase with an increase in the size of Ru species. Moreover, H$_2$ spillover suppressed the removal of formed H$_2$O in this reaction. Due to the above-mentioned reasons, an optimal activity in CO$_2$ methanation was obtained over CeO$_2$-supported Ru nanoclusters. Navarro-Jaen et al.[162] employed polyol method to synthesize a series of Ru/Al$_2$O$_3$ catalysts with different Ru crystallite sizes (16-28 nm) but same loading. The authors found that the CH$_4$ yield increased with an increase in the size of Ru crystallites and claimed that the multiple Ru sites on large particle are necessary to activate CO$_2$ and H$_2$ simultaneously.

1.2.2.3. Reaction mechanisms

Numerous studies have contributed to mechanistic aspects of CO$_2$ methanation, however, no general consensus has been achieved yet.[163] Two different reaction mechanisms, CO pathway[126, 164-166] and formate pathway[145, 166-168], were developed and are widely discussed, featuring metal-carbonyls and formates as the key intermediate species, respectively. The dominant difference between these two mechanisms is the presence or the absence of adsorbed CO intermediates on the catalyst surface. The kind of the reaction mechanism has been proved to highly depend on the nature of active sites, the kind of support and the reaction conditions. Wang et al.[166] claimed Ru surface and oxygen vacancy as active site in CO$_2$ methanation over Ru/Al$_2$O$_3$ and Ru/CeO$_2$, respectively through detailed mechanistic studies including *operando* XANES, Raman and DRIFT spectra. For Ru/Al$_2$O$_3$, surface carbonyl signal in DRIFTS experiments appeared with reaction temperature above 100 °C, but Ru-carbonyl signal did not shift in the range of 100-200 °C when ^{12}CO$_2$+H$_2$ was switch to ^{13}CO$_2$+H$_2$ in DRIFTS cell. Such shift of Ru-carbonyl occurred at above 250 °C. This was consistent with the onset temperature of CO$_2$ methanation over Ru/Al$_2$O$_3$ catalysts. On the contrary, the reaction rate of CH$_4$ formation over Ru/CeO$_2$ was successfully correlated with the concentration of oxygen vacancy.[169] The authors proposed that CO$_2$ was adsorbed on an

oxygen vacancy as carboxylate species, which was further hydrogenated to formate species. The next step, i.e., dissociation of formate to methanol, was regarded as the rate-determining step. The resulted methanol can be hydrogenated into methane quickly. However, a recent study revealed that the CO_2 methanation activity cannot be positively correlated with the concentration of oxygen vacancy of CeO_2 in Ru/CeO_2 catalysts with different Ru particle size and CO route was identified as main reaction pathway.[161] The hydrogenation ability of Ru-CO species was identified as the key factor for achieving high selectivity to CH_4 or to the by-product, CO.

Very recently, Lopez-Rodriguez et al. disclosed the critical role of Ru sites and CeO_2 support. They monitored structural evolvements of Ru and CeO_2 and the formation of surface species using NAP-XPS technique and DRIFT experiments, accompanied by DFT calculations. Most of RuO_2 and partial Ce^{4+} on the surface of Ru/CeO_2 were reduced under reducing conditions to Ru^0 and Ce^{3+}, respectively. The latter process also indicates the formation of oxygen vacancies. After exposing to the reaction atmosphere (CO_2:$4H_2$), the percentages of Ru^0 and Ce^{3+} decreased even at 100 °C due to their oxidation by *O produced from the dissociative adsorption of CO_2 on Ru and oxygen vacancies. On the one hand, the dissociative of CO_2 adsorption on Ru resulted in Ru-carbonyl groups as confirmed by *in situ* DRIFT experiments. The hydrogenation of Ru-CO, *via* *COH or formyl groups *CHO, led to the formation of CH_4 and was determined to be RDS according to DFT calculations. On the other hand, CO_2 adsorption on ceria can proceed either on surface oxygen sites to from carbonate species (*OCOO) or on oxygen vacancies to form carboxylates species ($CO_2^{\delta-}$). The carbonate species are thermodynamically stable, while carboxylates can be hydrogenated to formate or simply split to adsorbed CO. The formate species also can decompose to CO above 200 °C as observed from *in situ* DRIFT spectra. Considering the lower CO adsorption ability on Ru sites in comparison with ceria, ceria was proposed to be CO reservoir. Through CO spillover, more Ru-CO can be formed and finally hydrogenated to CH_4.

1.2.3.   Methanol production-oriented CO_2 hydrogenation

Methanol, a high-value compound, is regarded as an important platform chemical in the further scenario of energy conversion, which can be used in many existing industrial processes. Therefore, the production methanol is one of the most promising process in CO_2 conversion due to the increase in the global methanol market.[170] In the reaction of CO_2 hydrogenation to methanol, CO is also formed as by-product through the RWGS reaction. As shown in Equation 1-3, methanol production from CO_2 is an exothermic process, implying the

forward reaction is favored by lower reaction temperatures. Moreover, methanol production is also benefited by higher reaction pressure because of the decrease in the number of molecules.

$$CO_2 + 3H_2 \rightarrow CH_3OH + H_2O \quad \Delta H_{298K} = -49.5 \text{ kJ mol}^{-1} \quad\quad \text{Equation 1-3}$$
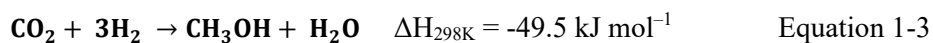
To date, many kinds of catalysts have been investigated for methanol production from CO_2. Among them, Cu-based catalysts received the most attentions. The forthcoming sections will focus on the different active sites and reaction mechanisms of methanol production from CO_2.

1.2.3.1. Active sites, promotors, and supports

Cu-based catalysts. The catalyst formulation $Cu/ZnO/Al_2O_3$ has been applied in methanol synthesis using a mixture of CO, CO_2 and H_2 since the late 1960s.[81, 171] However, some fundamental aspects regarding the nature of active sites, the exact role of Cu and ZnO, and the synergy effect of Cu-ZnO are still in dispute, especially under industrially-relevant reaction conditions of 5-10 MPa and 230-300 °C.

The effects of composition of $Cu/ZnO/Al_2O_3$ on CO_2 conversion and methanol selectivity were studied by Sun et al.[172] who found an optimal catalyst with the Cu/Zn ratio of 1-2 and 10 at.% Al. The introduction of Al decreased the mean crystallite sizes of catalyst and made copper and zinc amorphous-like or as less-ordered structures. The turnover frequency of methanol formation related to Cu^0 atoms decreased with an increase in the surface area of Cu^0, implying that metallic Cu was not the only active site. A Cu^0-Zn^0 surface alloy was found during reaction and proposed to influence catalyst activity based on the results of *operando* EXAFS.[173] Furthermore, it was suggested that Cu-Zn alloys, instead of metallic Cu, played a dominant role for the activity of methanol synthesis from CO_2 over Cu/ZnO based-catalysts.[174] Cu^0 steps in proximity to a $Zn^{\delta+}$ atom were identified as active site by Behrens et al.[175] in industrial $Cu/ZnO/Al_2O_3$ catalyzed methanol synthesis. The authors claimed that both Cu steps and $Zn^{\delta+}$ atom at stepped Cu surface were required because they provided adsorption site for oxygen-bound reaction intermediates.

According to the above discussion, active sites on $Cu/ZnO/Al_2O_3$ catalysts can be classified into four types: metallic Cu, Cu^0-Zn^0 alloy, Cu-ZnO interface (including ZnO or ZnO_x layer on Cu^0), stepped Cu with $Zn^{\delta+}$. By using reversible poisoning strategy with pulsing different poisons (NH_3, NO, dimethylamine, monomethylamine and trimethylamine), Laudenschleger et al.[176] revealed TOS (time on stream)-dependent restructuring of active sites in $Cu/ZnO/Al_2O_3$ in CO_2-containing syngas-based methanol synthesis. They changed dynamically with TOS from Cu^0-Zn^0 alloy to Cu steps and $Zn^{\delta+}$ atom and finally to Cu^0

coated by ZnO_x or ZnO layer. Such changes in the kind of active sites led to catalyst deactivation under industrially relevant conditions. Recently, Beck et al.[177] revealed that the structure of working industrial $Cu/ZnO/Al_2O_3$ catalyst was highly dependent on the reaction pressure. This research highlighted the importance of *operando* studies.

For Cu/ZnO-based catalysts, ZrO_2 was also employed as promotor and support. Its role has been investigated in several works.[178-179] Wang et al.[178] highlighted the important role of ZnO-ZrO_2 interfaces for methanol formation, because $Cu/ZnO/ZrO_2$ was more active than Cu/ZnO and Cu/ZrO_2. It was proposed that ZnO-ZrO_2 interfaces were responsible for CO_2 adsorption due to the formed oxygen vacancies, while H_2 activation occurred on metallic Cu sites. There are also some reports contributing to understand the kind of active sites in Cu/ZrO_2 catalyst in the absence of ZnO.[180-184] Combing *in situ* IR, NMR spectroscopies and DFT calculations, Larmier et al.[183] claimed that Cu-ZrO_2 interface benefited the methanol formation through formate species which was regarded as the key intermediate in CO_2 hydrogenation to methanol.

In₂O₃-based catalysts. The investigation on In_2O_3-based catalysts in methanol synthesis from CO_2 goes back to the theoretical study by Ge et al.[185-186] and experimental studies by Su et al.[187] and Martin et al.[188]. Even though commercial In_2O_3 displayed a higher CO_2 conversion (7.1%) and methanol formation rate (3.69 mol kg_{cat}^{-1} h^{-1}) at 330 °C and 40 bar, the selectivity to methanol (39.7%) was still lower than Cu-based catalysts.[187] Later on, Martin et al. synthesized bulk In_2O_3 catalysts, which shown superior catalytic performance in comparison with Cu-ZnO-Al_2O_3 catalysts regarding the space time yield of methanol and selectivity to methanol. Specifically, the methanol selectivity can reach to almost 100 % at reaction temperature of 200-300 °C, while this valve for Cu-ZnO-Al_2O_3 catalyst was only 5-60%. The authors also found that electronical interaction between In_2O_3 and ZrO_2 or co-feeding CO can enhance the space time yield of methanol. This improvement was induced by an increased number of oxygen vacancies, which were identified as active sites in In_2O_3-based catalyst systems. Structural evolutions of model In_2O_3 catalyst during activation and deactivation in the course of methanol synthesis was probed by Tsoulalou et al.[189] using *operando* X-ray absorption spectroscopy, X-ray powder diffraction and *in situ* TEM techniques. It was revealed that the activation stage was associated with the formation of oxygen vacancy sites (In_2O_{3-x}), while the deactivation with time on stream was attributed to the over-reduction of such active phase to metallic In under reaction conditions (300 °C, 20 bar).

With respect to the selectivity to methanol and the formation rate of methanol, monoclinic ZrO_2 (m-ZrO_2) supported In_2O_3 catalyst was superior to its counterpart, such as supported on Al_2O_3, CeO_3 and tetragonal ZrO_2 (t-ZrO_2).[188, 190] The multiple functions (as catalyst support, promoter and even active species) of m-ZrO_2 were investigated by different groups.[179, 190-192] It was reported that the geometric nature of InO_x supported on ZrO_2 determined the reaction pathway to methanol or CO.[191] In this study, the behavior (decomposition or hydrogenation) of formate, identified as key intermediate, was found to be influenced by InO_x loading, and finally affect the selectivity to methanol or CO. With the indium loading of 0.1 wt.%, vast indium-zirconia interfaces promoted the decomposition of formate species, resulting in CO formation. While zirconia modulated crystalline In_2O_3 with 2.5-5 wt.% indium loading favored the transformation of formate into methanol due to the suitable bonding strength. The authors further proved that the formed active In-O_v-Zr structure, when indium sites were dispersed in the lattice of m-ZrO_2, was more stable against the above-discussed over-reduction under reaction conditions than In-O_v-In.[192] While such over-reduction only can be partially suppressed for t-ZrO_2 supported In_2O_3 catalyst.

New kinds of catalysts. Binary solid solutions ZnO-ZrO_2, even without Cu species, were first reported to be active for methanol synthesis from CO_2 and H_2 by Li's group[193-194] and then has been studied extensively[195-199]. The conversion of CO_2 and the selectivity to methanol reached to 13% and 86% over 13%ZnO-ZrO_2 catalyst, respectively, at 320 °C and 50 bar.[193] Such excellent performance was attributed to a synergetic effect between Zn and Zr, which enhanced the ability of ZnO-ZrO_2 to activate H_2 and CO_2 compared to pure ZnO and ZrO_2. *In situ* DRIFTS experiments and DFT calculations confirmed that formate pathway to methanol was more favorable than CO pathway over this ZnO-ZrO_2 catalyst.

In addition to the above-introduced catalysts, Pt-based catalysts[200-201], Co-based catalysts[202-204] and MoS_2[205] have been reported to be active for CO_2 hydrogenation to methanol. Chen et al.[200] developed a highly selective catalyst, Pt single atoms embedded into MIL-101(Pt_1@MIL), which showed methanol selectivity of 90.3% in aqueous CO_2 hydrogenation. Pt single atoms with coordinated O atoms were identified as active sites. However, CO was the main product over its counterpart possessing Pt nanoparticles (Pt_n@MIL). Even though Co-based catalysts have been regarded to be active for CO and CH_4 formation in CO_2 hydrogenation,[91, 95-96] Wang et al. reported a selective Co catalyst with methanol selectivity above 70% owing to optimizing the kind of support.[202] In their study, the usage of amorphous silica led to the formation of Co-O-SiO_n interfaces. The breakage of C-O bond in *CH_3O which was the intermediate identified by spectroscopic experiments was less favorable on Co

oxide surface. Therefore, the formation of CO and CH_4 was suppressed. Very recently, a novel catalyst, MoS_2 was reported for CO_2 hydrogenation into methanol.[205] It reached a CO_2 conversion of 12.5% with 94.3% methanol selectivity at the reaction temperature as low as 180 °C. The active site was determined to be in-plane sulfur vacancy which enhanced both CO_2 dissociation and H_2 activation.

1.2.3.2. Reaction mechanism

Overall, there are two generally accepted reaction pathway towards methanol formation from CO_2: (1) CO intermediate followed by subsequent hydrogenation; (2) formate pathway.[16, 146, 206] The dominant of each reaction pathway is still in debate, especially regarding to the role of formate species which is regarded as a real intermediate or mere spectator.

The prevalence of individual reaction pathways may strongly relate to the property of oxide support, i.e., reducible metal oxide and unreducible metal oxide.[207-209] In a work reported by Rodriguez et al.[209], they used DFT calculations to elucidate the reaction path of methanol synthesis from CO_2 over a highly active copper-ceria catalyst. Specifically, the calculations proposed that CO_2 was initially hydrogenated to carboxyl species (*HOCO) which could decompose to *CO and *OH with a very low energy barrier (4.6 kcal/mol). The formation of formate species was not considered here due to their high stability. The subsequent hydrogenation of *CO gave *HCO, H_2CO, and H_3CO. Therefore, the authors concluded that the RWGS reaction and methanol synthesis shared the same intermediate (*HOCO). During *in situ* IR experiment, *CO, *HCO, *H_2CO and *H_3CO were not observed probably due to their short residence time. The same reaction mechanism, RWGS+CO-hydro, was proposed to be more reliable for methanol synthesis over Cu/ZrO_2 and Cu/TiO_2 catalysts.[207] Contrarily, formate species was regarded as a spectator and led to poisoning of catalyst surface, as concluded from DFT calculations and spectroscopic measurements. However, the same authors proposed that formate intermediate dominated the reaction path of CO_2 hydrogenation to methanol over Cu/ZnO catalyst.[208]

A systematic study with respect to reaction intermediates and mechanisms over $Cu/ZnO/ZrO_2$ catalyst was presented by Wang et al.[178]. After exposing the catalyst to CO_2, only carbonate species was observed in the DRIFT spectrum. When CO_2 was replaced by H_2, the bands for formate species appeared with a decrease in the intensity of carbonate bands. Meanwhile, no CO was formed during the process. Moreover, the bands of methoxy (*CH_3O) were observed on the surface at ambient pressure and its intensity increased with time accompanied by a decrease in the concentration of formate species. This implied that CO_2 was adsorbed into
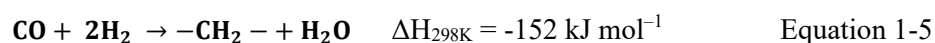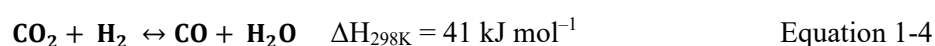
oxygen vacancies located at ZnO/ZrO_2 interface in the form of carbonate, the hydrogenation of carbonate into formate was very quick followed by the hydrogenation of the latter to methoxy species. These findings confirmed that CO_2 hydrogenation into methanol over $Cu/ZnO/ZrO_2$ catalyst followed the formate pathway. However, it should be noted that the hydrogenation of formate to methoxy was not observe in *in situ* DRIFTS experiments performed at realistic conditions (3 MPa). DFT calculations revealed that the hydrogenation of *HCOO to H_2COO was kinetically easier than the *H-assisted dissociation of *HCOO to HCO and finally to *CO. The hydrogenation of CO_2 into formate on the oxygen vacancies of Indium oxide was also identified to be thermodynamically and kinetically favorable.[185, 210]

1.2.4. Higher hydrocarbons production-oriented CO_2 hydrogenation

Considering the increasing global demand for light olefins, aromatics and fuels, and the energy crisis based on the fossil fuels (coal, crude oil, etc.), the hydrogenation of CO_2 with H_2 generated from H_2O using renewable energy provides a promising alternative pathway to produce higher hydrocarbons in the future energy scenario. According to the catalysts utilized in this process and the desired products, two different reaction schemes have been developed, including FTS based- and methanol reaction based-CO_2 hydrogenation.

1.2.4.1. CO mediated route over Fe-based catalysts

CO_2 hydrogenation into higher hydrocarbons through a CO intermediate is also called CO_2-based Fischer Tropsch synthesis (CO_2-FTS). The overall reaction scheme comprises two steps: (1) the formation of CO from CO_2 *via* the RWGS reaction (Equation 1-4); (2) the subsequent CO hydrogenation through the CO-FTS reaction (Equation 1-5).

$$\mathbf{CO_2 + H_2 \leftrightarrow CO + H_2O} \quad \Delta H_{298K} = 41 \text{ kJ mol}^{-1} \qquad \text{Equation 1-4}$$

$$\mathbf{CO + 2H_2 \rightarrow -CH_2- + H_2O} \quad \Delta H_{298K} = -152 \text{ kJ mol}^{-1} \qquad \text{Equation 1-5}$$

Based on the substantial knowledge obtained from the CO-FTS reaction, both Fe- and Co-based catalysts have been investigated in the CO_2-FTS reaction. The latter materials have been reported to selectively catalyze CH_4 formation because they are unable to catalyze the RWGS reaction.[95, 211-212] On the contrary, Fe-based catalysts have been widely studied since they are efficient both for the RWGS and CO_2-FTS reactions. Such catalysts also suffer from high selectivity to CH_4 (> 30% at industrially relevant CO_2 conversion) which can be produced either from CO_2 *via* CO_2 methanation or from CO in the CO-FTS reaction.

Iron-based catalysts and their structural evolution. It has been generally accepted that Fe-based catalysts, initially in the form of iron oxides, underwent severe

transformation/reconstruction/self-organization under CO/CO$_2$-FTS conditions.[213-221] This phenomenon related with the formation of iron carbides through a reaction of Fe/Fe$_3$O$_4$ with chemisorbed carbon produced from CO.[213, 221-222] The time needed for approaching pseudo steady-state in CO$_2$-FTS is longer than that in CO-FTS due to the lower CO concentration in the former process as shown by Riedel et al.[213, 221]. Therefore, almost no hydrocarbons were observed over a Fe-Al-Cu-K catalyst in the first 100 min, whereas the converted CO$_2$ gave CO and iron carbides. Hereafter, the production of hydrocarbons dominated the whole CO$_2$ conversion. This implied that iron carbides are the real active sites for the second step (CO hydrogenation) in the course of CO$_2$-FTS. The formation of iron carbides from iron nitride was also reported very recently.[217] The iron-carbonyl mediated process was proposed to responsible for the above structural transformation. The dynamic restructuring of iron-based catalysts, starting from α-Fe$_2$O$_3$ and γ-Fe$_2$O$_3$, was monitored by *operando* Raman and XRD techniques. It was spectroscopically disclosed that iron carbides were produced from metallic Fe which was formed through reduction of iron oxides by hydrogen. Zhu et al.[216] analyzed a working Fe-based catalyst by (quasi) *in situ* XPS and XRD experiments. Those authors proposed that the carburization of iron oxide and the reoxidation of iron carbide by H$_2$O determined surface catalyst composition, a core-shell model structure Fe$_3$O$_4$@(Fe$_5$C$_2$+Fe$_3$O$_4$). Han´s group studied the full life cycle (activation, reaction and deactivation) of a Fe-based catalyst in CO$_2$ hydrogenation.[214] Unlike the above results reported by Zhu et al.[216], Han et al.[214] concluded that the oxidation of Fe$_5$C$_2$ into Fe$_3$O$_4$ was irreversible under reaction conditions and responsible for the loss of activity. However, no iron carbide formation was observed on SiO$_2$ or Al$_2$O$_3$ supported Fe nanoparticle catalyst in NAP-XPS experiments (mbar range of pressure) and *in situ* XAS experiments (catalytically relevant conditions) conducted by Shaikhutdinov et al.[219]. Recently, our group determined that the steady-state composition after CO$_2$-FTS reaction depended on the initial composition (Fe$_x$O$_y$C$_z$) and the position along the catalyst bed due to the restructuring of Fe$_x$O$_y$C$_z$.[38]

Promoters, supports, and reaction conditions. A great number of works have contributed to understanding the influence of promoters, supports and reaction conditions on the catalytic performance of Fe-catalyzed CO$_2$-FTS reaction. Both bulk and supported Fe-based catalysts have been proved to be effective in CO$_2$-FTS reaction. Typical supports are Al$_2$O$_3$, SiO$_2$, TiO$_2$ and zeolite. The often-used promoters can be classified into categories according to their position in the periodic table: (1) alkali metals, especially Na and K; (2) transition metals, e.g., Cu, Zn and Mn. As mentioned above, most unpromoted Fe-based catalysts possess high selectivity to CH$_4$ and produce very small amount of C$_{5+}$ hydrocarbons. Therefore, the on-

going research focuses on design highly active catalyst with low CH_4 selectivity and high selectivity to light olefins and C_{5+} fuels. With different promoters, either activity or product distribution can be optimized.

A systematic study for search appropriate CO_2-FTS catalysts with different formulations was presented by Rodemerck et al.[223] using an evolutionary strategy based on genetic algorithm. Through analyzing catalytic performance obtained from more than 260 catalysts, it was identified that K and Co or Zn should be used for Fe to improve the yield to C_{5+}-hydrocarbons. Indeed, K or Na has been consistently agreed to suppress the CH_4 formation, to inhibit the secondary hydrogenation of light olefins to paraffins, and to increase the chain growth probability in the CO_2-FTS reaction.[224-225] The positive effect of K on the formation of Fe_5C_2 was confirmed by *in situ* XRD and magnetometry techniques.[226] Moreover, no effect of K on the activity of RWGS reaction was found, but it was determined that the presence of K was detrimental to the activity of CO-FTS reaction. However, Amoyal et al. concluded that K strongly increased the activity of RWGS reaction over Fe-Al-O spinel catalyst because of the increase in the number of oxygen vacancy which was regarded as active site in the redox mechanism dominated RWGS reaction.[225] Those author also determined the effect of K on the second step (CO-FTS) of CO_2-FTS over promoted and unpromoted Fe_5C_2 catalysts. On the one hand, it was found that K decreased the intrinsic activity (TOF) of methanation reaction and FTS reaction in CO hydrogenation. On the other hand, the amount of surface C-vacancies and surface iron atoms, which contributed to CO adsorption, increased in the K-promoted catalysts. This explained why the overall catalyst activity increased in the presence of potassium. Liang et al. performed micro-calorimetric experiments and revealed that both the overall number of CO_2 adsorption sites and their strength (evidenced by the differential adsorption heat) were enhanced by adding of Na to Fe-based catalysts.[227] Potassium was also reported to be able to decrease catalyst affinity to H_2 as evidenced by a lower H_2 chemisorption uptake.[228] This is also a reason for the higher olefin content over K-promoted Fe-based catalysts in comparison with their unpromoted counterparts. However, the usage of K, Rb or Cs resulted in heavy carbon deposits on the catalyst surface, which decreased the efficiency of FTS reaction and made the promoted catalyst less selective to higher hydrocarbons as reported by Shafer et al.[229]. Han et al.[230] highlighted the important role of carbonaceous K-Fe_5C_2 interface for achieving high yield of high-valued olefins in CO_2 hydrogenation. The promotion effect of alkali metal promoter was also featured by its electronic effect on Fe-based catalysts. For example, sodium was reported to donate electrons

to Fe_5C_2 surface.[231] This reason was assumed to explain the enhancement of CO_2 adsorption and dissociation on Na-promoted Fe_5C_2.

Fe-containing bimetallic catalysts, such as Ru-Fe[232], Fe-Co[233-234] and Fe-Zn[235], have demonstrated promising catalytic performance in CO_2 hydrogenation. It was reported that the ruthenium-iron oxide heterodimer catalyst was benefited by the H_2 activation of Ru phase.[232] The overlay of FeO_x onto Ru upon reductive treatment resulted in core-shell structure, which increased the yield of hydrocarbons by four times. Hwang et al.[234] deposited Fe on a Co-NC support (N-coordinated Co single-atom carbon) and investigated the catalytic performance of Fe-Co alloy (FeK/Co-NC). The Co single atom on carbon support favored the formation of Fe-Co alloy, which was stable during reduction and reaction. Compared with the co-impregnated catalyst (FeCo-K/NC), FeK/Co-NC shown a lower CH_4 selectivity and higher selectivity to C_{5+}-hydrocarbons. It was reported that Fe2Zn1 catalyst exhibited an extraordinary stability over 200 h on stream in CO_2 hydrogenation.[235] The presence of Zn was proposed to suppress the oxidation of FeC_x by H_2O. Zn was also regarded as an electronic promoter.[236] Specifically, the chemical valence of Zn in ZnO_x varied between 0 and +2, implying the electronic donating from Zn to Fe.

For supported Fe-based catalysts, their activity and selectivity may be influenced by the kind of support. Wang et al.[237] compared potassium-modified Fe-based catalysts based on different support materials (Al_2O_3, ZrO_2, TiO_2, SiO_2, Meso-carbon and carbon nanofiber). They found that SiO_2 was less suitable for Fe to achieve high CO_2 conversion and high productivity to C_{2+}-hydrocarbons. Whereas ZrO_2-supported Fe catalysts was the most active and selective one with the CO_2 conversion of 42% and light olefins selectivity of 46%. TiO_2-supported Fe-based catalyst was reported to be more selective for producing C_5-C_{15} hydrocarbons than its counterparts supported on Al_2O_3 and SiO_2. A series of ZrO_2 materials with different specific surface area were prepared and used to load Fe.[37] In this way, the particle size (2.5-12.9 nm) of Fe_2O_3 can be tuned. The Fe particle size effects on the primary reaction (RWGS and CO_2 methanation) and the secondary reaction (CO-FTS) were studied. It was found RWGS reaction and CO_2 methanation were favored at the size of 6.1-12.9 nm. The larger particles at 2.5-9.8 nm were able to show higher chain growth probability dur to more terrace sites.

Reaction conditions, including pre-treatment procedure, reaction pressure, temperature, residence time and the ratio of H_2 to CO_2 are important parameters influencing catalytic performance.[20] Regarding this point, a systematic work was presented by Rodemerck et al.[223], where an optimal catalyst, 0.07Ru0.3Zn20Fe1.1K/TiO2, was used. Generally, the first step

(RWGS) of CO_2-FTS will be thermodynamically favored at higher reaction temperature due to its endothermal nature. With increasing the reaction temperature from 250 °C to 350 °C, CO_2 conversion increased from 7% to 41%. While the selectivity to CO dropped to 18% from 75% due to an increase in the rate of CO consumption with rising reaction temperature. Therefore, the selectivity to C_2-C_4 and C_{5+}-hydrocarbons increased. Using higher H_2/CO_2 ratio also can shift the equilibrium to the forward direction of the RWGS reaction and result in higher CO_2 conversion. However, CH_4 selectivity will also be enhanced under such conditions. A strong increase in CO_2 conversion was observed over K-Fe15 catalyst when operating pressure was increased form ambient pressure to 5 bar.[224] CO was the main product at ambient pressure because the reaction rate of CO-FTS was extremely low. This implied that elevated pressures are necessary for production of higher hydrocarbons from CO_2.[238] By increasing the space velocity, the selectivity to CO increased strongly with the minor change in CH_4 selectivity, indicating CO was primary product.[224] Meanwhile, the selectivity to higher hydrocarbons decreased because their formation needs higher contact time.

Reaction mechanisms. As aforementioned, in the first step, CO_2 is converted to CO *via* the RWGS reaction, and the details of the mechanism can be found in section 1.2.1.4. The formed *CO species can be activated on iron carbides followed by chain growth polymerization (including chain initiation, propagation and termination) reaction to produce hydrocarbons (Fischer-Tropsch synthesis).[23, 25, 239] Even though the question on the active sites of CO-FTS reaction is still disputed, most authors claimed that iron carbides are active.[240-241] Different reaction mechanisms had been developed to describe this polymerization process with various initiator and monomer species, and have been summarized in some detailed review articles.[25, 242-244] A short overview of these CO-FTS mechanisms will be presented here.
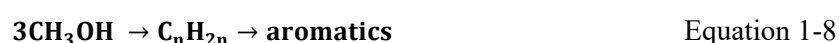
(1). Surface enolic mechanism.[245-246] In this mechanism, CO adsorption occurs in an undissociated way. The chemisorbed CO reacts with H to form enolic species (HCOH) followed by the condensation reaction between two enolic groups with the formation of H_2O. Additionally, enolic species is regarded as monomer. The chain termination processes *via* desorption to form acid or hydrogenation/desorption to produce alcohols and hydrocarbons.

(2). Surface carbide mechanism.[247-248] The dissociative adsorption of CO and H_2 produces surface carbon and hydrogen. The hydrogenation of surface carbon gives CH_2 species, which acts as a monomer. The consecutive insertion of CH_2 species results in chain growth. Finally, hydrogen addition or β-hydride abstraction, namely chain termination, forms alkanes or alkene, respectively.

(3). CO insertion mechanism.[249-250] This mechanism proposes that molecularly adsorbed CO acts as a monomer and methyl group acts as an initiator. CO can be inserted into metal alkyl bond, which results in enol group and leads to chain growth. The hydrogenation of the growing chain results in chain termination.

1.2.4.2. Methanol mediated route over OXZEO (metal oxide + zeolite) catalysts

The concept of bifunctional catalysts (metal oxide coupled with zeolite) for hydrocarbon synthesis from CO_x was first realized in the hydrogenation of syngas to lower olefins.[251-252] In this regard, methanol synthesis from CO_2 over metal oxide catalyst and C-C coupling reaction over zeolite occur simultaneously. As aforementioned, methanol synthesis is an exothermic reaction and favored at relatively lower reaction temperature (200-300 °C). However, an optimal reaction temperature for the C-C coupling reaction is 400-500 °C.[253] At such high temperature, the competitive RWGS reaction is favored and would suppress methanol pathway from CO_2. Therefore, the mismatching of methanol synthesis and C-C coupling in reaction temperature is the big challenges for efficient production of hydrocarbons over bifunctional catalysts. Meanwhile, the RWGS reaction should be suppressed as much as possible. To this end, the methanol synthesis coupled with the methanol conversion into lower olefin (MTO, Equation 1-6, 1-7) or aromatization of methanol (MTA, Equation 1-8) can realize the lower olefin[45, 254-256] or aromatics[46-47, 257-259] production from CO_2 over OXZEO catalysts.

$2CH_3OH \rightarrow C_2H_4 + 2H_2O$ $\quad \Delta H_{298K} = -29.3 \text{ kJ mol}^{-1}$ $\quad$ Equation 1-6

$3CH_3OH \rightarrow C_3H_6 + 3H_2O$ $\quad \Delta H_{298K} = -102.3 \text{ kJ mol}^{-1}$ $\quad$ Equation 1-7

$3CH_3OH \rightarrow C_nH_{2n} \rightarrow \text{aromatics}$ $\quad$ Equation 1-8

Lower olefins production. SAPO-34 zeolite has been recognized as the most promising catalyst for the conversion of methanol into lower olefins.[260-262] A tandem catalyst composed of a physical mixture of ZnO-ZrO$_2$ and Zn-modified SAPO-34 zeolite was first reported by Li et al.[44]. The selectivity to lower olefins among total hydrocarbons was 80% in at the CO selectivity of 47%. It was proposed that methanol synthesis from CO_2 and H_2 occurred on ZnO-ZrO$_2$ catalyst, while Zn-doped SAPO zeolite was responsible for the methanol conversion into hydrocarbons. It should be noted that the CO selectivity over ZnO-ZrO$_2$ catalyst alone was much higher than that over tandem catalyst under same reaction conditions (380 °C and 20 bar), implying that the methanol formation was enhanced over ZnO-ZrO$_2$ in the presence of the SAPO-34 zeolite. DRIFTS and chemical trapping experiments confirmed

that the transfer of CH_xO species formed on $ZnO-ZrO_2$ to SAPO-34 was crucial for the efficient production of lower olefins from CO_2. By taking the advantages of indium oxide in methanol synthesis from CO_2, the combination of In-Zr composite oxide and SAPO-34 zeolite was reported as an efficient catalyst for direct production of lower olefins from CO_2.[45] With respect to the integration manner of two components, it was revealed that the granule stacking was superior to mortar mixing of powder and dual-bed mode.

A spinel binary oxide ($ZnAl_2O_4$ or $ZnGa_2O_4$) was integrated with SAPO-34 zeolite to fabricate a bifunctional catalyst used for direct conversion of CO_2 to lower olefins.[255] Methanol and DME were found to be the key intermediates. CO_2 adsorption and activation were proved to be related to the density of oxygen vacancies, while -Zn-O- sites were responsible for H_2 activation. A high selectivity of lower olefins was achieved over $ZnAl_2O_4$/SAPO-34 and $ZnGa_2O_4$/SAPO-34 with about 15% CO_2 conversion and 50% CO selectivity. It should be noted that the proportion of ethene and propene can reach to 87% among the light olefins detected. To this end, Wang et al.[256] constructed a $Zn_{0.5}Ce_{0.2}Zr_{1.8}O_4$/H-RUB-13 catalyst system and contributed to regulate the relative amounts of specific olefins. *In situ* spectroscopic experiments, isotopic-labeling technique and DFT calculations confirmed that methanol formation followed the pathway where formate and methoxyl acted as key intermediates over $Zn_{0.5}Ce_{0.2}Zr_{1.8}O_4$ solid solution. While the RWGS reaction was strongly suppressed, leading to a low CO selectivity of 26.5 % in contrast to 50% obtained over other bifunctional catalysts.

Aromatics production. Generally, H-ZSM-5 with high Bronsted acidity can enhance the aromatization process for converting the primary olefins formed from methanol to aromatics.[263-264] A first work focused on aromatics formation from CO_2 was reported by Ni et al. using ZnAlO$_x$&H-ZSM-5 bifunctional catalyst.[46] The composite catalyst displayed a high selectivity to aromatics (73.9% in hydrocarbons) with a low selectivity to CH_4 of 0.4% at CO_2 conversion of 9.1%. Methanol and DME were proposed to be formed on ZnAlO$_x$ surface, then transferred into H-ZSM-5 to produced olefins and aromatics. Upon adding CO (5.42 vol %) into the CO_2-containing reaction feed, the RWGS reaction was strongly suppressed (CO selectivity of 41% and 12% with and without CO, respectively) over Cr_2O_3/H-ZSM-5 catalyst.[258] Moreover, the side reaction, such as the isomerization of p-xylene (PX), can be eliminated when HSM-5 was coated by silicate-1. Finally, the proportion of BTX (benzene, toluene, and xylenes) and PX was increased from 13.2% and 7.6% to 43.6% and 25.3% respectively in total aromatics. When ZnZrO solid solution was integrated with ZSM-5, the selectivity to aromatics in hydrocarbons could reach to 73% at CO_2 conversion of 14%.[47] A

similar catalyst system for aromatics production from CO_2 was also reported by Zhang et al.[265]. It was proved that the amount of oxygen vacancies of oxide component (ZnO-ZrO$_2$) governed the formation of methanol intermediate.

Reaction mechanisms. Methanol synthesis has been widely accepted as the first step of CO_2 hydrogenation into lower olefins or aromatics following methanol-mediated pathway, and its mechanism has been discussed in detail as shown in section 1.2.3.2. The mechanisms of methanol-to-hydrocarbons (MTH) includes direct mechanism and HCP (hydrocarbons pool)/dual-cycle (olefinic cycle and aromatic cycle) mechanism and have been summarized in some excellent reviews.[253, 266-268] SAPO-34 zeolite has been widely used for methanol to olefins process due to its relatively low acidity and high hydrothermal stability. The stronger acidic strength and large microporous channels of HZSM-5 zeolite enable it to catalyze oligomerization and aromatization. However, CO_2 hydrogenation into lower olefins or aromatics over OXZEO catalysts seems to be not a simple sum of methanol synthesis and MTO or MTA as proposed by Li group.[44] The further deeper studies on the fundamental insights into this process are highly needed for better design efficient catalysts.

1.3. Catalysis informatics

1.3.1. The development of catalysis informatics

The appearance of the term "catalysis informatics" can be tracked back to the work reported by Knapman in 2001[269] and its application in heterogeneous catalysis received increasing attention in the last few years[270-273]. Catalysis informatics can be generally understood as the extraction of knowledge, the application of data mining, and the implementation of analysis tools for fostering the discovery of efficient heterogeneous catalysts.[274] Similarly, Takahashi et al. define the catalyst informatics into three key components: collecting catalyst data, transferring catalyst data to catalyst design and developing platform for catalyst informatics.[275] In the past and even the present stage of catalysis research, trial-and-error discovery[276] and the usage of model catalysts[277] have been employed as general strategies for finding and optimizing catalyst materials, as well as for understanding reaction mechanisms. Two representative examples are Fischer-Tropsch process and ammonia synthesis. The raising of catalysis informatics can lead to a paradigm shift regarding catalysis research.

The complexity of catalytic reactions in heterogeneous catalysis makes the catalysis informatics different from the existed cheminformatics[278] and material informatics[279]. First, the composition of catalyst, typically solid materials, is not static under working conditions and influenced by the chemical potential of reaction atmosphere. Second, the surface

composition is usually not same with bulk phase, making the appropriate characterization more difficult. Therefore, data collection, the first step of catalysis informatics, should focus not only on the physicochemical properties of catalyst itself, but also on the reaction conditions and the catalytic performance. Additionally, the "negative data" which is usually not reported in literature could be very important for data analysis in catalysis informatics. Therefore, it is required that the data should be diverse. The development of catalysis informatics is always accompanied with the development of high-throughput experiment techniques and high-throughput calculations. The former technique can produce parallel catalytic data with good consistent feature. The collected data, including catalytic properties, reaction conditions, catalyst characterization, surface information regarding intermediates and computational data should be organized with different manners.

The valuable information and knowledge can be derived from the above-mentioned data through applying suitable analysis tools of data science and machine learning. Machine learning methods allow researcher to handle data in a multi-dimensional space. In other words, the data science and machine learning[280], e.g., classification, regression, clustering, manifold learning, domain adaptation and so on, contribute to establishing real structure-property-reactivity relationships in catalysis and accelerating the discovery of efficient catalysts.[271] An important function of informatics in catalysis is to predict efficient catalysts. The development of catalysis informatics also needs an open space or platform which can include public databases, analysis tools and algorithm. Some progresses have been achieved in this area.[281]

1.3.2.   The application of catalysis informatics

The term of catalysis informatics has begun to attach attentions in the field of heterogeneous catalysis. A pioneering work which focused on the oxidative methane coupling (OCM) reaction was reported by Zavyalova et al.[282]. The authors collected more than 1870 data sets, consisting of catalyst compositions, reaction conditions and catalytic performance for each data set, from 1000 references dealing with the OCM reaction. The statistical analysis, including analysis of variance, regression tree and correlation analysis, towards the collected database allowed to establish composition-performance relationships and to identify the key elements whose oxide shown strong basicity and displayed higher C_{2+} products selectivity. The effective combinations of different key elements and useful promoters were also searched in this way. New catalyst systems based on Mg or La oxide with Cs, Ba or Ba (positive effect on C_2 selectivity) and Mn or W (positive effect on activity) as promoter were proposed. Furthermore, such ternary oxides catalysts were proved to be efficient for the OCM reaction

in a separate experimental study from Kondratenko et al.[270]. Recently, meta-analysis was employed to discover relationships between the physicochemical properties, but not just composition, of catalysts and their catalytic performance in OCM reaction, and to identify important descriptors influencing catalytic performance by combining the literature data, statistical tools and fundamental catalysts properties.[272] In this work, 1802 catalysts were divided into 10 groups according to four hypotheses. The element which can form stable carbonate at OCM reaction temperatures and another element which can form thermally stable oxide are needed for an efficient OCM catalysts.

As aforementioned, the literature data is an important source for data collection which is regarded as the first step of catalysis informatics. Next step, data analysis and knowledge extraction are essential for guiding catalyst design. Odabasi et al.[283] established a database using 4360 experimental data sets from the literatures for Au- and Pt- based materials used in the water gas shift (WGS) reaction. They used decision trees, artificial neural networks, and support vector machines to identify important factors that affect CO conversion in WGS reaction. The data mining method of regression tree analysis was also used by Fait et al.[284] for the literature data of methane oxidation to formaldehyde. The kind of support was identified to strongly affect the selectivity to formaldehyde. The unique catalytic performance of zeolite is usually associated with their special structure which partially determined by the synthesis conditions. Therefore, revealing the correlations between synthesis conditions and the structure descriptors is of interest for both industry and academia, and can be realized by using machine learning models as reported by Mureoka et al.[285].

Machine learning has also been used to predict physicochemical properties of various materials with relatively small size of database.[286-287] Some new or modified machine learning methods have been used in the field of heterogeneously catalysis informatics to predict catalyst formulations. For example, Suzuki et al.[288] developed a method based on elemental features as input variables instead of compositions to improve the prediction accuracy. Constrained principle component analysis was used to discovery new catalyst formulations of water gas shift reaction based on experiment data including catalyst composition and experimental conditions.[273] One also allowed to predict the influence of reaction conditions on catalytic performance. Machine learning was also reported to identify transition metal-based catalyst for hydrogen evolution reaction (HER).[289] Besides the function of prediction, machine learning also contributed to discover the correlation between the physicochemical properties of TM-based catalysts and their performance in HER.

2. Objectives and strategy of this work

2.1. Objectives

As demonstrated in the above literature overview, CO_2 hydrogenation to various products is continuously gaining academic and industrial interests as a promising methodology for producing valuable chemical compounds and fuels. The CO_2-FTS is an attractive approach to generate lower olefins and fuels. Fe-based catalysts used for this reaction possess various active sites responsible for the formation of CO, CH_4 and higher hydrocarbons, which are formed through a sequence of parallel and consecutive reactions. The sites are formed *in situ* upon reaction of iron oxides with CO_2, H_2, CO and H_2O. To improve catalyst activity and optimize the selectivity to the desired products, it is highly important to understand structure-performance relationships. However, the reaction-induced structural changes and the complex reaction network imped the elucidation of such correlations.

Against this background the present thesis aims to elucidate fundamental factors determining reaction-induced restructuring of Fe-based catalysts and their consequences for product selectivity from mechanistic and kinetic viewpoints. To address the above challenges and to achieve these general objectives, the results presented and discussed in this thesis were derived through an approach combining different complementary tools, i.e., *in situ/ex situ* spectroscopic methods, space and time resolved characterization techniques for catalyst structure and reaction kinetics, transient kinetic studies with isotopically labelled molecules, as well as mathematical analysis of literature data. In details, the specific scientific aims are described as follows:

1. to identify important descriptor(s) affecting catalyst performance and to establish property-performance relationships for guiding catalyst design and process optimization through mathematical approach. To this end, different statistical analysis tools were applied to analyze available experimental data about the CO_2-FTS reaction with the purpose to derive statistically proven knowledge which is to be used for preparing effective catalysts.

2. to reveal the fundamental origins of promotion effect of alkali metal promoters for Fe-based catalysts in CO_2-FTS reaction. To this end, a series of catalysts promoted by an alkali metal (Li, Na, K, Rb or Cs) with various loadings were synthesized. They were tested under steady-state conditions in fix-bed reactors and under transient conditions in a temporal analysis of products (TAP) reactor.

3. to disclose crucial physicochemical properties of promotor-free Fe-based catalysts relevant for controlling product selectivity. In particular, it is important to understand how and why bare Fe_2O_3 is converted into other phases, especially iron carbides, under CO_2-FTS conditions and to check if the presence of iron carbides is really the only prerequisite for ensuring high selectivity to C_{2+}-hydrocarbons.

4. to investigate re-structuring of iron oxides under CO_2-FTS conditions in a manner of spatially resolved approach and to monitor the phase distribution of the working catalyst along the catalyst bed.

2.2. Strategy and outline

The strategy used for achieving the above-defined objectives is discussed below. In **Section 4.1**, the factors influencing the catalytic performance of Fe-based catalysts were identified by statistical analysis. For this purpose, a database including more than 350 data sets was created. For each data set, it contains the detailed composition of catalyst, reduction and rection conditions, and catalytic performance. On this basis, regression trees analysis, ANOVA and comparison of mean values were used to derive fundamentals of performance indicator and guide catalysis design. So-developed Mn-K/Fe catalysts were tested in CO_2-FTS reaction and compared with other state-of-the-art catalysts.

In **Section 4.2**, the effects of alkali metal (Li, Na, K, Rb, or Cs) promoters for Fe_2O_3 on (i) reaction-induced formation of iron carbide, (ii) catalysts activity for overall CO_2 conversion and transformation into individual reaction products, and (iii) product selectivity were investigated. To this end, bulk Fe_2O_3 catalysts promoted with one of the above-mentioned promoters with various loadings were prepared. As determined by Mössbauer spectra, XANES and XRD results, the presence of tiny amounts of alkali metal (atomic ratio of alkali metal to Fe of 0.001) does not influence the fraction of iron carbide in steady-state catalysts. However, these catalysts differ strongly in product selectivity. Spatially resolved steady-state kinetic analysis enabled to determine how catalyst efficiently depends on the kind of promoter. In this way, the effects of alkali metal on the intrinsic activity of CO_2 conversion and formation of individual products were determined. To rationalize the promoter-dependent catalytic performance, temporal analysis of products (TAP) technique was employed to elucidate the interaction of CO_2, CO, H_2 and C_2H_4 with different catalysts from a kinetic viewpoint. The rate constants of elementary CO_2 and CO activation steps were derived. Finally, the electronegativity of the alkali metal was successfully correlated with these rate constants, and with the rates of CO_2 conversion into C_{2+}-hydrocarbons and CH_4.

Section 4.3 deals with the identification of crucial physicochemical properties of bare α-Fe_2O_3, which influence its re-structuring under CO_2-FTS conditions and catalytic performance. To this end, a series of bulk bare α-Fe_2O_3 catalysts were prepared by different methods. H_2-TPR, *in situ*/*ex situ* XRD, *in situ* Raman and TGA analyses were used to study the reducibility of as-prepared α-Fe_2O_3. Combing CO_x-TPD, H_2-TPH and H_2-D_2 exchange experiments, the reducibility of α-Fe_2O_3 was established to affect its ability to in situ form iron carbides (produced from Fe_2O_3 during reaction) and the reactivity of the latter towards CO_2, CO and H_2 adsorption/activation. Therefore, the kinetics of two primary reactions (RWGS reaction and methanation reaction) can be tuned as proven by spatially resolved steady-state kinetic analysis. Moreover, the overall reaction scheme was established by analyzing conversion-selectivity relationships. The influence of reduction temperature on product distribution was dependent on the reducibility of iron oxide. Such effects were explained by the C/Fe ratio of *in situ* formed iron carbides as determined by the parameters of fitting Mössbauer spectra.

The main results and outcomes derived in this thesis are summarized in the **Conclusions**. The further developing directions of Fe-based catalysts in CO_2-FTS reaction are presented in **Outlook**.

3. Experimental part

3.1. Catalyst preparation methods

Synthesis of bulk α-Fe₂O₃ catalysts. Iron (III) nitrate nonahydrate (AR for Analysis) was purchased from Fisher Scientific. Ammonium hydroxide solution (25%, Ph. Eur.) and ethylene glycol (99%) were purchased from Roth. Citric acid (99%) was purchased from Sigma-Aldrich. All chemicals were used as received without further purification.

Bulk α-Fe₂O₃ materials were prepared by three different methods, namely chemical precipitation, sol-gel method, and thermal decomposition. For the chemical precipitation method, iron nitrate nonahydrate ($Fe(NO_3)_3 \cdot 9H_2O$) was used as precursor and ammonium hydroxide solution was used as precipitating agent. Briefly, a required amount of $Fe(NO_3)_3 \cdot 9H_2O$ was dissolved in deionized water followed by stirring for 30 min to obtain a clear solution. Then, an ammonium hydroxide solution was added dropwise into the above solution under stirring until pH of 9.5. After aging at room temperature for 3 h, the suspension was filtered, washed with deionized water several times until neutral pH value. Hereafter, the obtained precipitate was dried at 100 °C overnight. The as-synthesized solid material was then calcined at 400 °C for 6 h with a heating rate of 3 °C min^{-1}. A sol-gel method was also used to synthesis bulk α-Fe₂O₃. In this approach, a required amount of $Fe(NO_3)_3 \cdot 9H_2O$ was dissolved in deionized water to form a solution. $C_2H_6O_2$ (ethylene glycol) and $C_6H_8O_7$ (citric acid) were then added into the above solution with the molar ratio of Fe/ethylene glycol/citric acid of 1/1/2. The mixture was slowly heated at 80 °C to form a gel, followed by dried at 120 °C for 12 h. This catalyst precursor was calcined at 500 °C with a heating rate of 3 °C min^{-1} for 4 h. Bulk α-Fe₂O₃ was also prepared using a thermal decomposition method. A muffle furnace was first pre-heated to 600 °C. $Fe(NO_3)_3 \cdot 9H_2O$ precursor was then transferred into the pre-heated furnace and treated at 600 °C for 6h in the muffle furnace.

Synthesis of promoted α-Fe₂O₃ catalysts. Manganese(II)-nitrate tetrahydrate (Mn $(NO_3)_2 \cdot 4H_2O$, 98.5%, Merck), potassium nitrate (KNO_3, 99%, Merck), lithium nitrate ($LiNO_3$, 99.9%, Merck), sodium nitrate ($NaNO_3$, 99.5%, Merck), rubidium nitrate ($RbNO_3$, 99.8%, Alfa Aesar) and cesium nitrate ($CeNO_3$, 99.9%, ChemPur) were used as received.

A series of xMn-K/Fe (x stands for the atomic ratio of Mn/K with 0.4, 0.7, 1.2, 2 or 5, while the molar ratio of K/Fe was kept constant at 0.005) catalysts were prepared by an incipient wetness impregnation method. α-Fe₂O₃ obtained through a chemical precipitation method (see above) was impregnated with an aqueous solution of KNO_3 and Mn $(NO_3)_2 \cdot 4H_2O$. A K or

Mn-promoted Fe_2O_3 catalyst was also prepared with K/Fe or Mn/Fe of 0.005 and named as 0.005K/Fe or 0.005Mn/Fe. After impregnation, the samples were dried at 100 °C overnight and calcined in a muffle furnace at 400 °C with a heating rate of 5 °C min^{-1} for 5 h.

Using α-Fe_2O_3 synthesized by a chemical precipitation method, a series of alkali metal promoted catalysts were prepared by an incipient wetness impregnation method. The catalysts are abbreviated as xAM/Fe (AM = Li, Na, K, Rb, or Cs). Briefly, α-Fe_2O_3 material was impregnated with a respective solution of alkali-metal nitrate followed by drying at 100 °C for 12 h. The samples were calcined in a muffle furnace at 400 °C with a heating rate of 3 °C min^{-1} for 5 h. The obtained catalysts are abbreviated as xAM/Fe, where x stands for the nominal molar ratio of alkali metal to Fe (x = 0, 0.001, 0.005, 0.02, and 0.05 for K; x = 0.001 and 0.05 for Li, Na, Rb or Cs).

3.2. Catalyst characterization methods

Inductively coupled plasma optical emission spectroscopy (ICP-OES) was used to analyze the content of Fe and the loading of promoters, except for Cs, which was determined by atomic absorption spectroscopy, using Varian 715-ES ICP-Emission-Spectrometer. Aqua regia (8 mL) was used to dissolve sample (10 mg). The sample digestion was performed with a preparation system (Multiwave PRO, Anton Paar) operated at 220 °C and 50 bar using a microwave-assisted method. The digested solution was then diluted to 100 mL for the experiment of ICP-OES. The data analysis was carried out on the software (ICP Expert) of 715-ES.

Ex situ X-ray diffraction (XRD) patterns were recorded on a Stoe Stadi P transmission diffractometer with a DECTRIs Mythen2 1K detector and Ge(111) monochromatized Mo Kα_1 radiation (50 kV, 40 mA, 0.70930 Å). The sample was grinded to a fine powder and put between two acetate foils for the measurement. Data acquisition parameter were adapted to sample scattering properties. Peak positions and profile were fitted by Pseudo-Voigt function with the HighScore Plus software package (Panalytical). Phase identification was proceeded by using the PDF-2 database of the International Center of Diffraction Data 2016 (ICDD). The size of α-Fe_2O_3 crystallites was calculated according to the Scherrer equation using (012), (104), (110), (113), (024) and (116) reflexes and an average value was presented. Quantitative phases analysis was carried out by the Rietveld method in HighScore plus software.

In situ XRD studies were performed on a Stoe Stadi P diffractometer equipped with a Stoe ht2-in situ oven and a Mythen 1K detector in Debye-Scherrer geometry using monochromatized Mo Kα1 radiation (50 kV, 40 mA, 0.70930 Å). The sample was grinded,

pressed to pellets by a pressure of 10 tons. The pellet was crushed and sieved to particle with fraction of 100-150 μm. A specimen was filled into a quartz glass capillary (about 2 mm outer diameter, 1 mm inner diameter, opened on both sides) until a height of about 6 mm and fixed by quartz glass wool. The quartz glass capillary was placed into the oven and flushed with He with flowrate of 10 mL min^{-1}. The sample was heated to a desired temperature in He flow. Hereafter, a flow of H_2/He (1:1, 10 mL min^{-1}) was introduced for reduction treatment and the reduction process was monitored using static data collection over a 17° angular region (Mo-radiation). Gas dosage was controlled by a set of Bronkhorst mass flow controllers.

Nitrogen adsorption-desorption experiments were performed on BELSORP-mini II instrument or ASAP 2020 setup (Micromeritics, USA) and evaluated according to the Brunauer-Emmett-Teller (BET) method to determine the specific surface area of as-prepared catalysts. Before the measurements, the samples were heated at 250 °C in vacuum for 2 h.

Temperature-programmed reduction with H_2 (H_2-TPR) experiments were performed to analyze the reducibility of the samples. The experiments were carried out using an in-house-developed setup including eight continuous-flow quartz reactors (Figure A-1). Each sample (15 mg) was treated at 300 °C in Ar flow with a flowrate of 10 mL min^{-1} for 2 h to remove adsorbed water followed by cooling down to 50 °C in Ar flow. Hereafter, the samples were heated to 900 °C with a heating rate of 10 °C min^{-1} in a flow of 5 vol.% H_2 in Ar (10 mL min^{-1}). An online mass spectrometer (Pfeiffer Vacuum OmniStar GSD 320) was used to detect the signals at m/z units of 2, 18 and 40 which correspond to H_2, H_2O and Ar, respectively.

Thermogravimetric analysis (TGA) measurements under isothermal conditions were used to study the reduction of Fe_2O_3 using a SETSYS Evolution 16/18 (Setaram). Typically, 20 mg of Fe_2O_3 sample was put into a cup of balance, then the enclosed volume was evacuated at room temperature. The sample was heated up to 300 °C with a heating rate of 10 °C min^{-1} in He (20 mL min^{-1}) under ambient pressure and pre-treated until no mass changes were observed. Hereafter, He was replaced by a flow of 50 vol.% H_2 in He (32 mL min^{-1}) and the variation of mass of sample was recorded for 3 h until the reduction process was completed.

Mössbauer spectra were recorded using a conventional spectrometer (NZ-640, Hungary) at room temperature equipped with ^{57}Co in a matrix of metallic rhodium with a constant acceleration mode. The isomer shift (IS) was referenced to α-Fe. When processing the spectra, an in-house developed program was used for their deconvolution into Lorentzian functions.

X-ray absorption spectra at the Fe K absorption edge were measured at the P65 beamline of the PETRA III synchrotron radiation source (DESY, Hamburg, Germany) in transmission mode. The energy of X-ray photons was selected by a Si (111) double-crystal monochromator and the beam size was set by means of slits to 0.3 (vertical) × 1 (horizontal) mm^2. The extended X-ray absorption fine structure spectrum (EXAFS) background was subtracted using the Athena program from the IFFEFIT software package. The k^2-weighted EXAFS functions were Fourier transformed (FT) in the range of 2-12.3 $Å^{-1}$ of k and multiplied by a Hanning window with sill size of 1 $Å^{-1}$.

Temperature-programmed desorption of CO_2 or CO (CO_2-TPD or CO-TPD) experiments were carried out in the same setup used for H_2-TPR tests (Figure A-1) to investigate the interaction of CO/CO_2 with catalyst. Reduced or spent catalyst (50 mg of each sample for CO_2-TPD experiment and 15 mg of each sample for CO-TPD experiment) was heated in Ar (10 mL min^{-1}) at 300 °C for 2 h followed by cooling down to 50 °C in the same flow. In the case of CO_2-TPD experiments with reduced catalysts, the latter were obtained after the reduction of fresh catalysts under same conditions applied before CO_2-FTS tests. CO_2 or CO was adsorbed at room temperature until the MS signal of CO_2 or CO did not change. Hereafter, the samples were purged in Ar and kept at this temperature for 1 h to remove physically adsorbed CO_2 or CO. The samples were heated in a flow of Ar (10 mL min^{-1}) to 800 °C with a heating rate of 10 °C min^{-1}. An online mass spectrometer (Pfeiffer Vacuum OmniStar GSD 320) was used to monitor argon, CO_2 and CO at m/z of 40, 44 and 28, respectively.

Temperature-programmed hydrogenation of spent catalysts coupled with mass spectroscopy (TPH) was performed in the same setup used for H_2-TPR and CO/CO_2-TPD experiments (Figure A-1). Briefly, the spent catalyst (50 mg) was placed in a quartz reactor and fixed by quartz wool. The samples were heated to 300 °C with a heating rate of 10 °C min^{-1} in Ar for 2 h. After cooling to room temperature in the same flow, the reactor was heated up to 900 °C in 5 vol.% H_2/Ar flow (10 mL min^{-1}) with a heating rate of 10 °C min^{-1} and kept for 90 min at 900 °C. Methane formed due to the hydrogenation of carbonaceous species was detected at m/z of 15 (CH_3) using online mass spectrometer (Pfeiffer Vacuum OmniStar GSD 320).

H_2-D_2 exchange experiments were performed in a flow reactor at 300 °C with spent catalysts. Each sample (15 mg) was loaded in a quartz reaction tube and fixed with a quartz wool. After Ar treatment at 300 °C for 30 min, the samples were exposed to a gas mixture (2.5 vol.% D_2-2.5 vol.% H_2 in Ar) with 5 mL min^{-1}. The outlet gas was analyzed by an online mass

spectrometer (Pfeiffer Vacuum OmniStar GSD 320). HD was monitored at m/z of 3. A bypass (using an empty reactor) measurement was also carried out to make sure that the HD formation was catalyzed by the sample. Thus, the HD signals related to the catalyst were obtained by subtracting the background determined in the bypass test.

In situ FTIR experiments were carried out on a Nicolet iS10 infrared spectrometer (Thermo Scientific) equipped with a mercury cadmium telluride (MCT) detector and an in-house-developed high-pressure FTIR cell[290]. The spectra were recorded in transmission mode at resolution of 4 cm^{-1} and 64 scans. 50 mg of sample in powder were pressed into a wafer with diameter of 20 mm. The samples were pre-reduced at 400 °C in 50 vol.% H_2/He flow for 2h. After the reduction, the samples were exposed to a gas mixture containing 20 vol.% CO_2, 60 vol.% H_2 and 20 vol.% He (all Air Liquide) with a total gas flow rate of 50 mL min^{-1}. The temperature and pressure were 250 °C and 15 bar, respectively. An initial spectrum was collected before the introduction of the reactants and used as background. The spectra were collected by subtracting the background spectrum at various time points throughout the reaction.

In situ and *ex situ* Raman micro-spectroscopic investigations were performed on a Renishaw inVia Raman microscope. For *ex situ* Raman experiments, a spatula tip of the sample was placed on a microscope slide and a 633 nm laser light was used with a laser power of 0.17–1.7 mW. For *in situ* experiments, the Raman microscope is additionally equipped with a Linkam reaction cell, which acts as a fixed-bed flow reactor. The ceramic reactor was filled with 40–50 mg of the catalyst which leads to a filling height of approximately 4 mm. All gases were dosed by mass flow controllers. For the reduction experiments the catalysts were heated in He up to the desired temperature (400 °C) and flushed with He for 30 min. Then, the catalysts were exposed to a H_2/He feed (1/2, 15 mL min^{-1}) for 120 min.

The X-ray Photoelectron Spectroscopy (XPS) measurements were performed on an ESCALAB 220iXL (Thermo Fisher Scientific) with monochromated Al Kα radiation (E = 1486.6 eV). Samples were prepared on a stainless-steel holder with conductive double-sided adhesive carbon tape. The electron binding energies were obtained with charge compensation using a flood electron source and referenced to the C 1s core level of carbon at 284.8 eV (C-C and C-H bonds).

3.3. Steady-state catalytic tests

Catalytic tests were performed in an in-house developed reaction setup containing 51 parallel continuous-flow fixed-bed reactors (stainless-steel tube with outer and inner diameters of 6 and 4 mm, respectively). The flow rates of reactant gases were controlled by using mass-flow controllers (Bronkhorst). After mixing, the feed gas was homogeneous distributed into each rector through high pressure-drop capillaries. Typically, 300 mg of catalyst (250−450 μm fraction) was loaded in a reactor within its isothermal zone. On the top of each catalyst bed, 700 mg of SiC (ESK-SiC, F30, 500−710 μm fraction) were placed to ensure a plug flow and to pre-heat the feed components. The catalysts were *in situ* pre-reduced at 400°C (unless otherwise specified) and 15 bar with a flow of 50 vol.% H_2 in N_2 (12 mL min^{-1}) for 2 h prior to the reaction. After the reduction, the reactors were cooled down to the reaction temperature and a mixture of reactant gases (CO_2:H_2:N_2 = 1:3:0.3) was introduced into the reactors with a flow rate of 5.8 mL min^{-1}. The total pressure was 15 bar unless otherwise specified. To avoid condensation of heavy products, stainless steel lines between the reactor outlet and the GC inlet were kept at around 180 °C. The high-throughput set-up was equipped with multiway-valves, allowing the injection of gases coming from each reactor one by one into gas chromatograph for product analysis. The interval between analysis was 17 min.

The inlet and outlet gas compositions were analyzed by an on-line gas chromatograph (Agilent 7890A) equipped with a flame ionization detector (FID) and a thermal conductivity detector (TCD). C_1-C_8 hydrocarbons and C_9-C_{18} hydrocarbons were separated by AL/S column and FFAP column, respectively, and detected by FID. The separation of CO_2, H_2, N_2, CO was realized by HP Plot/Q and MolSieve 5A columns which were connected to TCD detector. The conversion of CO_2 ($X(CO_2)$) and the selectivity of gas-phase products ($S(i)$) were calculated according to Equation 3-1 and 3-2, respectively. The formation rate of light olefins and C_{2+}-hydrocarbons were calculated by Equation 3-3 and 3-4 respectively.

$$X(CO_2) = 1 - \frac{\dot{n}_{CO_2}^{out}}{\dot{n}_{CO_2}^{in}} \qquad \text{Equation 3-1}$$

$$S(i) = \frac{a_i \dot{n}_i^{out}}{\sum_{i=1}^{n} a_i \dot{n}_i^{out}} \qquad \text{Equation 3-2}$$

$$r(C_2^= - C_4^=) = \frac{F_{feed} \cdot \frac{P_{(CO_2)}}{P_{(total)}} \cdot X(CO_2) \cdot S(C_2^= - C_4^=)}{V_m \cdot m_{cat}} \qquad \text{Equation 3-3}$$

$$r_{C_{2+}} = \frac{F_{feed} \cdot \frac{P_{(CO_2)}}{P_{(total)}} \cdot X(CO_2) \cdot S(C_{2+})}{V_m \cdot m_{cat}} \qquad \text{Equation 3-4}$$

where n_i with superscripts "in" and "out" stands for molar flow of components measured at the reactor inlet and outlet, respectively. a_i is the number of carbon atoms in the reaction products. Reaction-induced change in the number of moles was considered by using N_2 as an internal standard. F_{feed} is a volumetric flow rate of feed gas (mL min^{-1}), $P(total)$ is the total pressure, $p(CO_2)$ is the partial pressure of CO_2, and V_m is the molar volume.

For spatially resolved kinetic analysis, catalyst amounts of 50, 20, 10, 5 and 3 mg were used to achieve catalyst beds with different lengths (Figure 3-1), while the total feed flow was constant, i.e. 5.8 mL min^{-1}. Thus, it is possible to achieve different levels of CO_2 conversion. The segmental rates of CO_2 conversion, CH_4 formation and C_{2+}-hydrocarbons formation were calculated as Equation 3-5.

$$r(CO_2) = \frac{\dot{n}^a_{CO2} - \dot{n}^{a+1}_{CO2}}{m^{a+1} - m^a} \; or \; r_i = \frac{\dot{n}^{a+1}_i - \dot{n}^a_i}{m^{a+1} - m^a}$$ Equation 3-5

where $\dot{n}$ and m represent the molar outlet flows of CO_2, CH_4 or C_{2+}-hydrocarbons and catalyst amount, respectively. The superscripts $a+1$ or a are used to distinguish different layers.
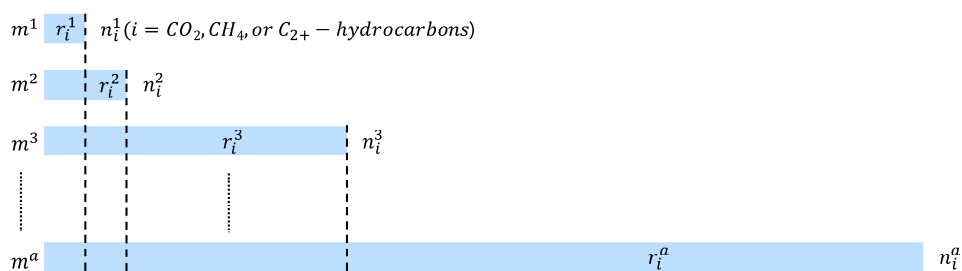
Figure 3-1 Graphical representation of segment definition along catalyst bed.

3.4. Transient kinetic experiments

3.4.1.   Temporal analysis of products

Adsorption/activation of CO_2, H_2, CO and C_2H_4 over promoted or unpromoted catalysts as well as H/D exchange were studied in the temporal analysis of products reactor (TAP-2 system). The reactor system, with a resolution of approximately 100 μs, has been introduced in detail elsewhere[291-292]. Typically, each catalyst (50 mg, 250−450 μm fraction) was placed between two layers of quartz particles (250−355 μm) in a quartz-tube reactor within its isothermal zone. No catalyst treatment was performed prior to the experiments. The reactor was evacuated at room temperature to about 10^{-5} Pa and then heated to 300 °C with a heating rate of 10 °C min^{-1}. Hereafter, single pulse experiments with CO_2/Ar = 1:1, H_2/Ar = 1:1, CO/Ar = 1:1, C_2H_4/Ar = 1:1 or H_2/D_2/Ar = 1:1:1 mixture were performed at 300°C. Additional H/D exchange tests were performed at 400 °C.

Mass transport can be quantitatively described by the Knudsen diffusion and any collisions between gas-phase species are minimized due to an overall pulse size below 10^{15} molecules. Therefore, only heterogeneous reaction steps were analyzed. Gas-phase components leaving the reactor were analyzed by an on-line quadrupole mass spectrometer (HAL RC 301 Hiden Analytical). The following AMUs were used for identification of different compounds: 44 (CO_2), 28 (CO, CO_2), 26 (C_2H_4), 4 (D_2), 3 (HD), 2 (H_2) and 40 (Ar). Pulses were repeated 10 times for each AMU and averaged to improve the signal-to-noise ratio. The concentration of the feed components and the reaction products was determined from the respective AMU using standard fragmentation patterns and sensitivity factors, which arise from the different ionization probabilities of individual compounds.

The kinetic evaluation of transient responses of CO_2 and CO was performed according to the methods described in previous works[293-294]. The microreactor was regarded as a one pseudo-homogeneous reactor and could be divided into three different zones: upstream inert zone, catalyst zone and downstream inert zone. Mass balances for gas-phase and surface species outside the catalyst layer were described according to Equations 3-6 and 3-7, respectively:

$$\frac{\partial C_i}{\partial t} = D_{Knudsen}^{eff} \times \frac{\partial^2 C_i}{\partial x^2} \qquad \text{Equation 3-6}$$

$$\Theta_i = 0 \qquad \text{Equation 3-7}$$

In the catalyst zone, the reaction term was included in the mass balances for gas-phase (Equation 3-8) and surface species (Equation 3-9):

$$\frac{\partial C_i}{\partial t} = D_{Knudsen}^{eff} \times \frac{\partial^2 C_i}{\partial x^2} + \sum_j \rho_{cat} v_{ij} r_j \qquad \text{Equation 3-8}$$

$$\frac{\partial \Theta_m}{\partial t} = \sum_j \frac{v_{ij} r_j}{C_{total}} \qquad \text{Equation 3-9}$$

with

$$r_j = k_j \prod_1 C_i^{n_i} \prod_m \Theta_m^{n_m} \qquad \text{Equation 3-10}$$

Where C_{total} is the total concentration of surface species and $D_{Knudsen}^{eff}$ is the effective Knudsen diffusion coefficient of gas-phase species, $0 \leqslant n_i \leqslant 1$, $0 \leqslant n_m \leqslant 2$, $\theta_i = C_i / C_{total}$.

In brief, the fitting procedure is based on a numerical solution of partial differential equations describing the processes of diffusional transport, adsorption/desorption, and the catalytic reaction in the micro-reactor. The resulting partial differential equations were transformed into coupled ordinary differential equations by a spatial approximation and then integrated by

numerical routine PDEONE. The search for kinetic parameters was performed in a wide range of possible values (10^{-4}–10^{8}) using first a genetic algorithm to find good starting values and then the Nelder-Mead simplex algorithms. The quality of fit was characterized by an objective function defined as the sum of squares of the shortest deviation between the respective points of the experimental data and simulated data. Moreover, the fitting for each catalyst was repeated at least 10 times. Typically, same solution with the lowest residuum was obtained several times. A sensitivity analysis was applied to check the significance of the parameters obtained from the best kinetic model. To this end, each parameter was varied until the objective function changed by 10%. Thus, if the change in the parameter is larger than 10%, this parameter does not significantly contribute to the goodness of the fit. To check if the parameters correlate, the Jacobi-matrix approach was applied.

For distinguishing between reversible and irreversible adsorption, the experimental responses of the components after pulsing of $CO_2/Ar = 1:1$, $CO/Ar = 1:1$, $C_2H_4/Ar = 1:1$ mixture were transformed into a dimensionless form as suggested in Ref.[291]. To this end, the gas flow at the reactor outlet, F_i (mol s^{-1}), and the recording time (t(s)) were converted according to Equations 3-11 and 3-12, respectively.

$$\bar{F}_i = \frac{F_i}{N_{pi}/V_{void}} = \frac{F_i \varepsilon_b L^2}{N_{pi} D_{ei}} \qquad \text{Equation 3-11}$$

$$\tau = \frac{t D_{ei}}{\varepsilon_b L^2} \qquad \text{Equation 3-12}$$

where N_{pi} is the number of moles of components i in the inlet pulse, ε_b is the fractional voidage of the packed bed in the reactor, L is the length of the packed bed in the reactor, D_{ei} is the effective diffusion coefficient of each component.

3.4.2.   Steady-state isotopic transient kinetic analysis

The steady-state isotopic transient kinetic analysis (SSITKA) reactor system used in the present study has been described in detail in our previous work[295]. Briefly, 50 mg of catalyst was loaded in a fixed-bed reactor to achieve a GHSV (gas hourly space velocity) of 36,000 mL g_{cat}^{-1} h^{-1} for CO_2-FTS reaction. The catalysts were initially reduced at 400 °C and 15 bar under 50 vol.% H_2 in N_2 (12 mL min^{-1}) for 2 h. The reactor was then cooled down to 300 °C in Ar and the pressure was decreased to 1.5 bar. Finally, a $1CO_2/11H_2/7Ar$ feed was introduced into the reactor for 1.5 h. Hereafter, the feed was replaced by an isotopic-labelled feed $^{13}CO_2/H_2/He/Ar$. When a new steady state was reached after the isotopic switch, the back switch to the non-labelled feed was performed. The feed components and the reaction products were measured online by an Agilent 7890A gas chromatograph using the same

method as described in section "Steady-state catalytic tests" as well as by an online quadrupole mass spectrometer (Balzers Omni Star). The lifetime of surface intermediates (τ_i, i = CH$_x$, CO) was determined from the area under the normalized transient curve[296]. The number of surface intermediates (Ni) was calculated according to the following equation:

$$N_i = \frac{F_{i,out}}{m_{cat}} \tau_i \qquad \text{Equation 3-13}$$

where, $F_{i,out}$ stands for the molar flow rate of product i in the outlet stream off reactor, m_{cat} is the mass of catalyst, and τ_i is the lifetime of surface intermediate.

3.5. Statistical methods

Regression tree analysis. Regression trees are regression models visualized in form of tree graphs[282, 284]. Regression tree analysis are defined on multi-dimensional domains, in which the components can be real number intervals and finite sets with or without ordering. Their value sets are intervals of real numbers, which are mapped by repeatedly splitting the set of available input data into disjoint subsets. The applied splitting approach should ensure the sum of squared errors (SSE) relative to the mean values of the response in above subsets is smallest. Therefore, a set $S = \{x_1, \ldots, x_n\}$ of input data accompanied by the dependent variables $y_1, \ldots, y_n$, e.g., the selectivity of C$_{2+}$-hydrocarbons, is taken into account. If the set S can be divided into two subsets S_1 and S_2, then the SSE for the split (S_1, S_2) can be obtained according to the following equation.

$$\text{SSE}(S_1, S_2) = \sum_{x_i \in S_1} \left(y_i - \frac{1}{|S_1|}\sum_{x_i \in S_1} y_i\right)^2 + \sum_{x_i \in S_2} \left(y_i - \frac{1}{|S_2|}\sum_{x_i \in S_2} y_i\right)^2 \qquad \text{Equation 3-14}$$

where $|S_i|$ stands for the number of elements in the set S_i.

In other words, among all possible splitting options, a split (S_1^*, S_2^*) resulting in a smallest SSE should be chosen. The entire set S of available input data is first subjected by above splitting approach, then it is applied into the obtained sets S_1^*, S_2^*, etc. If needed, this splitting would continue, finally leading to a hierarchy in the space of input variables.

The most suitable tree size is usually adopted using a cross-validation method and it can be described as follows:

(i) The dataset of catalytic performance is stochastically divided into k parts with approximately same size.

(ii) For each tree size, k trees, ranging from $Tr(1)$ to $Tr(k)$, are established. Thus, the tree $(Tr(i))$ is constructed using all parts besides the *i-th*, whereas the *i-th* part works as test data to determine the error of $Tr(i)$ predictions.
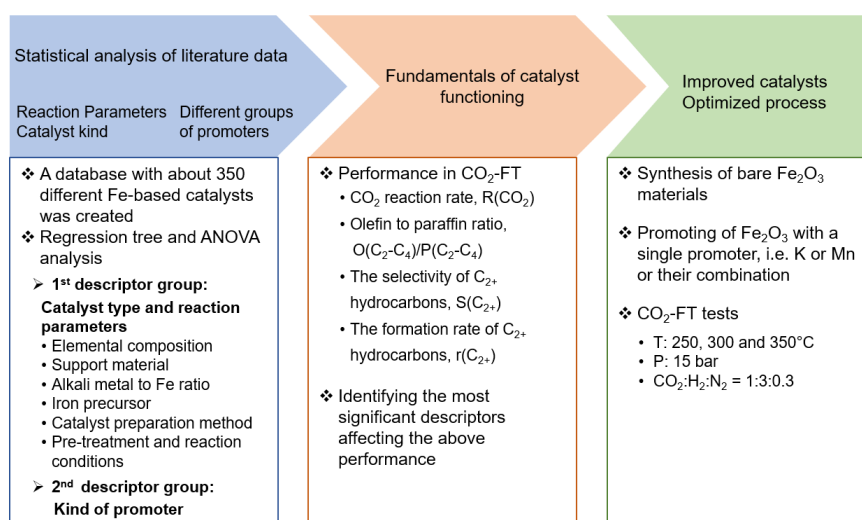
(iii) To assess the quality of the tree size, the SSE values of the test data are determined on all k trees with this size.

Analysis of Variance (ANOVA). ANOVA is a possible approach for evaluating whether a numerical response variable is affected by some factors with two or a small number of possible values, e.g., the presence of a particular element or the combination of elements. In the field of catalysis, these response variables could be yield, selectivity or conversion. Therefore, ANOVA considers the measured variance of the response for values of the factor, such as the measured variance of selectivity between an element being and not being present. Then it calculates how likely it is to obtain a variance at least as large as the measured value if the factor has no effect on the response, that is, if the probability distribution of the response is the same for all possible values of the factor. The realized significance of the response factor can be obtained from the calculated likelihood of the measured variance, also named as p value. Generally, the factor is strongly or highly significant for the response if the achieved significance is < 1%. It is significant if the achieved significance is < 5%.

4. Results and discussion

4.1. Unraveling property-performance relationships in CO_2-FTS over Fe-based catalysts through catalysis informatics and experimental validation

As discussed in the Introduction CO_2-FTS offers a promising methodology on mitigating global greenhouse effect and provides an alternative way for producing valuable chemicals and fuels. Fe_3O_4 and FeC_x (iron carbides) are responsible for the RWGS and CO-FTS reactions, respectively. The direct CO_2 methanation (Sabatier reaction) can also occur. However, the complexity in both catalyst structure (e.g., multi-Fe-containing phases involved and different iron carbides) and reaction mechanism of Fischer-Tropsch has hindered the deeper understanding of CO_2-FTS reaction. The design of Fe-based catalysts for this reaction heavily relied on empirical approach which is still popular in the field of heterogeneous catalysis up to now. As introduced in the section of 1.3, the development of catalysis informatics or data science enables us to design catalyst for a given reaction in a more intelligent way. Here, we combined mathematical approaches, i.e., regression trees, analysis of variance (ANOVA) and comparison of mean values, to establish correlations of catalyst composition or operation parameters with catalyst performance in CO_2-FTS and to identify property-performance relationships. The most decisive descriptors and possible property-performance relationships are identified and proposed through statistical analysis. Finally, the statistically established correlations are validated by experimental tests to check the predictive power of our approach in catalyst design (Scheme 4-1).

Statistical analysis of literature data

Reaction Parameters   Different groups
Catalyst kind   of promoters

- ❖ A database with about 350 different Fe-based catalysts was created
- ❖ Regression tree and ANOVA analysis
  - ➢ 1st descriptor group: **Catalyst type and reaction parameters**
    - Elemental composition
    - Support material
    - Alkali metal to Fe ratio
    - Iron precursor
    - Catalyst preparation method
    - Pre-treatment and reaction conditions
  - ➢ 2nd descriptor group: **Kind of promoter**

Fundamentals of catalyst functioning

- ❖ Performance in CO_2-FT
  - CO_2 reaction rate, $R(CO_2)$
  - Olefin to paraffin ratio, $O(C_2\text{-}C_4)/P(C_2\text{-}C_4)$
  - The selectivity of C_{2+} hydrocarbons, $S(C_{2+})$
  - The formation rate of C_{2+} hydrocarbons, $r(C_{2+})$
- ❖ Identifying the most significant descriptors affecting the above performance

Improved catalysts
Optimized process

- ❖ Synthesis of bare Fe_2O_3 materials
- ❖ Promoting of Fe_2O_3 with a single promoter, i.e. K or Mn or their combination
- ❖ CO_2-FT tests
  - T: 250, 300 and 350°C
  - P: 15 bar
  - CO_2:H_2:N_2 = 1:3:0.3

Scheme 4-1 A schematical workflow of our mathematical approach for identifying property-performance relationships.

4.1.1. Statistical analysis of literature data

A database including 352 data sets from available literatures reporting Fe-based materials catalyzed CO_2-FTS reaction was created. Only articles that include quantitative catalyst composition, fully described pre-treatment and reaction conditions, as well as complete catalytic performance were included in the database. For each data set, the detailed catalyst composition (elements composition, the kind of promoter, support material, the ratio to promoter to Fe, the used Fe precursor in catalyst preparation, and catalyst preparation method), the type of catalyst (bulk & un-promoted, bulk & promoted, supported & un-promoted, and supported & promoted), pre-treatment and reaction conditions, as well as catalytic performance were listed. Possible relevant parameters affecting catalytic performance are divided into two groups for statistical analysis: (i) the type of catalyst and reaction parameters, and (ii) promoters (Scheme 4-1). The overall rate of CO_2 conversion ($R(CO_2)$), the formation rate of C_{2+}-hydrocarbons ($r(C_{2+})$), the selectivity to C_{2+}-hydrocarbons ($S(C_{2+})$), and the ratio of lower olefins ($O(C_2-C_4)$) to lower paraffins ($P(C_2-C_4)$) were chose as the target properties.
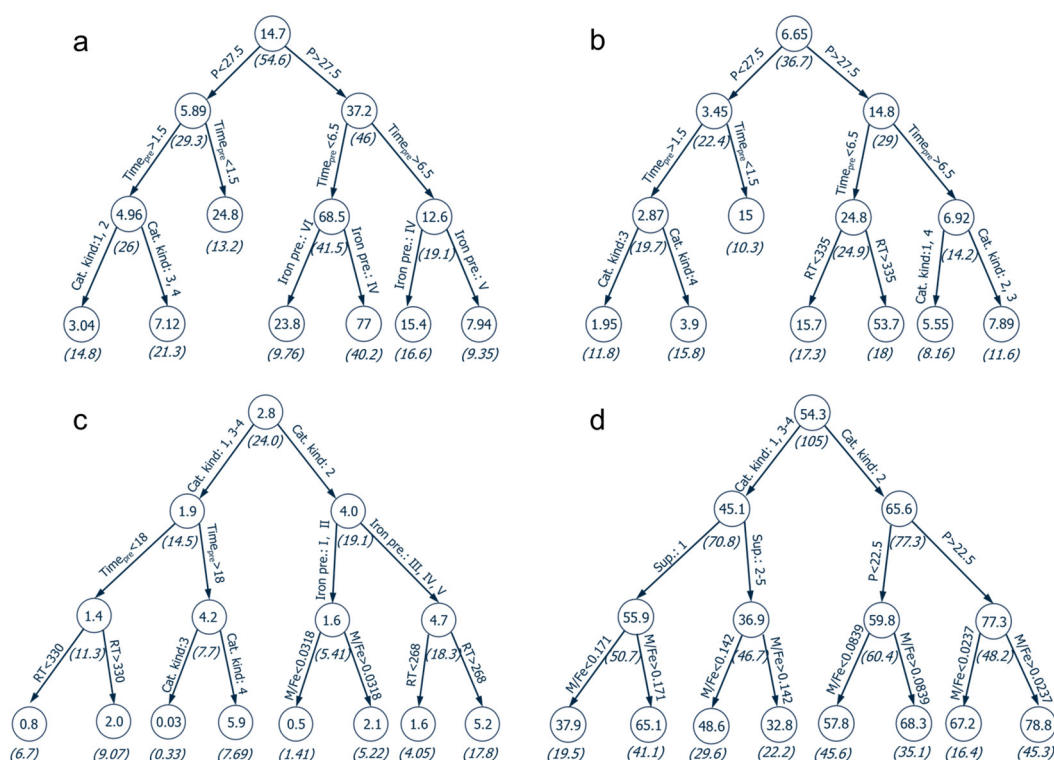
Figure 4-1 Regression trees obtained on the basis of the first group of descriptors for (a) the overall rate of CO_2 conversion, (b) formation rate of C_{2+}-hydrocarbons, (c) the ratio of lower olefins to lower paraffins and (d) selectivity of C_{2+}-hydrocarbons. Each node is labeled with the mean value of performance and the square root of SSE for each split (italic, in brackets). Decoding of the kind of catalyst: (1) bulk & un-promoted, (2) bulk & promoted, (3) supported & un-promoted and (4) supported & promoted. Iron precursors: (I) ammonium ferric citrate, (II) iron(III) chloride, (III) commercial oxide, (IV) iron nitrate, (V) iron(III) chloride/iron(II) chloride and (VI) iron(III) acetylacetonate. Support materials: (1) Al_2O_3, (2) Carbon materials, (3) SiO_2, (4) TiO_2 and (5) ZrO_2.

The first group of descriptors in Scheme 4-1 was subjected to the regression trees analysis for identifying the most important catalyst properties and operation parameters. Figure 4-1 exemplarily shows the first four nodes in the regression trees determined for $R(CO_2)$, $r(C_{2+})$, $O(C_2-C_4)/P(C_2-C_4)$ and $S(C_{2+})$. While the full regression trees in terms of different catalytic performance can be found in Figure A-2–Figure A-5. The numerical values in circles refer to the mean values of each catalytic performance. The significance of a certain descriptor decreases from root to leaf in the corresponding regression trees. The reaction pressure is identified as the most decisive parameter for $R(CO_2)$, followed by catalyst pre-treatment time and the kind of iron precursor for catalyst preparation (Figure 4-1a). Total reaction pressure has also the biggest influence on the formation rate of C_{2+}-hydrocarbons (Figure 4-1b). While the type of catalyst is the most significant factor for the $O(C_2-C_4)/P(C_2-C_4)$ ration and $S(C_{2+})$. Promoted bulk Fe-based catalysts are favorable to improving the content of olefins in light hydrocarbons (C_2-C_4) and for strengthening C-C coupling reaction (Figure 4-1c, d).
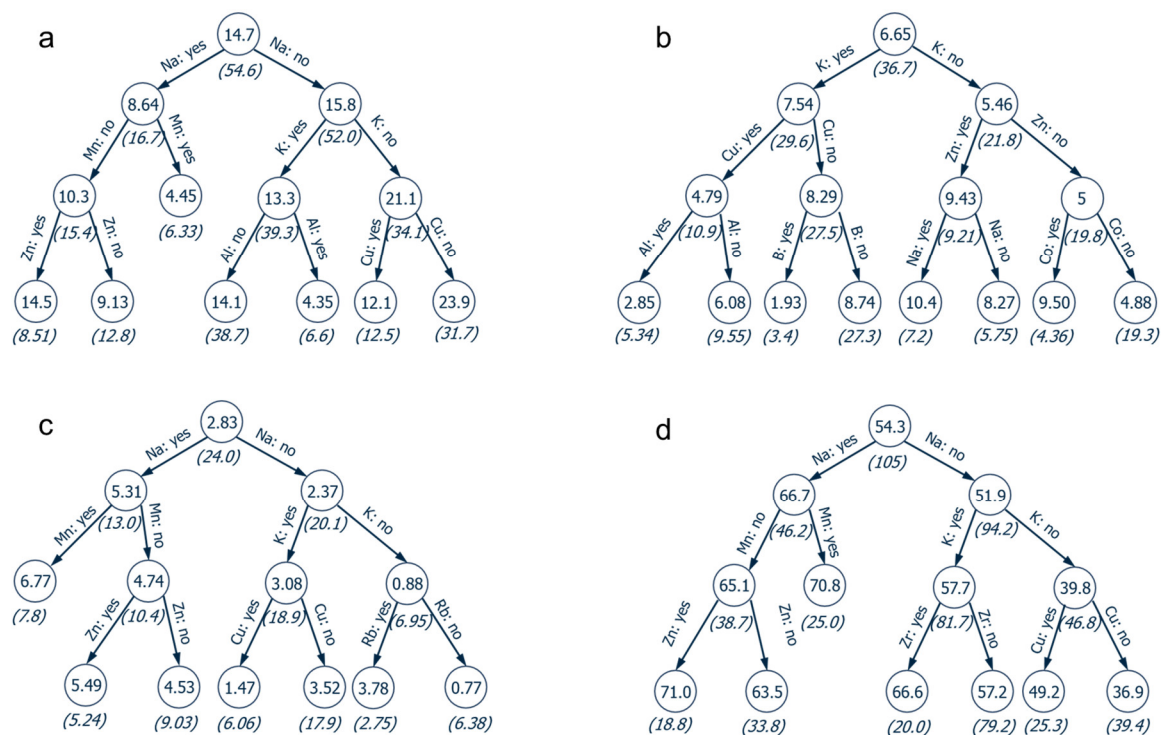
Figure 4-2 Regression trees obtained on the basis of the second group of descriptors for (a) the overall rate of CO_2 conversion, (b) formation rate of C_{2+}-hydrocarbons, (c) the ratio of lower olefins to lower paraffins and (d) selectivity of C_{2+}-hydrocarbons. Each node is labeled with the mean value of performance and the square root of SSE for each split (see the values in the brackets).

Based on the above analysis, promoters for iron oxides seem to play an important role for achieving high $O(C_2-C_4)/P(C_2-C_4)$ and $S(C_{2+})$. Therefore, now we focus on the second group of descriptors in Scheme 4-1, i.e., promoters. This group was applied to regression trees

analysis for identifying key promoter(s) influencing $R(CO_2)$, $r(C_{2+})$, $O(C_2\text{-}C_4)/P(C_2\text{-}C_4)$ and $S(C_{2+})$ as seen in Figure 4-2 and the complete trees in Figure A-6-Figure A-9. Among all promoters, sodium is determined to be the most decisive one for $R(CO_2)$, however, with a negative effect (Figure 4-2a). Regarding to the formation rate of C_{2+}-hydrocarbons, potassium is identified to have the strongest positive influence (Figure 4-2b). While the presence of sodium can enhance both the $O(C_2\text{-}C_4)/P(C_2\text{-}C_4)$ ratio and the selectivity to C_{2+}-hydrocarbons (Figure 4-2c, d). Following the regression tree shown in Figure 4-2c, it can be found that the combination of alkali metal promoter (e.g., Na) and transition metal (Mn or Zn) is an effective strategy for enhancing the ratio of lower olefins to lower paraffins. Moreover, such combination also benefits the selectivity to C_{2+}-hydrocarbons (Figure 4-2d).
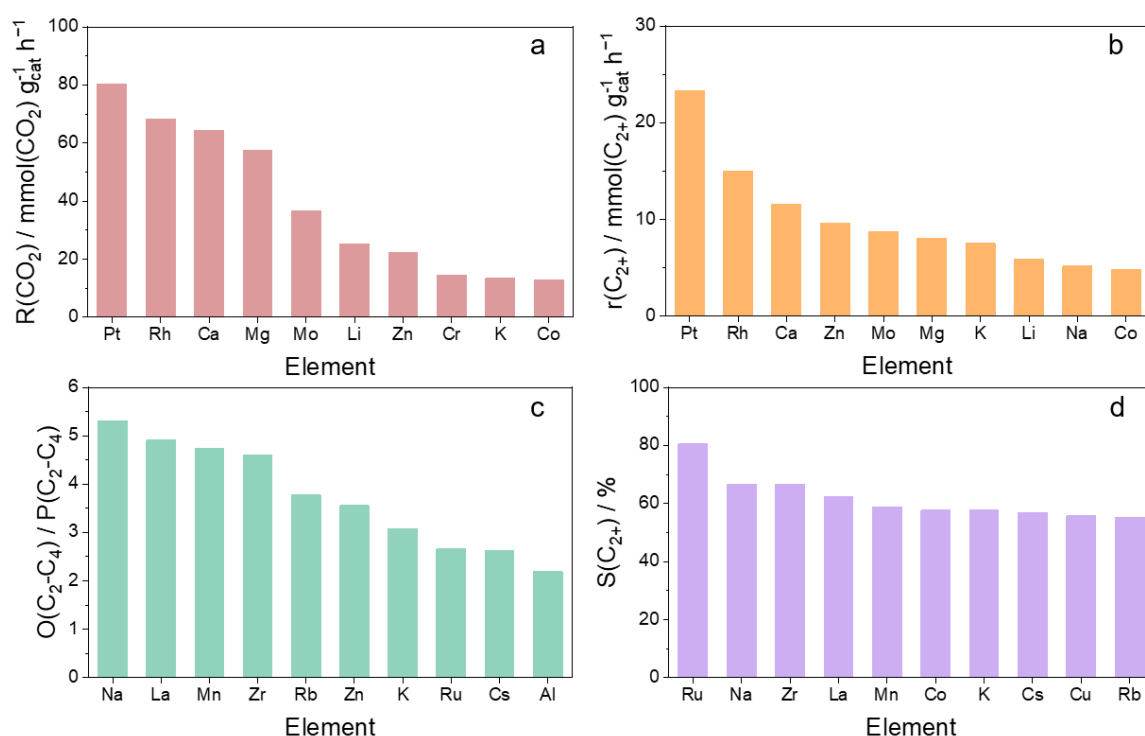
Figure 4-3 Average values of (a) overall CO_2 conversion rate, (b) formation rate of C_{2+}-hydrocarbons, (c) ratio of light olefins to light paraffins and (d) selectivity to C_{2+}- hydrocarbons over Fe-based catalysts with a certain element as promoter.

To evaluate the effect of each promoter on catalytic performance, all catalysts containing a certain promoter element were chosen and their average performance in terms of $R(CO_2)$, $r(C_{2+})$, $O(C_2\text{-}C_4)/P(C_2\text{-}C_4)$ and $S(C_{2+})$ was calculated (Figure 4-3). In this case, other promoter(s) may exist in the catalyst besides the certain promoter listed. It is evident that the overall rate of CO_2 conversion and the rate of formation rate of C_{2+}-hydrocarbons as well as their selectivity could be benefited by the presence of noble metal, e.g., Pt and Rh (Figure 4-3a, b and d). Additionally, alkali-earth metals (Ca and Mg) favored $R(CO_2)$ and $r(C_{2+})$. The

enhancements caused by Pt and Rh probably can be attributed to the ability of these metals to activate H_2. On the other hand, the increased basicity due to the presence of alkali-earth elements may contribute to CO_2 adsorption. However, noble metals are inefficient in improving the ratio of light olefins to light paraffins. Clearly, higher coverage by hydrogen species would favor the hydrogenation of the olefins, which are primary products in the CO-FTS reaction. On the contrary, the catalysts are characterized by high $O(C_2\text{-}C_4)/P(C_2\text{-}C_4)$ if they are promoted by Na or La (Figure 4-3c).

Next, we turn to discuss the case that catalysts contain a single promoter or a certain combination of promoters (Figure 4-4). When Pt or Rh exist alone in catalysts, high rates of CO_2 conversion and C_{2+}-hydrocarbon formation are obtained (Figure 4-4a, b). While a single promoter cannot guarantee high selectivity to these hydrocarbons and high $O(C_2\text{-}C_4)/P(C_2\text{-}C_4)$ as shown in Figure 4-4c, d. The usage of binary promoters was identified to enhance these two catalyst properties strongly, especially for the combination of two categories of promoters, i.e., alkali metal and another metal element.
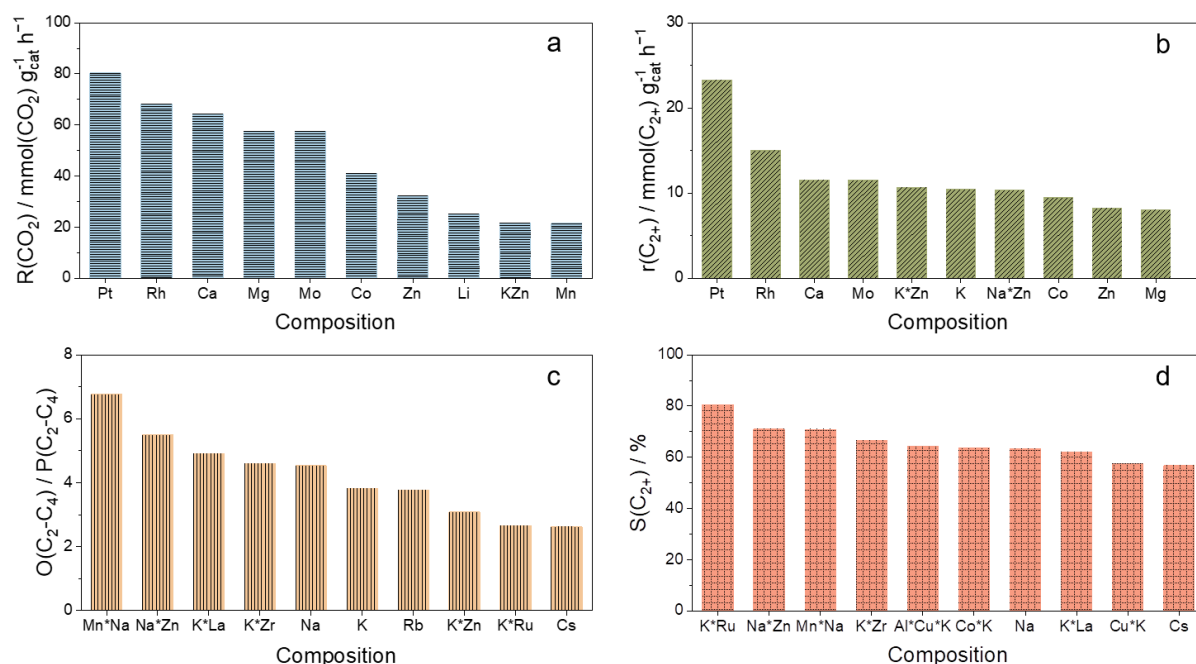
Figure 4-4 Average values of catalytic performance in terms of (a) overall CO_2 conversion rate, (b) formation rate of C_{2+}- hydrocarbons, (c) ratio of light olefins to light paraffins and (d) selectivity to C_{2+}-hydrocarbons) over Fe-based catalysts with single promoter or a certain combination of various promoters.

To further identify the significance of each individual promoter and their specific combinations, a multiway ANOVA (analysis of variance) approach was applied. The determined promoters and their significance are presented in Table 4-1. It should be noted that

the level of significance is inversely proportional to the numerical values listed in the column of "Significance level".

Table 4-1 Significant promoters determined by the ANOVA analysis

R(CO_2)		r(C_{2+})		O(C_2-C_4)/P(C_2-C_4)		S(C_{2+})	
Promoter	Significance level	Promoter	Significance level	Promoter	Significance level	Promoter	Significance level
Pt	0.004	B	0.071	Na	1.30E-06	Na	1.27E-06
Rh	0.017	Pt	0.089	Rb	0.041	Mo	0.112
Ca	0.027	Zr	0.174	Cr	0.133	Cr	0.114
K	0.043	La	0.236	Cs	0.168	Mg	0.132
Mg	0.055	Rh	0.332	Cu	0.201	Ru	0.176
Na	0.094	K	0.360	K	0.223	Zr	0.184
Mo	0.197	Ru	0.461	Mo	0.266	Ca	0.199
K&Mn	0.105	K&Co	0.183	K&Cu	9.51E-05	Na&Mn	0.131
K&Cu	0.207	K&Cu	0.370	Na&Mn	0.145	Na&Zn	0.163
Na&Mn	0.518	K&Mo	0.448	K&Mn	0.249	K&Co	0.245

The elements in this table can be divided into several groups and the role of each category can be understood as follows: (i) noble metal (Pt, Ru and Rh), which can catalyze the RWGS reaction, i.e., the first step of CO_2-FTS; (ii) alkali metals (K, Na, Rb and Cs) and alkali-earth metals (Ca and Mg), which enhance catalyst basicity and modify overall catalyst electronic properties; (iii) transition metals (Mo, Zr, Cu, and Cr), which were generally reported to modulate the reducibility of iron oxides. Moreover, several binary promotors are highlighted in this table including the combination of Na or K with another kind of metals, e.g., transition metal (Cu, Zn or Co).

The importance of combining two categories of promoters is exemplarily shown in Figure 4-5 in terms of O(C_2-C_4)/P(C_2-C_4) where Na and K were selected to represent the category of alkali metal element, and Zn and Mn were chosen as typical promoters from the group of transition metals. The effect of Zn or Mn as promoter alone is limited to achieve high O(C_2-C_4)/P(C_2-C_4). When combining them with other promoter(s), this ratio strongly increases from 1.37 to 3.56 and from 0.05 to 4.73, for Zn or Mn, respectively. The effectiveness of the combination containing K depends on the other promoter(s) in this combination. For example, combination of K with Cu does not have a positive effect on O(C_2-C_4)/P(C_2-C_4) (Figure A-8). Liu et al.[297] reported a O(C_2-C_4)/P(C_2-C_4) ratio of 4.9 for a FeZn/nanocarbon catalyst. However, this value increased to 5.71 over FeZnK/nanocarbon.
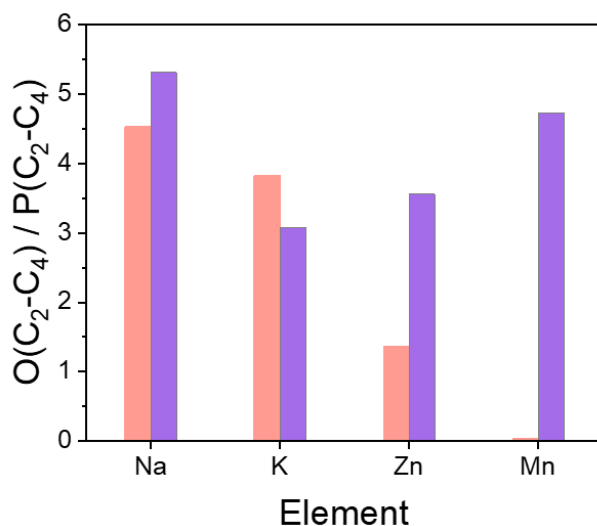
Figure 4-5 The O(C_2-C_4)/P(C_2-C_4) ratio for Fe-based catalysts containing Na, K, Zn or Mn either as single promoter (pink) or combining with other possible promoter(s) (purple).

4.1.2. Establishing property-performance relationships

Considering the importance of promoters for the CO_2-FTS reaction, an attempt was made to establish the relationships between catalyst property related to promoter and catalytic performance. It was found that the normalized CO_2 conversion rate and CH_4 selectivity can be correlated to the electronegativity of the kind of promoter used for Fe-based catalysts (Figure 4-6). Both the CO_2 conversion rate and CH_4 selectivity decrease with a decrease in the electronegativity of promoter. The electronic properties of Fe-containing active sites modified by different promoters may influence the adsorption and activation of CO_2, H_2 and CO, accordingly, and thus affect the surface H/C ratio which determine the reactivity and selectivity of CO or CO_2 hydrogenation.
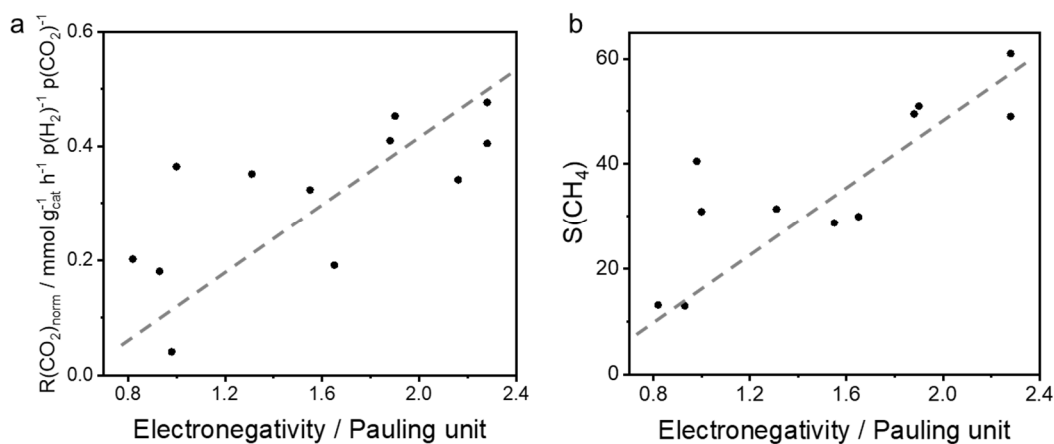
Figure 4-6 (a) CO_2 conversion rate normalized by partial pressure of CO_2 and H_2 and (b) the methane selectivity as a function of the electronegativity of promotor. The data used here was obtained at reaction temperature of 320 °C in the database.

4.1.3. Physicochemical properties of designed catalysts

The above-described statistical analysis has revealed that the promoted Fe-based catalysts are necessary to achieve desired overall reaction rate, selectivity to C_{2+}-hydrocarbons and proportion of lower olefins. The combination of alkali and transition metals as binary promoters was identified to be effective for improving catalytic properties. To prove these statistical results experimentally, a series of bulk iron oxide catalysts promoted by K, Mn or Mn&K with different K/Mn ratios were prepared by incipient wetness impregnation method as described in section 3.1. The nominal ratio of K/Fe or Mn/Fe is 0.005 for the catalysts containing single promoter (K or Mn) and they are denoted as 0.005K/Fe or 0.005Mn/Fe. For the catalysts promoted by Mn and K together (xMn-K/Fe, x = Mn/Fe molar ratio), the ratio of Mn/Fe ratio varies as 0.4, 0.7, 1.2, 2 or 5 with a constant K/Fe molar ratio of 0.005. The promoter-free iron oxide was synthesized by a chemical precipitation method and abbreviated as Fe_2O_3-P. Moreover, these catalysts were tested for the CO2-FTS reaction under the same reaction conditions. Therefore, the influence induced by different reaction conditions in literatures can be avoided.

Table 4-2 Selected physicochemical properties of iron oxide catalysts promoted by Mn, K or Mn&K.

Catalyst	Crystallite size [a] (nm)	BET surface area (m^2 g^{-1})	Mn/Fe [b] molar ratio	K/Fe [b] molar ratio	$n(H_2)$ (mmol H_2 g^{-1})	$n(H_2)$/ $n(Fe_2O_3)$	$T_{max,TPR}$ (°C)
Fe_2O_3-P	16	41	--	--	8.3	1.3	377
0.005Mn/Fe	19	37	0.0053	--	11.2	1.8	388
0.005K/Fe	19	25	--	0.0046	9.4	1.5	383
0.4Mn-K/Fe	19	38	0.0022	0.0051	11.8	1.9	375
0.7Mn-K/Fe	18	38	0.0044	0.0059	11.9	1.9	388
1.2Mn-K/Fe	18	27	0.0069	0.0055	11.4	1.8	396
2Mn-K/Fe	19	36	0.010	0.0051	10.6	1.7	392
5Mn-K/Fe	18	28	0.028	0.0051	12.8	2.0	370

[a] The crystallite size of α-Fe_2O_3 was determined according to Scherrer equation.

[b] The actual contents of K and Mn were measured by ICP-OES method.

The fresh and spent catalysts were thoroughly characterized by the state-of-the-art techniques to examine their physicochemical properties. The actual contents of K and/or Mn are close to their nominal values as measured by ICP-OES (Table 4-2). The introduction of promoter(s) leads to a decrease in the specific surface area (Table 4-2). Only hematite phase (α-Fe_2O_3) was identified in all promoted and unpromoted catalysts according to their XRD patterns (Figure A-10 in appendix). No K- or Mn-relevant phases were found probably due to the low concentration of the promoters favouring their high dispersion. Moreover, the effect of

promoters(s) on the size of α-Fe$_2$O$_3$ crystallites is minor. The size was calculated according to Scherrer equation (Table 4-2).

It has been well documented that iron oxides during reduction and CO/CO$_2$-FTS reaction are transformed into iron carbides which are accepted as the active phases.[240, 298] Therefore, we examined the composition of spent catalysts by means of XRD (Figure 4-7). Both Fe$_3$O$_4$ and Fe$_5$C$_2$ exist in the spent catalysts, but the former is dominant. The presence of Mn alone as promoter did not induce significant changes in the composition of spent Fe$_2$O$_3$-P and 0.005Mn/Fe catalysts. However, evident peaks of Fe$_5$C$_2$ can be found in the XRD pattern of 0.005K/Fe spent catalyst, implying K promoted the formation of Fe$_5$C$_2$. Such effect is stronger when K and Mn coexist together.
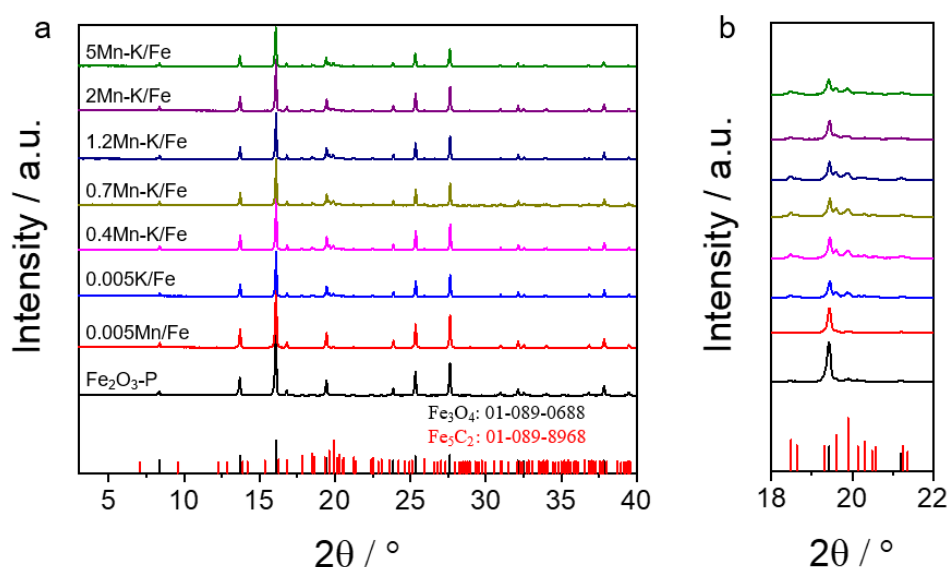
Figure 4-7 XRD patterns of spent catalysts in the 2θ range (a) from 5 to 40° and (b) from 18 to 22°.

We also examined the reducibility of promoted and unpromoted iron oxides through H$_2$-TPR experiments. Two H$_2$ consumption peaks can be found in H$_2$-TPR profiles regardless the used materials (Figure 4-8a). The first H$_2$ consumption peak belong to the reduction of Fe$_2$O$_3$ to Fe$_3$O$_4$, while the second peak is broader in its shape and attributed to the reduction of Fe$_3$O$_4$ to FeO and/or metallic Fe. The presence of Mn and/or K affects the position of H$_2$ consumption peaks with different tendencies and extents. The maximum of the first peak shifts to higher temperature for 0.005Mn/Fe and 0.005K/Fe compared with Fe$_2$O$_3$-P (Figure 4-8a, Table 4-2). This is also valid for the onset temperature of the second peak. These results implies that K and Mn hinder the reduction of Fe$_2$O$_3$ and Fe$_3$O$_4$ to Fe. Such effect becomes more significant in the case of xMn-K/Fe and increases with the increasing of Mn/Fe ratio until 1.2. When the Mn/Fe ratio is increased further to 2 and 5, the peaks shift to lower temperature in comparison

with 1.2Mn-K/Fe. Moreover, it was found that the amount of reducible iron oxides increases for Mn and/or K promoted catalysts as evidenced by the ratio of consumed H_2 to iron oxide.
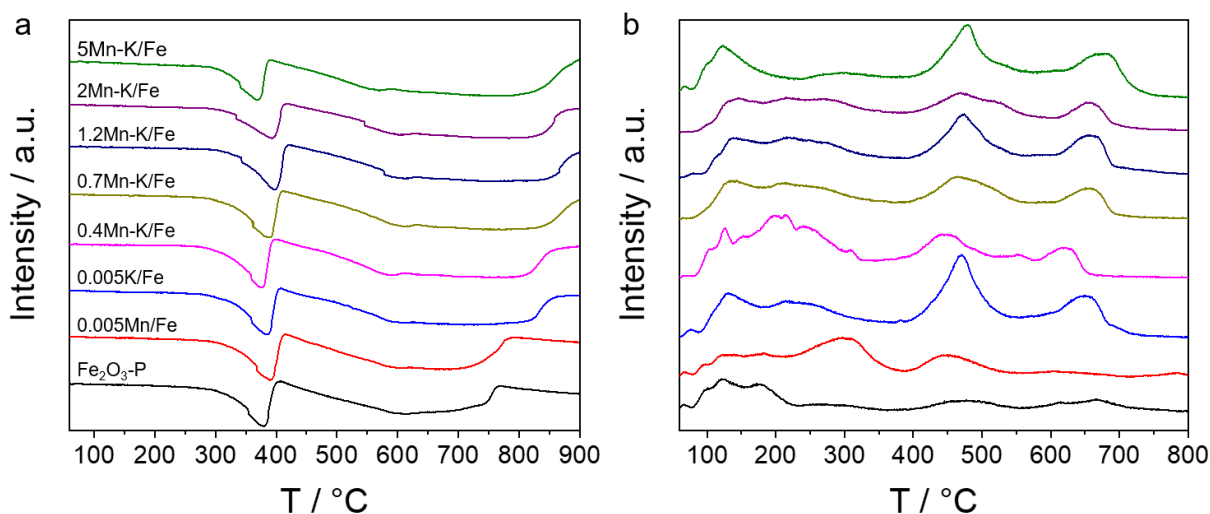
Figure 4-8 (a) H_2-TPR profiles and (b) CO_2-TPD profiles of fresh and reduced Fe_2O_3-P, 0.005K/Fe, 0.005Mn/Fe and xMn-K/Fe catalysts, respectively.

Temperature-programmed desorption of CO_2 (CO_2-TPD) was analyzed to probe basic properties of reduced and spent catalysts. The CO_2-TPD profiles obtained for the reduced catalysts are presented in Figure 4-8b. The weakly adsorbed CO_2 results in the desorption peak between 80 and 200 °C. This peak becomes weaker for 0.005Mn/Fe, but another peak at around 300 °C appears. For other catalysts, a very broad peak can be found below 300 °C. The most obvious difference among these reduced catalysts in CO_2-TPD profiles comes from the desorption behavior above 400 °C. Only two peaks with very weak intensity can be observed in this region for Fe_2O_3-P and 0.005Mn/Fe. These two peaks become much stronger for the catalyst modified with K (0.005K/Fe), indicating more adsorption sites induced by the adding of K. However, they are weaker and shift to lower temperatures for Mn and K co-promoted catalyst (0.4Mn-K/Fe). With the increase in Mn/K ratio from 0.4 to 5, these two peaks increasingly shift two higher temperatures, implying that the strength of CO_2 adsorption increases with the Mn/K ratio.

Different from the reduced catalysts, their spent counterparts possess CO_2 desorption peaks only above 400 °C (Figure A-11). The dominant desorption peak locates at 400-500 °C. The strength of CO_2 adsorption on spent catalysts follows the order of Fe_2O_3-P < 0.005Mn/Fe < 0.005K/Fe as indicated by the temperature of the main desorption peak. Moreover, desorption peaks for 0.005K/Fe and 0.005Mn/Fe are much stronger in their intensities than that of Fe_2O_3-P. No significant difference in terms of adsorption strength is found between 0.005K/Fe and

the catalysts promoted by Mn and K together with Mn/K ratio of 0.4, 0.7 and 1.2. When this ratio increases further to 2 and 5, CO_2 desorption peak shifts to lower temperature and becomes weaker in intensity. In conclusion, the presence of Mn or K could enhance the ability of catalyst to adsorb CO_2. However, too high concentration of Mn in K-promoted catalyst plays a negative role for CO_2 adsorption. Due to the importance of CO_2 adsorption in its conversion reaction, the strong differences in the CO_2 adsorption behavior between promoted catalysts and unpromoted catalyst are expected to affect their catalytic performance in CO_2 hydrogenation reaction.

4.1.4. Catalytic performance of designed catalysts

The designed catalysts were tested in the CO_2-FTS reaction at different reaction temperatures of 250-350 °C and 15 bar. As described in section 3.3, all catalysts were reduced in 50 vol.% H_2/N_2 for 2 hours prior to the reaction. First, we focus on the effect of reaction temperature and catalyst formulation on CO_2 conversion and the selectivity to higher hydrocarbons (Figure 4-9). Regardless of the kind of catalysts, increasing reaction temperature improves CO_2 conversion expectedly. Such enhancement is much stronger from 250 °C to 300 °C for xMn/Fe catalysts, but less pronounced from 300 °C to 350 °C (Figure 4-9a).
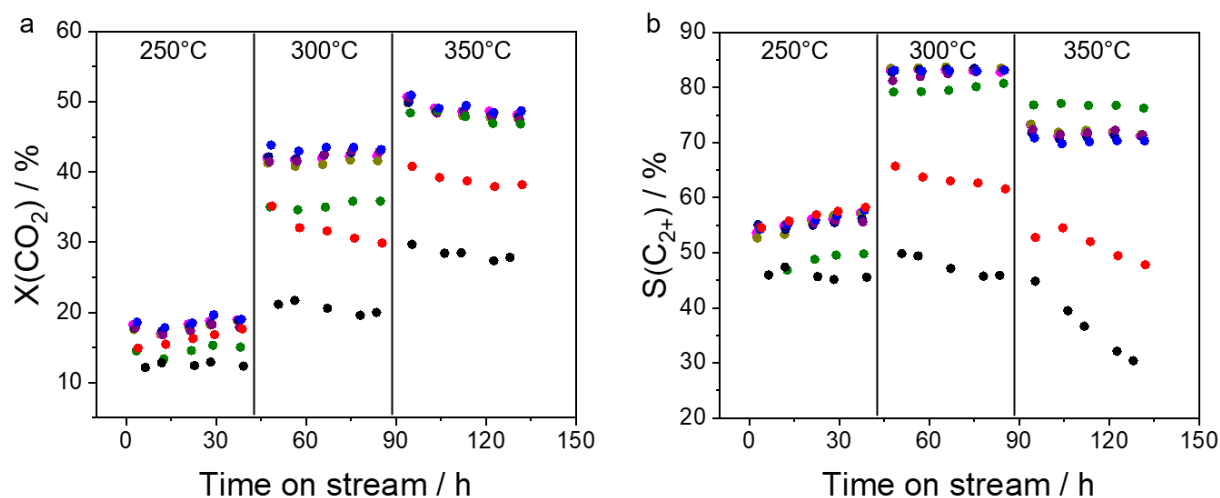
Figure 4-9 The effect of temperature on (a) CO_2 conversion and (b) the selectivity to C_{2+}-hydrocarbons in CO_2 hydrogenation over Fe_2O_3-P (black circles), 0.005Mn/Fe (red circles), 0.005K/Fe (blue circles), 0.4Mn-K/Fe (magenta circles), 0.7Mn-K/Fe (dark yellow circles), 1.2Mn-K/Fe (navy circles), 2Mn-K/Fe (purple circles) and 5Mn-K/Fe (olive circles). Reaction conditions: 300 mg, $H_2/CO_2/N_2$ = 3/1/0.3, total flow of 5.8 mL/min, total pressure of 15 bar.

Different from CO_2 conversion, the highest selectivity to C_{2+}-hydrocarbons is achieved at 300 °C for all catalysts. When the reaction temperature was increased to 350 °C further, the selectivity to C_{2+}-hydrocarbons does not increase, but slightly decrease especially for

promoted catalysts. As will be shown later, the selectivity to CH_4 increases with an increase in the reaction temperature from 300 °C to 350 °C.

The CO_2 conversion over different catalysts is compared at 250-350 °C (Figure 4-9a, Figure A-12a). The promoter-free catalyst Fe_2O_3-P displays the lowest CO_2 conversion. The presence of Mn increases CO_2 conversion at reaction temperatures. A further enhancement in CO_2 conversion can be found over 0.005K/Fe compared with Fe_2O_3-P and 0.005Mn/Fe. With the addition of Mn to 0.005K/Fe catalyst, no further increase in CO_2 conversion is observed, even it drops slightly for the 5Mn/Fe catalyst.
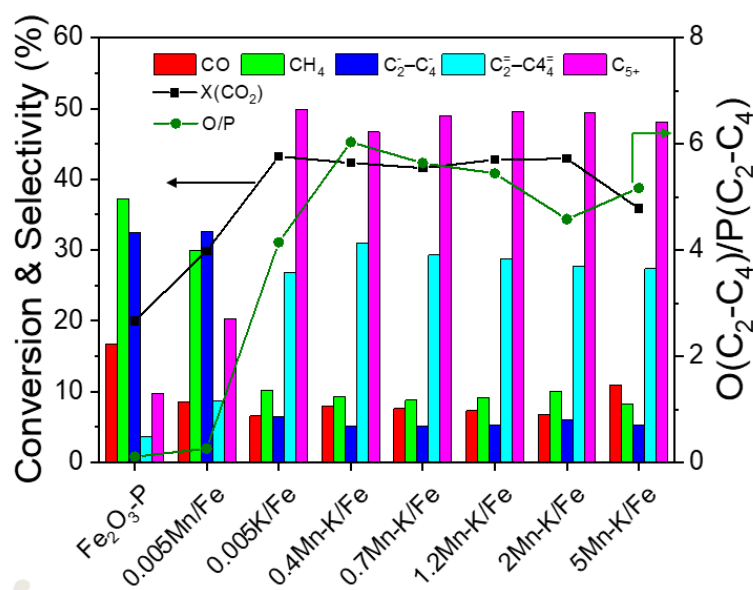
Figure 4-10 CO_2 conversion ($X(CO_2)$) and product distribution over different catalysts. Reaction conditions: 300°C, 15 bar, H_2:CO_2:N_2 = 3:1:0.3, 45 hours on stream.

Not only CO_2 conversion but also product distribution over different catalysts are compared in Figure 4-10 at the reaction temperature of 300 °C. Clearly, promoting of Fe_2O_3-P with Mn decreases the selectivity to CH_4 (29.9 *vs*. 37.2%) and increases the selectivity to light olefins (3.6 *vs*. 8.6%) and C_{5+}-hydrocarbons (9.7 *vs*. 20.4%) compared with the promoter-free catalyst. Much more significant changes are observed over 0.005K/Fe catalyst as evidenced by the decrease in CH_4 selectivity from 37.2 % to 10.2 %, the decrease in the selectivity to light paraffins from 32.4% to 6.5%, the increase in selectivity to light olefins from 3.6% to 26.8% and the increase in selectivity to C_{5+}-hydrocarbons from 9.7% to 50.0%. More importantly, the ratio of light olefins to light paraffins is enhanced by about 37 times after adding of K (0.11 and 4.14 without and with K, respectively). This parameter reaches 6.03 over 0.4Mn-K/Fe. However, the ratio of K to Mn does not affect this performance strongly (Figure 4-10), even though a slight decrease in $O(C_2$-$C_4)$/$P(C_2$-$C_4)$ is observed. It has been

53

reported that potassium as promoter can suppress methanation reaction and inhibit the hydrogenation of olefins in the CO/CO$_2$-FTS reactions.[224, 228] The results presented here indicate that the combination of K and Mn gives rise to a synergetic role on the basis of the promotion effect of potassium.

Considering both CO$_2$ conversion and product distribution, an optimal catalytic performance is obtained over the catalyst promoted by K and Mn together with Mn/K ratio of 0.4 (Figure 4-10). Therefore, the effectiveness of combining two categories of promoters, specifically alkali metal promoter and transition metal promoter, revealed by statistical analysis approach was verified in design active and selective catalysts here.
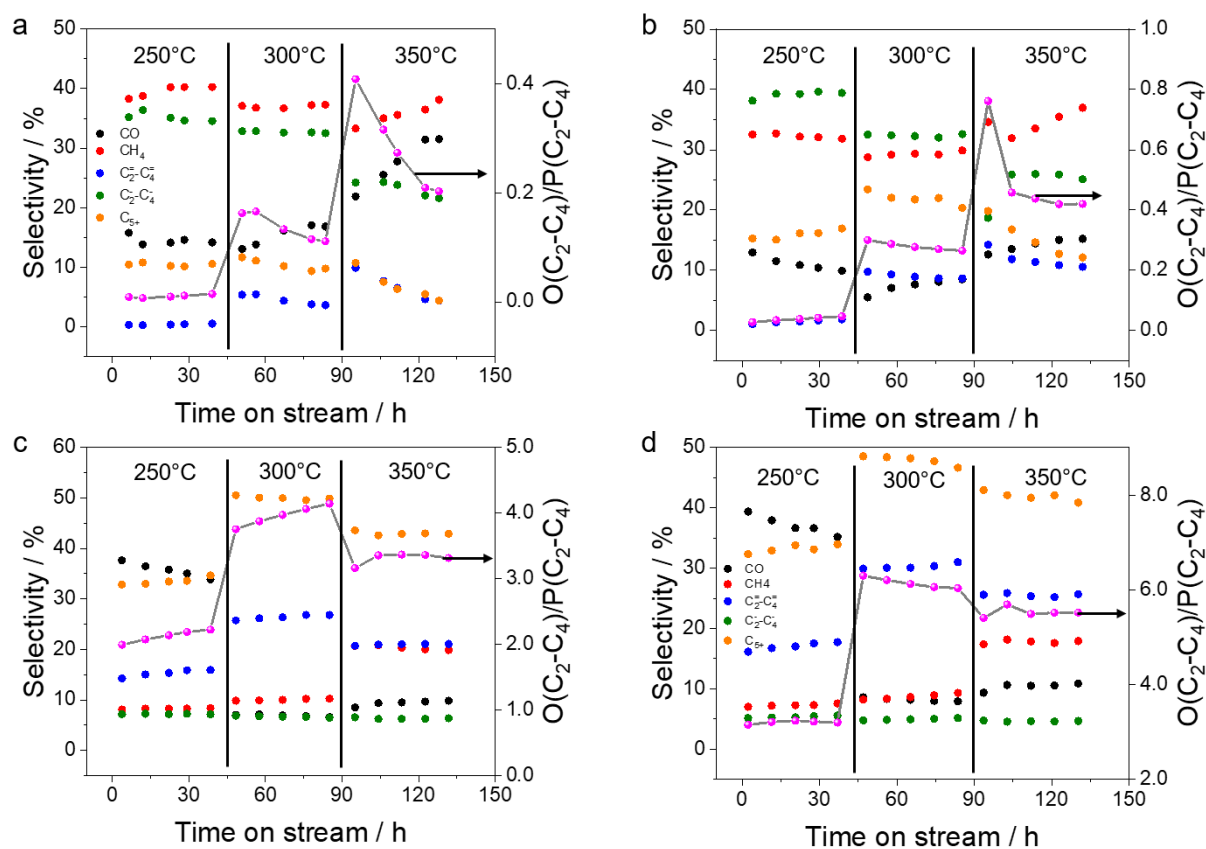
Figure 4-11 Product distribution with time on stream at different reaction temperatures over (a) Fe$_2$O$_3$-P, (b) 0.005Mn/Fe, (c) 0.005K/Fe and (d) 0.4Mn-K/Fe catalysts. Reaction conditions: 300 mg, H$_2$/CO$_2$/N$_2$ = 3/1/0.3, total flow of 5.8 mL/min, total pressure of 15 bar.

The stability of promoter-free and promoted catalysts in the CO$_2$-FTS reaction is presented in Figure 4-11. This catalyst property is highly influenced by both reaction temperature and catalyst formulation. For the unpromoted catalyst Fe$_2$O$_3$-P, a heavy deactivation is observed at the reaction temperature of 350 °C (Figure 4-11a), even though it works relatively stable at lower temperatures (250 and 300 °C). Moreover, the selectivity to light olefins and C$_{5+}$-hydrocarbons decreases, while the selectivity to CO and CH$_4$ increases. These results imply

that the second step, CO-FTS, is hindered over the deactivated catalyst. Moreover, the ratio of light olefins to light paraffins drops strongly with time on stream at 350 °C due to a decrease in the selectivity to light olefins. Similar phenomena are also observed over Mn-promoted catalyst (Figure 4-11b). However, K- or Mn-K-promoted catalyst displays excellent stability even at 350 °C (Figure 4-11c, d), which mainly attributed to the presence of potassium, but not Mn. Potassium may inhibit the sintering of iron carbides, the re-oxidation of iron carbides, and/or the formation of inactive carbon on the catalyst surface, which are regarded as the reasons for the deactivation of CO/CO_2 hydrogenation over Fe-based catalysts.

Table 4-3 The comparison of catalytic performance of the catalyst designed in this work and various state-of-the-art Fe-based materials reported in literatures using a feed with the ratio of H_2/CO_2 of 3.

Catalyst	T (°C)	P (bar)	GHSV (mL g_{cat}^{-1} h)	X(CO_2) (%)	S(CO) (%)	S(CH_4) (%)	S($C_2^=$-$C_4^=$) (%)	r($C_2^=$-$C_4^=$) (mmol g_{cat}^{-1} h)	S(C_{2+}) (%)	O(C_2-C_4) / P(C_2-C_4)	Ref.
92.6Fe7.4K	300	25	560	41.7	6.0	10.3	21.6	0.54	83.8	3.48	[299]
10Fe0.8K0.53Co	300	25	560	54.6	2.0	18.9	24.4	0.81	79.1	3.17	[300]
K-Fe15	300	10	2700	48.5	10.6	15.0	35.0	5.12	74.4	5.00	[224]
1% Na-10% Fe/ZrO_2	340	20	1200	39.0	21.0	12.4	28.9	1.44	46.6	5.57	[237]
10Fe3Zn1K /Al_2O_3	400	30	3600	38.6	33.3	35.8	7.5	1.16	30.9	0.5	[301]
$CuFeO_2$-12	300	10	1800	18.1	31.9	2.7	21.3	0.76	65.4	7.0	[302]
5Na/Fe	340	20	1200	24.0	21.0	20.4	24.5	0.73	47.3	1.5	[303]
FeNa(0.43)	320	30	2000	39.6	14.0	13.6	39.5	3.35	72.5	5.6	[304]
20Fe-1K/m-ZrO_2	340	20	1200	30.3	19.9	51.0	12.6	0.41	30.0	0.7	[305]
ZnFeOx-4.25Na	320	30	4000	38.4	11.2	9.3	29.4	4.84	75.2	7.7	[306]
0.005K/Fe	300	15	1160	43.5	6.8	10.1	26.8	1.40	82.9	4.1	This work
0.4Mn-K/Fe	300	15	1160	42.3	8.0	8.9	30.4	1.54	83.1	6.0	This work

To highlight the designed catalyst in this work and prove the power of the statistical analysis in catalyst design, the catalytic performance over 0.005K/Fe and 0.4Mn-K/Fe catalysts are compared with those over the state-of-the-art Fe-based catalysts reported in literatures. To this end, operation parameters and catalytic performance including CO_2 conversion, selectivity to CO, CH_4, light olefins and C_{2+}-hydrocarbons, the ratio of light olefins to light paraffins, and the formation rate of light olefins from selected literatures and this work are listed in Table 4-3. Clearly, the catalysts designed here are superior to or at least comparable with other Fe-based catalysts with respects to both activity and selectivity. Further, the comparison is presented in a way of the dependence of selectivity to C_{2+}-hydrocarbons on CO_2 conversion

(Figure 4-12). It is evident that both high CO_2 conversion and desired selectivity to higher hydrocarbons can be achieved simultaneously.
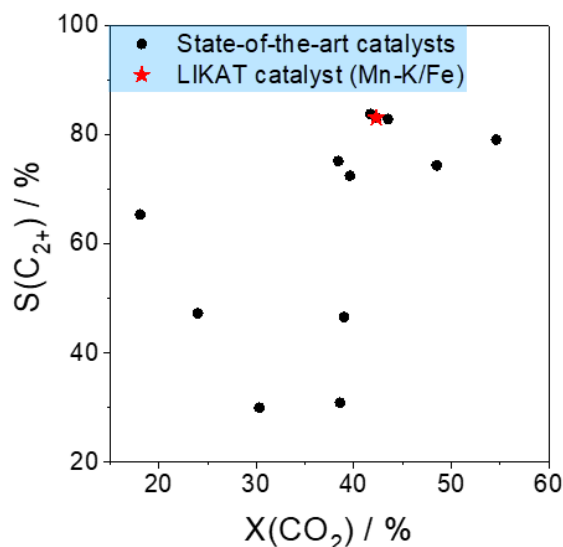
Figure 4-12 The comparison of the optimal catalyst designed here with other reported state-of-the-art Fe-based catalysts in terms of the dependence of selectivity to C_{2+}-hydrocarbons on CO_2 conversion.

4.1.5. Summary

Hereby, this work has shown that the approach of statistical analysis of literature data is suitable for purposeful catalyst development and design of catalysts with desired catalytic performance in the CO_2-FTS reaction. Using available literature data on this reaction, a database was created which includes more than 350 data sets. Each data set contains detailed catalyst-relevant information, operation conditions, and catalytic performance. The most significant parameters are identified through regression tress analysis, ANOVA, and comparison of mean values. Such approach allows us to establish property-performance relationships based on the knowledge obtained in above statistical analysis. Finally, the statistically relevant conclusions were successfully validated by experimental studies.

This concept and methodology presented in this work may be useful for other important reactions in designing catalysts and optimizing operation parameters. Nevertheless, it is highly important to provide fundamental chemical insights into the above statistically established property-performance relationships. Specifically, the understanding on the effect of basic physicochemical properties of Fe-based catalysts and the effect of alkali metal promoters on CO_2 hydrogenation will be shown in the next sections.

4.2. Identifying performance descriptors in CO_2 hydrogenation over iron-based catalysts promoted with alkali metals

Alkali metals have been widely used in many industrially relevant processes, e.g., CO-FTS and ammonia synthesis. Numerous studies also contributed to understanding of the promotion effect of alkali metals on performance of Fe-based catalysts in CO_2 hydrogenation. It has been accepted that the presence of K or Na can strongly inhibit the formation of methane. However, the fundamentals behind their effect are rarely investigated through experimental evidence partially due to the complex mechanism of this reaction. Moreover, there is no consistent conclusion on the effect of alkali metal promoter on the activity in CO_2-FTS over Fe-based catalysts. It was also reported that the presence of alkali metal promoter influences the carburization of Fe/FeO_x during reaction. However, some important questions remain unclear. For example, does the formation of iron carbide depend on the kind of alkali metals and on the amount of alkali metal promoter?

Considering the above concerns and questions, an approach was developed to disclose the promotion effect of alkali metals on CO_2-FTS over Fe-based catalysts. It combines the state-of-the-art methods for characterization of fresh and spent catalysts with spatially resolved steady-state experiments and transient kinetic analysis. Specially, temporal analysis of products (TAP) with sub-millisecond resolution can provide kinetic information about activation of individual feed components and reaction products on the level of near elementary step. Using the TAP reactor, it was possible to provide deeper insights into the interactions of feed (CO_2 and H_2 in this case) and intermediate (CO and C_2H_4) compounds with the surface of reduced and spent catalysts. These interactions play an essential role in determining catalyst activity and, more importantly, product selectivity. On the other hand, spatially resolved catalytic tests offer an opportunity to get an insight into catalyst efficiency and to understand how individual reaction rates change along the catalyst bed.

4.2.1. Platform of catalysts and phase transformation induced by reaction

Based on promoter-free α-Fe_2O_3 material synthesized by a chemical precipitation method, a series of bulk Fe_2O_3 catalysts with an alkali metal (Li, Na, K, Rb or Cs) promoter were prepared through an incipient wetness impregnation method as introduced in 3.1. They are denoted as xAM/Fe with x representing the nominal atom ratio of alkali metal promotor to Fe of 0.001, 0.005, 0.02 or 0.05. The loadings of alkali metal promoters were measured by ICP-OES or AAS method (Table A-1) and they are close to the nominal values. X-ray diffraction (XRD) patterns demonstrate the typical peaks of hematite (α-Fe_2O_3, ICDD 01-072-0469) for

all samples (Figure 4-13). No other phases were identified. The presence α-Fe$_2$O$_3$ is confirmed by transmission electron micrographs (TEM) images of representative samples (0AM/Fe, 0.001K/Fe and 0.05K/Fe) as seen in Figure A-13. The fringes spacings with 0.27 and 0.37 nm of adjacent lattice planes correspond to the (104) facet and (012) facet, respectively, of hematite, which is consistent with the rhombohedral structure identified by XRD. The hematite structure was retained after the addition of promoter. This was confirmed by XRD patterns (Figure 4-13) and selected area electron diffraction patterns (SAED, Figure A-13c, f and i) which display few spots assigned to hematite.
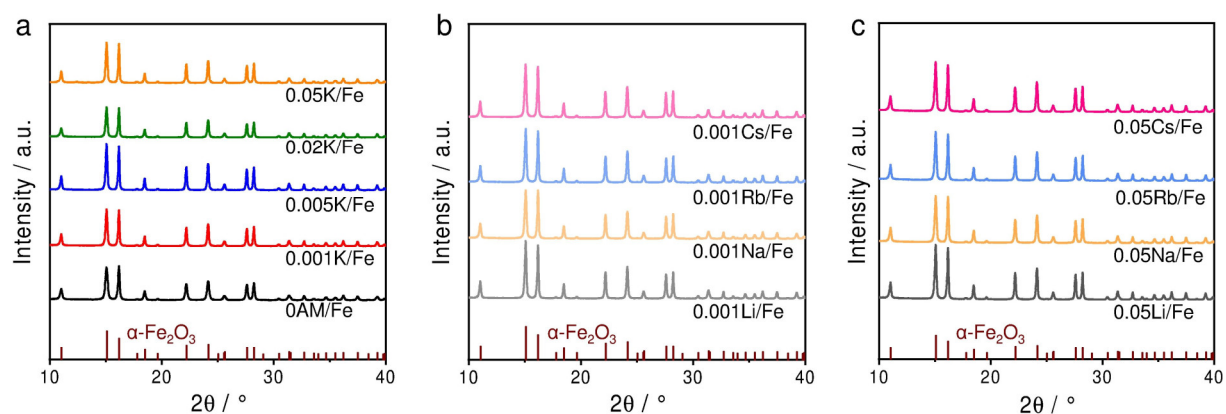
Figure 4-13 The X-ray diffraction (XRD) patterns of as-prepared unpromoted (0AM/Fe) and promoted (xAM/Fe) catalysts.

Temperature-programmed reduction with H$_2$ (H$_2$-TPR) was used to investigate how the kind of promoter and its loading affect reducibility of α-Fe$_2$O$_3$. The obtained H$_2$-TPR profiles are shown in Figure 4-14. The reduction of α-Fe$_2$O$_3$ proceeds in the following steps: α-Fe$_2$O$_3$ to Fe$_3$O$_4$, Fe$_3$O$_4$ to FeO/Fe and finally FeO to Fe (Figure 4-14a).
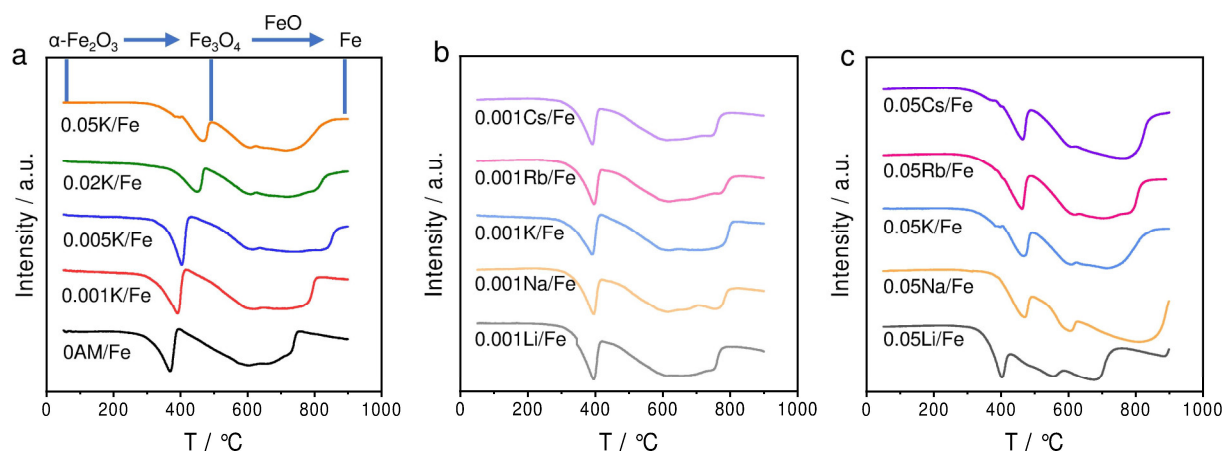
Figure 4-14 H$_2$-TPR profiles of as-prepared unpromoted (0AM/Fe) and promoted catalysts (xAM/Fe).

Obviously, the introduction of potassium to α-Fe$_2$O$_3$ shifts the H$_2$ consumption profile to higher temperature and such phenomenon becomes more pronounced with increasing K/Fe

ratio (Figure 4-14a), which suggests that the introduction of potassium hampered the reduction of iron oxide. In the case of other alkali metal promoters, the H_2-TPR profiles were found to be similar and independent on the kind of alkali promoter for 0.001AM/Fe (Figure 4-14b). When the ratio of AM/Fe increased to 0.05, the reduction occurred at higher temperatures compared with 0.001AM/Fe and this inhibition effect was less obvious in the presence of Li promoter (Figure 4-14c).

The potential of these catalysts in CO_2 hydrogenation at industrially relevant degrees of CO_2 conversion (> 20%) was evaluated. Selected catalytic data are presented in Figure 4-15 and Figure A-14. Compared with 0AM/Fe, 0.001AM/Fe catalysts display higher CO_2 conversion, lower selectivity to CH_4, higher selectivity to light olefins and C_{5+}-hydrocarbons apart from 0.001Li/Fe. Similar catalytic performance was also established for 0.001K, Rb or Cs/Fe catalysts. The promotion effect is enhanced when the loading of alkali promoters increases further (Figure A-14).
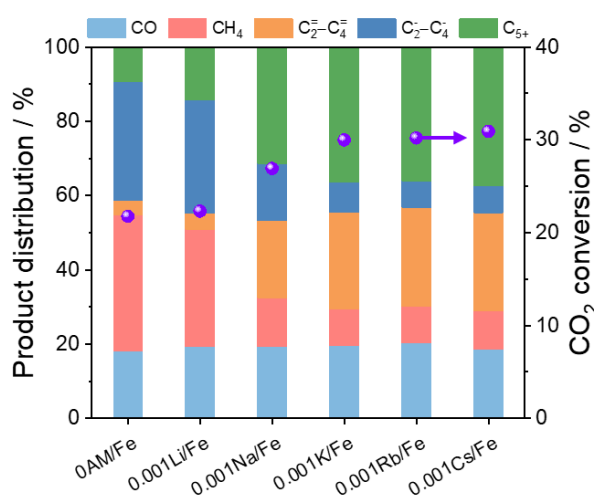
Figure 4-15 CO_2 conversion and product selectivity of CO_2-FTS reaction over 0AM/Fe and 0.001AM/Fe catalysts. Reaction conditions: 15 bar, 300 °C, feed composition of $3H_2/CO_2/0.3N_2$ and GHSV of 1160 mL g_{cat}^{-1} h^{-1} for 90 h. The catalysts were initially reduced at 15 bar and 400 °C using a mixture of $H_2/N_2=1$ for 2 h.

To reveal the origins of the different performance of differently promoted catalysts, structural properties of spent catalysts were elucidated. Fe_3O_4 and Fe_5C_2 are qualitatively identified in all spent catalysts indicated by the presence of their characteristic peaks in XRD patterns (Figure A-15). Apparently, the characteristic peaks of Fe_5C_2 for promoted catalysts with high AM/Fe ratio of 0.05 were much stronger than those for 0AM/Fe and 0.001AM/Fe. The promoted spent catalysts with AM/Fe of 0.001 displayed similar XRD patterns to their unpromoted counterpart (0AM/Fe), where the peaks of Fe_5C_2 were very weak. The co-

existence of Fe_3O_4 and Fe_5C_2 in selected spent catalysts was also confirmed by TEM and SAED analyses (Figure A-16).

In comparison with XRD, Mössbauer spectroscopy can detect non-crystalline Fe-containing phases (Figure 4-16a, Figure A-17 and Figure A-18). Thus, this technique was also used for quantitative characterization of spent catalysts. Mössbauer spectra gave a quantitative result regarding to the composition of iron phases (Figure 4-16b). Indeed, the difference in the content of Fe_5C_2 was quite small between 0.001AM/Fe (5.3-8.7%) and 0AM/Fe (5.3%), which agrees with XRD results. However, the catalysts show strong differences in the selectivity to CH_4 and C_{2+}-hydrocarbons. Thus, no clear correlation regarding the content of Fe_5C_2 and the catalytic performance could be found. With an increase in the ratio of K to Fe from 0.001 to 0.005, the fraction of Fe_5C_2 in spent catalysts was strongly increased from 5.3% to 21.3%. However, a slight increase in Fe_5C_2 fraction was found when K/Fe ratio was further increased to 0.02 and 0.05. Therefore, the content of alkali dopants has a strong effect on the iron carbide concentration in spent catalysts.
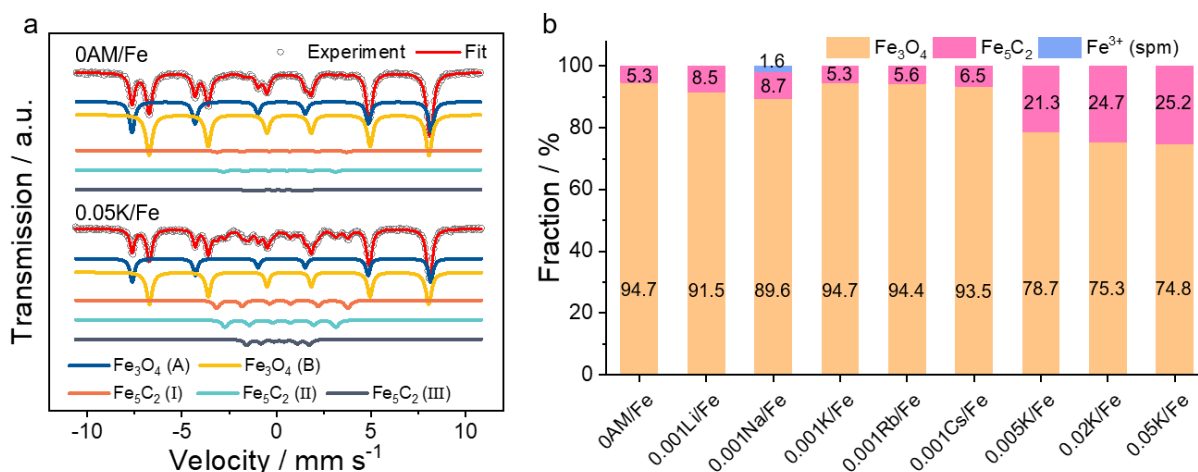
Figure 4-16 (a) Mössbauer spectra of spent 0AM/Fe and 0.05K/Fe catalysts. (b) Composition of spent catalysts as determined from Mössbauer spectra.

Selected spent catalysts were further characterized by XANES and EXAFS techniques (Figure 4-17), which probe the local structure of iron and its oxidation state. Figure 4-17a shows the X-ray absorption near edge structure spectra (XANES) at Fe K-edge. In comparison with the reference Fe_2O_3 (Fe^{3+}), a higher intensity at the pre-edge (7114 eV) was determined in spent catalysts. The XANES spectra of 0AM/Fe and 0.001AM/Fe spent catalysts resemble that of Fe_3O_4 reference spectrum. This means that Fe_3O_4 exists as the dominant phase in these catalysts. Moreover, the intensity of pre-edge in the spectrum of 0.05K/Fe is apparently higher than that of 0AM/Fe and 0.001AM/Fe and approaches the

intensity in the spectra of Fe foil and iron carbide. While the white-line peak (7131 eV) intensity is lower in 0.05K/Fe than in 0.001AM/Fe. These results clearly suggest that spent 0.05K/Fe contains more iron carbide than 0AM/Fe and 0.001AM/Fe, and the addition of tiny amount of alkali elements (AM/Fe = 0.001) to Fe_2O_3 does not promote efficiently the formation of this species, in agreement with the XRD and Mössbauer spectra results. The EXAFS spectra further prove that O and not C is the main neighbor for Fe in 0AM/Fe and 0.001AM/Fe (Figure 4-17b). For 0.05K/Fe, the contribution of C atoms increases (shift to higher r values and a shoulder at 1.84 Å), possibly due to higher content of iron carbides.
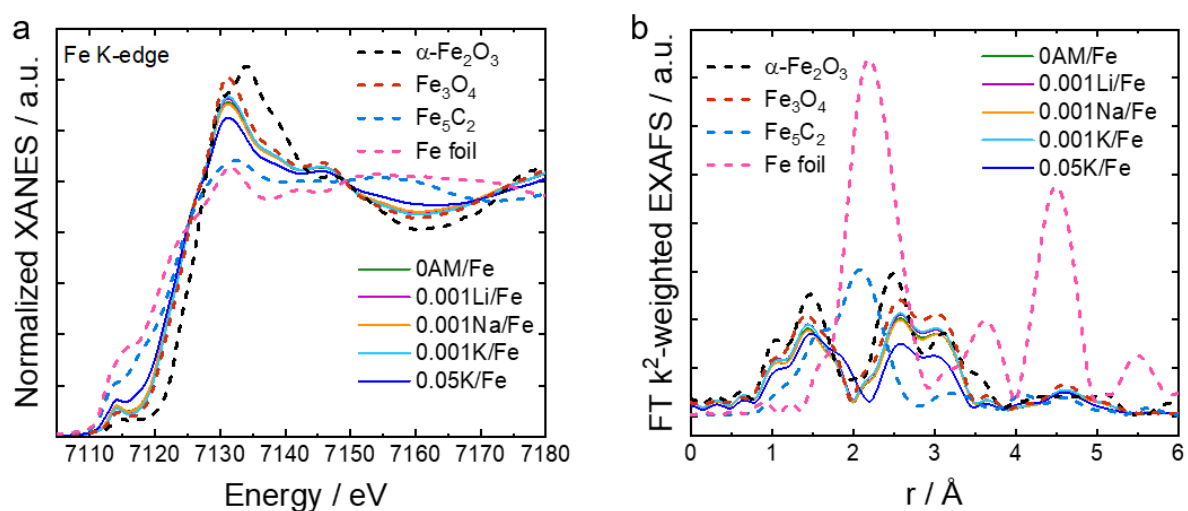
Figure 4-17 (a) X-ray absorption near edge structure (XANES) spectra and extended X-ray absorption fine structure (EXAFS) spectra at Fe K-edge of spent 0AM/Fe, 0.001AM/Fe and 0.05K/Fe.

The promoter's concentration has a stronger effect on the formation of iron carbides. It has been reported that iron carbides, the active sites for hydrocarbon production in CO/CO_2 hydrogenation[19, 307-308], are formed through re-structuring of Fe-containing phases under CO_2-FTS conditions and the presence of K promotes its formation[228]. However, our results here cannot support the previous conclusions but suggest that the positive effect of alkali metals on carbide formation during reaction is strongly dependent on the concentration of alkali metal promoter. The composition of spent 0.001AM/Fe catalysts was quite similar with each other. Therefore, the effect of alkali dopants on the difference in product selectivity ion CO_2-FTS (Figure 4-15) cannot be simply attributed to the difference in the steady-state phase composition. In addition to the above aspects, the interaction of reactants, intermediates and products with catalyst surface are also essential in determining catalyst activity and product selectivity as discussed below.

4.2.2. Effects of alkali metal promoters on activation of CO_2, CO, C_2H_4 and H_2

It was proposed that the interaction (adsorption, activation, dissociation) of CO_2, CO, H_2 and C_2H_4 with catalyst surface is affected by the alkali metal promoter. Such effect depends on the kind of alkali metals and determine the activity and selectivity for CO_2-FTS reaction. C_2H_4 was selected as a model reactant to study olefin adsorption relevant for secondary hydrogenation reactions of primary formed olefins to paraffins. To this end, both reduced (contain Fe_3O_4 and metallic Fe) and spent (contain Fe_3O_4 and Fe_5C_2) 0.001AM/Fe catalysts were tested in the TAP reactor to analyze initial steps relevant for the formation of Fe_5C_2 species and for their ability to activate the above-mentioned components, respectively. It should be noted that the catalysts with the lowest promoter amount are important to avoid any direct participation of promotors in activation of the feed components and in product formation. Additionally, the CO_2 adsorption/desorption behavior over reduced and spent catalysts was also checked by CO_2-TPD method.

4.2.2.1. Adsorption and activation of CO_2 over xAM/Fe catalysts

CO_2 pulse tests with a mixture of CO_2/Ar (1:1) carried out with reduced and spent catalysts (0AM/Fe and 0.001AM/Fe) in the TAP reactor were evaluated to derive mechanistic and kinetic insights into CO_2 activation. Using a model-free approach developed for this technique[291], the experimental responses of CO_2 and Ar were transformed into dimensionless form to distinguish between reversible and irreversible CO_2 interaction. The dimensionless Ar response stands for pure diffusion process (standard diffusion curve). The CO_2 response crosses standard diffusion curve regardless of the absence/presence of alkali dopant, the type of alkali promoters, and the states of catalysts (reduced catalysts in Figure A-19 and spent catalysts in Figure 4-18). This implies a reversible adsorption of CO_2.

Moreover, the CO_2 responses recorded over 0.001Na/Fe and 0.001K/Fe exhibit more noticeable tailing than those of 0AM/Fe and 0.001Li/Fe catalysts, and a delayed crossing position between CO_2 response and Ar response was observed for the former catalysts. The above results indicate that the strength of interaction between CO_2 and the studied catalysts increases as 0AM/Fe ≈ 0.001Li/Fe < 0.001Na/Fe < 0.001K/Fe.
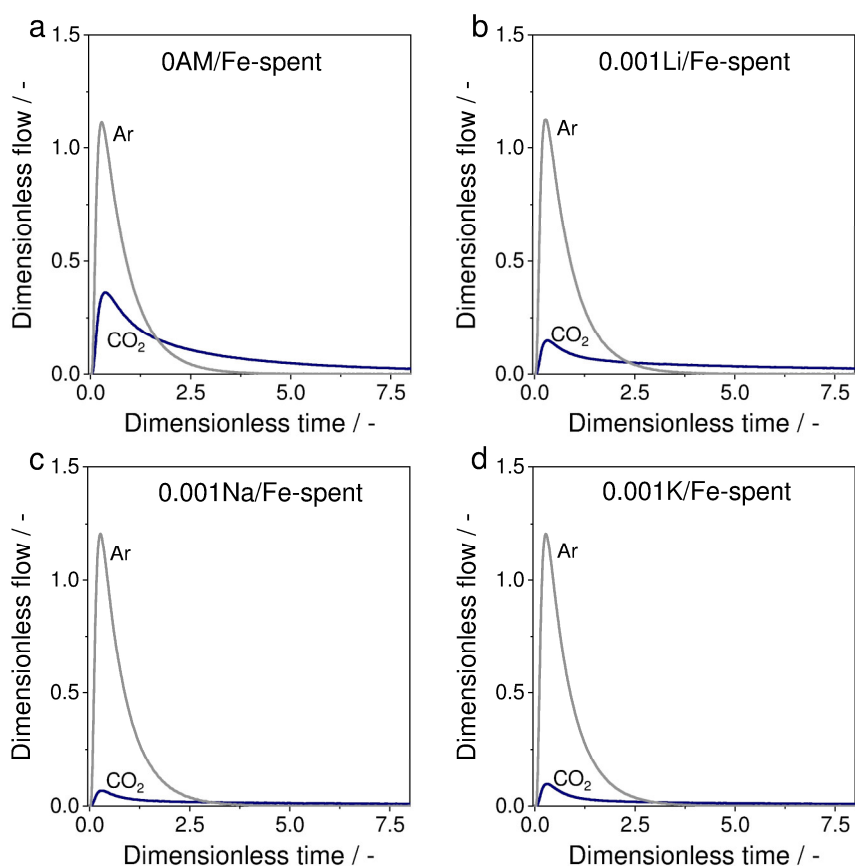
Figure 4-18 Dimensionless responses of CO_2 and Ar after pulsing of a CO_2/Ar (1:1) mixture at 300°C over spent catalysts of (a) 0AM/Fe, (b) 0.001Li/Fe, (c) 0.001Na/Fe and (d) 0.001K/Fe.

On this basis various microkinetic models of CO_2 adsorption/activation (Table A-2) were developed and applied for fitting the experimental CO_2 responses. These models were discriminated and the best description towards experimental response was obtained with Model 4 as indicated by the smallest residual among four different models (Table A-3). This model suggests a reversible non-dissociative adsorption of CO_2 and a reversible dissociation of molecularly adsorbed CO_2. The simulated and experimental responses of CO_2 obtained over spent catalysts are presented in Figure 4-19 (the best model) and Figure A-20 (other models), while those over reduced catalysts can be found in Figure A-21.

Through this approach, the kinetic parameters of elementary steps in this model were obtained (Table A-4 and Figure 4-20). Additionally, sensitivity analysis was performance to check the reliability of the derived kinetic parameters. The confidence interval for each parameter is listed along with the parameter (Table A-4). The small width of confidence intervals presented in Table A-4 proves the validity of derived kinetic parameters.
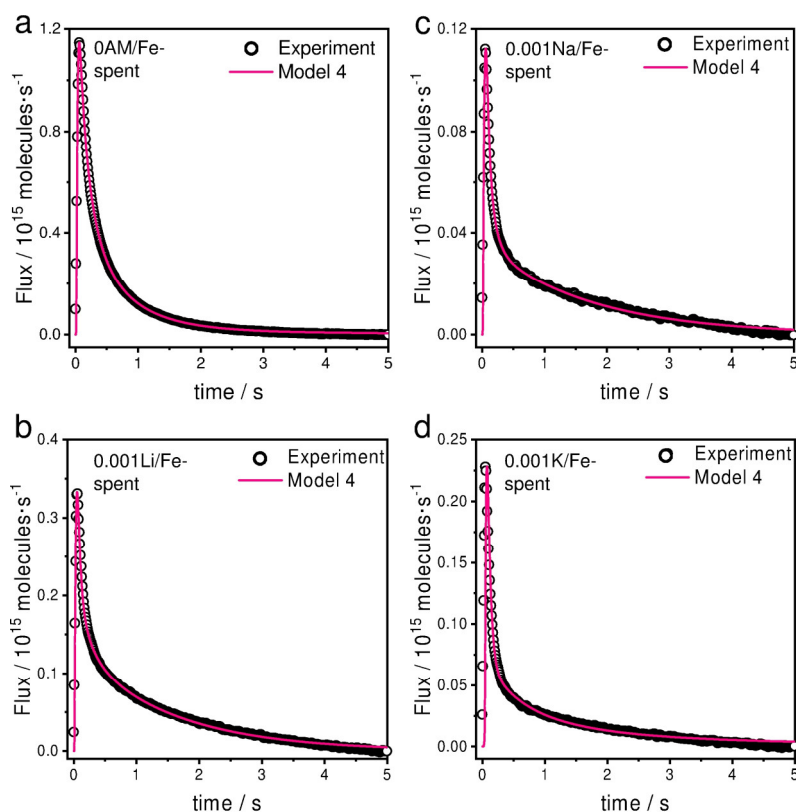
Figure 4-19 Comparison of simulated responses obtained with Models 4 (the best model, see Table A-2) with the experimental CO_2 responses recorded after pulsing of a CO_2/Ar (1:1) mixture at 300°C over spent catalysts 0AM/Fe and 0.001AM/Fe (AM = Li, Na or K).
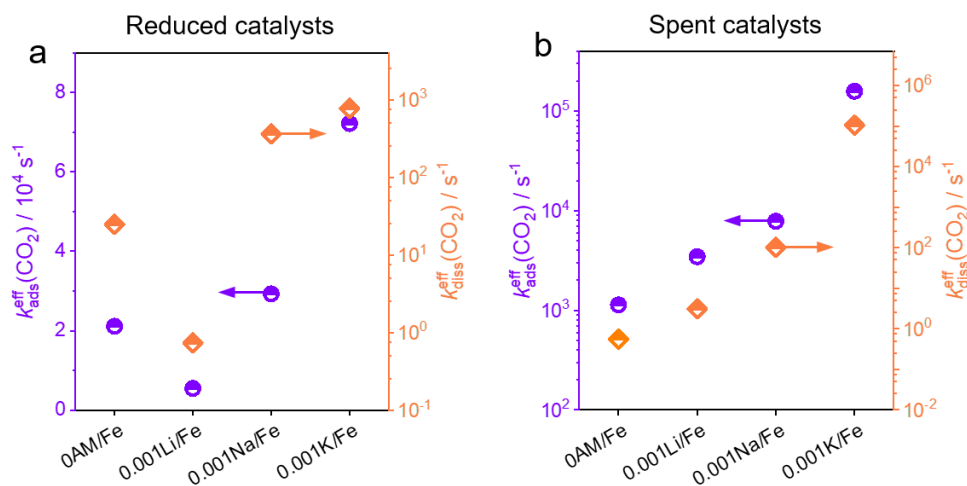
Figure 4-20 Rate constants of CO_2 adsorption ($k_{ads}^{eff}(CO_2)$) and dissociation of adsorbed CO_2 ($k_{diss}^{eff}(CO_2)$) obtained from the best model (Model 4, Table A-2) for (a) reduced catalysts and (b) spent catalysts.

As seen in Figure 4-20, the ability of Fe and Fe_5C_2 to adsorb CO_2 and most importantly to dissociate adsorbed CO_2 species to surface CO and O depend on the type of alkali metal promoters. Due to the correlation between the total concentration of active sites (C_{total}) and the rate constants of adsorption ($k_{ads}(CO_2)$) or dissociation ($k_{diss}(CO_2)$), only their product

(efficient constant) could be calculated and denoted as k_{ads}^{eff} or k_{diss}^{eff}. Both the efficient adsorption constant, k_{ads}^{eff} (CO_2), and the efficient dissociation constant of adsorbed, k_{diss}^{eff}(CO_2), increase in the order of 0.001Li/Fe < 0.001Na/Fe < 0.001K/Fe regardless of reduced or spent catalysts. On the other hand, for reduced catalysts, these parameters for 0AM/Fe are higher than for 0.001Li/Fe (Figure 4-20a). While these parameters for spent 0AM/Fe catalysts are lowest among the spent catalysts (Figure 4-20b). In the case of the reduced catalysts, the rate constant of adsorbed CO_2 desorption, k_{des}(CO_2), decreases in the order of 0AM/Fe > 0.001Na/Fe ≈ 0.001K/Fe (Table A-4). While the ratio of rate constant of molecular CO_2 adsorption to that of CO_2 desorption, k_{ads}^{eff}(CO_2) / k_{des}(CO_2), increases in above order. Reduced 0.001Li/Fe catalyst has the highest value of the constant of CO_2 desorption, but the lowest value of k_{ads}^{eff}(CO_2) / k_{des}(CO_2).

The constant of CO_2 desorption of spent 0.001Na/Fe and 0.001K/Fe catalysts is lower than that of spent 0AM/Fe and 0.001Li/Fe. Interestingly, k_{ads}^{eff}(CO_2) / k_{des}(CO_2) determined for alkali-metal-promoted catalysts is much higher than that for promoter-free catalyst 0AM/Fe and increases in the order 0.001K/Fe > 0.001Na/Fe > 0.001Li/Fe.

Even though both reduced and spent catalysts contain Fe_3O_4 existed as the main phase, they differ strongly in the kinetic parameters of individual steps of CO_2 activation. Which phase, i.e., metallic Fe (present in reduced catalysts only), Fe_3O_4 (present in both reduced and spent catalysts as main phase), or Fe_5C_2 (present in spent catalysts only) is the main component participating in CO_2 activation? To answer this question, CO_2-TPD experiments were performed. Both reduced and spent catalysts were used in this context.

CO_2 desorption from reduced 0AM/Fe takes place in four temperature regions with maxima at around 100, 305, 475, and 620 °C (Figure 4-21a). With respect to different alkali metal dopants, the CO_2-TPD profiles of reduced 0.001AM/Fe resemble that obtained over reduced 0AM/Fe catalyst except for the slightly higher CO_2 uptake over the formers (Figure 4-21a). It is obvious that both the amount of desorbed CO_2 and the strength of CO_2 adsorption increased gradually with increasing K content, especially for the strong adsorption sites, indicated by the higher desorption temperature above 600 °C (Figure 4-21b). When the ratio of AM/Fe increased to 0.05, the amount of desorbed CO_2 increased strongly except for reduced 0.05Li/Fe (Figure 4-21c). Moreover, the strength of CO_2 adsorption over 0.05Na/Fe was weaker than K-, Rb- or Cs-containing catalysts.

65
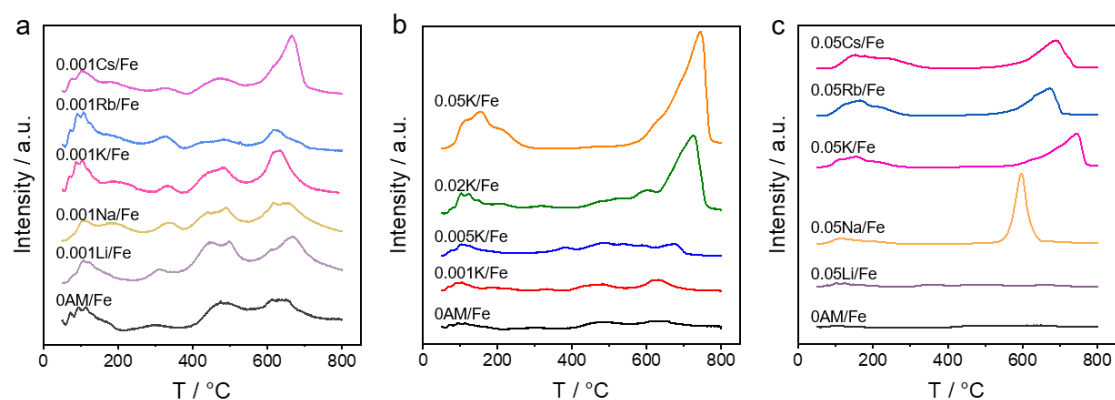
Figure 4-21 CO$_2$-TPD profiles recorded over reduced catalysts with different alkali metal promotors.

In comparison with the reduced catalysts, CO$_2$ desorption from the spent catalysts occurs in a narrower temperature range of 400–600 °C (Figure 4-22). The CO$_2$-TPD profiles of the spent 0AM/Fe and 0.001AM/Fe materials are characterized by a well resolved maximum at about 550 °C with a shoulder at slightly lower temperature (Figure 4-22a). This shoulder becomes more pronounced in the presence of Na, K, Rb or Cs. An additional small less-resolved peak of CO$_2$ desorption at about 470 °C can also be identified. Compared with the spent 0AM/Fe catalyst, the spent xK/Fe (x $>=$ 0.005) catalysts exhibit much stronger CO$_2$ adsorption capability, and the desorption peak shifts to higher temperatures (Figure 4-22b), implying that basic sites become stronger in the K/Fe system and their concentration also increases. For the 0.05AM/Fe spent catalysts, both the strength and the concentration of basic sites are affected by the kind of promoter and rises in the order of Li < Na < K < Rb < Cs (Figure 4-22c).
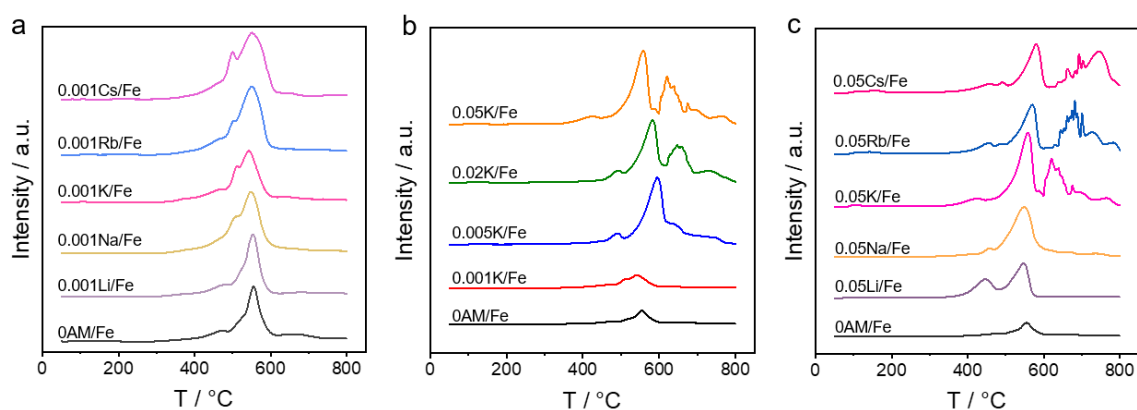
Figure 4-22 CO$_2$-TPD profiles recorded over spent catalysts with different alkali metal promotors.

Considering the totally different CO$_2$-TPD profiles obtained over reduced and spent catalysts, it is possible to answer the question: which Fe-containing phase plays a dominant role in CO$_2$ adsorption. As aforementioned, reduced catalysts contain Fe and Fe$_3$O$_4$, while spent catalysts contain Fe$_5$C$_2$ and Fe$_3$O$_4$. Fe$_3$O$_4$ is the main phase regardless the states of catalyst (reduced

66

and spent). Exemplarily, the fractions of Fe_3O_4 in reduced 0AM/Fe and 0.001K/Fe are 68.9 and 67.4% , respectively, as determined through the quantitative analysis for XRD patterns. On the other hand, the fraction of Fe_3O_4 phase in spent 0AM/Fe and 0.001K/Fe is 94.7% (Figure 4-16b). Moreover, the amount of adsorbed CO_2 is calculated (Figure A-22). Clearly, very strong differences in the strength of adsorption sites (indicated by the desorption temperatures in Figure 4-21 and Figure 4-22) and the concentration of these sites (indicated by the amount of CO_2 uptake in Figure A-22) between reduced and spent catalysts can be found. If Fe_3O_4 phase is responsible for CO_2 adsorption, then the above-mentioned differences should not be observed. Therefore, it was speculated that Fe in reduced catalysts and Fe_5C_2 in spent catalysts are the main components participating in CO_2 adsorption.

4.2.2.2. Interaction of CO with reduced or spent catalysts

CO/Ar (1:1) pulse experiments were performed with reduced and spent catalysts to investigate how the presence of alkali metal dopant affects (i) the first step (CO activation) of carburization of Fe/Fe_3O_4 and (ii) CO activation over FeC_x/Fe_3O_4, respectively. The CO responses obtained for spent catalysts are presented in the dimensionless form in Figure 4-23, while the corresponding results for reduced catalysts are shown in Figure A-23.
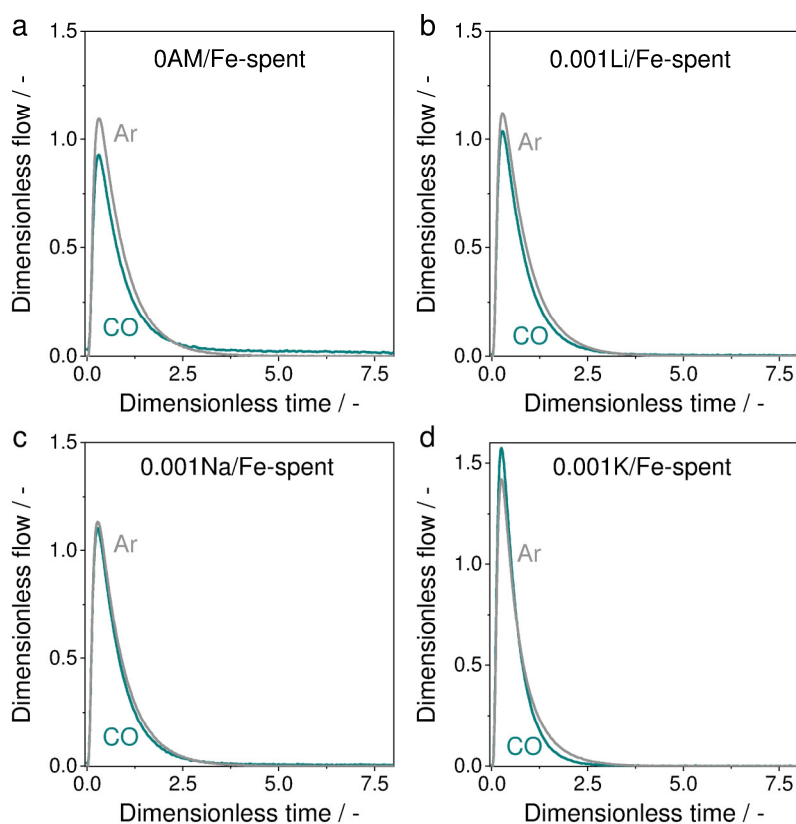
Figure 4-23 Dimensionless responses of CO and Ar after pulsing of a CO/Ar (1:1) mixture at 300°C over spent catalysts of (a) 0AM/Fe, (b) 0.001Li/Fe, (c) 0.001Na/Fe and (d) 0.001K/Fe.

No obvious difference between the CO response and the standard diffusion curve (Ar response) is found for the reduced 0.001Li/Fe catalyst (Figure A-23), suggesting that CO simply diffuses similarly to Ar. On the contrary, a reversible interaction was established between CO and 0AM/Fe, 0.001Na/Fe, 0.001K/Fe as well as spent 0.001Li/Fe (Figure A-23 and Figure 4-23).

A simple diffusion model and three adsorption/activation models (Table A-5) were developed to simulate CO responses. The diffusion model described the CO response over 0.001Li/Fe reduced catalyst (Figure A-24) with the smallest deviation (Table A-6). In agreement with the above-discussed dimensionless CO responses, the kinetic evaluations suggests that the interaction between CO and reduced 0.001Li/Fe catalyst is rather weak.
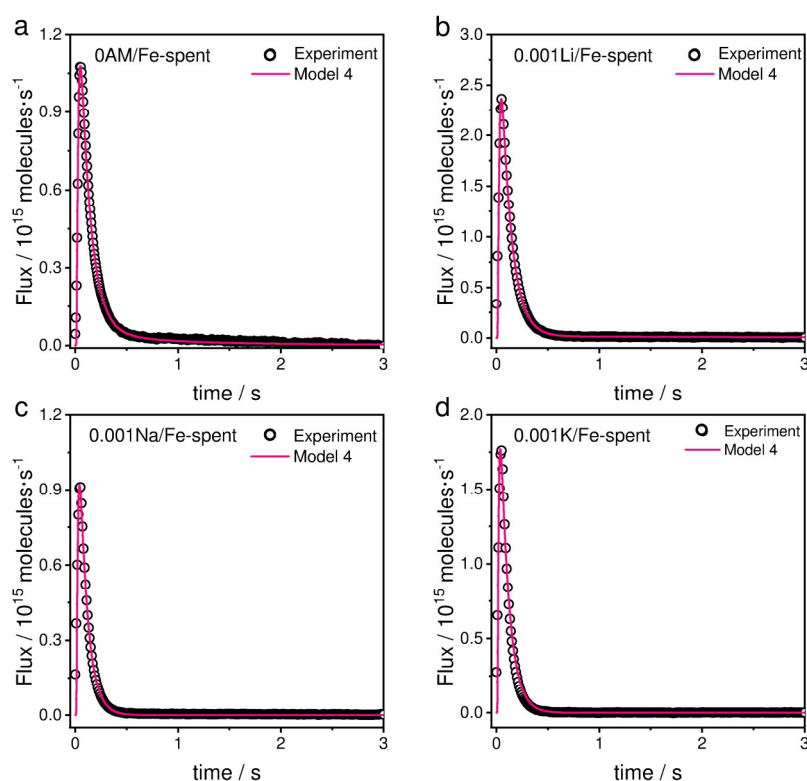
Figure 4-24 Comparison of simulated responses obtained using the best model (Model 4, Table A-5) with the experimental CO responses recorded after pulsing of a CO/Ar (1:1) mixture at 300°C over spent catalysts of (a) 0AM/Fe, (b) 0.001Li/Fe, (c) 0.001Na/Fe and (d) 0.001K/Fe.

The experimental CO responses for all spent catalysts (Figure 4-24) and other reduced catalysts (Figure A-24) except 0.001Li/Fe were described by a model considering reversible CO adsorption and dissociation of adsorbed CO species (Model 4, Table A-5) with the smallest deviation (Table A-6). The obtained kinetic parameters with the corresponding confidence interval are listed in Table A-7, and exemplarily shown in Figure 4-25. For the reduced catalyst, both the constant of CO adsorption (k_{ads}^{eff}(CO)) and the constant of

dissociation of adsorbed CO (k_{diss}^{eff}(CO)) increase in the order of 0AM/Fe < 0.001Na/Fe < 0.001K/Fe (Figure 4-25a). The lowest constant of CO desorption was determined over 0AM/Fe among reduced catalysts (Table A-7). However, for spent catalysts, the constant of CO adsorption is found to be largest over 0AM/Fe and decreases in the order of 0AM/Fe > 0.001Li/Fe > 0.001Na/Fe > 0.001K/Fe (Figure 4-25b). The rate constants of dissociation of adsorbed CO over spent catalysts follow the same order as observed for their reduced counterparts (Figure 4-25).
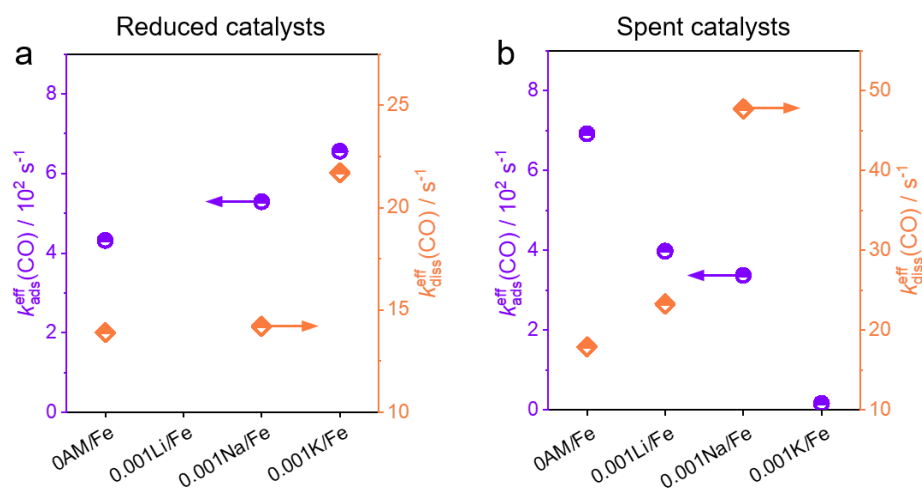
Figure 4-25 CO adsorption (k_{ads}^{eff}(CO)) and dissociation of adsorbed CO (k_{diss}^{eff}(CO)) obtained from the best model (Model 4, Table A-5) for (a) reduced and (b) spent catalysts, respectively.

4.2.2.3. Interaction of C_2H_4 with reduced or spent catalysts

As olefins are primary products in CO-FTS, C_2H_4 was selected as a model olefin to analyze if and how the presence of alkali metal promoter affects its adsorption/desorption property. This catalyst characteristics should influence olefin/paraffin ratio and probably chain growth. The dimensionless responses obtained after pulsing of a mixture of C_2H_4/Ar (1:1) over spent catalysts at 300°C are summarized in Figure A-25. It is evident that C_2H_4 responses obtained over 0AM/Fe and 0.001Li/Fe crosse the Ar responses, indicating a reversible adsorption of C_2H_4 on these two catalysts. Contrarily, there is no visible difference between the C_2H_4 and Ar responses of 0.001Na/Fe and 0.001K/Fe, i.e., ethylene adsorbs very weakly over these catalysts. Thus, the kind (Li, Na or K) of alkali metal promoter affects the strength of ethylene adsorption, which decrease in the order Li > Na ≈ K. The weaker the adsorption, the higher the olefin to paraffin ratio among C_2-C_4 hydrocarbons as shown in Figure A-26.

4.2.2.4. The activation of H_2 over reduced or spent catalysts

When a H_2/D_2/Ar = 1/1/1 mixture was pulsed over reduced or spent 0.001AM/Fe catalysts at 300 °C (a representative reaction temperature), HD was observed (Figure 4-26 and Figure A-

27). The concentration of HD formed in these tests represents the catalyst ability for breaking the H-H and D-D bonds and forming the H-D bond. The kind of alkali metal promoter is decisive for these processes. For the reduced catalysts, promoting of Fe_2O_3 with Li enhances hydrogen activation, while 0.001Na/Fe and 0.001K/Fe do not differ from 0AM/Fe in this regard (Figure A-27).
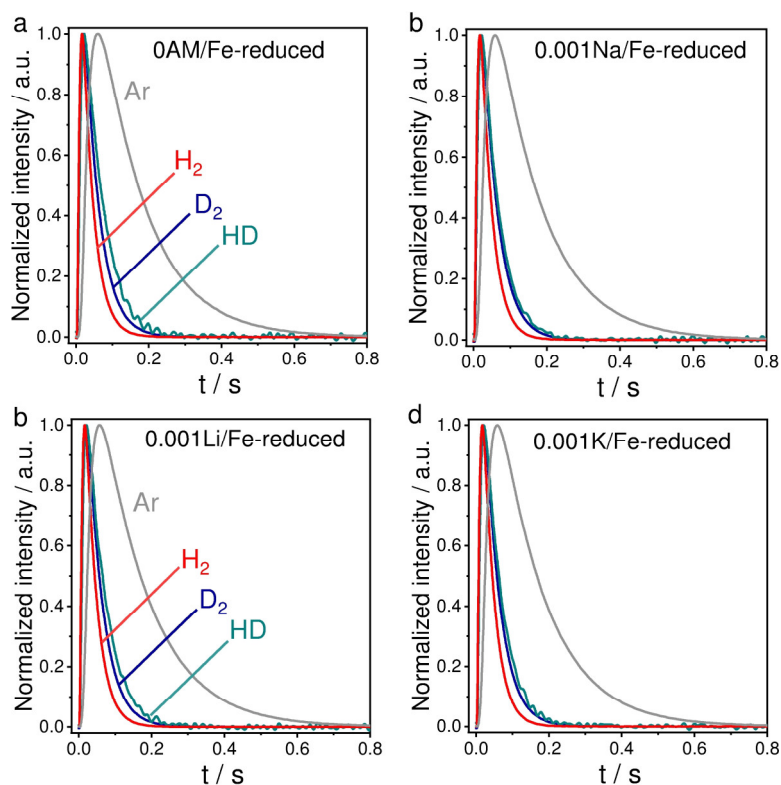
Figure 4-26 Height-normalized responses of Ar, H_2, D_2 and HD obtained after pulsing of $H_2/D_2/Ar$ (1:1:1) at 300 °C over reduced catalysts.

In general, reduced catalysts show higher activity towards H_2 activation than their spent counterparts. This effect may be related to the presence of metallic Fe responsible for this process in the reduced materials. Spent 0AM/Fe and 0.001Li/Fe also catalyse the H/D exchange but with a lower activity than their reduced counterparts (Figure A-27 and Figure A-28). This result suggests that Fe_5C_2 is less active for hydrogen activation than metallic Fe. No HD formation was observed on spent 0.001Na/Fe and 0.001K/Fe catalysts.

4.2.3.   Spatially resolved kinetic analysis of CO_2-FTS reaction

The CO_2 hydrogenation progress over Fe-based catalysts was monitored through acquiring spatially resolved profiles of CO_2 conversion and products formation along the catalyst bed. Here, the amount of tested catalyst varied, but using a constant total flow of reactants. Thus, the segmental rates of CO_2 conversion into different reaction products in CO_2-FTS reaction,

i.e., the rate in a certain catalyst segment (Figure 4-27a, also see section 3.3), were determined under steady-state conditions over Fe-based promoted and dopant-free catalyst.
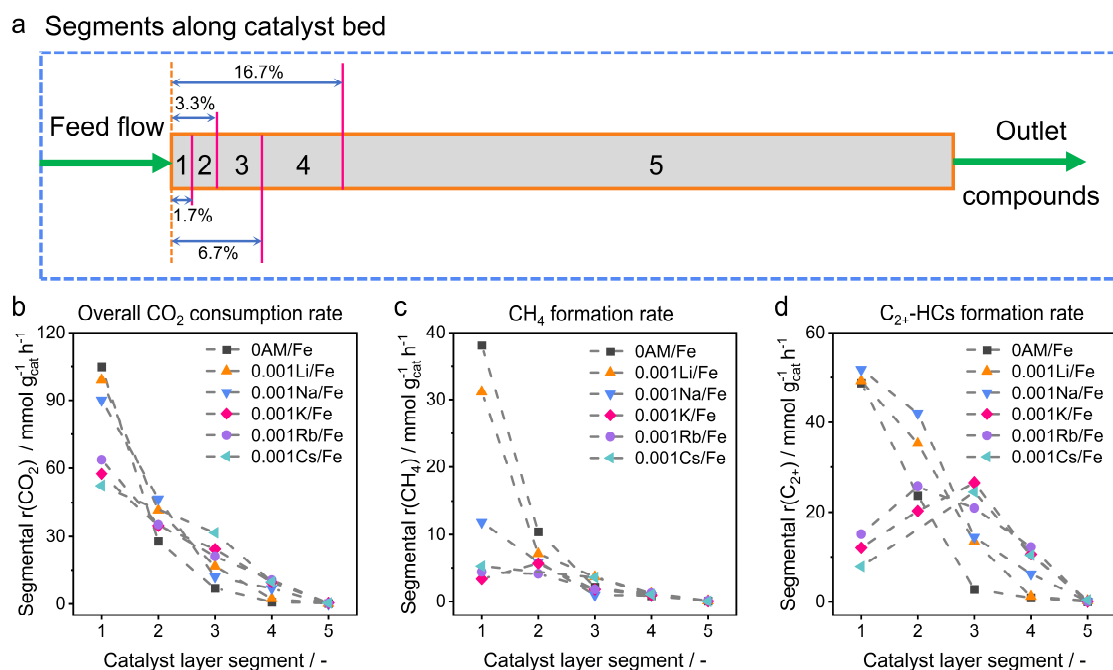
Figure 4-27 (a) Schematic representation how the segments are defined. The segmental rates of (b) overall CO_2 conversion ($r(CO_2)$), (c) CH_4 formation ($r(CH_4)$) and (d) C_{2+}-hydrocarbons formation ($r(C_{2+})$) for 0AM/Fe and 0.001AM/Fe catalysts. Reaction conditions: $H_2/CO_2/N_2$ = 3/1/0.3, 15 bar and 300 °C.

The rate of overall CO_2 conversion (Figure 4-27b) decreases downstream from segment to segment due to a decrease in CO_2 partial pressure and accordingly transition from differential to integral reactor operation. Such tendency is also observed over 0.05AM/Fe catalysts (Figure A-29a). The strength of this decrease depends, however, on the kind of promoter. The segmental rate of CO_2 conversion drops significantly over 0AM/Fe, 0.001Li/Fe and 0.001Na/Fe. However, the decrease of this rate along the catalyst bed is much slower for 0.001K, Ru or Cs/Fe catalysts. Thus, these catalysts are more efficient for CO_2 conversion in comparison with 0AM/Fe and 0.001Li/Fe as the catalyst bed increases. To compare all the catalysts in terms of their intrinsic activity for CO_2 conversion, we use the $r_1(CO_2)$ values determined in the first catalyst layer, where differential reactor operation can be assumed. On this basis, the promoters K, Rb or Cs seem to hinder this catalyst property. The following activity order is established: 0AM/Fe ~ Li/Fe > Na/Fe > Rb/Fe ~ K/Fe ~ Cs/Fe.

The catalysts also differ in the segmental rate of CH_4 formation (Figure 4-27c and Figure A-29b) in a similar manner as in the rate of overall CO_2 consumption. The difference is, however, significantly larger. The rate over 0AM/Fe and 0.001Li/Fe decreases strongly from segment to segment due to an integral reactor operation. The rate of CO_2 conversion into CH_4

71

over 0.001Na, K, Rb or Cs/Fe catalyst is dramatically lower and does not change apparently for the latter three catalyst. In terms of intrinsic CO_2 conversion rate into methane ($r_1(CH_4)$), the catalysts can be ordered as follows: AM/Fe > Li/Fe >> Na/Fe > K/Fe ~ Rb/Fe ~ Cs/Fe.

The segmental rate of CO_2 conversion into C_{2+}-hydrocarbons ($r(C_{2+})$) was also determined (Figure 4-27d and Figure A-29c). 0AM/Fe, Li/Fe and Na/Fe shows the highest activity within about 1.7% upstream catalyst layer. However, when the layer of 0AM/Fe increases up to 3.3 and 6.7%, the segmental rate declines drastically by a factor of 2.6 and 23, respectively. Similar changes are also valid for 0.001Li/Fe. Contrarily, 0.001 K, Rb or Cs/Fe does not lose their activity within the 16.7% upstream layer and the segmental rate of C_{2+}-hydrocarbons formation passes a maximum between the first 3.3 and 6.7% layers. After the first 3.3% layer, they outperform 0AM/Fe and 0.001Li/Fe. The following order of intrinsic activity of C_{2+}-hydrocarbons formation is obtained: 0AM/Fe ~ Li/Fe ~ Na/Fe >> K/Fe ~ Rb/Fe ~ Cs/Fe.

As the CO_2 conversion in the first segment can be regarded as differential process, the above results explicitly reveal that doping of Fe_2O_3 with Na, K, Rb or Cs lowers the intrinsic activity of CO_2 conversion to different extents, while Li-containing Fe catalyst behaves similarly as 0AM/Fe. More importantly, Na and K significantly reduce the differential rate of CH_4 formation in the first segment by a factor of 3.3 and 12.8, respectively (Figure 4-27c). Meanwhile, the intrinsic activity of C_{2+}-hydrocarbons formation was also hindered by alkali metal promoters but to different extents.

4.2.4. Network of product formation in CO_2-FTS reaction

Knowing reaction networks of product formation is crucial to understand the processes occurring inside chemical reactors. Here, the influence of alkali metal promoters on the formation of CO, CH_4 and C_{2+}-hydrocarbons in the CO_2-FTS reaction was analyzed. Promoted Fe catalysts with different alkali metal dopants and loadings and their unpromoted counterpart were tested at different degrees of CO_2 conversion to establish selectivity-conversion relationships for CO, CH_4, light olefins and C_{2+}- and C_{5+}-hydrocarbons. To get different degrees of CO_2 conversion, gas hourly space velocity was changed.

For all the catalysts investigated, CO selectivity has a positive value at zero CO_2 conversion and decreases with an increase in CO_2 conversion (Figure 4-28a). Such dependence suggests that CO is directly produced from CO_2 through the RWGS reaction as a primary product and then consumed in other consecutive reactions as rection progresses. In contrast to CO, the selectivity to higher hydrocarbons increases with an increase in CO_2 conversion (Figure

4-28b). This means that these products are formed through CO hydrogenation, i.e., through the CO-FTS reaction.
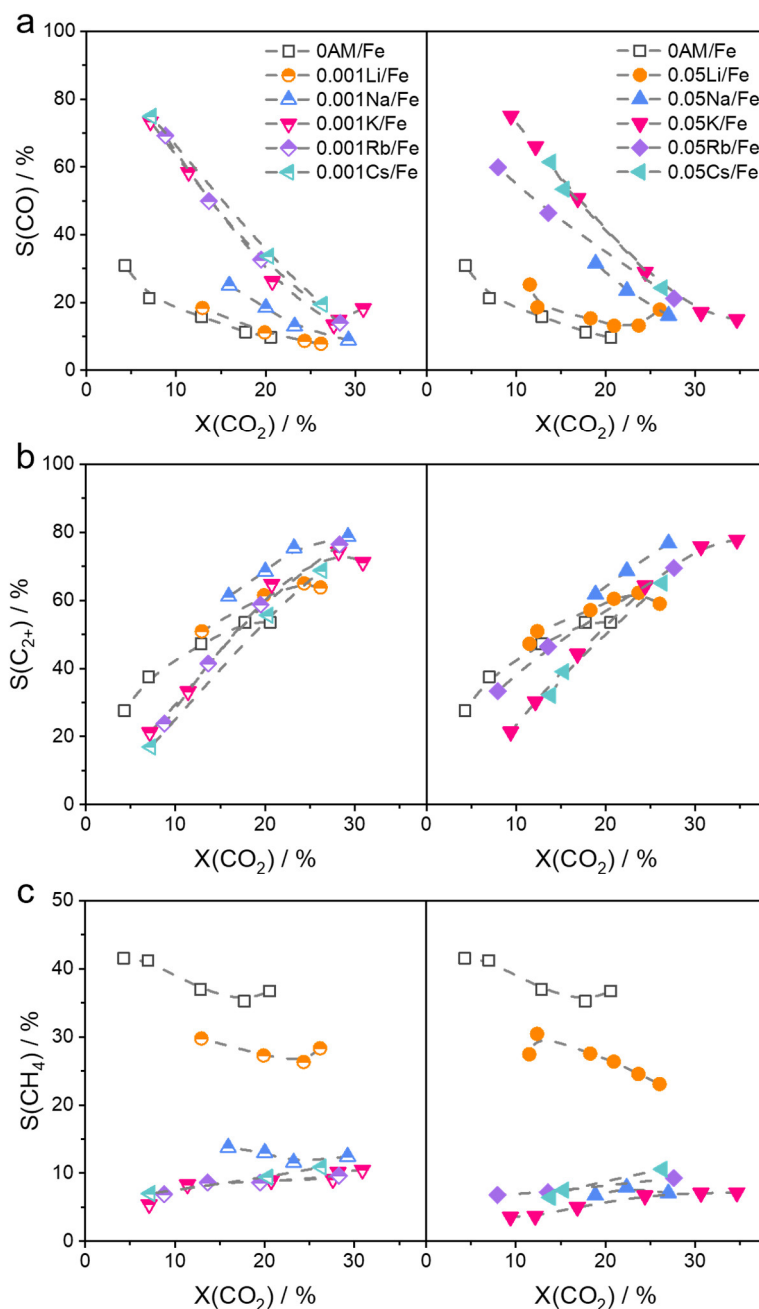

Figure 4-28 Selectivity-conversion relationships for (a) CO, (b) C_{2+}-hydrocarbons and (c) CH_4 over 0AM/Fe and xAM/Fe catalysts. Reaction conditions: 300°C, 15 bar, $H_2/CO_2/N_2 = 3/1/0.3$, after 40 h on stream.

The selectivity to C_{2+}-hydrocarbons over K-, Rb- or Cs-promoted catalysts at CO_2 conversion below 17% is lower than that over 0.001Li/Fe and 0AM/Fe. The highest C_{2+}-selectivity of about 80% was achieved over Na- or K-containing catalysts at CO_2 conversion above 25%, while the corresponding values for 0.05Li/Fe, 0AM/Fe are below 60%. The selectivity passes over a maximum with rising CO_2 conversion. The maximum position shifts to higher CO_2

conversion in the order 0AM/Fe < 0.001Li/Fe < 0.001Na/Fe ~ 0.001K/Fe. Such maximum position is absent in the studied range of CO_2 conversion for all 0.05AM/Fe catalysts except 0.05Li/Fe.

The selectivity to CH_4 over 0.001K/Fe, 0.001Rb/Fe and 0.001Cs/Fe catalysts is close to zero at CO_2 conversion of zero (Figure 4-28c). This implies that the contribution of CO_2 methanation (undesired pathway) to CH_4 formation is very slight. With the progress of CO_2 conversion, this selectivity slightly increases due to CO hydrogenation to this hydrocarbon. On the contrary, the CH_4 selectivity over 0AM/Fe, 0.001Li/Fe and 0.001Na/Fe is significantly higher than zero at zero conversion of CO_2 (Figure 4-28c). This means that CH_4 is formed through CO_2 methanation. CO selectivity decreases but CH_4 selectivity is hardly affected with rising CO_2 conversion. Such dependence indicates that the conversion of CO to this product is strongly inhibited. The CH_4 selectivity follows the order of 0AM/Fe > 0.001Li/Fe > 0.001Na/Fe > 0.001K/Fe ~ 0.001Rb/Fe ~ 0.001Cs/Fe at the full range of CO_2 conversion studied. The above order in terms of CH_4 selectivity is also valid for the 0.05AM/Fe catalysts. Moreover, the CH_4 selectivity further decreases over 0.05AM/Fe (AM = Na, K, Rb, or Cs) in comparison with their counterparts with AM/Fe ratio of 0.001.

The selectivity to light olefins ($C_2^=$-$C_4^=$) over the 0AM/Fe and 0.001AM/Fe catalysts first increases, then drops as the CO_2 conversion increases further (Figure A-30a). This is due to their secondary hydrogenation to alkanes. However, this undesired hydrogenation was alleviated by the usage of alkali metal dopants as evidenced by shifting of the maximum to higher CO_2 conversion for promoted catalysts. The strength of such inhibition effect follows the order of Li ≤ Na < K ~ Rb ~ Cs. Such phenomenon is even not observed when AM/Fe ratio is increased to 0.05 except for Li (Figure A-30b).

Based on the above discussion, the RWGS and CO_2 methanation reactions are two primary pathways occurring in parallel in the process of CO_2 hydrogenation over Fe-based catalysts. CO can be further hydrogenated to methane and higher hydrocarbons. Thus, the overall rection network regarding product formation does not change with or without alkali metal promoter. However, the undesired CO_2 methanation reaction is significantly suppressed over promoted catalysts with exception of xLi/Fe. Moreover, such effect depends on the kind of alkali metal promoters. The reaction network, and popularities of two primary reaction (RWGS and CO_2 methanation) over different Fe-based catalysts are schematically shown in Figure 4-29. What are the fundamental reasons for the above-discussed effects of the kind of

alkali metal promoter on the kinetics of reaction pathways leading to CH_4 and C_{2+}-hydrocarbons? The answer to this question will be discussed in the following section.
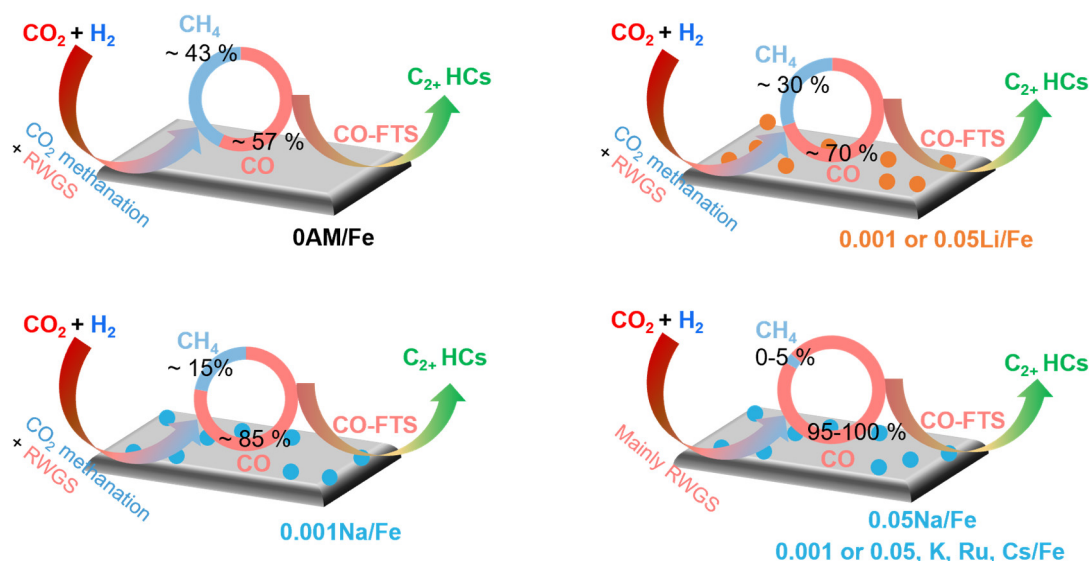

Figure 4-29 Gaphical representation of the reaction scheme of CO_2 conversion. The numerical values in ring represent the product selectivity to CH_4 and CO when CO_2 conversion is extrapolated to zero.

4.2.5. Factors affecting reactivity and product selectivity

The kinetics of activation of feed compounds and intermediates derived from transient experiments, and reaction kinetics analysis through spatially resolved approach allowed to investigate promoter-dependent activity (Figure 4-27) and product selectivity (Figure 4-28). 0AM/Fe and 0.001AM/Fe possessed similar amount of iron carbides, but differ strongly in product selectivity and activity depending on the presence/absence of promoter and the kind of alkali metal promoters. Inspired by rich knowledge about NH_3 synthesis[309-310] and CO-FTS[242, 311] reaction catalyzed by Fe-based catalysts with K modification, where local electronic effects of K were highlighted, electronic interactions between alkali metal promoter and Fe_5C_2 also seems to affect the activation of feed compounds.

To check this hypothesis, the electronic environment of Fe in spent catalysts was checked by XPS measurements (Figure A-31). The characteristic peaks of Fe $2p_{3/2}$ with binding energy of 706.8−707.5 eV could be assigned to Fe_xC_y species.[231, 238] Clearly, the peak of Fe_xC_y species shifts to lower binding energies for spent 0.001AM/Fe catalysts in comparison with spent 0AM/Fe catalyst (Figure A-31a, b), indicating the electron donating to Fe from alkali metal promoters. Such changes in the binding energy and the electron donation become significant with an increase in promoter loading (Figure A-31c, d). On the basis of XPS results, the Allen

scale electronegativity of alkali metal promoters is proposed to be a descriptor representing the electronic effects of alkali metals on catalyst activity and product selectivity in CO_2-FTS.

Indeed, the kinetic parameters of individual steps of CO_2 and CO activation can be correlated with the electronic effects of promoters. The rate constants of CO_2 adsorption ($k_{ads}^{eff}(CO_2)$) and dissociation of adsorbed CO_2 ($k_{diss}^{eff}(CO_2)$) over spent catalysts increase with an increase in the difference between the electronegativity of Fe and alkali metal promoter (Figure 4-30a, b). But the degrees of their increase are different as evidenced by an increase in the ratio of $k_{diss}^{eff}(CO_2)$ to $k_{ads}^{eff}(CO_2)$ (Figure 4-30c). Moreover, the equilibrium constant of CO_2 adsorption, $k_{ads}^{eff}(CO_2)$ / $k_{des}(CO_2)$, increases, too.
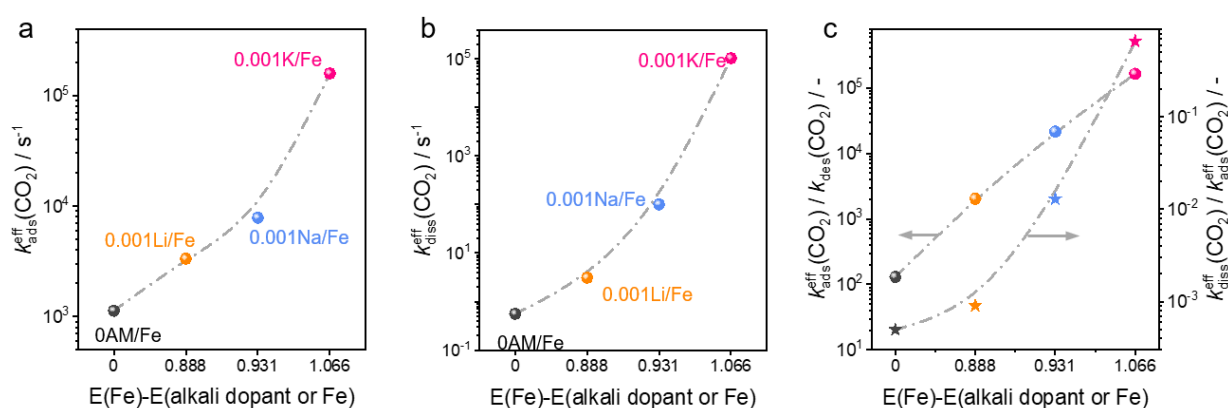
Figure 4-30 The rate constants of (a) adsorption of CO_2 ($k_{ads}^{eff}(CO_2)$), (b) dissociation of adsorbed CO_2 ($k_{diss}^{eff}(CO_2)$), and (c) ratios of $k_{ads}^{eff}(CO_2)$ to $k_{des}(CO_2)$ and of $k_{diss}^{eff}(CO_2)$ to $k_{ads}^{eff}(CO_2)$ versus the difference in the Allen scale electronegativity of iron and alkali metals.

An inverse dependence was obtained for the rate constant of CO adsorption ($k_{ads}^{eff}(CO)$) (Figure 4-31a). Although it was not possible to precisely determine the rate constant of dissociation of adsorbed CO ($k_{diss}^{eff}(CO)$) for 0.001K/Fe, an increase in this constant follows the order of 0AM/Fe < 0.001Li/Fe < 0.001Na/Fe (Figure 4-31b). Thus, the electronegativity seems to be important for breaking the CO bond as evidenced by the higher ratio of $k_{diss}^{eff}(CO_2)$ / $k_{ads}^{eff}(CO_2)$ determined over promoted catalysts (Figure 4-31c). The activation of H_2 is influenced by the electronic properties of catalyst. The H/D exchange activity of catalysts decreases with the increasing of electronegativity of promoter (Figure A-32).
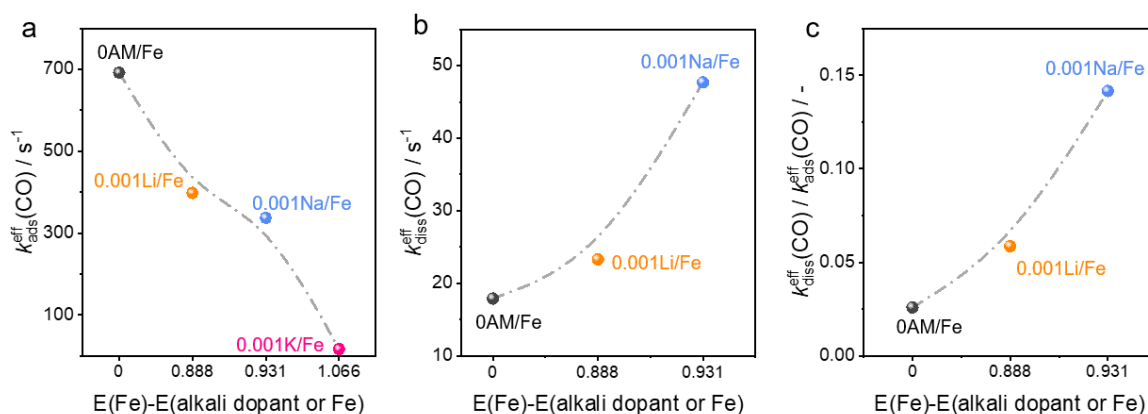
Figure 4-31 The rate constants of (a) adsorption of CO ($k_{\mathrm{ads}}^{\mathrm{eff}}$(CO)), (b) dissociation of adsorbed CO ($k_{\mathrm{diss}}^{\mathrm{eff}}$ (CO)), and (c) ratio of $k_{\mathrm{diss}}^{\mathrm{eff}}$(CO) to $k_{\mathrm{ads}}^{\mathrm{eff}}$(CO) versus the difference in the Allen scale electronegativity of iron and alkali metals.

The above results reveals that the electronegativity of promoter governs the ability of catalyst to activate CO_2, CO and H_2. Further, the latter information can be related with the reaction activity of CO_2-FTS reaction (Figure 4-32). The intrinsic rate of CH_4 formation decreases with an increase in the ratio of $k_{\mathrm{diss}}^{\mathrm{eff}}$($CO_2$) / k_{ads}(CO_2) (Figure 4-32a), suggesting that the interaction of CO_2 with catalyst may strongly intervene the kinetics of products formation. The higher constant of $k_{\mathrm{ads}}^{\mathrm{eff}}$(CO) favors the C_{2+}-hydrocarbons formation (Figure 4-32b).
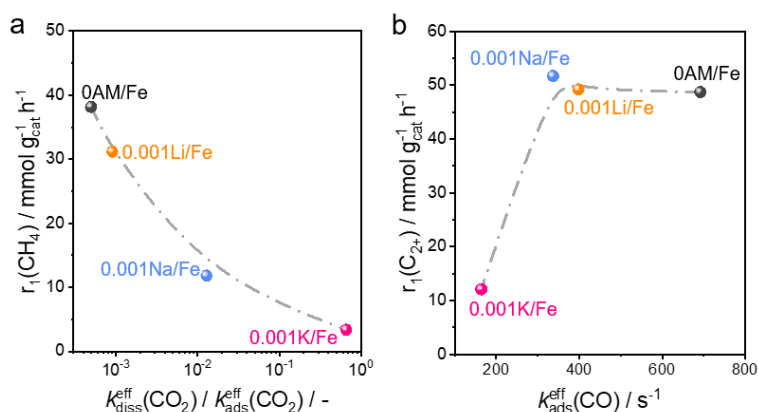
Figure 4-32 The rates of (a) CH_4 (r_1(CH_4)) and (b) C_{2+}-hydrocarbons (r_1(C_{2+})) formation in the first segment of 0AM/Fe and 0.001AM/Fe versus $k_{\mathrm{diss}}^{\mathrm{eff}}$($CO_2$) / $k_{\mathrm{ads}}^{\mathrm{eff}}$($CO_2$) and $k_{\mathrm{ads}}^{\mathrm{eff}}$(CO), respectively.

Combining the relationships established in Figure 4-30-Figure 4-32, the rates of CO_2 conversion into CH_4 and C_{2+}-hydrocarbons in the first catalyst layer segment (differential reactor operation) can be successfully correlated with the difference between the electronegativity of Fe and alkali metal for 0.001AM/Fe. (Figure 4-33a, b). Such relationships are also suitable for 0.05AM/Fe catalysts (Figure A-33).
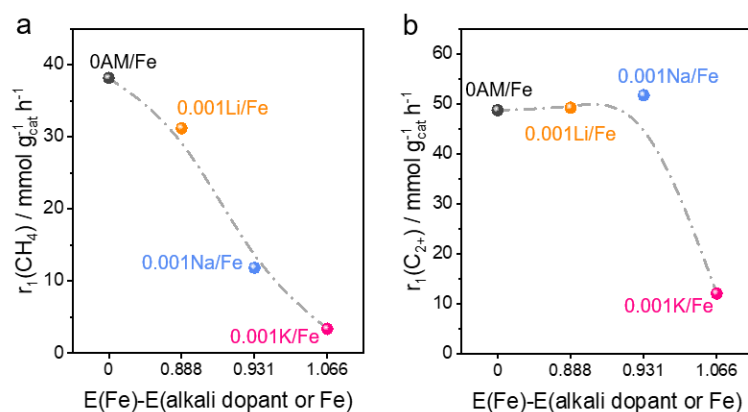
Figure 4-33 The rates of (a) CH_4 ($r_1(CH_4)$) and (b) C_{2+}-hydrocarbons ($r_1(C_{2+})$) formation in the first segment versus the difference in the Allen scale electronegativity of iron and alkali metals.

Above discussions explained the underlying reasons of effects of alkali metal promoters for Fe-based catalysts in CO_2 hydrogenation. Electronic properties are important for turning the strength of CO_2 adsorption and its dissociation into absorbed CO and O species. The ability for dissociation of adsorbed CO species into the individual surface components is also enhanced by increasing the electronegativity of promoters. Contrarily, the catalyst ability to generate surface hydrogen species from gas-phase H_2 is inhibited. These elementary steps determine the ratio of C to H on catalyst surface. Thus, a suitable C/H ratio is required for the selective production of C_{2+}-hydrocarbons, for lowering the possibility of methanation pathway and for hindering consecutive hydrogenation of primarily formed olefins to paraffins.

4.2.6.   Summary

In this study, a series of Fe catalysts with different kinds and amounts of alkali metals were prepared and evaluated to probe the effect of the promoters on the intrinsic activity and the reaction scheme of product formation over Fe-based catalysts in CO_2 hydrogenation. The underlying fundamentals of promotion effects were revealed from kinetic and mechanistic viewpoints. Through spatially resolved kinetic analyses under steady state, it was found that the intrinsic activity follows the order of 0AM/Fe ~ Li > Na/Fe > K/Fe ~ Rb/Fe > Cs/Fe. Further, transient kinetic studies in the TAP reactor suggest that the presence of alkali metal promoter can modify the adsorption and activation of H_2, CO_2, CO and C_2H_4, thus finally tune the concentration of surface carbon and hydrogen species which determine product selectivity of Fe-based catalysts in CO_2 hydrogenation. We expect that the fundamental insights elucidated here can be further extendible to other hydrogenation processes where metal oxide promoters play significant roles.

4.3. Activity and selectivity descriptors for iron carbides in CO_2 hydrogenation

As aforementioned in Introduction, product selectivity in CO_2 hydrogenation is determined by the interplay of the kinetics of these pathways. Therefore, it is highly important to establish relationships between the kinetics and catalyst physicochemical properties for offering a basis for purposeful catalyst design. The usage of alkali metals, copper, manganese and/or cerium as promoters for iron oxides endorses the formation of iron carbides and accordingly improves the efficiency of production of C_{2+}-hydrocarbons. The results presented in section 4.2 contributed to understanding the promotion effects induced by alkali metal promoters. Moreover, the statistical analysis of literature data on CO_2-FTS (section 4.1) revealed that non-promoted iron oxides after re-structuring can also produce C_{2+}-hydrocarbon efficiently and the preparation method can play a significant role. However, it remains unclear which physicochemical properties of iron oxide itself affect its *in situ* transformation into iron carbides and if the presence of the latter is really the only prerequisite for ensuring high selectivity to the desired hydrocarbons.

Considering the above challenges, the principles for controlling both desired and undesired hydrogenation reactions in CO_2-FTS are highly needed to be understood. To eliminate any effects of support materials or promoters, a series of bulk Fe_2O_3 materials containing single-phase hematite with different size of crystallites was developed (Figure 4-34a). It is suggested that (ii) redox properties of iron oxides should play an important role for the carburization process and (ii) the relative enrichment of surface hydrogen species and carbon species governs both activity and product selectivity. The importance of iron carbides is also analyzed by considering their spatial distribution along the catalyst bed. Finally, the sophisticated mechanistic and kinetic analyses are performed to identify activity- and selectivity-relevant factors.

4.3.1. Fresh Fe_2O_3 materials and their physicochemical properties

In this work, conventional chemical precipitation (Fe-CP), sol-gel (Fe-SG) and one-step thermal decomposition (Fe-TD) methods were employed to synthesis iron oxide with single-phase of hematite (α-Fe_2O_3, see section 3.1). As shown in Figure A-34, the XRD patterns of all fresh catalysts show obvious diffraction peaks for the hematite phase (ICDD 01-072-0469). The average crystallite size of each catalyst was determined by Scherrer equation and ranged from 15−30 nm (Table A-8) dependent on the preparation methods. The sample obtained through the precipitation method, Fe-CP, is composed of the smallest Fe_2O_3 crystallites of 15

nm. The crystallite sizes of Fe-SG and Fe-TD are 25 and 30 nm, respectively. The specific surface areas of all samples were calculated according to the Brunauer-Emmett-Teller (BET) method and listed in Table A-8. The highest specific surface area of 37 m^2 g^{-1} is determined for Fe-CP, which is more than three times as high as that for Fe-TD (11 m^2 g^{-1}).

The H_2-TPR experiments were used to evaluate the reducibility of calcined iron oxides from the differently synthetic methods (Figure 4-34b). The overall signal in H_2-TPR profile contains two main parts. The first part is a sharp peak located at 250−450°C, representing the reduction of hematite (α-Fe_2O_3) to magnetite (Fe_3O_4). The temperature at the maximum of the first sharp peak ($T_{max,I}$) for different catalysts and the amount of H_2 consumption in this range ($n_{H_2,I}$) are displayed in Table A-8. The second peak, which is assigned to the reduction of Fe_3O_4 to FeO or/and Fe, is badly resolved because of the complexity of Fe_3O_4 reduction. Generally, the reduction of Fe_2O_3 follows the mechanism of $Fe_2O_3 \rightarrow Fe_3O_4 \rightarrow$ FeO (Fe) $\rightarrow$ Fe, corresponding to two temperatures at the maximum of H_2 consumption in H_2-TPR profiles. The $T_{max,I}$ value for the Fe-CP catalyst was determined to 371°C, which was lower than those for Fe-SG and Fe-TD (381 and 386°C, respectively). Moreover, the onset temperatures for the reduction of magnetite ($T_{on,II}$) in the TPR profiles are found to be 395, 406 and 432°C for Fe-CP, Fe-SG and Fe-TD, respectively. In addition, the H_2 consumption ends at 750°C for Fe-CP. Whereas, the reduction of Fe-SG and Fe-TD do not complete even with the temperature above 900°C. It is evident that both $T_{max,I}$ and $T_{on,II}$ increase significantly with increasing crystallite size of the studied samples. Based on above findings, the following reducibility scale was drawn as Fe-CP > Fe-SG > Fe-TD.

The ability of different Fe_2O_3 samples to release its lattice oxygen was also investigated by means of TGA (thermogravimetric analysis) experiments at 300 °C (Figure A-35). The mass of samples decreases after they were exposed to reducing agent H_2. Such decrease resulted from the reaction of Fe_2O_3 with H_2 and associated with the formation of Fe_3O_4 and Fe. The TGA curve of Fe-CP is steeper compared with other samples, indicating a higher reduction rate. In addition, a plateau is achieved after about 125 min for Fe-CP exposing in H_2, while the Fe-SG and Fe-TD samples need longer time, which also suggests than Fe-CP is easier reducible. The plateau stage characterizes the complete reduction of Fe_2O_3 into Fe. The results of TGA under isothermal conditions agree with those of H_2-TPR experiments.
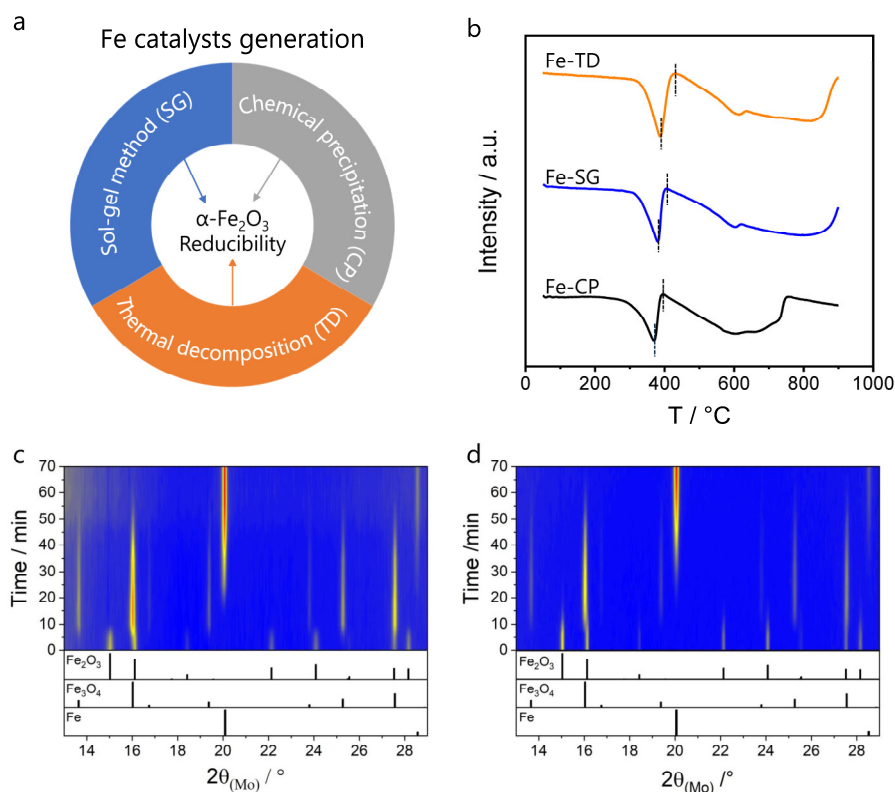
Figure 4-34 (a) Overview of catalyst preparation methods. (b) H_2-TPR profiles of as-prepared Fe_2O_3. Heatmap of *in situ*-collected XRD patterns during reduction for (c) Fe-CP and (d) Fe-TD. *In situ* XRD conditions: 300 °C, 1 bar, H_2/He (1:1, 10 mL/min).

Further kinetic and mechanistic insights into phase transformations during the reduction of α-Fe_2O_3 were derived from *in situ* XRD (Figure 4-34c, d) and *in situ* Raman spectroscopic (Figure A-36) studies at 350 °C with two representative samples (Fe-CP and Fe-TD). The evolution of iron phases upon reductive (H_2/He = 1:1) treatment at 350 °C was probed by *in situ* XRD (Figure A-37) and reveals that α-Fe_2O_3 was exclusively converted to Fe_3O_4 fast at the beginning stage of reduction. Therefore, the content of Fe_3O_4 increased with time and no metallic Fe was observed within 10 min, which clearly suggests that the reduction of α-Fe_2O_3 follows the consecutive pathway as observed from our H_2-TPR results. The faction of Fe_3O_4 reaches its maximum value after 15 min on H_2 stream for Fe-CP and after 24 min on H_2 stream for Fe-TD (Figure A-37). Hereafter, the concentration of the Fe_3O_4 phase diminished gradually due to its reduction to metallic iron. Raman spectra of fresh catalysts display the characteristic bands of hematite (Figure A-36). α-Fe_2O_3 disappeared fast after Fe-CP and Fe-TD were exposed in H_2/He at 400 °C companied with the appearance of a new band at 650 cm^{-1}, implying the formation of Fe_3O_4 as we observed from *in situ* XRD. Its intensity first increases with time on H_2/He and reaches to the maximum value after about 30 min on H_2

stream. Hereafter, the intensity of this band decreases due to the transformation of Fe_3O_4 to metallic Fe which is not observable by Raman spectroscopy.

In summary, the obtained results clearly indicate that the Fe-CP catalyst, which possesses the smallest crystallite size of Fe_2O_3, showed higher reducibility compared to the other tested Fe_2O_3 catalysts. This finding agrees with previous studies where the dependency of reducibility of small oxide clusters (i.e., ceria and titanium dioxide) on their size was uncovered by calculation and experiment studies.[312-314]

4.3.2. Controlling product selectivity

As Fe_2O_3 must be reduced to Fe_3O_4/Fe before starting CO_2-FTS, we investigated whether product selectivity can be controlled through reductive treatment of catalysts strongly differing in their redox properties. To this end, the Fe-CP, Fe-SG and Fe-TD catalysts were reduced at 300, 400 or 500 °C in a flow of 50 vol.% H_2 in N_2 at 15 bar for 2 h and then (without exposure to air) applied for CO_2-FTS at 350 °C and same pressure.
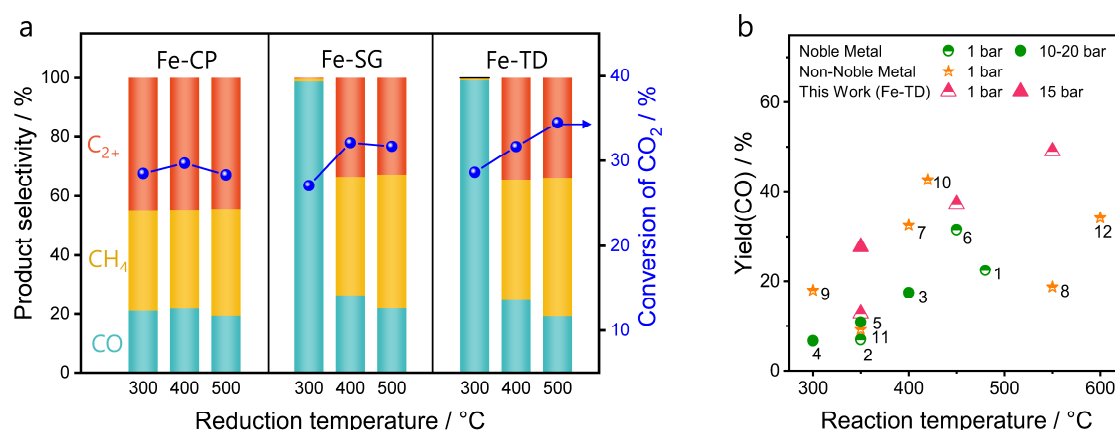
Figure 4-35 (a) CO_2 conversion and product distribution over Fe-CP, Fe-SG and Fe-TD reduced at 300, 400 or 500° C in 50 vol.% H_2 in N_2 for 2 h prior to CO_2-FTS. Reaction conditions: T = 350 °C, $H_2/CO_2/N_2$ = 3/1/0.3, GHSV= 1160 mL $g_{cat}^{-1} h^{-1}$, P = 15 bar, time on stream of 10 h. (b) A comparison of CO yield obtained over Fe-TD reduced at 300 °C and the state-of-the-art catalysts under different reaction conditions. (1) 0.1Ru/Al_2O_3 (ref.[35]); (2) K80-Pt/L (ref.[34]); (3) 8-Pt/Au@Pd@1Co (ref.[32]); (4) 5Ir/Ce (ref.[101]); (5) Rh@S-1 (ref.[100]); (6) Pd/BNCT (ref.[315]); (7) Fe-Cu/Al_2O_3 (ref.[55]); (8) 3 wt.% Ni/Ce-Zr-O (ref.[65]); (9) SCuCe-re (ref.[316]); (10) 7.4Ni/ZIF-8-C (ref.[317]); (11) Co_3O_4-2h (ref.[39]); (12) $BaCe_{0.2}Zr_{0.6}Y_{0.16}Zn_{0.04}O_3$ (ref.[318]); (13) TiFe/C (ref.[319]); (14) P-K-Mo_2C/γ-Al_2O_3 (ref.[108]). More details are provided in Table A-9.

Neither CO_2 conversion nor product distribution over the Fe-CP catalyst are affected by the reduction temperature (Figure 4-35a). The selectivity to CO, CH_4 and C_{2+}-hydrocarbons is about 22, 32 and 45% at CO_2 conversion of about 30%, respectively. Contrarily, product distribution over the Fe-SG and Fe-TD catalysts is highly sensitive to the reduction temperature. When the catalysts were reduced at 400 or 500 °C, they perform similarly to the

Fe-CP catalyst. However, CO is practically the only product formed over the Fe-SG and Fe-TD catalysts reduced at 300 °C (Figure 4-35a). Importantly, the catalysts are compared at close degrees of CO_2 conversion. Thus, the effect of the latter on product selectivity can be excluded. The near to 100% CO selectivity at high CO_2 conversion means that the RWGS reaction proceeds, while CO-FTS and CO/CO_2 methanation are suppressed even at 15 bar and in excess of H_2 (the ratio of H_2/CO_2 is 3). The formation of hydrocarbons in CO_2-FTS is favored by high pressure. It is also valid for CO-FTS as reported that the specific CO conversion rate over Fe-based catalysts at 20 bar is five to fifteen times higher than that at 1 bar.[298]

To further investigate the efficiency of Fe-TD in the RWGS reaction, this catalyst was first reduced at 300 °C and tested at ambient pressure and different temperatures using a feed with the H_2/CO_2 ratio of 3 (Figure A-38). The conversion of CO_2 increases from 12.5 to 49.4% with an increase in the reaction temperature from 350 to 550 °C. However, the selectivity to CO is not affected and keeps constant above 95%. The developed catalyst shows unexpectedly high CO yield and selectivity (Figure 4-35b, Table A-9) in comparison with other state-of-the-art RWGS catalysts based on noble metals and non-noble metal oxides.

4.3.3. Reaction scheme of product formation in CO_2-FTS

Even though Fe-CP, Fe-SG and Fe-TD reduced at 400 °C displayed similar product distribution at CO_2 conversion of about 30%, it is necessary to check the if the reaction pathways are same for these catalysts. To this end, the dependence of product selectivity on CO_2 conversion was determined over the catalysts reduced at 400 °C. For all catalysts, the selectivity to CO increases with a decrease in CO_2 conversion (Figure 4-36a), implying that CO was formed from CO_2 directly as a primary product and then consumed in other reaction(s). CO selectivity does not seem to reach 100% upon extrapolation to zero CO_2 conversion, indicating that CO is not the only product directly formed from CO_2. Otherwise, the selectivity to CO should be 100% at zero CO_2 conversion. Meanwhile the selectivity to C_{2+}-hydrocarbons increases with rising CO_2 conversion (Figure 4-36b). These opposite dependences are due to the hydrogenation of primarily formed CO to C_{2+}-hydrocarbons.

Moreover, strong differences in the dependence of CH_4 selectivity on CO_2 conversion over differently prepared Fe_2O_3 can be observed (Figure 4-36c). CH_4 selectivity over Fe-CP catalyst seems to be hardly affected by changes in the CO_2 conversion and non-zero CH_4 selectivity is observed at zero CO_2 conversion. This means that CH_4 formation over this catalyst mainly occurs through the direct CO_2 methanation. Meanwhile, there is an obvious

trend in the decrease of CH_4 selectivity with dropping CO_2 conversion over Fe-SG and Fe-TD catalysts which indicates that CO hydrogenation also contributes to CH_4 formation over these catalysts. Considering that the direct hydrogenation of CO_2 to C_{2+}-hydrocarbons is negligible over Fe-based catalysts, it can be safely deduced that CO and CH_4 are primarily formed from CO_2 in parallel through the RWGS and CO_2 methanation reactions, respectively. Based on this discussion, an overall reaction network of CO_2-FTS reaction is proposed as seen in Figure A-39. According to this reaction network, CO_2 is first converted to CH_4 and CO. The latter product is further hydrogenated into C_{2+}-hydrocarbons through CO-FTS reaction. While the contribution of CO hydrogenation to CH_4 formation depends on the studied catalysts.
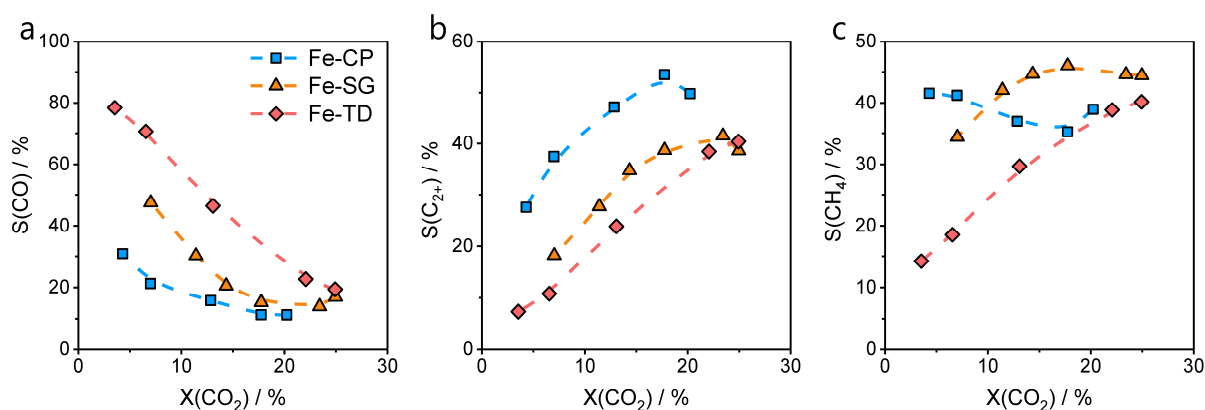
Figure 4-36 Selectivity-conversion relationships for (a) CO, (b) C_{2+}-hydrocarbons and (c) CH_4 formed over Fe-CP (square), Fe-SG (triangle) and Fe-TD (diamond) reduced at 400 °C in 50 vol% H_2 in N_2 for 2 h prior to CO_2-FTS. Reaction conditions: $H_2/CO_2/N_2 = 3/1/0.3$, P = 15 bar, T = 300 °C.

To quantitatively compare the catalysts in terms of their activity for the RWGS and CO_2 methanation reactions, we use the ratio of CO/CH_4 selectivity extrapolated to zero CO_2 conversion. The values determined for the Fe-CP, Fe-SG and Fe-TD catalysts are 1.4, 5.7 and 11.5, respectively (Table A-10). Thus, the CO_2 methanation plays an import role as primary reaction over Fe-CP but not over Fe-SG and Fe-TD. The catalysts also differ in their activity for CO hydrogenation to CH_4. This reaction is practically suppressed over Fe-CP as can be deduced from the absence of any significant effect of CO_2 conversion on the selectivity to this product (Figure 4-36c). Contrarily, the Fe-TD and Fe-SG catalysts reveal high activity towards CO hydrogenation to CH_4.

4.3.4. Spatially resolved kinetic analysis

The activity of catalysts for overall CO_2 conversion and product formation was analyzed through a spatially resolved method. This was possible when we carried out CO_2-FTS tests at different catalyst amounts but same total feed flow, i.e., different contact times. The length of

catalyst bed is normalized by the highest catalyst amount, which is 300 mg for all the catalysts. Thus, the position of different layers can be addressed by a scaling between 0 and 1. The latter value stands for the highest catalyst amount.

For all catalysts, the highest rate of overall CO_2 conversion is achieved in the first thin (about 2.5% of the total layer) upstream located layer. This rate decreases in the downstream located layers but to a different extent, which depends on the catalyst applied (Figure 4-37a). The strongest decrease was established for the Fe-CP catalyst followed by the Fe-SG and Fe-TD catalysts. The latter catalyst shows the highest rate in about 95% downstream-located catalyst layers. This distinctive behaviour can be related to the ability of the catalysts for CO_2 conversion to CH_4 or for CO conversion to CH_4 or higher hydrocarbons that is favourable from a thermodynamic viewpoint for shifting the equilibrium in the RWGS reaction.
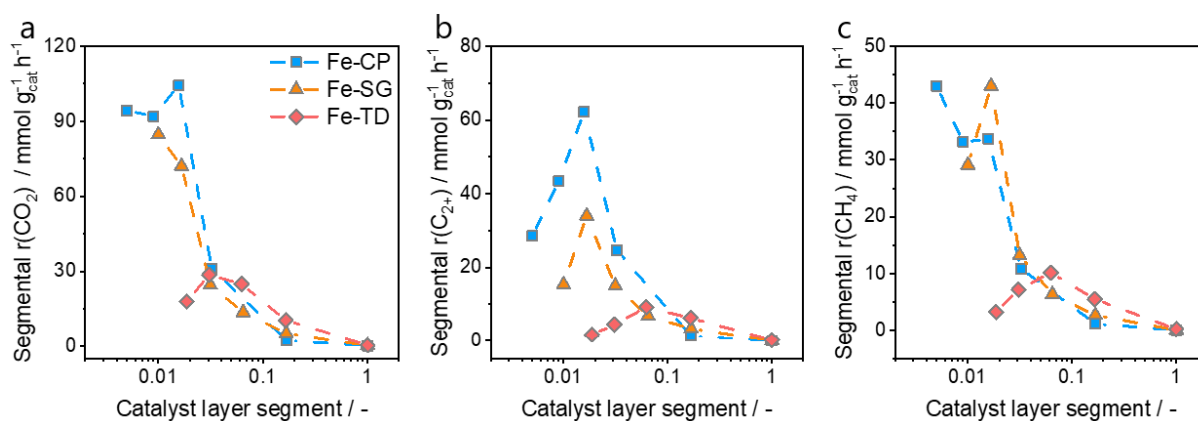
Figure 4-37 The segmental rates of (a) CO_2 consumption (r(CO_2)), (b) C_{2+}-hydrocarbons (r(C_{2+})) and (c) CH_4 (r(CH_4)) formation over Fe-CP (square), Fe-SG (triangle) and Fe-TD (diamond) reduced at 400 °C in 50 vol% H_2 in N_2 for 2 h prior to CO_2-FTS. Reaction conditions: $H_2/CO_2/N_2$ = 3/1/0.3, P = 15 bar, T = 300 °C.

To validate this hypothesis, we also calculated segmental rates of formation of C_{2+}-hydrocarbons and CH_4 (Figure 4-37b, c). The former passes a maximum in a certain bed position, which depends on the catalyst tested. The presence of the maximum implies that C_{2+}-hydrocarbons are produced through hydrogenation of CO and not directly from CO_2. The highest rate over Fe-CP and Fe-SG is achieved in about 2% upstream catalyst layer and decreases by a factor of 2 when the layer increases up to only 2.5% and declines drastically in the remaining downstream located layers. Contrarily, the Fe-TD catalyst reaches its maximal activity in about 7% upstream bed position. This high activity level for Fe-TD does not significantly reduce when the downstream catalyst layer is extended up to 17%. This catalyst also outperforms the Fe-CP and Fe-SG catalysts in 93% downstream located layer (Figure 4-37b,c).

The catalysts differ in the segmental rate of CH_4 formation, too. The rate over Fe-CP decreases downstream of the catalyst bed due to integral reactor operation. Such dependence supports our conclusion about direct CO_2 hydrogenation to CH_4 over this catalyst. However, most CH_4 is the secondary product over Fe-TD and Fe-SG because the segmental rate of CH_4 formation over these catalysts passes a maximum. And the pathway of direct CO_2 methanation plays a minor role. As in the case of C_{2+}-hydrocarbons, the Fe-TD catalyst shows lower methanation activity than Fe-CP and Fe-SG in the first 7% upstream layer but outperforms them in all downstream-located catalyst layers, however, at a very low level.

4.3.5. Fe-containing phases and surface carbon-containing species

As iron oxides undergo severe structural changes under CO_2-FTS conditions, we analyzed spent catalysts by XRD and Mössbauer spectroscopy to explain why differently reducible α-Fe_2O_3 materials differ in the effects of reduction temperature (Figure 4-35) and GHSV on product selectivity (Figure 4-36) and on the rates of overall CO_2 consumption and product formation (Figure 4-37).

Fe_3O_4 and metallic Fe are the only phases identified in the samples after reduction at 300 or 400 °C (Table A-11). The content of metallic iron increases with increasing reduction temperature. The reduced and spent catalysts are abbreviated as Fe-x-re y and Fe-x-re y-s, respectively, where x (CP, TD or SG) stands for the preparation method and y (300 or 400) represents the reduction temperature. The phases in spent catalysts after CO_2-FTS with catalyst reduced at 300 °C or 400 °C were also determined by XRD analysis (Figure A-40, Figure A-41) and Mössbauer spectroscopy (Figure 4-38a, Figure A-42 and Figure A-43). Fe-CP-re400-s and Fe-CP-re300-s are composed of Fe_5C_2 and Fe_3O_4 (Figure 4-38a, Figure A-43a). The contents of these compounds determined by Mössbauer spectra do not depend on the reduction temperature for Fe-CP (Figure 4-38b, Figure A-43d). In addition to Fe_5C_2 and Fe_3O_4, Fe_3C was identified in Fe-SG-re400-s and Fe-TD-re400-s (Figure 4-38a, Figure A-42 and Figure A-43b, c). The fraction of the carbides in these catalysts is higher than in Fe-CP-re400-s. However, the fraction of carbides significantly decreases when Fe-SG and Fe-TD had been reduced at 300 °C before starting CO_2-FTS, i.e., 4.7% vs. 13.5% and 6.2% vs. 18.3%.

Surprisingly, the most active Fe-CP catalyst for the formation of C_{2+}-hydrocarbons (Figure 4-37b) contains the lowest concentration of iron carbides, while the least active Fe-TD material possesses the highest concentration (Figure 4-38b). To clarify such discrepancy, we further explored the phase composition of these spent catalysts in a space-resolved manner

because such analysis can generally provide more comprehensive information about reaction-induced changes in the phase composition along the catalyst bed.
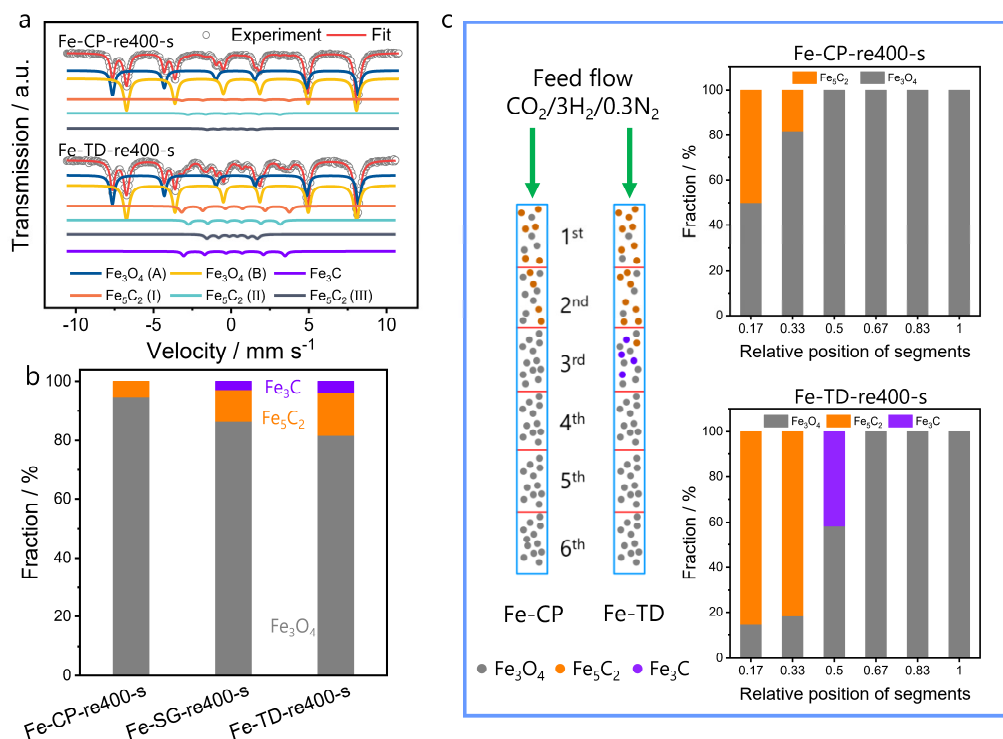

Figure 4-38 (a) Mössbauer spectra of spent catalysts after CO_2-FTS with reductive treatment at 400 °C (Fe-CP-re400-s and Fe-TD-re400-s) when 300 mg were applied. The corresponding spectrum of spent Fe-SG-re400-s catalyst is shown in Figure A-42. (b) The phase composition of spent catalysts obtained from the above Mössbauer spectra. (c) Spatially resolved phase composition of spent Fe-CP-re400-s and Fe-TD-re400-s obtained from the corresponding Mössbauer spectra in Figure A-44.

To this end, 300 mg of Fe-CP or Fe-TD was filled into reactor in such way that the whole bed was divided into 6 segments separated by a quartz wool (Figure 4-38c). The catalysts were tested in CO_2-FTS under the same conditions as in Figure 4-35. The first and second upstream located layers of spent Fe-CP exclusively contains Fe_3O_4 and Fe_5C_2 (Figure 4-38c) with the carbide fractions of 50.0 and 18.1%, respectively. These values are lower than 85.2 and 81.7% in spent Fe-CP. All other downstream-located layers of Fe-CP are composed of Fe_3O_4 exclusively. Contrarily, the third upstream located layer of spent Fe-TD contains Fe_3C. All other downstream located layers are composed of Fe_3O_4. The difference in the spatial distribution of iron carbides between Fe-CP and TD may explain why they differ in reaction behavior along catalyst bed, i.e., segmental rates of overall CO_2 consumption and conversion into C_{2+}-hydrocarbons and CH_4 (Figure 4-37).

Fe_3O_4 is known to catalyse the RWGS reaction to produce CO from CO_2. This reaction is typically very fast and can quickly reaches to the equilibrium in particularly due to the

inhibiting effect of H_2O additionally formed through either CO or CO_2 hydrogenation reactions. The latter reactions can, however, help to shift the equilibrium if their rates are higher than the rate of CO formation from CO_2. As iron carbides are responsible for CO-FTS, their absence in downstream located layers of Fe-CP should be the reason for the strong decrease in the rates of CO_2 conversion into C_{2+}-hydrocarbons and overall CO_2 consumption along the catalyst bed (Figure 4-37). The slow decrease of CO_2 conversion rate from segment to segment for Fe-TD could originate from its broad distribution of iron carbides from top to bottom in reactor.

XAS analysis was further employed to probe structural features and chemical state of iron in the first upstream layer of Fe-CP-re400-s and Fe-TD-re400-s where they show significant differences in the activity and product selectivity. The chemical state of iron in Fe-TD-re400-s is like that in Fe_5C_2 (Figure A-45a). This conclusion is also supported by the Fourier transformed EXAFS spectrum at the Fe K-edge (Figure A-45b). Fe-Fe and Fe-C scattering at 2.2 and 1.6 Å match those of the Fe_5C_2 reference spectrum. Iron in Fe-CP-re400-s should be in higher oxidation state in comparison to Fe-TD-re400-s as concluded from the intensity of the white-line peak (7131 eV). In agreement, the intensity of the signal characteristic for the Fe-C scattering is much weaker and an obvious peak of Fe-Fe signal (2.6 Å) Fe_3O_4 is present (Figure A-45b).

Further factors relevant for catalyst activity and product selectivity were elucidated through analyzing surface carbon-containing species in spent catalysts, which can play an essential role in CO-FTS over catalysts based on oxides of Fe, Co, or Ni.[320-322] According to the "competition model" proposed by Niemantsverdriet and van der Kraan[337], the species formed from CO would be involved in three different and competitive ways: (i) reaction with metallic Fe and/or Fe_3O_4 to form carbide in the case of Fe-based catalyst, (ii) reaction with surface H-containing species to produce CH_x-monomer, and (iii) formation of inactive carbon deposits. The nature of carbon species influences catalytic properties of Fe-based catalysts in CO hydrogenation.[323-324] Against this background, we carried out H_2-temperature programmed hydrogenation (TPH) tests with spent catalysts and their characterization by Raman spectroscopy to investigate how the reducibility of iron oxides and reductive treatments temperature affect the formation of carbon-containing species.

All catalysts produced CH_4 in the TPH experiments. Thus, they must contain surface carbon-containing species reacting with H_2. The CH_4 profiles are characterized by several maxima in the temperature range from 200 to 900 °C (Figure 4-39, Table A-12). CH_4 formation below

300 °C (α) and between 350 and 450 °C (β) is due to the hydrogenation of adsorbed atomic carbon or/and surface carbon and polymeric and/or amorphous carbon aggregates, respectively.[322, 325] All these species are considered to be active in CO-FTS. Adsorbed atomic carbon or/and surface carbon are exclusively present on the surface of Fe-CP-re400-s. This catalyst and all other tested catalysts also possess polymeric and/or amorphous carbon species. These species on the surface of spent Fe-CP materials should, however, differ from those on the surface of spent Fe-SG and Fe-TD because they are hydrogenated at much lower temperatures (Figure 4-39, Table A-12). No significant effect of reduction temperature before CO_2-FTS tests on the hydrogenation temperature of such species could be identified. However, an additional CH_4 peak centered at 510 °C could be found on Fe-TD-re400-s catalyst and assigned to polymeric carbon with high stability.

The sharp peak of CH_4 with the maximum at around 530 °C (γ_1) is seen in the TPH profile of Fe-CP-re400-s (Figure 4-39a) and can be attributed to the hydrogenation of Fe_5C_2 as suggested in a previous study of Bartholomew et al.[322]. This iron carbide on the surface of Fe-SG-re400-s and Fe-TD-re400-s should differ from that on Fe-CP-re400-s and are more heterogeneous in their morphology/nanostructure because they are hydrogenated at higher temperatures (558 and 610 °C) and in a broader temperature range (Figure 4-39). More importantly, the reactivity of Fe_5C_2 with H_2 for spent Fe-SG and Fe-TD decreases when reduction temperature of 300 °C was applied before CO_2-FTS, indicated by the CH_4 peaks move to higher temperatures, i.e., 676 and 650 °C for Fe-SG-re300-s and Fe-TD-re300-s, respectively. While no such effect of reduction temperature can be established for Fe-CP catalyst.
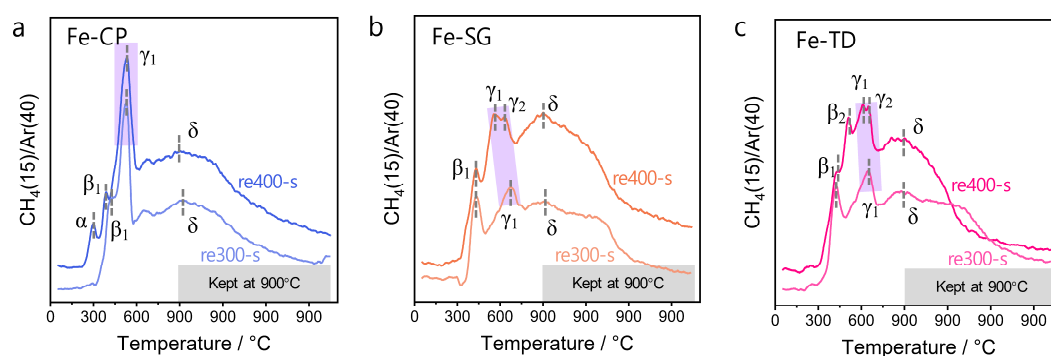
Figure 4-39 Temperature-programmed profiles of CH_4 formed upon hydrogenation (5vol.% H_2/Ar flow) of spent (a) Fe-CP, (b) Fe-SG and (c) Fe-TD catalysts after CO_2-FTS with reductive treatment at 400 °C or 300 °C.

The switch off further CO hydrogenation over Fe-SG and Fe-TD catalysts reduced at 300 °C should be related with the low reactivity of iron carbide on the surfaces of these catalysts. A

89

peak of CH_4 formation with the maximum at about 640 °C in the TPH profiles of Fe-SG-re400-s and Fe-TD-re400-s can be assigned to Fe_3C, which was also detected only in these catalysts by Mössbauer spectroscopy (Figure 4-38, Figure A-42) and XRD (Figure A-40). This carbide should have lower reactivity towards hydrogenation in comparison with Fe_5C_2 due to the stronger Fe-C bond[326], and therefore possesses higher hydrogenation temperature.

The formation of CH_4 over all spent catalysts above 690 °C is related to the hydrogenation of graphitic deposits, which are detrimental for CO-FTS as they cover active iron carbide sites. The spent Fe-CP catalysts contain the lowest amount of such undesired deposits. This conclusion is also supported by the Raman spectroscopic results (Figure A-46). The intensity of the bands at 1585 cm^{-1} (G-band) and 1325 cm^{-1} (D-band), which are characteristic for carbon deposits[327], is significantly higher in the spectra of spent Fe-SG and Fe-TD than in that of spent Fe-CP. In agreement with Mössbauer and XRD data, the latter catalyst contains higher concentration of Fe_3O_4 as concluded from the intensity of the band at 667 cm^{-1}.

4.3.6.   Iron carbides and their ability to activate CO_2, CO and H_2

To derive an insight into the first steps upon formation of steady-state catalyst composition, catalysts reduced at 300 or 400 °C were tested for their ability to adsorb/desorb CO_2 by means of CO_2-TPD experiments. Four CO_2 desorption peaks with maxima at 100-150, 280-330, 450-520, and 600-680 °C are seen in the CO_2-TPD profile of Fe-CP reduced at 400 °C (Figure A-47a). They are denoted as α, β, γ and δ according to rising desorption maximal temperature (Figure A-47).

Peak β in the profiles of Fe-SG and Fe-TD reduced at 400 °C is less resolved. This is also valid for all catalysts reduced at 300°C. Regardless of the kind of catalyst and reduction temperature, the intensity of peak β is very low. Irrespective of catalyst reduction temperature, strong adsorption sites characterized by peaks γ and δ dominant on the surface of all catalysts (> 75%, Table A-13). Almost identical total amount of desorbed CO_2 was determined for three catalysts after reduction at 400 °C (Table A-13). However, the relative fraction and CO_2 desorption amount at high temperatures (peaks γ and δ) are distinct: Fe-CP-re400 (75.7%, 5.7 μmol g^{-1}) < Fe-CP-re400 (87.5%, 6.4 μmol g^{-1}) < Fe-CP-re400 (90.2%, 6.6 μmol g^{-1}). The distribution/relative fraction of CO_2 adsorption sites is not affected by the reduction temperature before CO_2 hydrogenation.

In contrast to the reduced catalysts, CO_2 desorption from their spent counterparts occurs in a narrow temperature range between 400 and 750 °C with a much higher desorption amount (Figure 4-40, Table A-14). The difference between these two catalyst groups may be caused

by the presence of iron carbides in the spent catalysts. The CO_2-TPD profiles are deconvoluted into four peaks according to the desorption temperatures. The total amount of desorbed CO_2 over this series of spent catalysts (Fe-x-re400-s) follows the order of Fe-CP-re400-s < Fe-SG-re400-s < Fe-TD-re400-s, which coincides with the amount of iron carbides in these three catalysts (Figure 4-40c). In comparison with Fe-CP-re400-s, Fe-SG-re400-s and Fe-TD-re400-s possess stronger CO_2 adsorption sites as reflected by higher relative area fractions of desorption peak above 550 °C (Table A-14). Besides, the concentration of CO_2 adsorption sites decreases when the catalysts were reduced at 300 instead of at 400 °C before the CO_2-FTS reaction especially for Fe-SG and Fe-TD. This can be explained by the obvious decrease in the amount of iron carbide for these two catalysts when changing reduction temperature from 400 °C to 300 °C. Therefore, it can be assumed that the iron carbides contribute most of sites for CO_2 adsorption. Again, CO_2 desorption obviously shifts to higher temperatures over Fe-SG-re300-s and Fe-TD-re300-s (Figure 4-40b). Thus, carbides in spent Fe-CP differ from those in Fe-SG and Fe-TD in terms of the interaction strength of these catalysts with CO_2. A linear correlation between the amount of desorbed CO_2 and the amount of Fe_5C_2 can be established (Figure 4-40c), which also proves that CO_2 adsorption mainly occurs on iron carbides, but not iron oxides.
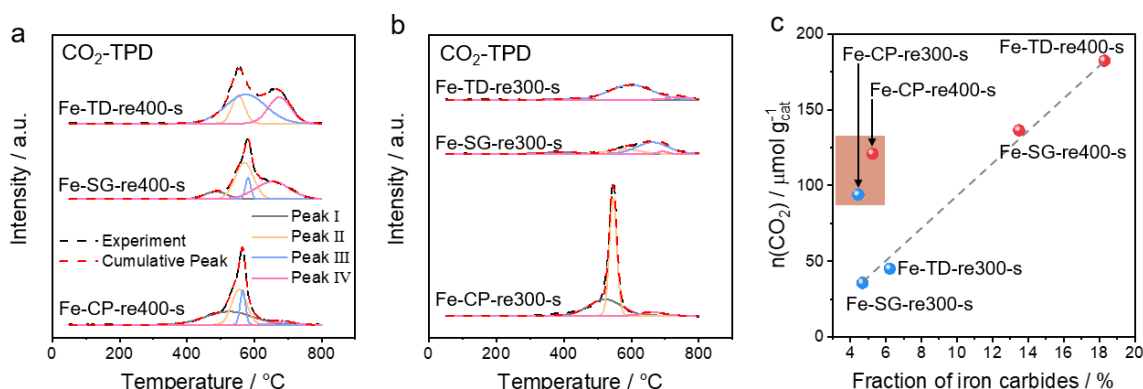
Figure 4-40 Temperature-programmed desorption profiles of CO_2 of (a) Fe-x-re400-s and (b) Fe-x-re300-s, where x stands for CP, SG or TD. (c) The amount of CO_2 ($n(CO_2)$) desorbed from different spent materials versus the concentration of iron carbides.

Do the studied spent catalysts differ in H_2 activation? This step is highly relevant for the RWGS, direct CO_2 methanation and CO hydrogenation reactions. Thus, we carried out H_2-D_2 exchange tests with the catalysts after CO_2-FTS with reduction at 400 °C. Briefly, a gas flow (2.5 vol.% D_2-2.5 vol.% H_2 in Ar) was introduced into reactor at 300 °C where spent catalyst was loaded. H_2, D_2 and HD were monitored by an online mass spectrometer. The amount of HD formed over Fe-CP-re400-s is 2.4 and 4 times higher than that over Fe-SG-re400-s and

Fe-TD-re400-s, respectively (Figure 4-41a). To get further insights into the effect of H_2 activation, the HD formation rates normalized with respect to Fe-CP-re400-s are correlated with the ratio of rates of two primary reactions (RWGS and CO_2 methanation) and the formation rates of C_{2+}-hydrocarbons at CO_2 conversion of about 10% (Figure 4-41b). Clearly, the high ability to activate H_2 facilitates the tendency of CO_2 methanation as primary reaction instead of the RWGS reaction. Thus, spent Fe-CP catalyst possessing the highest capability to H_2 activation displays the lowest value of $r_{RWGS,p} / r_{CH_4,p}$, while Fe-TD shows a very low selectivity to CH_4 at the beginning stage of CO_2 hydrogenation. On the other hand, the easier H_2 activation promotes the formation of C_{2+}-hydrocarbons.
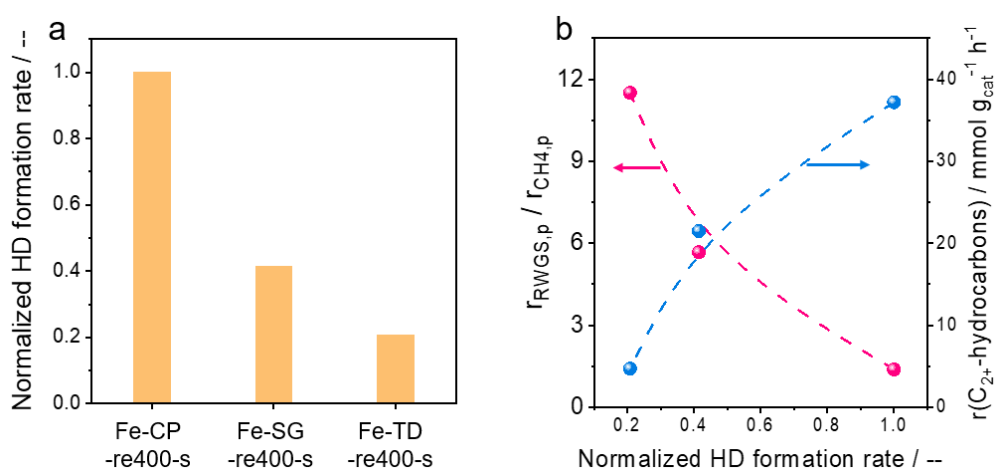
Figure 4-41 (a) The normalized HD formation rate over Fe-x-re400-s as obtained from H_2-D_2 exchange experiments. (b) The ratio of the rate of CO formation (RWGS reaction) as primary reaction to that of CH_4 formation (CO_2 methanation) as primary reaction and the formation rate of C_{2+}-hydrocarbons versus the normalized HD exchange rate. The formation rate of C_{2+}-hydrocarbons was determined at 300 °C, 15 bar, H_2/CO_2 = 3:1 and about 10% CO_2 conversion.

CO desorption from spent catalysts was also investigated because this intermediate is involved in the formation of C_{2+}-hydrocarbons. As in the case of CO_2 adsorption, Fe-CP-re400-s possesses higher concentration and more uniform sites for CO adsorption in comparison with Fe-TD-re400-s and Fe-SG-re400-s (Figure 4-42a, Table A-15). Surprisingly, no CO desorption could be seen CO-TPD tests with Fe-SG-re300-s and Fe-TD-re300-s (Figure 4-42b), showing the poor ability to adsorb CO similar with the low reactivity of iron carbide for these two spent catalysts with H_2 (Figure 4-39). Contrarily, Fe-CP-re300-s has uniform CO adsorption sites characterized by the maximal CO desorption rate at about 520 °C. This value is slightly lower than 546 °C determined for Fe-CP-re400-s. On this basis we safely conclude that iron carbides in spent Fe-CP differ from those in spent Fe-SG and Fe-TD

in terms of CO adsorption/desorption as we have observed the difference in TPH experiment (Figure 4-39).
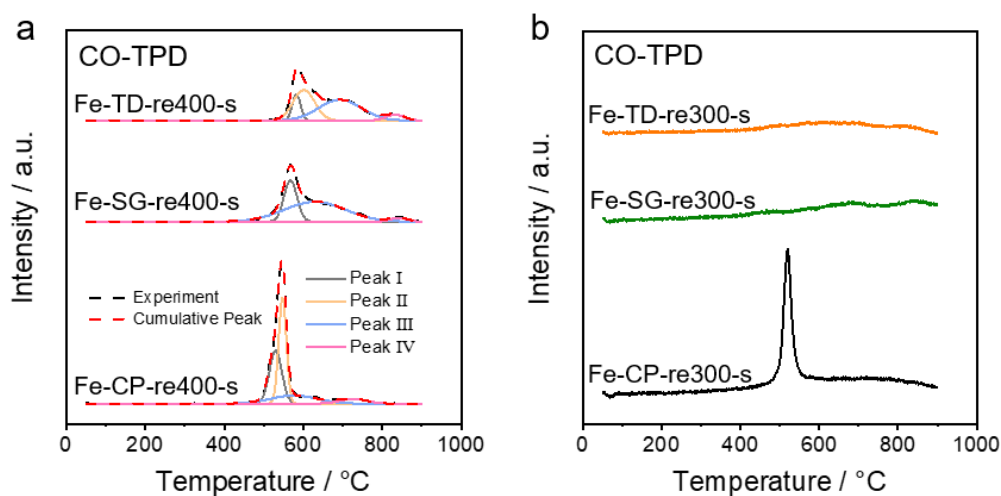

Figure 4-42 Temperature-programmed desorption profiles of CO of (a) Fe-x-re400-s and (b) Fe-x-re300-s.

4.3.7. Surface intermediates and their lifetime

Steady-state isotopic transient kinetic analysis (SSITKA) is a powerful technique for quantifying the concentration of surface intermediates leading to a certain gas-phase product and their lifetime.[296, 328] SSITKA experiments were performed under typical methanation conditions, i.e., 1.5 bar and the H_2/CO_2 ratio of 11 to avoid the formation of heavy hydrocarbons as suggested in literature for CO-FTS.[328-329] It should be noted that the distinctive ability of Fe-CP, Fe-SG and Fe-TD for CO_2 hydrogenation, CO formation and its consecutive hydrogenation are not influenced by pressure (Table A-16). Thus, ambient pressure SSITKA tests should be representative for high pressure CO_2-FTS experiments.

The catalysts were initially treated in a $^{12}CO_2/H_2/Ar=1/11/7$ feed until a pseudo steady-state operation was achieved followed by switching to a $^{13}CO_2/H_2/He/Ar=1/11/0.5/6.5$ feed for another steady-state and then back to the non-labelled feed. The normalized transients of He, ^{13}CO and $^{13}CH_4$ obtained after the second switch are shown in Figure 4-43. The responses of ^{13}CO formed over the Fe-CP, Fe-SG and Fe-TD catalysts are visibly different. The difference between the He response (representing simple diffusion) and the ^{13}CO response increases in the order Fe-TD < Fe-SG < Fe-CP (Figure 4-43a). Using the ^{13}CO transient, the number of surface intermediates leading to this product (N_{CO}) and their lifetime (τ_{CO}) were determined according to the theory of SSITKA.[296] The highest N_{CO} and τ_{CO} values were obtained for Fe-CP followed by Fe-SG and finally Fe-TD (Figure 4-43c, d).

The deviation of $^{13}CH_4$ response from He increases with the order of Fe-CP < Fe-SG < Fe-TD (Figure 4-43b). The number of surface intermediates leading to CH_4 (N_{CH4}) and their lifetime time (τ_{CHx}) were determined from the transient response of $^{13}CH_4$. The former for Fe-CP is about 1.2 and 2.7 times higher than the corresponding values for Fe-SG and Fe-TD (Table A-16). The catalysts also differ in the lifetime of such intermediates. The shortest-lived species exist on the surface of Fe-CP, while longest-lived are present on the surface of Fe-TD (Figure 4-43c).
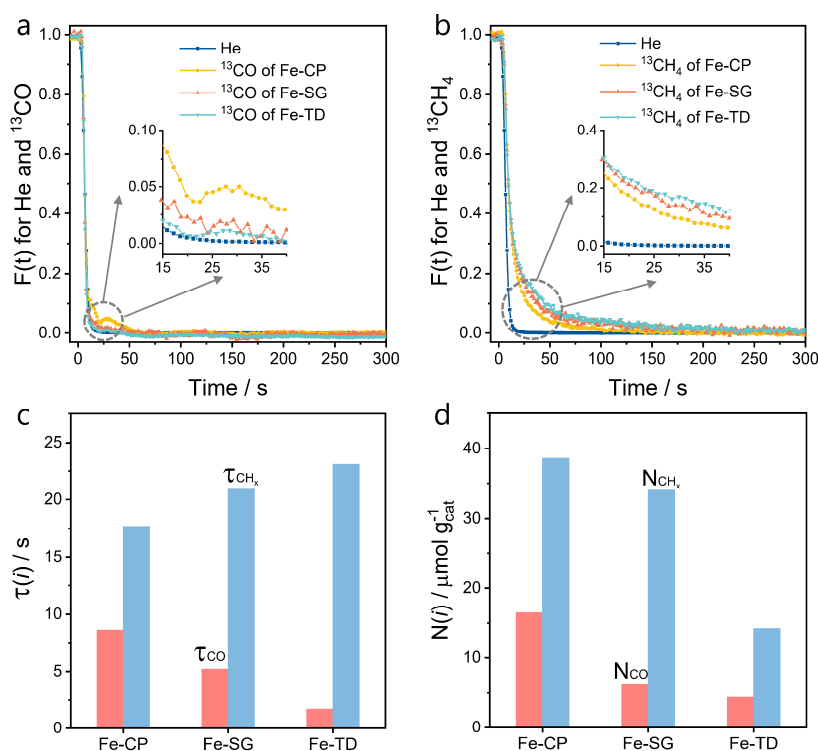
Figure 4-43 Transients of normalized concentration of (a) He and ^{13}CO or (b) He and $^{13}CH_4$ during a back-switch from $^{13}CO_2/11H_2/0.5He/6.5Ar$ to $^{12}CO_2/11H_2/7Ar$ in SSITKA experiments over different catalysts at 300 °C and 1.5 bar with GHSV of 36,000 mL $g_{cat}^{-1}h^{-1}$. (c) The lifetime and (d) the number of surface intermediates leading to CO or CH_x over different catalysts as determined from the above SSITKA tests.

In situ FTIR experiments were performed at 15 bar to further investigate the origin(s) of the distinct product distribution in CO_2-FTS over the Fe-CP and Fe-TD catalysts. The samples were initially reduced at 400 °C, then exposed to a $CO_2/H_2/He = 1/3/1$ feed at 250 °C and 15 bar. The spectra obtained after different exposure times are shown in Figure 4-44. No bands characteristic of surface intermediates like carbonates and formates could be seen in these spectra. This is obviously due to their fast transformation into gaseous products. The RWGS reaction takes place over both catalysts as evidenced by the presence of bands characteristic of CO (band at 2143 cm^{-1}) and H_2O (bands at 1300–1900 cm^{-1}). The intensity of bands centered at 3016/1305 cm^{-1} of Fe-CP catalyst, typical implying gas-phase CH_4[330], is much

higher than that of Fe-TD. This agrees with steady-state catalytic tests (Figure 4-44). It should be noted that in the ν(C–H) region an asymmetry of the rotational bands of methane can be observed in comparison with the typical spectrum of gas-phase methane. This is probably resulted from the bands of other possible products which C-H bands also appear in this region. This assumption is checked through subtracting the spectrum collected after 15 min on stream from the others (Figure A-48). Due to this correction, a δ(C–H) band around (1470 cm^{-1})[330-331] becomes visible in the spectrum of Fe-CP and its intensity increases with rising time on stream. The similar phenomenon is observed for the ν(C–H) band around 2960 cm^{-1}. Very weak C-H bands are visible at lower wavenumbers (2917 and 2850 cm^{-1}) in the non-compensated spectra of Fe-TD (Figure 4-44b). Therefore, the catalysts should differ in the kind and numbers of CH-containing species.
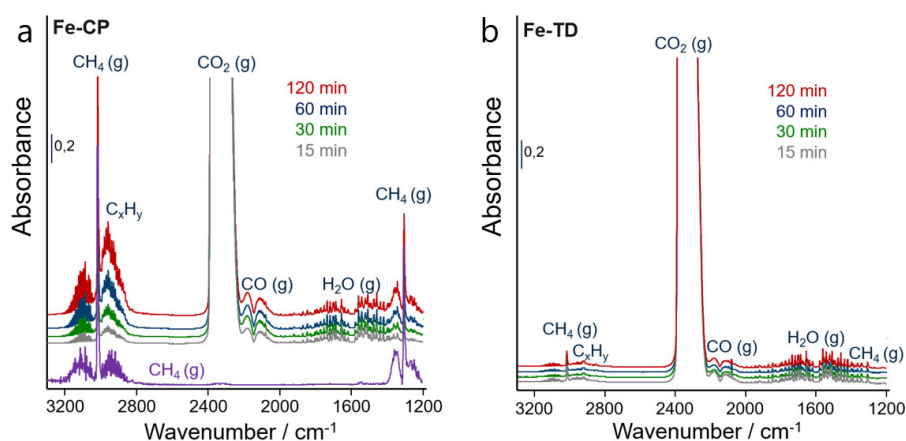
Figure 4-44 In situ time-resolved FTIR spectra recorded upon CO_2-FTS at 15 bar and 250 °C for 120 min over (a) Fe-CP and (b) Fe-TD reduced at 400 °C for 2 h.

4.3.8.   Establishing property-performance relationship

Based on the above detailed discussions, the reducibility of Fe_2O_3 seems to be an indirect descriptor for the properties of iron carbides formed through *in situ* re-structuring as well as for spatial distribution of iron carbides along catalyst bed in CO_2-FTS. Although the exact structure (e.g., the presence of surface defects or/and exposed faces) of Fe_5C_2 species remains unknown, they can be distinguished by their ability for CO, CO_2 and H_2 adsorption/activation (Figure 4-45).

Fe_5C_2 formed from easily reducible Fe_2O_3/Fe_3O_4 possesses higher concentration of CO_2 and CO adsorption sites with a moderate strength (desorption temperature below 550 °C and 600 °C, respectively) than the carbides originated from the iron oxides of moderate reducibility (Figure 4-45a, c). Redox property of iron oxides also seems to be an indicator for the reactivity towards H_2 of formed Fe_5C_2 determined through H_2-TPH experiments(Figure

4-45b, Table A-12) and for the ability to generate and bind surface intermediates leading to CO and CH_4 (Figure 4-43, Figure A-49) as well as to activate H_2 as evidenced by H/D exchange experiments (Figure 4-41). The above-discussed relationships should play an important role for CO_2-FTS because Fe_5C_2 formed from easily reducible Fe_2O_3/Fe_3O_4 show high activity towards CO conversion into C_{2+}-hydrocarbons (Figure A-50).
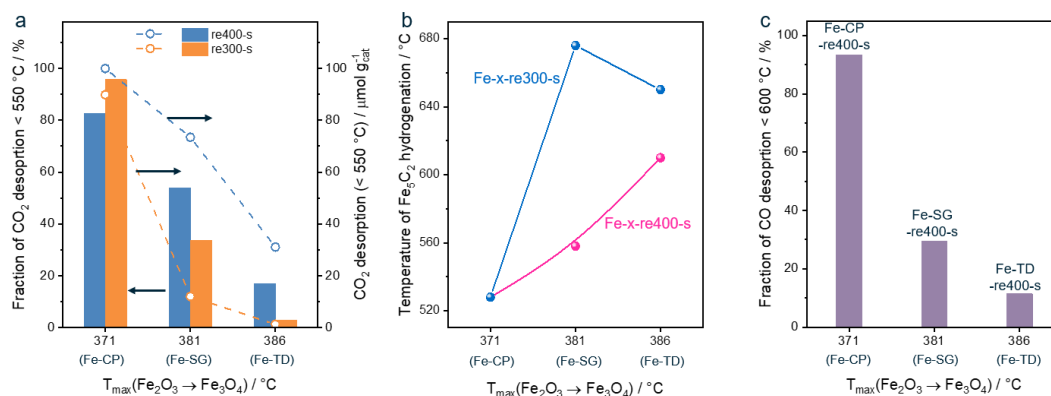
Figure 4-45 (a) The relative fraction of CO_2 desorption peaks below 550 °C and the amount of desorbed CO_2 below 550 °C from CO_2-TPD tests, (b) the temperature of the maximal rate of Fe_5C_2 hydrogenation in H_2-TPH experiments, and (c) the relative fraction of CO desorption peaks below 600 °C from CO-TPD tests versus the temperature of the maximal reduction rate of Fe_2O_3 to Fe_3O_4.

It should also be especially mentioned that Fe_5C_2 generated from heavily reducible α-Fe_2O_3 (Fe-TD and Fe-SG) reduced at 300 °C before starting CO_2-FTS shows very low ability to adsorb CO. Therefore, any consecutive hydrogenation reactions of this gas-phase intermediate are strongly hindered and near 100% CO selectivity can be obtained at high degrees of CO_2 conversion and even at 15 bar in excess of H_2 (Figure 4-35).

The parameters obtained from fitting Mössbauer spectra, especially hyperfine field, provide important hints regarding the overall structural property of Fe_5C_2 of spent catalysts (Table A-17). Hyperfine field was regarded as an important parameter indicating the C/Fe ratio of iron carbide phases.[332] Generally, the higher value of this parameter, the lower ratio of C/Fe is.[332] Further, the C/Fe ratio influences the oxidation state of Fe in iron carbide. It has been reported that both the C/Fe ratio and the oxidation state of Fe affect the CO hydrogenation in CO-FTS reaction because they influence the electron density of Fe in iron carbides and further influence the strength Fe-CO band.[298, 333] Lower oxidation state of Fe in iron carbide can strengthen Fe-C bonding, which is unfavorable for CO-FTS activity as proved by different groups.[240, 334-335]

The parameters, especially hyperfine field, obtained from fitting Mössbauer spectra of iron carbides in Fe-x-re400-s and Fe-x-re300-s catalysts are compared (Table A-17). No obvious changes in the hyperfine field between Fe-CP-re400-s and Fe-re300-s can be found, implying the similar C/Fe ratio of iron carbide in these two spent catalysts. This agrees with the consistency of catalytic performance of these two catalysts. However, the different reduction temperature before reaction results in the changes in the structure (C/Fe ratio) of iron carbides in spent catalysts for Fe-TD and Fe-SG, as evidenced by the difference in hyperfine field. Higher hyperfine field parameters are obtained over Fe-TD-re300-s compared with its counterpart initially reduced at 400 °C (Fe-TD-re400-s). A similar phenomenon is also observed for Fe-SG. The higher values of hyperfine field identified from Fe-TD-re300-s and Fe-SG-re300-s indicate the lower ratio of C/Fe of iron carbides in these spent catalyst in comparison with Fe-TD-re400-s and Fe-SG-re400-s. As discussed above, the lower C/Fe ratio would cause the lower oxidation state of Fe in iron carbides, which can be a reason for the low activity of CO-FTS reaction. Therefore, the change in the structural properties of iron carbides may explain the difference in product selectivity of Fe-TD or Fe-SG induced by the different reduction temperatures (Figure 4-35).

4.3.9. Summary

This study demonstrates how to control both desired and undesired hydrogenation reactions in the process of CO_2 hydrogenation over bulk iron catalysts. By varying reduction temperature, the product selectivity could be regulated strongly but depending on the reducibility of as-prepared Fe_2O_3 catalysts. Through in-depth characterization and detailed kinetic & mechanistic analyses, catalyst ability for activation of gas-phase CO, CO_2 and H_2 as well as the nature of carbon species on catalyst surface were concluded to govern both activity and product selectivity. In details, iron carbide produced from easily reducible Fe_2O_3/Fe_3O_4 reveal higher concentration of CO_2/CO adsorption sites with a moderate strength. They also display higher ability towards H_2 activation and form long-lived surface intermediates yielding CO but short-lived intermediates yielding CH_4. The origin(s) for the effect of reduction temperature on product selectivity was identified from the aspect of structural property (C/Fe) of *in situ* formed iron carbides. The C/Fe ratios of iron carbides in Fe-TD-re300-s and Fe-SG-re300-s is lower than those in Fe-TD-re400-s and Fe-SG-re400-s. While no changes in C/Fe ratio could be found for two Fe-CP spent catalysts (Fe-CP-re300-s and Fe-CP-re400-s). As CO has versatile applications in the chemical industry, the achieved performance in combination with the abundance of Fe and the simplicity of catalyst preparation method supports the vision of CO_2-based generation of commodity products.

5. Conclusions

This thesis contributed to establishing catalyst property-performance relationships in the CO_2-FTS reaction over Fe-based catalysts through different approaches. Using catalysis informatics with statistical tools, effective transient kinetic experiments, spatially resolved methodologies, as well as the state-of-the-art characterization techniques, important descriptors influencing catalyst activity and selectivity were identified. The importance of re-structing of iron oxides during reduction and CO_2-FTS reaction was also highlighted in this thesis. The central conclusions are summarized as follows.

Statistical analysis of available experimental literature data for CO_2-FTS reaction allowed to identify property-performance correlations typically hidden in the vast body of existing experimental data. Starting from large number of literature data, comprehensive statistical analysis was used to explore useful information and deduce general rules which are favor for catalyst design and optimizing reaction operation. Total pressure has the most decisive effect on the CO_2 conversion rate and C_{2+}-HCs formation rate. While the kind of catalyst is the most decisive factor for $O(C_2\text{-}C_4)/P(C_2\text{-}C_4)$ and $S(C_{2+})$, which are favored by the combination of alkali metal with transition metal as co-promoters. This conclusion was experimentally validated. A series of catalysts promoted by Mn and/or K were synthesized and tested in CO_2-FTS reaction. The optimal catalyst (0.4Mn-K/Fe) is superior or comparable with other state-of-the-art Fe-based catalysts in terms of catalytic performance. In addition, the statistical analysis suggested that the ability of catalysts for CO_2 conversion and CH_4 formation can be correlated to the electronegativity of promoters applied. This statement was also experimentally proven as described below.

Fe-based catalysts with different alkali metals and their amounts were prepared and evaluated to probe the fundamentals of promotion effects of alkali metals on the intrinsic activity and the reaction scheme of product formation in CO_2 hydrogenation from kinetic and mechanistic viewpoints. Through spatially resolved kinetic analyses under steady-state, it was established that the intrinsic activity towards overall CO_2 consumption and formation of individual products follows the order: 0AM/Fe ~ Li/Fe > Na/Fe > K/Fe ~ Rb/Fe > Cs/Fe. The strongest inhibiting effect of K, Rb or Cs was established for the undesired CO_2 methanation reaction. Further, transient kinetic studies in the TAP reactor revealed that the presence of alkali metal promoter modifies catalyst ability to interact/activate H_2, CO_2, CO and C_2H_4. This catalyst property is decisive for the steady-state concentration of surface carbon and hydrogen species

which determine the activity and product selectivity in CO_2-FTS. The presence of alkali metal promoter influences the local electronic state of Fe in iron carbides. Thus, the electronegativity of alkali metal promoter is proposed to correlate with the intrinsic activity of CH_4 and C_{2+}-hydrocarbons formation, as well as the rate constants of elementary steps of CO/CO_2 activation. The alkali metal with lower electronegativity enhances the ability of iron carbides to adsorb and activate CO_2, but has a negative effect on CO adsorption and H_2 activation. These fundamental insights elucidated here are expected to be helpful for other hydrogenation processes.

Using promoter-free catalysts, important physicochemical properties of Fe_2O_3 were identified as indicators both for the *in situ* formation of catalytically active (Fe_3O_4 and FeC_x) phases and catalytic performance. The reactivity of iron carbide species formed from differently reducible Fe_2O_3 depends on the temperature of reductive catalyst treatment before CO_2-FTS and influences the ability to adsorb/activate CO_2, CO and H_2. CO_2 and CO prefer to be adsorbed with a moderate strength on iron carbides originated from easily reducible Fe_2O_3. Such iron carbides reveal higher reactivity with H_2 as determined by temperature-programmed hydrogenation tests. CO hydrogenation is strongly hindered on iron carbides produced from heavily reducible Fe_2O_3 when it was initially reduced at a low temperature (300 °C). As concluded from the results of fitting of Mössbauer spectra, these iron carbides possess a lower C/Fe ratio and a lower oxidation state of Fe in comparison with their counterparts generated from heavily reducible Fe_2O_3 reduced. The low CO-FTS activity of iron carbides with the low C/Fe ratio could rationalize the effect of reduction temperature on product selectivity when using differently reducible Fe_2O_3.

6. Outlook

In addition to the established property-performance relationships and factors affecting activity and selectivity identified in this thesis, further attentions should be paid to the design of catalysts with well-defined morphology and crystal facets from more microscopic level, e.g., using crystal engineering and more precise synthetic method. The termination configuration on the surface of iron carbides was rarely studied in literatures. It could have a strong influence on the adsorption and activation of CO_2, CO and H_2 and give more fundamentals in terms of the effect of C/Fe ratio of iron carbide on the activity of CO_x-FTS reaction. Besides alkali metal promoters used in this thesis, other promoter(s), e.g., various transition metals, has been widely employed for Fe-based catalyst in CO_x-FTS reaction. However, the fundamental study regarding their promotion effect is still rare. Even though the relationship between the property (electronegativity) of transition metal promoter and catalytic performance was established in this study through statistical analysis, further experimental works are needed to extend the existing relationships.

It is needed to systematically investigate the effects of operation parameters on catalyst performance. In this thesis, the effects of reaction temperature on CO_2 conversion and product distribution were investigated. Other reaction parameters such as reaction pressure, H_2/CO_2 ratio, pre-treatment conditions should be studied further from experimental side. This would accelerate the process optimization for achieving high activity and desired product distribution over Fe-based catalysts. Even though the effects of pre-treatment procedure, including atmosphere, temperature, and time, of Fe-based catalysts on their performance in CO-FT have been well documented, the systematic study of this aspect in CO_2 hydrogenation over Fe-based catalysts is highly needed. It should be noted that the excellent stability was found for promoted catalysts, for example the designed Mn-K/Fe catalysts in **4.1.4**. However, such effect of promoter has not been fully understood. It is expected to take the advantages of *in situ/operando* techniques to obtain deeper insights for the excellent stability induced by the presence of potassium. Moreover, the regeneration method for Fe-based catalysts in CO_2-FTS reaction is desired to be developed considering its industrial application.

Reference

1. Karl Thomas, R.; Trenberth Kevin, E., *Science* **2003,** 302, 1719–1723.

2. O'Neill, B. C.; Carter, T. R.; Ebi, K.; Harrison, P. A.; Kemp-Benedict, E.; Kok, K.; Kriegler, E.; Preston, B. L.; Riahi, K.; Sillmann, J.; van Ruijven, B. J.; van Vuuren, D.; Carlisle, D.; Conde, C.; Fuglestvedt, J.; Green, C.; Hasegawa, T.; Leininger, J.; Monteith, S.; Pichs-Madruga, R., *Nature Climate Change* **2020,** 10, 1074–1084.

3. Hoegh-Guldberg, O.; Jacob, D.; Taylor, M.; Guillén Bolaños, T.; Bindi, M.; Brown, S.; Camilloni, I. A.; Diedhiou, A.; Djalante, R.; Ebi, K.; Engelbrecht, F.; Guiot, J.; Hijioka, Y.; Mehrotra, S.; Hope, C. W.; Payne, A. J.; Pörtner, H. O.; Seneviratne, S. I.; Thomas, A.; Warren, R.; Zhou, G., *Science* **2019,** 365, eaaw6974.

4. Lacis Andrew, A.; Schmidt Gavin, A.; Rind, D.; Ruedy Reto, A., *Science* **2010,** 330, 356-359.

5. Cai, B.; Cui, C.; Zhang, D.; Cao, L.; Wu, P.; Pang, L.; Zhang, J.; Dai, C., *Appl. Energy* **2019,** 253, 113579.

6. Zheng, X.; Streimikiene, D.; Balezentis, T.; Mardani, A.; Cavallaro, F.; Liao, H., *J. Cleaner Prod.* **2019,** 234, 1113–1133.

7. Levi, P. G.; Cullen, J. M., *Environ. Sci. Technol.* **2018,** 52, 1725–1734.

8. https://climate.nasa.gov/vital-signs/carbon-dioxide/.

9. https://ourworldindata.org/co2-and-other-greenhouse-gas-emissions.

10. Agreement, P. In *Paris agreement*, Report of the Conference of the Parties to the United Nations Framework Convention on Climate Change (21st Session, 2015: Paris). Retrieved December, HeinOnline: 2015; p 2017.

11. Chen, J. M., *The Innovation* **2021,** 2, 100127.

12. Centi, G.; Quadrelli, E. A.; Perathoner, S., *Energy Environ. Sci.* **2013,** 6.

13. Kondratenko, E. V.; Mul, G.; Baltrusaitis, J.; Larrazábal, G. O.; Pérez-Ramírez, J., *Energy Environ. Sci.* **2013,** 6, 3112–3135.

14. Aresta, M.; Dibenedetto, A.; Quaranta, E., *J. Catal.* **2016,** 343, 2–45.

15. Burkart, M. D.; Hazari, N.; Tway, C. L.; Zeitler, E. L., *ACS Catal.* **2019,** 9, 7937–7956.

16. De, S.; Dokania, A.; Ramirez, A.; Gascon, J., *ACS Catal.* **2020,** 10, 14147–14185.

17. Li, Y.; Sun, Y.; Qin, Y.; Zhang, W.; Wang, L.; Luo, M.; Yang, H.; Guo, S., *Adv. Energy Mater.* **2020,** 10, 1903120.

18. Xu, H.; Shang, H.; Wang, C.; Du, Y., *Coord. Chem. Rev.* **2020,** 418, 213374.

19. Wang, W.; Wang, S. P.; Ma, X. B.; Gong, J. L., *Chem. Soc. Rev.* **2011,** 40, 3703–3727.

20. Saeidi, S.; Amin, N. A. S.; Rahimpour, M. R., *J. CO2 Util.* **2014,** 5, 66–81.

21. Marques Mota, F.; Kim, D. H., *Chem. Soc. Rev.* **2019,** 48, 205–259.

22. Ye, R. P.; Ding, J.; Gong, W.; Argyle, M. D.; Zhong, Q.; Wang, Y.; Russell, C. K.; Xu, Z.; Russell, A. G.; Li, Q.; Fan, M.; Yao, Y. G., *Nat. Commun.* **2019,** 10, 5698.

23. Ronda-Lloret, M.; Rothenberg, G.; Shiju, N. R., *ChemSusChem* **2019,** 12, 3896–3914.

24. Lee, S.-B.; Kim, J.-S.; Lee, W.-Y.; Lee, K.-W.; Choi, M.-J. In *Carbon Dioxide Utilization for Global Sustainability, Proceedings of 7ththe International Conference on Carbon Dioxide Utilization*, 2004; pp 73-78.

25. Saeidi, S.; Najari, S.; Fazlollahi, F.; Nikoo, M. K.; Sefidkon, F.; Klemeš, J. J.; Baxter, L. L., *Renewable Sustainable Energy Rev.* **2017,** 80, 1292–1311.

26. Jiang, Y.; Long, R.; Xiong, Y., *Chem. Sci.* **2019,** 10, 7310–7326.

27. Kattel, S.; Liu, P.; Chen, J. G., *J. Am. Chem. Soc.* **2017,** 139, 9739–9754.

28. Vrijburg, W. L.; Garbarino, G.; Chen, W.; Parastaev, A.; Longo, A.; Pidko, E. A.; Hensen, E. J. M., *J. Catal.* **2020,** 382, 358–371.

29. Parastaev, A.; Muravev, V.; Osta, E. H.; van Hoof, A. J.; Kimpel, T. F.; Kosinov, N.; Hensen, E. J., *Nat. Catal.* **2020,** 3, 526–533.

30. Gaikwad, R.; Reymond, H.; Phongprueksathat, N.; von Rohr, P. R.; Urakawa, A., *Catal. Sci. Technol.* **2020,** 10, 2763–2768.

31. Behrens, M.; Studt, F.; Kasatkin, I.; Kühl, S.; Hävecker, M.; Abild-Pedersen, F.; Zander, S.; Girgsdies, F.; Kurr, P.; Kniep, B.-L.; Tovar, M.; Fischer, R. W.; Nørskov, J. K.; Schlögl, R., *Science* **2012,** 336, 893–897.

32. Zhao, X.; Xu, H.; Wang, X.; Zheng, Z.; Xu, Z.; Ge, J., *ACS Appl. Mater. Interfaces* **2018,** 10, 15096–15103.

33. Guo, Y.; Mei, S.; Yuan, K.; Wang, D.-J.; Liu, H.-C.; Yan, C.-H.; Zhang, Y.-W., *ACS Catal.* **2018,** 8, 6203–6215.

34. Yang, X.; Su, X.; Chen, X.; Duan, H.; Liang, B.; Liu, Q.; Liu, X.; Ren, Y.; Huang, Y.; Zhang, T., *Appl. Catal. B-Environ.* **2017,** 216, 95–105.

35. Kwak, J. H.; Kovarik, L.; Szanyi, J., *ACS Catal.* **2013,** 3, 2449–2455.

36. Yang, C.; Pei, C.; Luo, R.; Liu, S.; Wang, Y.; Wang, Z.; Zhao, Z.-J.; Gong, J., *J. Am. Chem. Soc.* **2020,** 142, 19523–19531.

37. Zhu, J.; Zhang, G.; Li, W.; Zhang, X.; Ding, F.; Song, C.; Guo, X., *ACS Catal.* **2020,** 10, 7424–7433.

38. Skrypnik, A. S.; Yang, Q.; Matvienko, A. A.; Bychkov, V. Y.; Tulenin, Y. P.; Lund, H.; Petrov, S. A.; Kraehnert, R.; Arinchtein, A.; Weiss, J.; Brueckner, A.; Kondratenko, E. V., *Appl. Catal. B-Environ.* **2021,** 291, 120121.

39. Yang, C.; Liu, S.; Wang, Y.; Song, J.; Wang, G.; Wang, S.; Zhao, Z. J.; Mu, R.; Gong, J., *Angew. Chem. Int. Ed.* **2019,** 58, 11242–11247.

40. Li, J.; Sun, L.; Wan, Q.; Lin, J.; Lin, S.; Wang, X., *J. Phys. Chem. Lett.* **2021**, 11415–11421.

41. Zhou, H.; Chen, Z.; Kountoupi, E.; Tsoukalou, A.; Abdala, P. M.; Florian, P.; Fedorov, A.; Müller, C. R., *Nat. Commun.* **2021,** 12, 5510.

42. Porosoff, M. D.; Yang, X.; Boscoboinik, J. A.; Chen, J. G., *Angew. Chem. Int. Ed.* **2014,** 53, 6705–6709.

43. Morse, J. R.; Juneau, M.; Baldwin, J. W.; Porosoff, M. D.; Willauer, H. D., *J. CO2 Util.* **2020,** 35, 38–46.

44. Li, Z.; Wang, J.; Qu, Y.; Liu, H.; Tang, C.; Miao, S.; Feng, Z.; An, H.; Li, C., *ACS Catal.* **2017,** 7, 8544–8548.

45. Gao, P.; Dang, S.; Li, S.; Bu, X.; Liu, Z.; Qiu, M.; Yang, C.; Wang, H.; Zhong, L.; Han, Y.; Liu, Q.; Wei, W.; Sun, Y., *ACS Catal.* **2018,** 8, 571–578.

46. Ni, Y.; Chen, Z.; Fu, Y.; Liu, Y.; Zhu, W.; Liu, Z., *Nat. Commun.* **2018,** 9, 3457.

47. Li, Z.; Qu, Y.; Wang, J.; Liu, H.; Li, M.; Miao, S.; Li, C., *Joule* **2019,** 3, 570–583.

48. Kaiser, P.; Unde, R. B.; Kern, C.; Jess, A., *Chem. Ing. Tech.* **2013,** 85, 489–499.

49. Daza, Y. A.; Kuhn, J. N., *RSC Advances* **2016,** 6, 49675–49691.

50. Chen, X.; Chen, Y.; Song, C.; Ji, P.; Wang, N.; Wang, W.; Cui, L., *Front. Chem.* **2020,** 8, 709–709.

51. Weatherbee, G. D.; Bartholomew, C. H., *J. Catal.* **1984,** 87, 352–362.

52. Kharaji, A. G.; Shariati, A.; Takassi, M. A., *Chin. J. Chem. Eng.* **2013,** 21, 1007–1014.

53. Kim, D. H.; Han, S. W.; Yoon, H. S.; Kim, Y. D., *J. Ind. Eng. Chem.* **2015,** 23, 67–71.

54. Loiland, J. A.; Wulfers, M. J.; Marinkovic, N. S.; Lobo, R. F., *Catal. Sci. Technol.* **2016,** 6, 5267–5279.

55. Pastor-Pérez, L.; Baibars, F.; Le Sache, E.; Arellano-García, H.; Gu, S.; Reina, T. R., *J. CO2 Util.* **2017,** 21, 423–428.

56. Pastor-Pérez, L.; Shah, M.; Le Saché, E.; Ramirez Reina, T., *Catalysts* **2018,** 8.

57. Chou, C.-Y.; Loiland, J. A.; Lobo, R. F., *Catalysts* **2019,** 9.

58. Sengupta, S.; Jha, A.; Shende, P.; Maskara, R.; Das, A. K., *J. Environ. Chem. Eng.* **2019,** 7, 102911.

59. Yang, L.; Pastor-Pérez, L.; Villora-Pico, J. J.; Gu, S.; Sepúlveda-Escribano, A.; Reina, T. R., *Appl. Catal. A-Gen.* **2020,** 593, 117442.

60. Gu, M.; Dai, S.; Qiu, R.; Ford, M. E.; Cao, C.; Wachs, I. E.; Zhu, M., *ACS Catal.* **2021,** 11, 12609–12619.

61. Peng, L.; Jurca, B.; Primo, A.; Gordillo, A.; Parvulescu, V. I.; García, H., *ACS Sustain. Chem. Eng.* **2021,** 9, 9264−9272.

62. Zhu, M.; Tian, P.; Ford, M. E.; Chen, J.; Xu, J.; Han, Y.-F.; Wachs, I. E., *ACS Catal.* **2020,** 10, 7857–7863.

63. Yang, L.; Pastor-Pérez, L.; Villora-Pico, J. J.; Sepúlveda-Escribano, A.; Tian, F.; Zhu, M.; Han, Y.-F.; Ramirez Reina, T., *ACS Sustain. Chem. Eng.* **2021,** 9, 12155−12166.

64. Wang, L.; Zhang, S.; Liu, Y., *J. Rare Earths* **2008,** 26, 66–70.

65. Sun, F.-m.; Yan, C.-f.; Wang, Z.-d.; Guo, C.-q.; Huang, S.-l., *Int. J. Hydrogen Energy* **2015,** 40, 15985–15993.

66. Rodrigues, M. T.; Zonetti, P. C.; Alves, O. C.; Sousa-Aguiar, E. F.; Borges, L. E. P.; Appel, L. G., *Appl. Catal. A-Gen.* **2017,** 543, 98–103.

67. Winter, L. R.; Gomez, E.; Yan, B.; Yao, S.; Chen, J. G., *Appl. Catal. B-Environ.* **2018,** 224, 442–450.

68. Millet, M.-M.; Algara-Siller, G.; Wrabetz, S.; Mazheika, A.; Girgsdies, F.; Teschner, D.; Seitz, F.; Tarasov, A.; Levchenko, S. V.; Schlögl, R.; Frei, E., *J. Am. Chem. Soc.* **2019,** 141, 2451–2461.

69. Wu, H. C.; Chang, Y. C.; Wu, J. H.; Lin, J. H.; Lin, I. K.; Chen, C. S., *Catal. Sci. Technol.* **2015,** 5, 4154–4163.

70. Gonçalves, R. V.; Vono, L. L. R.; Wojcieszak, R.; Dias, C. S. B.; Wender, H.; Teixeira-Neto, E.; Rossi, L. M., *Appl. Catal. B-Environ.* **2017,** 209, 240–246.

71. Chen, C.-S.; Budi, C. S.; Wu, H.-C.; Saikia, D.; Kao, H.-M., *ACS Catal.* **2017,** 7, 8367–8381.

72. Lu, B.; Kawamoto, K., *Mater. Res. Bull.* **2014,** 53, 70–78.

73. Vogt, C.; Groeneveld, E.; Kamsma, G.; Nachtegaal, M.; Lu, L.; Kiely, C. J.; Berben, P. H.; Meirer, F.; Weckhuysen, B. M., *Nat. Catal.* **2018,** 1, 127–134.

74. Gadalla, A. M.; Bower, B., *Chem. Eng. Sci.* **1988,** 43, 3049–3062.

75. Skorodumova, N. V.; Simak, S. I.; Lundqvist, B. I.; Abrikosov, I. A.; Johansson, B., *Phys. Rev. Lett.* **2002,** 89, 166601.

76. Hori, C. E.; Permana, H.; Ng, K. Y. S.; Brenner, A.; More, K.; Rahmoeller, K. M.; Belton, D., *Appl. Catal. B-Environ.* **1998,** 16, 105–117.

77. Wang, L.; Liu, H.; Liu, Y.; Chen, Y.; Yang, S., *J. Rare Earths* **2013,** 31, 969–974.

78. Bussche, K. M. V.; Froment, G. F., *J. Catal.* **1996,** 161, 1–10.

79. Shishido, T.; Yamamoto, M.; Li, D.; Tian, Y.; Morioka, H.; Honda, M.; Sano, T.; Takehira, K., *Appl. Catal. A-Gen.* **2006,** 303, 62–71.

80. Kam, R.; Selomulya, C.; Amal, R.; Scott, J., *J. Catal.* **2010,** 273, 73–81.

81. Martino, G.; Courty, P.; Marcilly, C.; Kochloefl, K.; Lunsford, J. H. In *Handbook of Heterogeneous Catalysis*, 1997; pp 1801–1900.

82. Fujita, S.-I.; Usui, M.; Takezawa, N., *J. Catal.* **1992,** 134, 220–225.

83. Ginés, M. J. L.; Marchi, A. J.; Apesteguía, C. R., *Appl. Catal. A-Gen.* **1997,** 154, 155–171.

84. Chen, C.-S.; Cheng, W.-H.; Lin, S.-S., *Catal. Lett.* **2000,** 68, 45–48.

85. Chen, C.-S.; Cheng, W.-H.; Lin, S.-S., *Chem. Commun.* **2001**, 1770–1771.

86. Stone, F. S.; Waller, D., *Top. Catal.* **2003,** 22, 305–318.

87. Álvarez Galván, C.; Schumann, J.; Behrens, M.; Fierro, J. L. G.; Schlögl, R.; Frei, E., *Appl. Catal. B-Environ.* **2016,** 195, 104–111.

88. Su, X.; Yang, X.; Zhao, B.; Huang, Y., *J. Energy Chem.* **2017,** 26, 854–867.

89. Chen, C.-S.; Cheng, W.-H.; Lin, S.-S., *Appl. Catal. A-Gen.* **2004,** 257, 97–106.

90. Zhang, X.; Zhu, X.; Lin, L.; Yao, S.; Zhang, M.; Liu, X.; Wang, X.; Li, Y.-W.; Shi, C.; Ma, D., *ACS Catal.* **2017,** 7, 912–918.

91. Wang, L.; Liu, H.; Chen, Y.; Zhang, R.; Yang, S., *Chem. Lett.* **2013,** 42, 682–683.

92. Wang, L.; Liu, H., *Catal. Today* **2018,** 316, 155–161.

93. Li, W.; Zhang, G.; Jiang, X.; Liu, Y.; Zhu, J.; Ding, F.; Liu, Z.; Guo, X.; Song, C., *ACS Catal.* **2019,** 9, 2739–2751.

94. Dostagir, N. H. M. D.; Rattanawan, R.; Gao, M.; Ota, J.; Hasegawa, J.-y.; Asakura, K.; Fukouka, A.; Shrotri, A., *ACS Catal.* **2021,** 11, 9450–9461.

95. Zhang, Y.; Jacobs, G.; Sparks, D. E.; Dry, M. E.; Davis, B. H., *Catal. Today* **2002,** 71, 411–418.

96. Wang, L.; Liu, H.; Chen, Y.; Yang, S., *Int. J. Hydrogen Energy* **2017,** 42, 3682–3689.

97. Chen, X.; Su, X.; Su, H.-Y.; Liu, X.; Miao, S.; Zhao, Y.; Sun, K.; Huang, Y.; Zhang, T., *ACS Catal.* **2017,** 7, 4613–4620.

98. Zhao, Z.; Wang, M.; Ma, P.; Zheng, Y.; Chen, J.; Li, H.; Zhang, X.; Zheng, K.; Kuang, Q.; Xie, Z.-X., *Appl. Catal. B-Environ.* **2021,** 291, 120101.

99. Chen, L.; Unocic, R. R.; Hoffman, A. S.; Hong, J.; Braga, A. H.; Bao, Z.; Bare, S. R.; Szanyi, J., *JACS Au* **2021,** 1, 977–986.

100. Wang, C.; Guan, E.; Wang, L.; Chu, X.; Wu, Z.; Zhang, J.; Yang, Z.; Jiang, Y.; Zhang, L.; Meng, X.; Gates, B. C.; Xiao, F.-S., *J. Am. Chem. Soc.* **2019,** 141, 8482–8488.

101. Li, S.; Xu, Y.; Chen, Y.; Li, W.; Lin, L.; Li, M.; Deng, Y.; Wang, X.; Ge, B.; Yang, C.; Yao, S.; Xie, J.; Li, Y.; Liu, X.; Ma, D., *Angew. Chem. Int. Ed.* **2017,** 56, 10761–10765.

102. Zhang, Y.; Zhang, Z.; Yang, X.; Wang, R.; Duan, H.; Shen, Z.; Li, L.; Su, Y.; Yang, R.; Zhang, Y.; Su, X.; Huang, Y.; Zhang, T., *Green Chem.* **2020,** 22, 6855–6861.

103. Li, X.; Lin, J.; Li, L.; Huang, Y.; Pan, X.; Collins, S. E.; Ren, Y.; Su, Y.; Kang, L.; Liu, X., *Angew. Chem. Int. Ed.* **2020,** 59, 19983−19989.

104. Xu, W.; Ramirez, P. J.; Stacchiola, D.; Rodriguez, J. A., *Catal. Lett.* **2014,** 144, 1418–1424.

105. Posada-Pérez, S.; Viñes, F.; Ramirez, P. J.; Vidal, A. B.; Rodriguez, J. A.; Illas, F., *Phys. Chem. Chem. Phys.* **2014,** 16, 14912–14921.

106. Porosoff, M. D.; Kattel, S.; Li, W.; Liu, P.; Chen, J. G., *Chem. Commun.* **2015,** 51, 6988–6991.

107. Liu, X.; Kunkel, C.; Ramírez de la Piscina, P.; Homs, N.; Viñes, F.; Illas, F., *ACS Catal.* **2017,** 7, 4323–4335.

108. Juneau, M.; Vonglis, M.; Hartvigsen, J.; Frost, L.; Bayerl, D.; Dixit, M.; Mpourmpakis, G.; Morse, J. R.; Baldwin, J. W.; Willauer, H. D.; Porosoff, M. D., *Energy Environ. Sci.* **2020,** 13, 2524–2539.

109. Figueras, M.; Gutiérrez, R. A.; Viñes, F.; Ramírez, P. J.; Rodriguez, J. A.; Illas, F., *ACS Catal.* **2021,** 11, 9679–9687.

110. Liu, X.; Pajares, A.; Calinao Matienzo, D. J. D.; Ramírez de la Piscina, P.; Homs, N., *Catal. Today* **2020,** 356, 384–389.

111. Abou Hamdan, M.; Nassereddine, A.; Checa, R.; Jahjah, M.; Pinel, C.; Piccolo, L.; Perret, N., *Front. Chem.* **2020,** 8.

112. Ma, Y.; Guo, Z.; Jiang, Q.; Wu, K.-H.; Gong, H.; Liu, Y., *J. Energy Chem.* **2020,** 50, 37–43.

113. Dasireddy, V. D. B. C.; Vengust, D.; Likozar, B.; Kovač, J.; Mrzel, A., *Renewable Energy* **2021,** 176, 251–261.

114. Pajares, A.; Prats, H.; Romero, A.; Viñes, F.; de la Piscina, P. R.; Sayós, R.; Homs, N.; Illas, F., *Appl. Catal. B-Environ.* **2020,** 267, 118719.

115. Ernst, K.-H.; Campbell, C. T.; Moretti, G., *J. Catal.* **1992,** 134, 66–74.

116. Yoshihara, J.; Campbell, C. T., *J. Catal.* **1996,** 161, 776–782.

117. Chen, C.-S.; Cheng, W.-H., *Catal. Lett.* **2002,** 83, 121–126.

118. Goguet, A.; Shekhtman, S. O.; Burch, R.; Hardacre, C.; Meunier, F. C.; Yablonsky, G. S., *J. Catal.* **2006,** 237, 102–110.

119. Gao, J.; Wu, Y.; Jia, C.; Zhong, Z.; Gao, F.; Yang, Y.; Liu, B., *Catal. Commun.* **2016,** 84, 147–150.

120. Kalamaras, C. M.; Americanou, S.; Efstathiou, A. M., *J. Catal.* **2011,** 279, 287–300.

121. Yang, Y.; Mims, C. A.; Disselkamp, R. S.; Peden, C. H. F.; Campbell, C. T., *Top. Catal.* **2009,** 52, 1440–1447.

122. Su, H.; Ye, Y.; Lee, K.-J.; Zeng, J.; Mun, B. S.; Crumlin, E. J., *J. Catal.* **2020,** 391, 123–131.

123. Falconer, J. L.; Zağli, A. E., *J. Catal.* **1980,** 62, 280–285.

124. Pu, T.; Shen, L.; Xu, J.; Peng, C.; Zhu, M., *AIChE Journal* **2022,** 68, e17458.

125. Feng, K.; Tian, J.; Guo, M.; Wang, Y.; Wang, S.; Wu, Z.; Zhang, J.; He, L.; Yan, B., *Appl. Catal. B-Environ.* **2021,** 292, 120191.

126. Jia, X.; Zhang, X.; Rui, N.; Hu, X.; Liu, C.-J., *Appl. Catal. B-Environ.* **2019,** 244, 159–169.

127. Zhou, R.; Rui, N.; Fan, Z.; Liu, C.-J., *Int. J. Hydrogen Energy* **2016,** 41, 22017–22025.

128. Wang, K.; Men, Y.; Liu, S.; Wang, J.; Li, Y.; Tang, Y.; Li, Z.; An, W.; Pan, X.; Li, L., *Fuel* **2021,** 304, 121388.

129. Li, J.; Lin, Y.; Pan, X.; Miao, D.; Ding, D.; Cui, Y.; Dong, J.; Bao, X., *ACS Catal.* **2019,** 9, 6342–6348.

130. Yan, X.; Liu, Y.; Zhao, B.; Wang, Z.; Wang, Y.; Liu, C.-j., *Int. J. Hydrogen Energy* **2013,** 38, 2283–2291.

131. Zhao, B.; Chen, Z.; Chen, Y.; Ma, X., *Int. J. Hydrogen Energy* **2017,** 42, 27073–27083.

132. Mihet, M.; Dan, M.; Barbu-Tudoran, L.; Lazar, M. D., *Catalysts* **2021,** 11.

133. Ye, R.-P.; Liao, L.; Reina, T. R.; Liu, J.; Chevella, D.; Jin, Y.; Fan, M.; Liu, J., *Fuel* **2021,** 285, 119151.

134. Zhang, X.; Sun, W.-j.; Chu, W., *J. Fuel Chem. Technol.* **2013,** 41, 96–101.

135. Guo, M.; Lu, G., *Catal. Commun.* **2014,** 54, 55–60.

136. Aziz, M. A. A.; Jalil, A. A.; Triwahyono, S.; Mukti, R. R.; Taufiq-Yap, Y. H.; Sazegar, M. R., *Appl. Catal. B-Environ.* **2014,** 147, 359–368.

137. Guilera, J.; del Valle, J.; Alarcón, A.; Díaz, J. A.; Andreu, T., *J. CO2 Util.* **2019,** 30, 11–17.

138. Danaci, S.; Protasova, L.; Lefevere, J.; Bedel, L.; Guilet, R.; Marty, P., *Catal. Today* **2016,** 273, 234–243.

139. Lin, J.; Ma, C.; Wang, Q.; Xu, Y.; Ma, G.; Wang, J.; Wang, H.; Dong, C.; Zhang, C.; Ding, M., *Appl. Catal. B-Environ.* **2019,** 243, 262–272.

140. Weber, S.; Abel, K. L.; Zimmermann, R. T.; Huang, X.; Bremer, J.; Rihko-Struckmann, L. K.; Batey, D.; Cipiccia, S.; Titus, J.; Poppitz, D.; Kübel, C.; Sundmacher, K.; Gläser, R.; Sheppard, T. L., *Catalysts* **2020,** 10.

141. Garbarino, G.; Kowalik, P.; Riani, P.; Antoniak-Jurak, K.; Pieta, P.; Lewalska-Graczyk, A.; Lisowski, W.; Nowakowski, R.; Busca, G.; Pieta, I. S., *Ind. Eng. Chem. Res.* **2021,** 60, 6554–6564.

142. Ashok, J.; Ang, M. L.; Kawi, S., *Catal. Today* **2017,** 281, 304–311.

143. Tada, S.; Shimizu, T.; Kameyama, H.; Haneda, T.; Kikuchi, R., *Int. J. Hydrogen Energy* **2012,** 37, 5527–5531.

144. Liu, J.; Wu, X.; Chen, Y.; Zhang, Y.; Zhang, T.; Ai, H.; Liu, Q., *Int. J. Hydrogen Energy* **2021.**

145. Cárdenas-Arenas, A.; Quindimil, A.; Davó-Quiñonero, A.; Bailón-García, E.; Lozano-Castelló, D.; De-La-Torre, U.; Pereda-Ayo, B.; González-Marcos, J. A.; González-Velasco, J. R.; Bueno-López, A., *Appl. Catal. B-Environ.* **2020,** 265, 118538.

146. Jangam, A.; Das, S.; Dewangan, N.; Hongmanorom, P.; Hui, W. M.; Kawi, S., *Catal. Today* **2020,** 358, 3–29.

147. Yan, B.; Zhao, B.; Kattel, S.; Wu, Q.; Yao, S.; Su, D.; Chen, J. G., *J. Catal.* **2019,** 374, 60–71.

148. Alrafei, B.; Polaert, I.; Ledoux, A.; Azzolina-Jury, F., *Catal. Today* **2020,** 346, 23–33.

149. Zhao, B.; Liu, P.; Li, S.; Shi, H.; Jia, X.; Wang, Q.; Yang, F.; Song, Z.; Guo, C.; Hu, J.; Chen, Z.; Yan, X.; Ma, X., *Appl. Catal. B-Environ.* **2020,** 278, 119307.

150. Garbarino, G.; Wang, C.; Cavattoni, T.; Finocchio, E.; Riani, P.; Flytzani-Stephanopoulos, M.; Busca, G., *Appl. Catal. B-Environ.* **2019,** 248, 286–297.

151. Gao, J.; Jiang, Q.; Liu, Y.; Liu, W.; Chu, W.; Su, D. S., *Nanoscale* **2018,** 10, 14207–14219.

152. Vrijburg, W. L.; Moioli, E.; Chen, W.; Zhang, M.; Terlingen, B. J. P.; Zijlstra, B.; Filot, I. A. W.; Züttel, A.; Pidko, E. A.; Hensen, E. J. M., *ACS Catal.* **2019,** 9, 7823–7839.

153. Vrijburg, W. L.; Garbarino, G.; Chen, W.; Parastaev, A.; Longo, A.; Pidko, E. A.; Hensen, E. J. M., *J. Catal.* **2020,** 382, 358–371.

154. Baysal, Z.; Kureti, S., *Appl. Catal. B-Environ.* **2020,** 262, 118300.

155. Kirchner, J.; Baysal, Z.; Kureti, S., *ChemCatChem* **2020,** 12, 981–988.

156. Kirchner, J.; Anolleck, J. K.; Lösch, H.; Kureti, S., *Appl. Catal. B-Environ.* **2018,** 223, 47–59.

157. Kirchner, J.; Zambrzycki, C.; Kureti, S.; Güttel, R., *Chem. Ing. Tech.* **2020,** 92, 603–607.

158. Iizuka, T.; Tanaka, Y.; Tanabe, K., *J. Catal.* **1982,** 76, 1–8.

159. Solymosi, F.; Erdöhelyi, A.; Bánsági, T., *J. Catal.* **1981,** 68, 371–382.

160. Scirè, S.; Crisafulli, C.; Maggiore, R.; Minicò, S.; Galvagno, S., *Catal. Lett.* **1998,** 51, 41–45.

161. Guo, Y.; Mei, S.; Yuan, K.; Wang, D.-J.; Liu, H.-C.; Yan, C.-H.; Zhang, Y.-W., *ACS Catal.* **2018,** 8, 6203–6215.

162. Navarro-Jaén, S.; Navarro, J. C.; Bobadilla, L. F.; Centeno, M. A.; Laguna, O. H.; Odriozola, J. A., *Appl. Surf. Sci.* **2019,** 483, 750–761.

163. Ashok, J.; Pati, S.; Hongmanorom, P.; Tianxi, Z.; Junmei, C.; Kawi, S., *Catal. Today* **2020,** 356, 471–489.

164. Ren, J.; Guo, H.; Yang, J.; Qin, Z.; Lin, J.; Li, Z., *Appl. Surf. Sci.* **2015,** 351, 504–516.

165. Zhu, M.; Tian, P.; Cao, X.; Chen, J.; Pu, T.; Shi, B.; Xu, J.; Moon, J.; Wu, Z.; Han, Y.-F., *Appl. Catal. B-Environ.* **2021,** 282, 119561.

166. Wang, F.; He, S.; Chen, H.; Wang, B.; Zheng, L.; Wei, M.; Evans, D. G.; Duan, X., *J. Am. Chem. Soc.* **2016,** 138, 6298–6305.

167. Xu, X.; Tong, Y.; Huang, J.; Zhu, J.; Fang, X.; Xu, J.; Wang, X., *Fuel* **2021,** 283, 118867.

168. Ye, R.-P.; Li, Q.; Gong, W.; Wang, T.; Razink, J. J.; Lin, L.; Qin, Y.-Y.; Zhou, Z.; Adidharma, H.; Tang, J.; Russell, A. G.; Fan, M.; Yao, Y.-G., *Appl. Catal. B-Environ.* **2020,** 268, 118474.

169. Wang, F.; Li, C.; Zhang, X.; Wei, M.; Evans, D. G.; Duan, X., *J. Catal.* **2015,** 329, 177–186.

170. Tackett, B. M.; Gomez, E.; Chen, J. G., *Nat. Catal.* **2019,** 2, 381-386.

171. Kotowski, W., *Chem. Techn.* **1963,** 15.

172. Sun, Q.; Zhang, Y.-L.; Chen, H.-Y.; Deng, J.-F.; Wu, D.; Chen, S.-Y., *J. Catal.* **1997,** 167, 92–105.

173. Grunwaldt, J. D.; Molenbroek, A. M.; Topsøe, N. Y.; Topsøe, H.; Clausen, B. S., *J. Catal.* **2000,** 194, 452–460.

174. Nakamura, J.; Choi, Y.; Fujitani, T., *Top. Catal.* **2003,** 22, 277–285.

175. Behrens, M.; Studt, F.; Kasatkin, I.; Kühl, S.; Hävecker, M.; Abild-Pedersen, F.; Zander, S.; Girgsdies, F.; Kurr, P.; Kniep, B.-L.; Tovar, M.; Fischer Richard, W.; Nørskov Jens, K.; Schlögl, R., *Science* **2012,** 336, 893–897.

176. Laudenschleger, D.; Ruland, H.; Muhler, M., *Nat. Commun.* **2020,** 11, 3898.

177. Beck, A.; Zabilskiy, M.; Newton, M. A.; Safonova, O.; Willinger, M. G.; van Bokhoven, J. A., *Nat. Catal.* **2021,** 4, 488-497.

178. Wang, Y.; Kattel, S.; Gao, W.; Li, K.; Liu, P.; Chen, J. G.; Wang, H., *Nat. Commun.* **2019,** 10, 1166.

179. Li, K.; Chen, J. G., *ACS Catal.* **2019,** 9, 7840–7861.

180. Tada, S.; Kayamori, S.; Honma, T.; Kamei, H.; Nariyuki, A.; Kon, K.; Toyao, T.; Shimizu, K.-i.; Satokawa, S., *ACS Catal.* **2018,** 8, 7809–7819.

181. Yang, M.; Yu, J.; Tong, X.; Sun, X.; Xu, H.; Sun, J., *Chem. Commun.* **2021,** 57, 7509–7512.

182. Samson, K.; Śliwa, M.; Socha, R. P.; Góra-Marek, K.; Mucha, D.; Rutkowska-Zbik, D.; Paul, J. F.; Ruggiero-Mikołajczyk, M.; Grabowski, R.; Słoczyński, J., *ACS Catal.* **2014,** 4, 3730–3741.

183. Larmier, K.; Liao, W.-C.; Tada, S.; Lam, E.; Verel, R.; Bansode, A.; Urakawa, A.; Comas-Vives, A.; Copéret, C., *Angew. Chem. Int. Ed.* **2017,** 56, 2318−2323.

184. Liu, T.; Hong, X.; Liu, G., *ACS Catal.* **2020,** 10, 93–102.

185. Ye, J.; Liu, C.; Mei, D.; Ge, Q., *ACS Catal.* **2013,** 3, 1296–1306.

186. Ye, J.; Liu, C.; Ge, Q., *J. Phys. Chem. C* **2012,** 116, 7817–7825.

187. Sun, K.; Fan, Z.; Ye, J.; Yan, J.; Ge, Q.; Li, Y.; He, W.; Yang, W.; Liu, C.-j., *J. CO2 Util.* **2015,** 12, 1–6.

188. Martin, O.; Martín, A. J.; Mondelli, C.; Mitchell, S.; Segawa, T. F.; Hauert, R.; Drouilly, C.; Curulla-Ferré, D.; Pérez-Ramírez, J., *Angew. Chem. Int. Ed.* **2016,** 55, 6261−6265.

189. Tsoukalou, A.; Abdala, P. M.; Stoian, D.; Huang, X.; Willinger, M.-G.; Fedorov, A.; Müller, C. R., *J. Am. Chem. Soc.* **2019,** 141, 13497−13505.

190. Frei, M. S.; Mondelli, C.; Cesarini, A.; Krumeich, F.; Hauert, R.; Stewart, J. A.; Curulla Ferré, D.; Pérez-Ramírez, J., *ACS Catal.* **2020,** 10, 1133–1145.

191. Chen, T.-y.; Cao, C.; Chen, T.-b.; Ding, X.; Huang, H.; Shen, L.; Cao, X.; Zhu, M.; Xu, J.; Gao, J.; Han, Y.-F., *ACS Catal.* **2019,** 9, 8785–8797.

192. Tsoukalou, A.; Abdala, P. M.; Armutlulu, A.; Willinger, E.; Fedorov, A.; Müller, C. R., *ACS Catal.* **2020,** 10, 10060−10067.

193. Wang, J.; Li, G.; Li, Z.; Tang, C.; Feng, Z.; An, H.; Liu, H.; Liu, T.; Li, C., *Sci. Adv.* **2017,** 3, e1701290.

194. Wang, J.; Tang, C.; Li, G.; Han, Z.; Li, Z.; Liu, H.; Cheng, F.; Li, C., *ACS Catal.* **2019,** 9, 10253–10259.

195. Huang, C.; Wu, Z.; Luo, H.; Zhang, S.; Shao, Z.; Wang, H.; Sun, Y., *ACS Appl. Energy Mater.* **2021,** 4, 9258–9266.

196. Ticali, P.; Salusso, D.; Ahmad, R.; Ahoba-Sam, C.; Ramirez, A.; Shterk, G.; Lomachenko, K. A.; Borfecchia, E.; Morandi, S.; Cavallo, L.; Gascon, J.; Bordiga, S.; Olsbye, U., *Catal. Sci. Technol.* **2021,** 11, 1249–1268.

197. Wang, X.; Wang, Y.; Yang, C.; Yi, Y.; Wang, X.; Liu, F.; Cao, J.; Pan, H., *Appl. Catal. A-Gen.* **2020,** 595, 117507.

198. Han, Z.; Tang, C.; Sha, F.; Tang, S.; Wang, J.; Li, C., *J. Catal.* **2021,** 396, 242–250.

199. Temvuttirojn, C.; Poo-arporn, Y.; Chanlek, N.; Cheng, C. K.; Chong, C. C.; Limtrakul, J.; Witoon, T., *Ind. Eng. Chem. Res.* **2020,** 59, 5525–5535.

200. Chen, Y.; Li, H.; Zhao, W.; Zhang, W.; Li, J.; Li, W.; Zheng, X.; Yan, W.; Zhang, W.; Zhu, J.; Si, R.; Zeng, J., *Nat. Commun.* **2019,** 10, 1885.

201. Gutterød, E. S.; Lazzarini, A.; Fjermestad, T.; Kaur, G.; Manzoli, M.; Bordiga, S.; Svelle, S.; Lillerud, K. P.; Skúlason, E.; Øien-Ødegaard, S.; Nova, A.; Olsbye, U., *J. Am. Chem. Soc.* **2020,** 142, 999–1009.

202. Wang, L.; Guan, E.; Wang, Y.; Wang, L.; Gong, Z.; Cui, Y.; Meng, X.; Gates, B. C.; Xiao, F.-S., *Nat. Commun.* **2020,** 11, 1033.

203. Wang, L.; Zhang, W.; Zheng, X.; Chen, Y.; Wu, W.; Qiu, J.; Zhao, X.; Zhao, X.; Dai, Y.; Zeng, J., *Nature Energy* **2017,** 2, 869–876.

204. Li, C.-S.; Melaet, G.; Ralston, W. T.; An, K.; Brooks, C.; Ye, Y.; Liu, Y.-S.; Zhu, J.; Guo, J.; Alayoglu, S.; Somorjai, G. A., *Nat. Commun.* **2015,** 6, 6538.

205. Hu, J.; Yu, L.; Deng, J.; Wang, Y.; Cheng, K.; Ma, C.; Zhang, Q.; Wen, W.; Yu, S.; Pan, Y.; Yang, J.; Ma, H.; Qi, F.; Wang, Y.; Zheng, Y.; Chen, M.; Huang, R.; Zhang, S.; Zhao, Z.; Mao, J.; Meng, X.; Ji, Q.; Hou, G.; Han, X.; Bao, X.; Wang, Y.; Deng, D., *Nat. Catal.* **2021,** 4, 242-250.

206. Cherevotan, A.; Raj, J.; Dheer, L.; Roy, S.; Sarkar, S.; Das, R.; Vinod, C. P.; Xu, S.; Wells, P.; Waghmare, U. V.; Peter, S. C., *ACS Energy Lett.* **2021,** 6, 509−516.

207. Kattel, S.; Yan, B.; Yang, Y.; Chen, J. G.; Liu, P., *J. Am. Chem. Soc.* **2016,** 138, 12440–12450.

208. Kattel, S.; Ramírez Pedro, J.; Chen Jingguang, G.; Rodriguez José, A.; Liu, P., *Science* **2017,** 355, 1296-1299.

209. Graciani, J.; Mudiyanselage, K.; Xu, F.; Baber Ashleigh, E.; Evans, J.; Senanayake Sanjaya, D.; Stacchiola Darío, J.; Liu, P.; Hrbek, J.; Sanz Javier, F.; Rodriguez José, A., *Science* **2014,** 345, 546–550.

210. Frei, M. S.; Capdevila-Cortada, M.; García-Muelas, R.; Mondelli, C.; López, N.; Stewart, J. A.; Curulla Ferré, D.; Pérez-Ramírez, J., *J. Catal.* **2018,** 361, 313–321.

211. Riedel, T.; Claeys, M.; Schulz, H.; Schaub, G.; Nam, S.-S.; Jun, K.-W.; Choi, M.-J.; Kishan, G.; Lee, K.-W., *Appl. Catal. A-Gen.* **1999,** 186, 201–213.

212. Mutschler, R.; Moioli, E.; Luo, W.; Gallandat, N.; Züttel, A., *J. Catal.* **2018,** 366, 139–149.

213. Schulz, H.; Schaub, G.; Claeys, M.; Riedel, T., *Appl. Catal. A-Gen.* **1999,** 186, 215–227.

214. Zhang, Y.; Cao, C.; Zhang, C.; Zhang, Z.; Liu, X.; Yang, Z.; Zhu, M.; Meng, B.; Xu, J.; Han, Y.-F., *J. Catal.* **2019,** 378, 51–62.

215. Zhang, Y.; Fu, D.; Liu, X.; Zhang, Z.; Zhang, C.; Shi, B.; Xu, J.; Han, Y.-F., *ChemCatChem* **2018,** 10, 1272−1276.

216. Zhu, J.; Wang, P.; Zhang, X.; Zhang, G.; Li, R.; Li, W.; Senftle Thomas, P.; Liu, W.; Wang, J.; Wang, Y.; Zhang, A.; Fu, Q.; Song, C.; Guo, X., *Sci. Adv.* **2022,** 8, eabm3629.

217. Zhao, B.; Sun, M.; Chen, F.; Shi, Y.; Yu, Y.; Li, X.; Zhang, B., *Angew. Chem. Int. Ed.* **2021,** 60, 4496–4500.

218. Skrypnik, A. S.; Yang, Q.; Matvienko, A. A.; Bychkov, V. Y.; Tulenin, Y. P.; Lund, H.; Petrov, S. A.; Kraehnert, R.; Arinchtein, A.; Weiss, J., *Appl. Catal. B-Environ.* **2021,** 291, 120121.

219. Lopez Luna, M.; Timoshenko, J.; Kordus, D.; Rettenmaier, C.; Chee, S. W.; Hoffman, A. S.; Bare, S. R.; Shaikhutdinov, S.; Roldan Cuenya, B., *ACS Catal.* **2021,** 11, 6175–6185.

220. Arinchtein, A.; Ye, M.-Y.; Geske, M.; Frisch, M.; Kraehnert, R., *Catalysts* **2021,** 11.

221. Riedel, T.; Schulz, H.; Schaub, G.; Jun, K.-W.; Hwang, J.-S.; Lee, K.-W., *Top. Catal.* **2003,** 26, 41–54.

222. Schulz, H.; Riedel, T.; Schaub, G., *Top. Catal.* **2005,** 32, 117–124.

223. Rodemerck, U.; Holeňa, M.; Wagner, E.; Smejkal, Q.; Barkschat, A.; Baerns, M., *ChemCatChem* **2013,** 5, 1948–1955.

224. Visconti, C. G.; Martinelli, M.; Falbo, L.; Infantes-Molina, A.; Lietti, L.; Forzatti, P.; Iaquaniello, G.; Palo, E.; Picutti, B.; Brignoli, F., *Appl. Catal. B-Environ.* **2017,** 200, 530–542.

225. Amoyal, M.; Vidruk-Nehemya, R.; Landau, M. V.; Herskowitz, M., *J. Catal.* **2017,** 348, 29–39.

226. Fischer, N.; Henkel, R.; Hettel, B.; Iglesias, M.; Schaub, G.; Claeys, M., *Catal. Lett.* **2016,** 146, 509–517.

227. Liang, B.; Duan, H.; Sun, T.; Ma, J.; Liu, X.; Xu, J.; Su, X.; Huang, Y.; Zhang, T., *ACS Sustain. Chem. Eng.* **2018,** 7, 925−932.

228. Ramirez, A.; Gevers, L.; Bavykina, A.; Ould-Chikh, S.; Gascon, J., *ACS Catal.* **2018,** 8, 9174−9182.

229. Shafer, W. D.; Jacobs, G.; Graham, U. M.; Hamdeh, H. H.; Davis, B. H., *J. Catal.* **2019,** 369, 239–248.

230. Han, Y.; Fang, C.; Ji, X.; Wei, J.; Ge, Q.; Sun, J., *ACS Catal.* **2020,** 10, 12098–12108.

231. Liu, X.; Zhang, C.; Tian, P.; Xu, M.; Cao, C.; Yang, Z.; Zhu, M.; Xu, J., *J. Phys. Chem. C* **2021,** 125, 7637–7646.

232. Aitbekova, A.; Goodman, E. D.; Wu, L.; Boubnov, A.; Hoffman, A. S.; Genc, A.; Cheng, H.; Casalena, L.; Bare, S. R.; Cargnello, M., *Angew. Chem. Int. Ed.* **2019,** 58, 17451−17457.

233. Gnanamani, M. K.; Jacobs, G.; Hamdeh, H. H.; Shafer, W. D.; Liu, F.; Hopps, S. D.; Thomas, G. A.; Davis, B. H., *ACS Catal.* **2016,** 6, 913–927.

234. Hwang, S.-M.; Han, S. J.; Park, H.-G.; Lee, H.; An, K.; Jun, K.-W.; Kim, S. K., *ACS Catal.* **2021,** 11, 2267–2278.

235. Zhang, C.; Cao, C.; Zhang, Y.; Liu, X.; Xu, J.; Zhu, M.; Tu, W.; Han, Y.-F., *ACS Catal.* **2021,** 11, 2121–2133.

236. Zhang, C.; Xu, M.; Yang, Z.; Zhu, M.; Gao, J.; Han, Y.-F., *Appl. Catal. B-Environ.* **2021,** 295, 120287.

237. Wang, J.; You, Z.; Zhang, Q.; Deng, W.; Wang, Y., *Catal. Today* **2013,** 215, 186–193.

238. Xu, Y.; Zhai, P.; Deng, Y.; Xie, J.; Liu, X.; Wang, S.; Ma, D., *Angew. Chem. Int. Ed.* **2020,** 59, 21736–21744.

239. Yang, H.; Zhang, C.; Gao, P.; Wang, H.; Li, X.; Zhong, L.; Wei, W.; Sun, Y., *Catal. Sci. Technol.* **2017,** 7, 4580–4598.

240. Yang, C.; Zhao, H.; Hou, Y.; Ma, D., *J. Am. Chem. Soc.* **2012,** 134, 15814–15821.

241. Galvis, H. M. T.; Bitter, J. H.; Khare, C. B.; Ruitenbeek, M.; Dugulan, A. I.; de Jong, K. P., *Science* **2012,** 335, 835–838.

242. Van Der Laan, G. P.; Beenackers, A. A. C. M., *Catal. Rev.* **1999,** 41, 255–318.

243. de Smit, E.; Weckhuysen, B. M., *Chem. Soc. Rev.* **2008,** 37, 2758–2781.

244. Davis, B. H., *Fuel Process. Technol.* **2001,** 71, 157–166.

245. Vannice, M. A., *Catal. Rev.* **1976,** 14, 153–191.

246. Huff, G. A.; Satterfield, C. N., *Ind. Eng. Chem. Process Des. Dev.* **1984,** 23, 696–705.

247. Biloen, P.; Helle, J. N.; Sachtler, W. M. H., *J. Catal.* **1979,** 58, 95–107.

248. Dictor, R. A.; Bell, A. T., *J. Catal.* **1986,** 97, 121–136.

249. Henrici-Olivé, G.; Olivé, S., *Angewandte Chemie International Edition in English* **1976,** 15, 136–141.

250. van Santen, R. A.; Markvoort, A. J., *ChemCatChem* **2013,** 5, 3384–3397.

251. Jiao, F.; Li, J.; Pan, X.; Xiao, J.; Li, H.; Ma, H.; Wei, M.; Pan, Y.; Zhou, Z.; Li, M.; Miao, S.; Li, J.; Zhu, Y.; Xiao, D.; He, T.; Yang, J.; Qi, F.; Fu, Q.; Bao, X., *Science* **2016,** 351, 1065–1068.

252. Cheng, K.; Gu, B.; Liu, X.; Kang, J.; Zhang, Q.; Wang, Y., *Angew. Chem. Int. Ed.* **2016,** 55, 4725−4728.

253. Tian, P.; Wei, Y.; Ye, M.; Liu, Z., *ACS Catal.* **2015,** 5, 1922–1938.

254. Dang, S.; Li, S.; Yang, C.; Chen, X.; Li, X.; Zhong, L.; Gao, P.; Sun, Y., *ChemSusChem* **2019,** 12, 3582–3591.

255. Liu, X.; Wang, M.; Yin, H.; Hu, J.; Cheng, K.; Kang, J.; Zhang, Q.; Wang, Y., *ACS Catal.* **2020,** 10, 8303–8314.

256. Wang, S.; Zhang, L.; Zhang, W.; Wang, P.; Qin, Z.; Yan, W.; Dong, M.; Li, J.; Wang, J.; He, L.; Olsbye, U.; Fan, W., *Chem* **2020,** 6, 3344–3363.

257. Zhang, J.; Zhang, M.; Chen, S.; Wang, X.; Zhou, Z.; Wu, Y.; Zhang, T.; Yang, G.; Han, Y.; Tan, Y., *Chem. Commun.* **2019,** 55, 973–976.

258. Wang, Y.; Tan, L.; Tan, M.; Zhang, P.; Fang, Y.; Yoneyama, Y.; Yang, G.; Tsubaki, N., *ACS Catal.* **2019,** 9, 895–901.

259. Zhou, C.; Shi, J.; Zhou, W.; Cheng, K.; Zhang, Q.; Kang, J.; Wang, Y., *ACS Catal.* **2020,** 10, 302–310.

260. Dai, W.; Wang, C.; Dyballa, M.; Wu, G.; Guan, N.; Li, L.; Xie, Z.; Hunger, M., *ACS Catal.* **2015,** 5, 317–326.

261. Liang, J.; Li, H.; Zhao, S.; Guo, W.; Wang, R.; Ying, M., *Appl. Cata.* **1990,** 64, 31–40.

262. Sun, Q.; Xie, Z.; Yu, J., *Natl. Sci. Rev.* **2017,** 5, 542-558.

263. Niu, X.; Gao, J.; Wang, K.; Miao, Q.; Dong, M.; Wang, G.; Fan, W.; Qin, Z.; Wang, J., *Fuel Process. Technol.* **2017,** 157, 99–107.

264. Niu, X.; Gao, J.; Miao, Q.; Dong, M.; Wang, G.; Fan, W.; Qin, Z.; Wang, J., *Microporous Mesoporous Mater.* **2014,** 197, 252–261.

265. Zhang, X.; Zhang, A.; Jiang, X.; Zhu, J.; Liu, J.; Li, J.; Zhang, G.; Song, C.; Guo, X., *J. CO2 Util.* **2019,** 29, 140–145.

266. Olsbye, U.; Svelle, S.; Bjørgen, M.; Beato, P.; Janssens, T. V. W.; Joensen, F.; Bordiga, S.; Lillerud, K. P., *Angew. Chem. Int. Ed.* **2012,** 51, 5810−5831.

267. Yarulina, I.; Chowdhury, A. D.; Meirer, F.; Weckhuysen, B. M.; Gascon, J., *Nat. Catal.* **2018,** 1, 398-411.

268. Stöcker, M., *Microporous Mesoporous Mater.* **1999,** 29, 3–48.

269. KNAPMAN, K., *Chimica oggi* **2001,** 19, 9–12.

270. Kondratenko, E. V.; Schlüter, M.; Baerns, M.; Linke, D.; Holena, M., *Catal. Sci. Technol.* **2015,** 5, 1668–1677.

271. Masood, H.; Toe, C. Y.; Teoh, W. Y.; Sethu, V.; Amal, R., *ACS Catal.* **2019,** 9, 11774–11787.

272. Schmack, R.; Friedrich, A.; Kondratenko, E. V.; Polte, J.; Werwatz, A.; Kraehnert, R., *Nat. Commun.* **2019,** 10, 441.

273. Smith, A.; Keane, A.; Dumesic, J. A.; Huber, G. W.; Zavala, V. M., *Appl. Catal. B-Environ.* **2020,** 263, 118257.

274. Medford, A. J.; Kunz, M. R.; Ewing, S. M.; Borders, T.; Fushimi, R., *ACS Catal.* **2018,** 8, 7403–7429.

275. Takahashi, K.; Takahashi, L.; Miyazato, I.; Fujima, J.; Tanaka, Y.; Uno, T.; Satoh, H.; Ohno, K.; Nishida, M.; Hirai, K.; Ohyama, J.; Nguyen, T. N.; Nishimura, S.; Taniike, T., *ChemCatChem* **2019,** 11, 1146–1152.

276. Mittasch, A.; Frankenburg, W. In *Advances in catalysis*, Elsevier: 1950; Vol. 2, p 81−104.

277. Goodman, D. W., *Chem. Rev.* **1995,** 95, 523–536.

278. Chen, W. L., *Journal of Chemical Information and Modeling* **2006,** 46, 2230–2255.

279. Sarkisov, L.; Kim, J., *Chem. Eng. Sci.* **2015,** 121, 322–330.

280. Toyao, T.; Maeno, Z.; Takakusagi, S.; Kamachi, T.; Takigawa, I.; Shimizu, K.-i., *ACS Catal.* **2019,** 10, 2260–2297.

281. Hummelshøj, J. S.; Abild-Pedersen, F.; Studt, F.; Bligaard, T.; Nørskov, J. K., *Angew. Chem. Int. Ed.* **2012,** 51, 272−274.

282. Zavyalova, U.; Holena, M.; Schlögl, R.; Baerns, M., *ChemCatChem* **2011,** 3, 1935–1947.

283. Odabaşı, Ç.; Günay, M. E.; Yıldırım, R., *Int. J. Hydrogen Energy* **2014,** 39, 5733–5746.

284. Fait, M. J. G.; Ricci, A.; Holena, M.; Rabeah, J.; Pohl, M. M.; Linke, D.; Kondratenko, E. V., *Catal. Sci. Technol.* **2019,** 9, 5111–5121.

285. Muraoka, K.; Sada, Y.; Miyazaki, D.; Chaikittisilp, W.; Okubo, T., *Nat. Commun.* **2019,** 10, 4459.

286. Sigman, M. S.; Harper, K. C.; Bess, E. N.; Milo, A., *Acc. Chem. Res.* **2016,** 49, 1292–1301.

287. Zhou, Z.; Li, X.; Zare, R. N., *ACS Cent. Sci.* **2017,** 3, 1337–1344.

288. Suzuki, K.; Toyao, T.; Maeno, Z.; Takakusagi, S.; Shimizu, K.-i.; Takigawa, I., *ChemCatChem* **2019,** 11, 4537–4547.

289. Wang, M.; Zhu, H., *ACS Catal.* **2021,** 11, 3930–3937.

290. Weiß, J.; Rautenberg, C.; Rall, T.; Kubis, C.; Kondratenko, E.; Bentrup, U.; Brückner, A., *Chemistry–Methods* **2021,** 1, 308–314.

291. Gleaves, J. T.; Yablonskii, G. S.; Phanawadee, P.; Schuurman, Y., *Appl. Catal. A-Gen.* **1997,** 160, 55–88.

292. Pérez-Ramírez, J.; Kondratenko, E. V., *Catal. Today* **2007,** 121, 160–169.

293. Rothaemel, M.; Baerns, M., *Ind. Eng. Chem. Res.* **1996,** 35, 1556–1565.

294. Soick, M.; Wolf, D.; Baerns, M., *Chem. Eng. Sci.* **2000,** 55, 2875–2882.

295. Reining, S.; Kondratenko, E. V.; Kalevaru, N. V.; Martin, A., *ACS Catal.* **2016,** 6, 4621–4629.

296. Shannon, S. L.; Goodwin Jr, J. G., *Chem. Rev.* **1995,** 95, 677–695.

297. Liu, J.; Sun, Y.; Jiang, X.; Zhang, A.; Song, C.; Guo, X., *J. CO2 Util.* **2018,** 25, 120–127.

298. Torres Galvis, H. M.; Bitter, J. H.; Davidian, T.; Ruitenbeek, M.; Dugulan, A. I.; de Jong, K. P., *J. Am. Chem. Soc.* **2012,** 134, 16207–16215.

299. Geng, S.; Jiang, F.; Xu, Y.; Liu, X., *ChemCatChem* **2016,** 8, 1303–1307.

300. Jiang, F.; Liu, B.; Geng, S.; Xu, Y.; Liu, X., *Catal. Sci. Technol.* **2018,** 8, 4097–4107.

301. Liu, J.; Zhang, A.; Jiang, X.; Liu, M.; Sun, Y.; Song, C.; Guo, X., *ACS Sustain. Chem. Eng.* **2018,** 6, 10182−10190.

302. Choi, Y. H.; Jang, Y. J.; Park, H.; Kim, W. Y.; Lee, Y. H.; Choi, S. H.; Lee, J. S., *Appl. Catal. B-Environ.* **2017,** 202, 605–610.

303. You, Z.; Deng, W.; Zhang, Q.; Wang, Y., *Chin. J. Catal.* **2013,** 34, 956–963.

304. Wei, J.; Sun, J.; Wen, Z.; Fang, C.; Ge, Q.; Xu, H., *Catal. Sci. Technol.* **2016,** 6, 4786–4793.

305. Gu, H.; Ding, J.; Zhong, Q.; Zeng, Y.; Song, F., *Int. J. Hydrogen Energy* **2019,** 44, 11808–11816.

306. Cui, X.; Gao, P.; Li, S.; Yang, C.; Liu, Z.; Wang, H.; Zhong, L.; Sun, Y., *ACS Catal.* **2019,** 9, 3866–3876.

307. de Smit, E.; Weckhuysen, B. M., *Chem. Soc. Rev.* **2008,** 37, 2758–2781.

308. de Smit, E.; Cinquini, F.; Beale, A. M.; Safonova, O. V.; van Beek, W.; Sautet, P.; Weckhuysen, B. M., *J. Am. Chem. Soc.* **2010,** 132, 14928–14941.

309. Schlögl, R. In *Handbook of Heterogeneous Catalysis*, G. Ertl, H. Knözinger, Schüth, F., Weitkamp, J., Eds. Wiley-VCH: Weinheim, 2008; pp 2501–2575.

310. Somorjai, G. A.; Materer, N., *Top. Catal.* **1994,** 1, 215–231.

311. Zhang, Q.; Kang, J.; Wang, Y., *ChemCatChem* **2010,** 2, 1030–1058.

312. Trovarelli, A.; Deleitenburg, C.; Dolcetti, G.; Lorca, J. L., *J. Catal.* **1995,** 151, 111–124.

313. Panagiotopoulou, P.; Christodoulakis, A.; Kondarides, D. I.; Boghosian, S., *J. Catal.* **2006,** 240, 114–125.

314. Zhang, Y.; Zhao, Y.; Otroshchenko, T.; Lund, H.; Pohl, M.-M.; Rodemerck, U.; Linke, D.; Jiao, H.; Jiang, G.; Kondratenko, E. V., *Nat. Commun.* **2018,** 9, 3794.

315. Sikora, E.; Prekob, Á.; Halasi, G.; Vanyorek, L.; Pekker, P.; Kristály, F.; Varga, T.; Kiss, J.; Kónya, Z.; Viskolcz, B., *ChemistryOpen* **2018,** 7, 789–796.

316. Yang, S.-C.; Pang, S. H.; Sulmonetti, T. P.; Su, W.-N.; Lee, J.-F.; Hwang, B.-J.; Jones, C. W., *ACS Catal.* **2018,** 8, 12056–12066.

317. Li, Y.; Cai, X.; Chen, S.; Zhang, H.; Zhang, K. H. L.; Hong, J.; Chen, B.; Kuo, D.-H.; Wang, W., *ChemSusChem* **2018,** 11, 1040–1047.

318. Kim, D. H.; Park, J. L.; Park, E. J.; Kim, Y. D.; Uhm, S., *ACS Catal.* **2014,** 4, 3117–3122.

319. Castells-Gil, J.; Ould-Chikh, S.; Ramírez, A.; Ahmad, R.; Prieto, G.; Gómez, A. R.; Garzón-Tovar, L.; Telalovic, S.; Liu, L.; Genovese, A.; Padial, N. M.; Aguilar-Tapia, A.; Bordet, P.; Cavallo, L.; Martí-Gastaldo, C.; Gascon, J., *Chem Catal.* **2021,** 1, 364–382.

320. Niemantsverdriet, J. W.; van der Kraan, A. M., *J. Catal.* **1981,** 72, 385–388.

321. Bianchi, D.; Borcar, S.; Teule-Gay, F.; Bennett, C., *J. Catal.* **1983,** 82, 442–456.

322. Xu, J.; Bartholomew, C. H., *J. Phys. Chem. B* **2005,** 109, 2392–2403.

323. Chun, D. H.; Park, J. C.; Hong, S. Y.; Lim, J. T.; Kim, C. S.; Lee, H.-T.; Yang, J.-I.; Hong, S.; Jung, H., *J. Catal.* **2014,** 317, 135–143.

324. Koeken, A. C. J.; Torres Galvis, H. M.; Davidian, T.; Ruitenbeek, M.; de Jong, K. P., *Angew. Chem. Int. Ed.* **2012,** 51, 7190−7193.

325. Peña, D.; Cognigni, A.; Neumayer, T.; van Beek, W.; Jones, D. S.; Quijada, M.; Rønning, M., *Appl. Catal. A-Gen.* **2018,** 554, 10–23.

326. Tang, L.; He, L.; Wang, Y.; Chen, B.; Xu, W.; Duan, X.; Lu, A.-H., *Appl. Catal. B-Environ.* **2021,** 284, 119753.

327. Paalanen, P. P.; van Vreeswijk, S. H.; Weckhuysen, B. M., *ACS Catal.* **2020,** 10, 9837–9855.

328. den Breejen, J. P.; Radstake, P. B.; Bezemer, G. L.; Bitter, J. H.; Frøseth, V.; Holmen, A.; de Jong, K. P., *J. Am. Chem. Soc.* **2009,** 131, 7197–7203.

329. Lohitharn, N.; Goodwin, J. G., *J. Catal.* **2008,** 260, 7–16.

330. Linstrom, P. J., *NIST chemistry webbook*. http://webbook. nist. gov: 2005.

331. Socrates, G., *Infrared and Raman characteristic group frequencies: tables and charts*. John Wiley & Sons: Chichester, 2004.

332. Liu, X.-W.; Zhao, S.; Meng, Y.; Peng, Q.; Dearden, A. K.; Huo, C.-F.; Yang, Y.; Li, Y.-W.; Wen, X.-D., *Sci. Rep.* **2016,** 6, 26184.

333. Wang, J.; Huang, S.; Howard, S.; Muir, B. W.; Wang, H.; Kennedy, D. F.; Ma, X., *ACS Catal.* **2019,** 9, 7976–7983.

334. Cheng, J.; Hu, P.; Ellis, P.; French, S.; Kelly, G.; Lok, C. M., *J. Phys. Chem. C* **2010,** 114, 1085–1093.

335. Chang, Q.; Zhang, C.; Liu, C.; Wei, Y.; Cheruvathur, A. V.; Dugulan, A. I.; Niemantsverdriet, J. W.; Liu, X.; He, Y.; Qing, M.; Zheng, L.; Yun, Y.; Yang, Y.; Li, Y., *ACS Catal.* **2018,** 8, 3304–3316.

Appendix

Figure A-1 A graph photo of in-house developed setup with eight continuous-flow fixed-bed quartz reactors for H_2-TPP, CO_2/CO-TPD, and TPH tests.
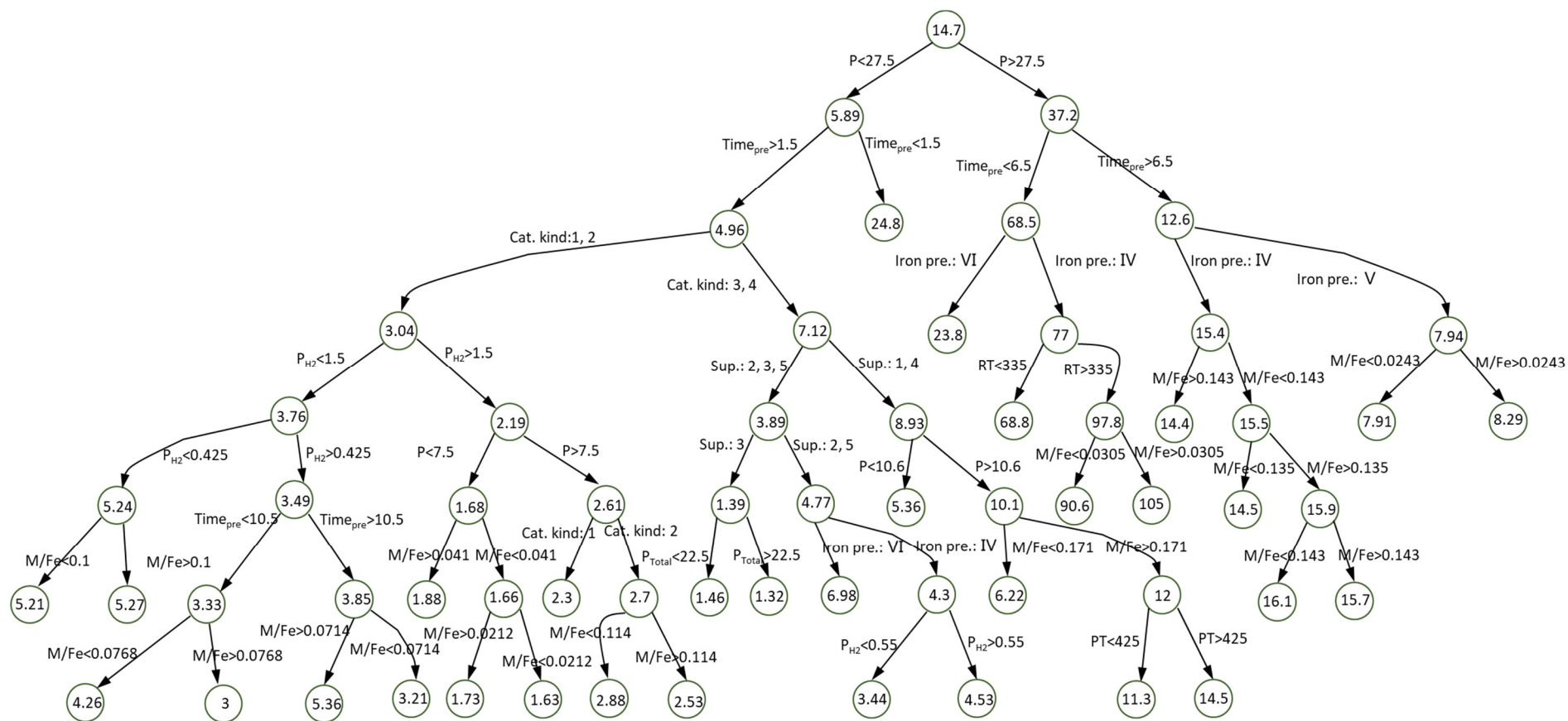
Figure A-2 Full regression tree of the first group of descriptors for the overall CO_2 reaction rate. Catalyst kind (Cat. kind) numbers: (1) bulk & non-promoted, (2) bulk & promoted, (3) supported & non-promoted and (4) supported & promoted. Iron precursors (Iron pre.): (I) ammonium ferric citrate, (II) iron(III) chloride, (III) commercial oxide, (IV) iron nitrate, (V) iron(III) chloride/iron(II) chloride and (VI) iron(III) acetylacetonate. Support materials (Sup.): (1) Al_2O_3, (2) Carbon materials, (3) SiO_2, (4) TiO_2 and (5) ZrO_2.
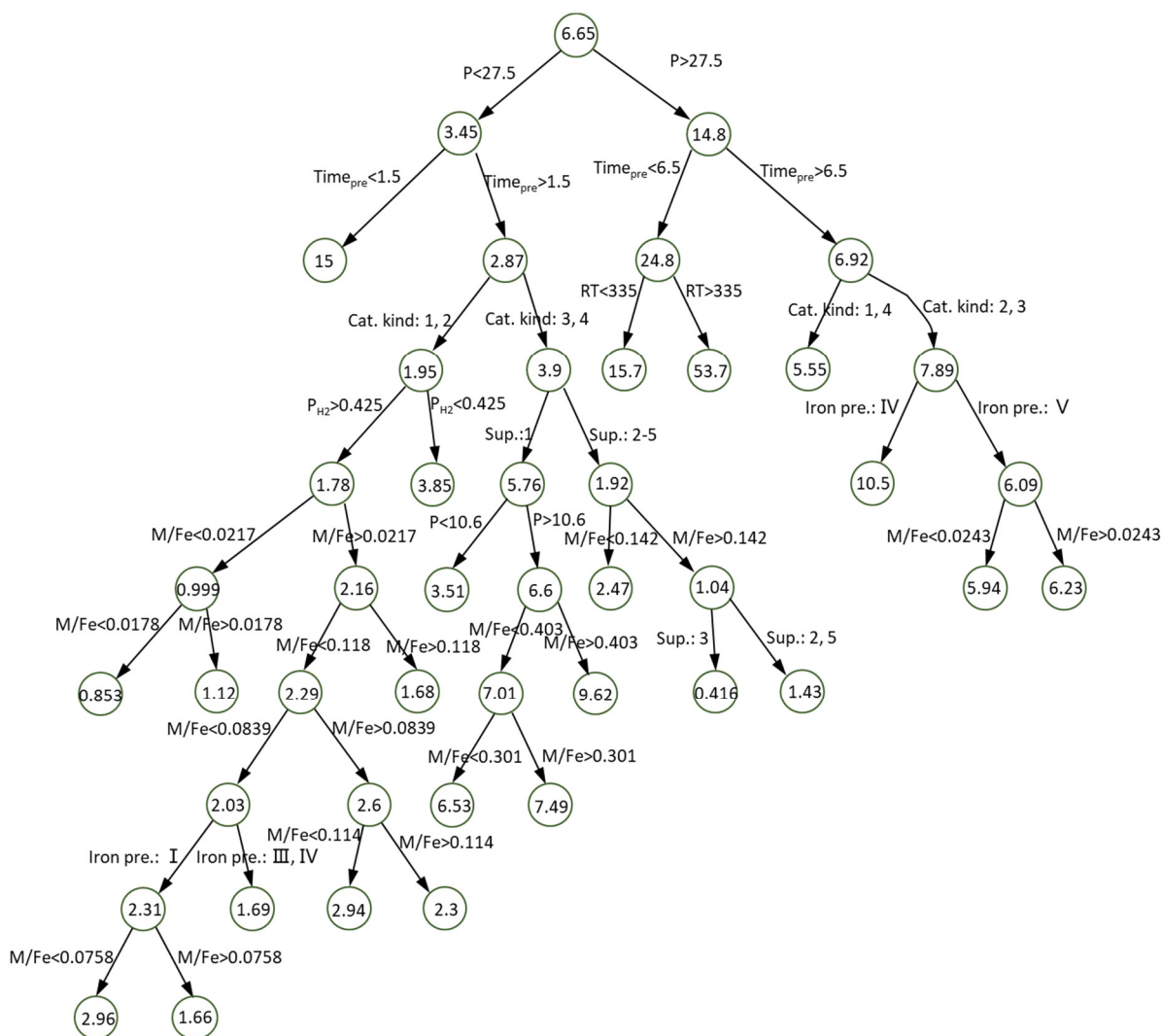
Figure A-3 Complete regression tree regarding to the first group of descriptors (see Scheme 4-1) for formation rate of C$_{2+}$- hydrocarbons. Catalyst kind (Cat. kind) numbers: (1) bulk & non-promoted, (2) bulk & promoted, (3) supported & non-promoted and (4) supported & promoted. Iron precursors (Iron pre.): (I) ammonium ferric citrate, (II) iron(III) chloride, (III) commercial oxide, (IV) iron nitrate, (V) iron(III) chloride/iron(II) chloride and (VI) iron(III) acetylacetonate. Support materials (Sup.): (1) Al$_2$O$_3$, (2) Carbon materials, (3) SiO$_2$, (4) TiO$_2$ and (5) ZrO$_2$.
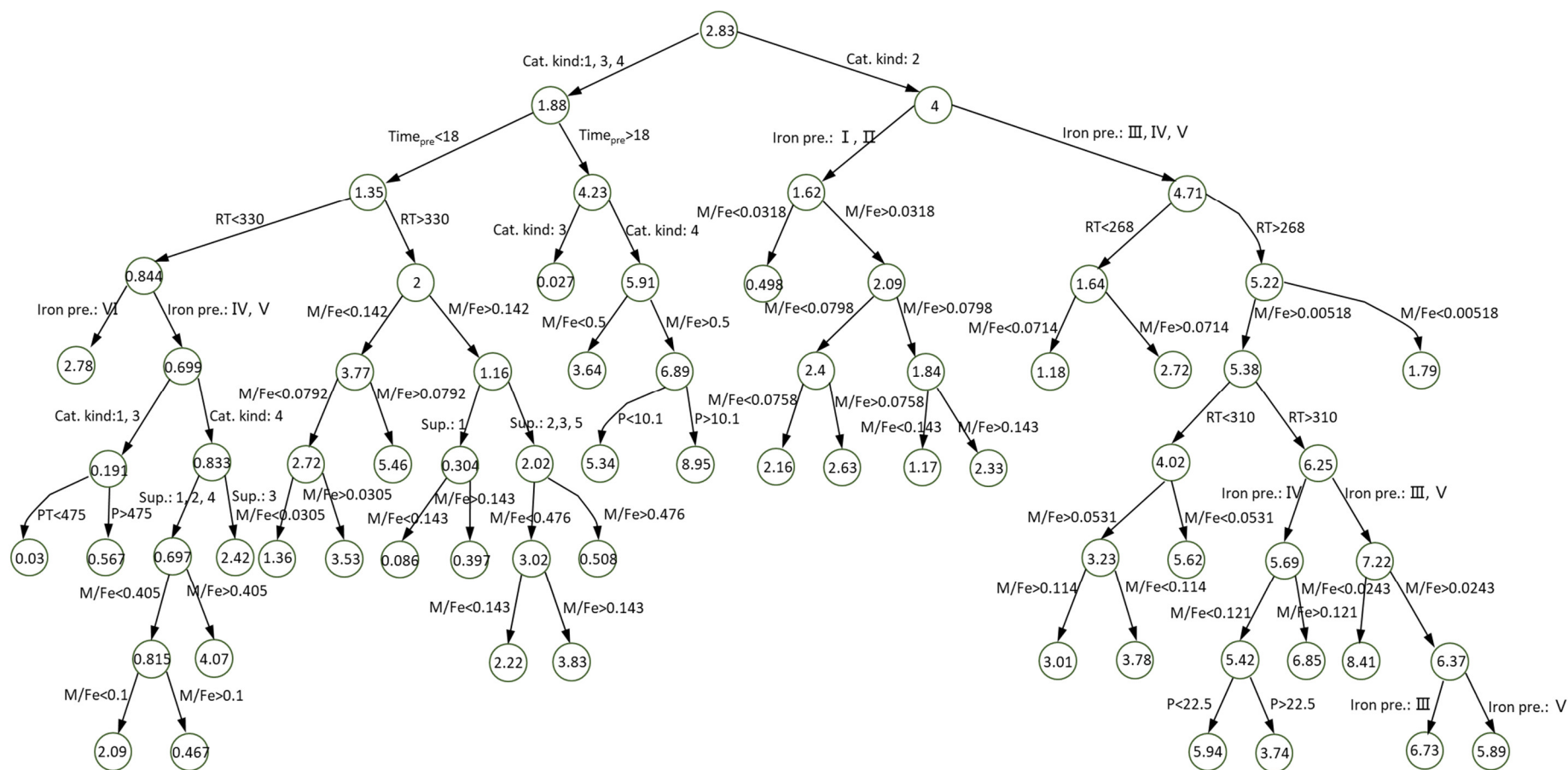
Figure A-4 Complete regression tree regarding to the first group of descriptors (see Scheme 4-1) for the ratio of olefins to paraffins. Catalyst kind (Cat. kind) numbers: (1) bulk & non-promoted, (2) bulk & promoted, (3) supported & non-promoted and (4) supported & promoted. Iron precursors (Iron pre.): (I) ammonium ferric citrate, (II) iron(III) chloride, (III) commercial oxide, (IV) iron nitrate, (V) iron(III) chloride/iron(II) chloride and (VI) iron(III) acetylacetonate. Support materials (Sup.): (1) Al_2O_3, (2) Carbon materials, (3) SiO_2, (4) TiO_2 and (5) ZrO_2.
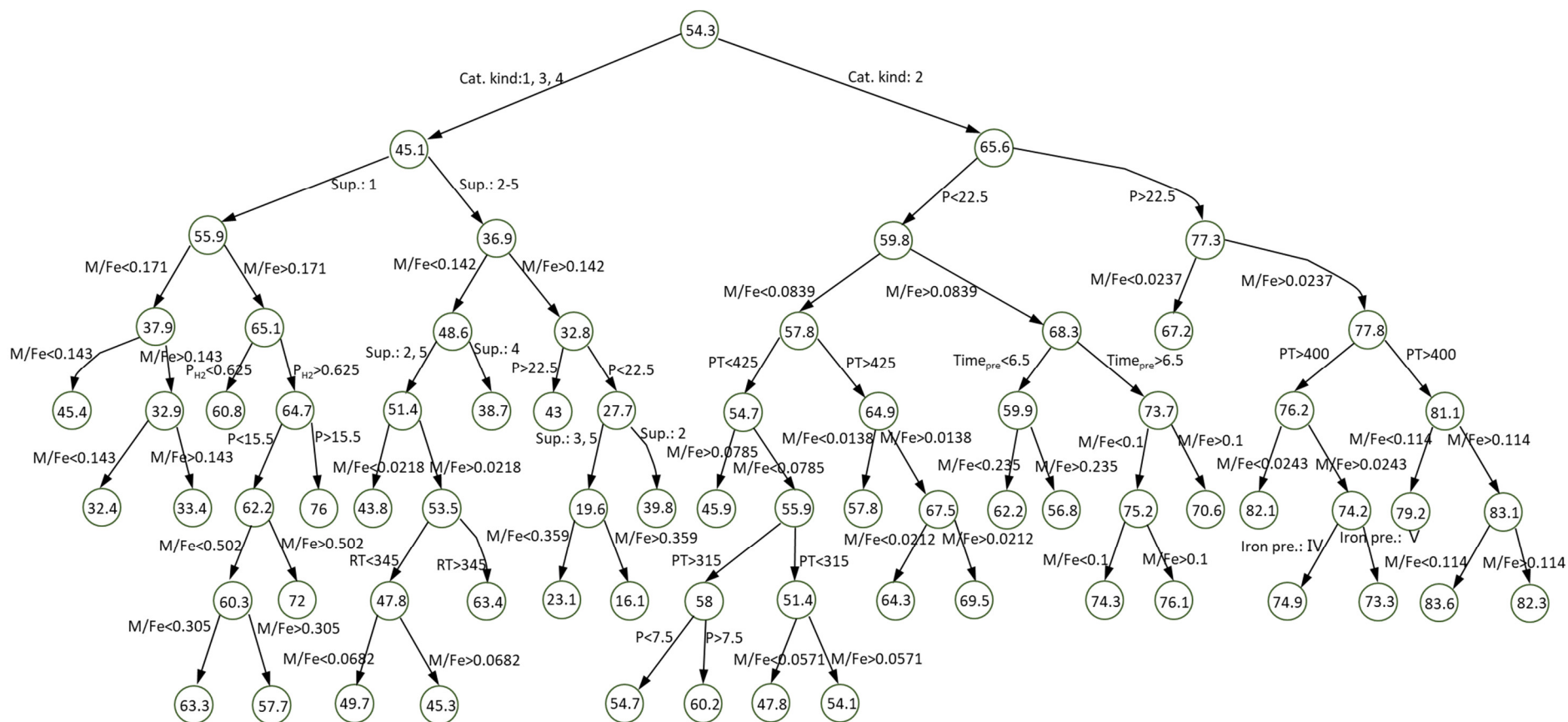
Figure A-5 Complete regression tree regarding to the first group of descriptors (see Scheme 4-1) for selectivity of C_{2+}- hydrocarbons. Catalyst kind (Cat. kind) numbers: (1) bulk & non-promoted, (2) bulk & promoted, (3) supported & non-promoted and (4) supported & promoted. Iron precursors (Iron pre.): (I) ammonium ferric citrate, (II) iron(III) chloride, (III) commercial oxide, (IV) iron nitrate, (V) iron(III) chloride/iron(II) chloride and (VI) iron(III) acetylacetonate. Support materials (Sup.): (1) Al_2O_3, (2) Carbon materials, (3) SiO_2, (4) TiO_2 and (5) ZrO_2.
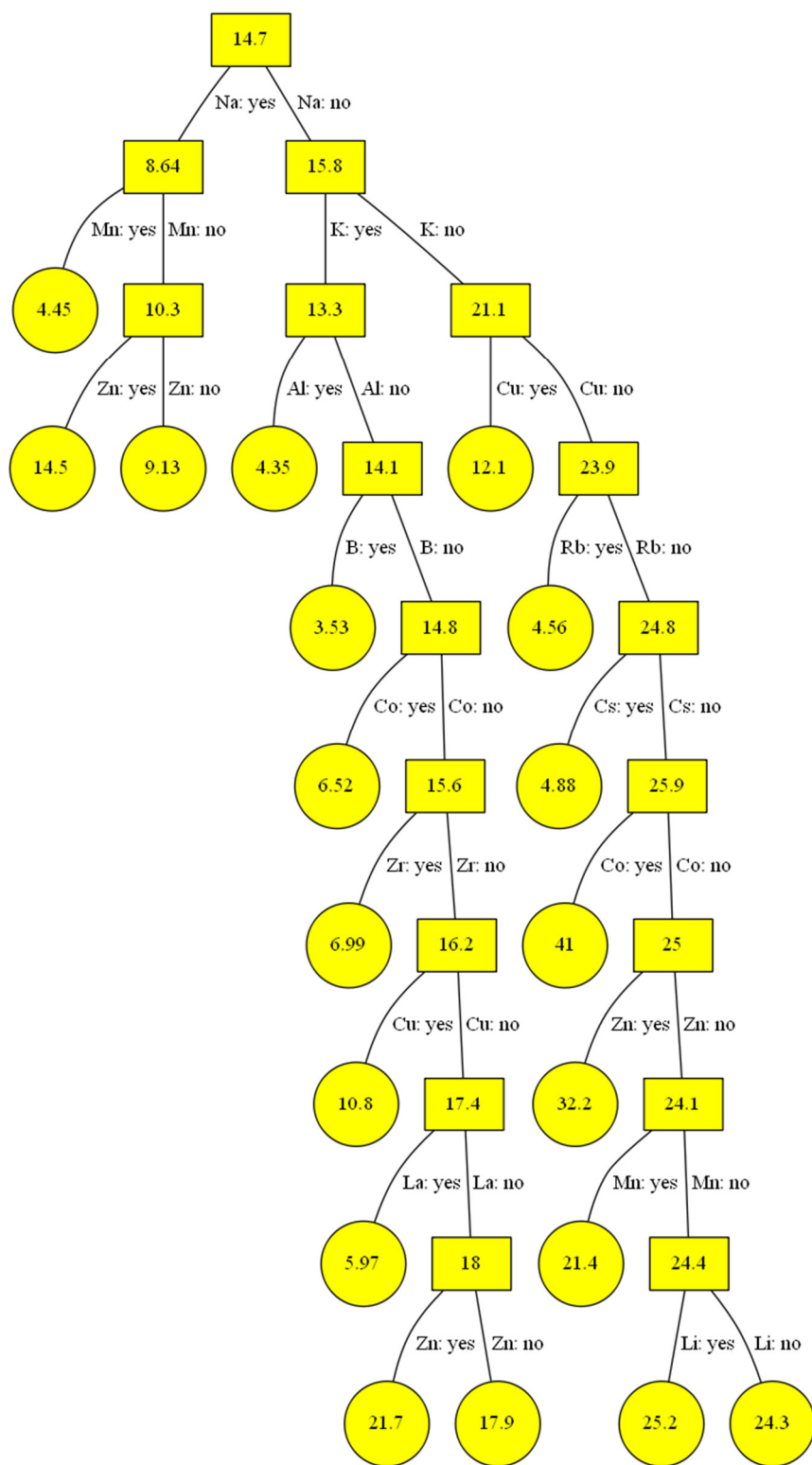
Figure A-6 Complete regression tree regarding to the second group of descriptors (see Scheme 4-1) for CO_2 reaction rate.
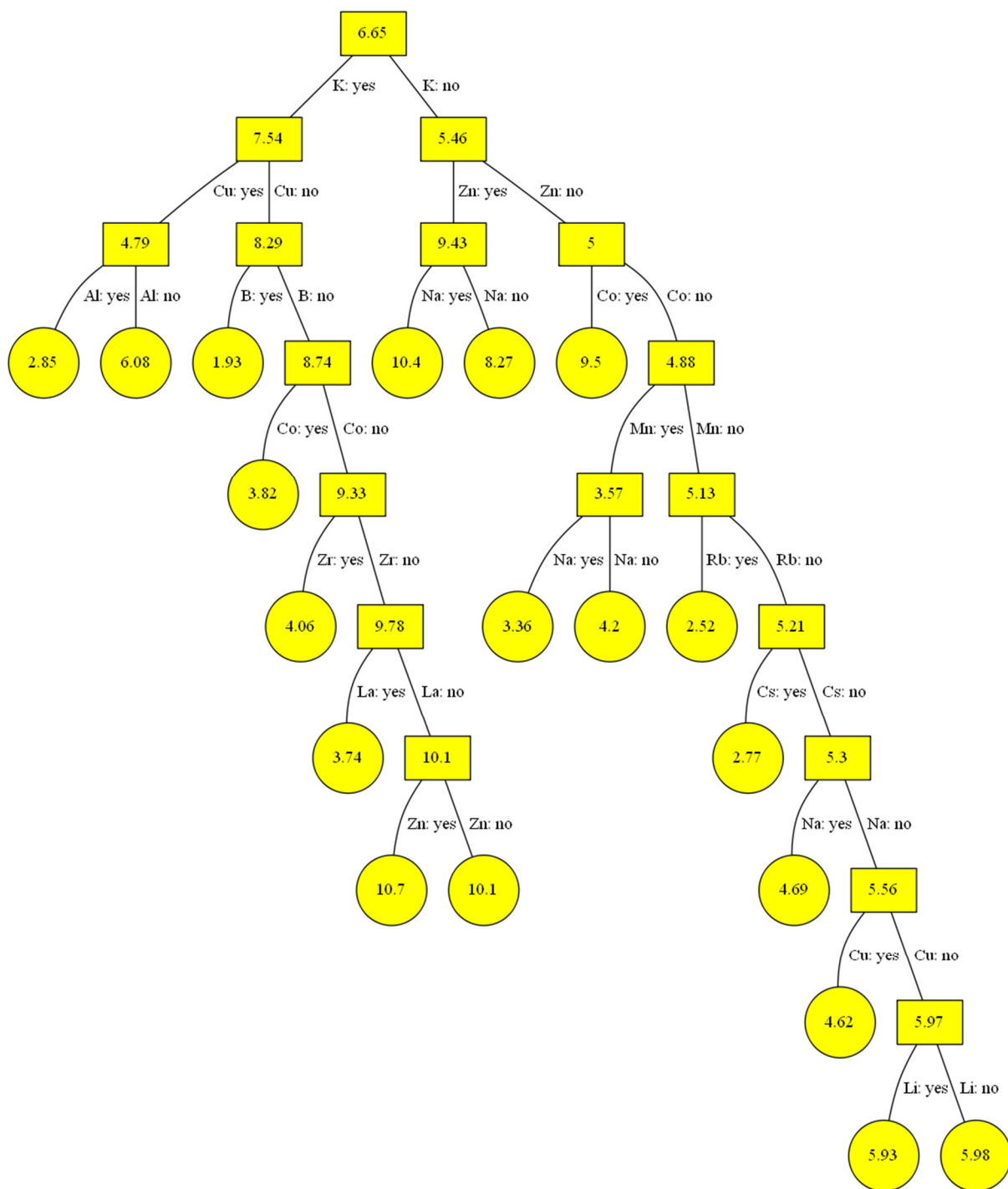
Figure A-7 Complete regression tree regarding to the second group of descriptors (see Scheme 4-1) for formation rate of C_{2+}- hydrocarbons.
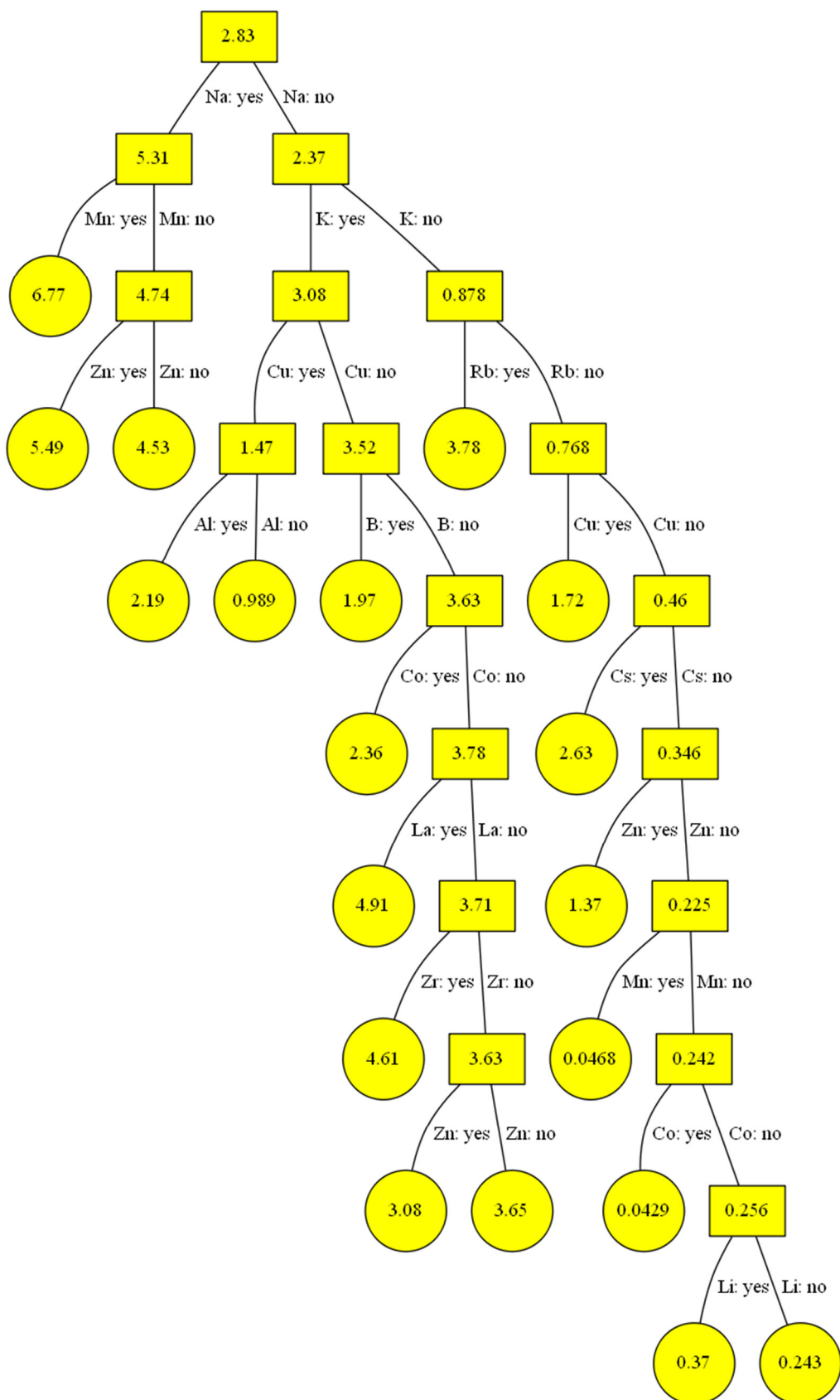
Figure A-8 Complete regression tree regarding to the second group of descriptors (see Scheme 4-1) for the ratio of olefins to paraffins in the C_2-C_4 range hydrocarbons.
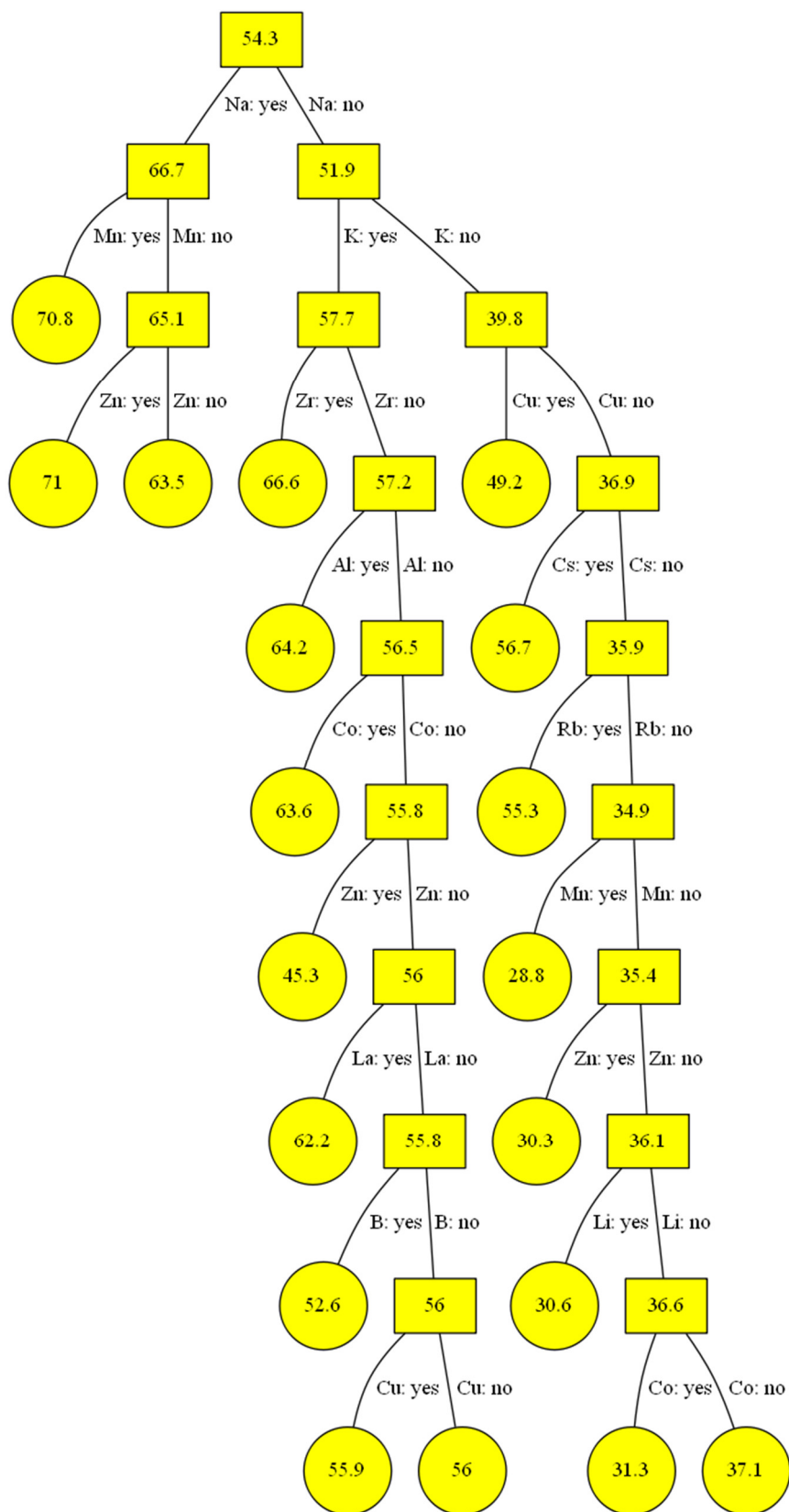
Figure A-9 Complete regression tree regarding to the second group of descriptors (see Scheme 4-1) for selectivity of C_{2+}- hydrocarbons.
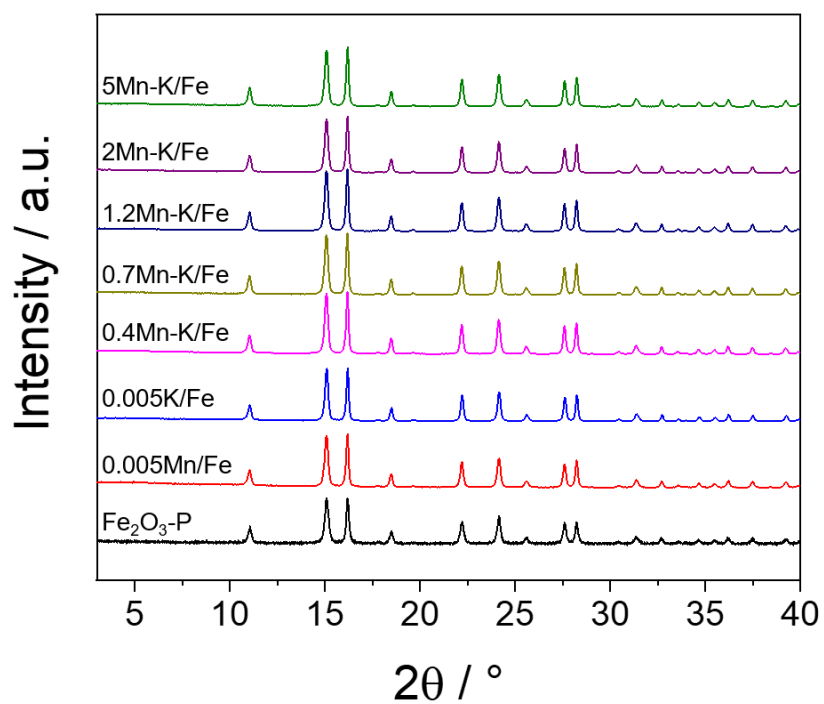
Figure A-10 XRD patterns of fresh catalysts.
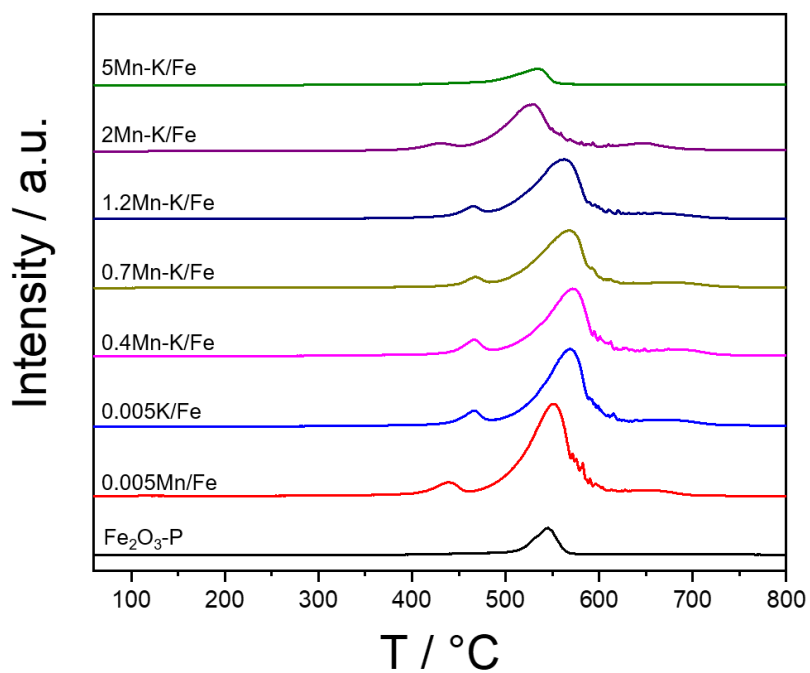
Figure A-11 CO$_2$-TPD profiles of spent catalysts.
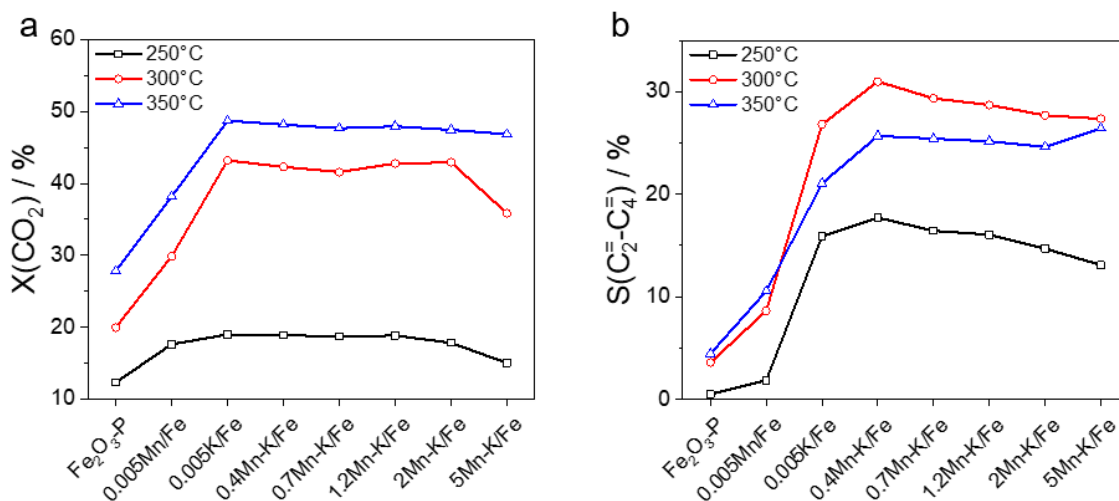
Figure A-12 Effect of Mn, K and Mn/K molar ratio in xMn-K/Fe catalysts on (a) CO_2 conversion ($X(CO_2)$) and (b) the selectivity to C_2-C_4 olefins ($S(C_2^=$-$C_4^=)$) at different reaction temperatures. Reaction conditions: 15 bar; 1160 mL h^{-1} g$_{cat}^{-1}$; H_2:CO_2:N_2 = 3:1:0.3; 45 h on-stream at each temperature.
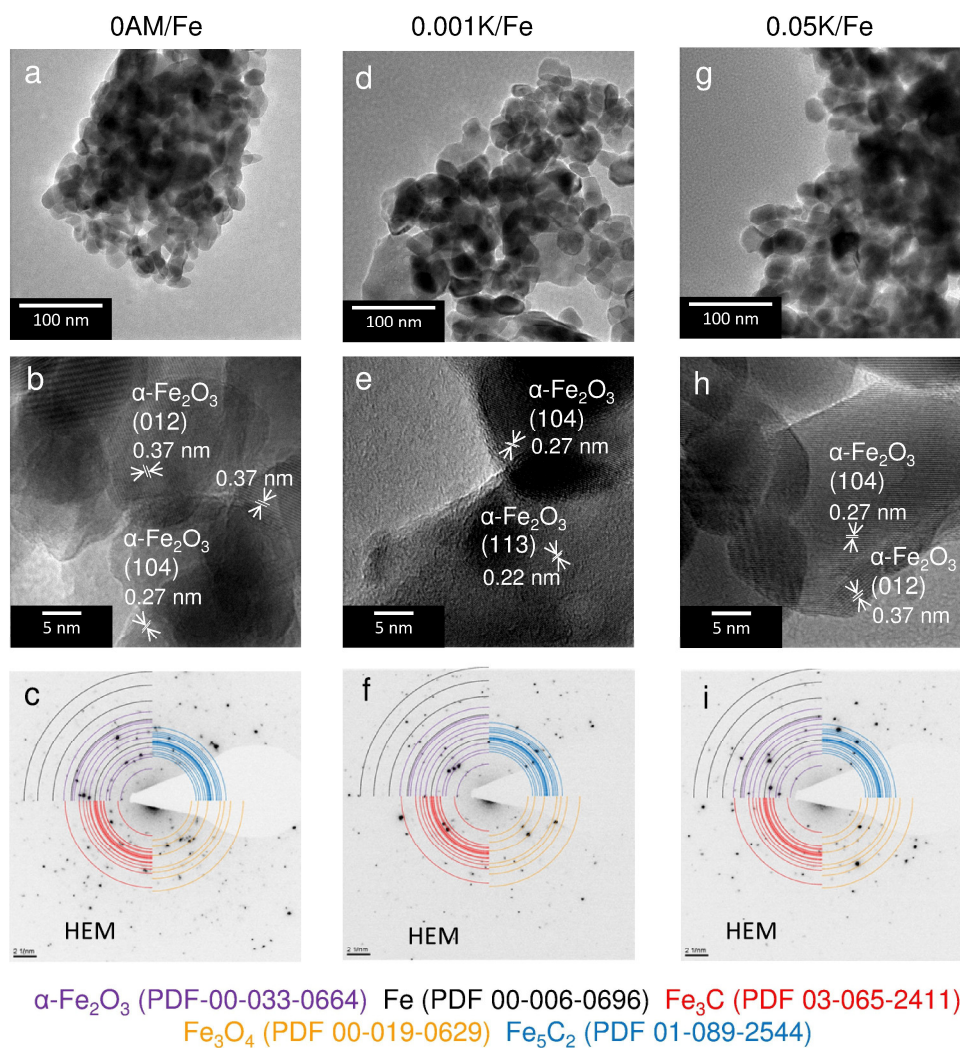
Figure A-13 TEM images and selected area electron diffraction (SAED) of (a–c) 0AM/Fe, (d–f) 0.001K/Fe, and (g–i) 0.05K/Fe.
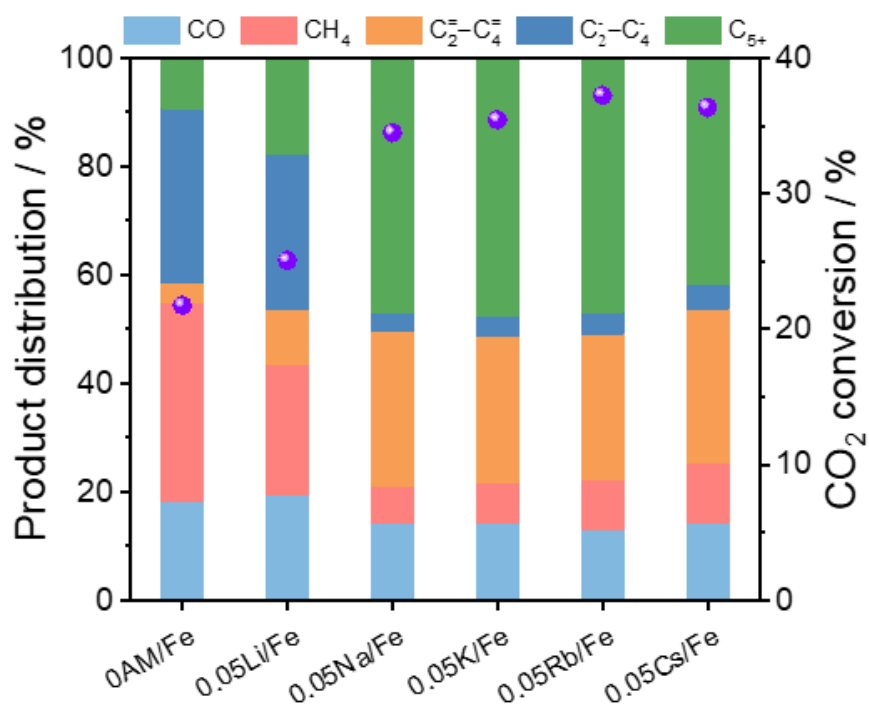
Figure A-14 The CO_2 conversion and detailed product distribution over xK/Fe and 0.05AM/Fe. The spent catalysts and catalytic performance were obtained after 90 h on reaction stream at 300 °C using a feed $3H_2/CO_2/0.3N_2$ with a GHSV of 1160 mL g_{cat}^{-1} h^{-1}; the catalysts were initially reduced at 400 °C in $1H_2/1N_2$ for 2 h.
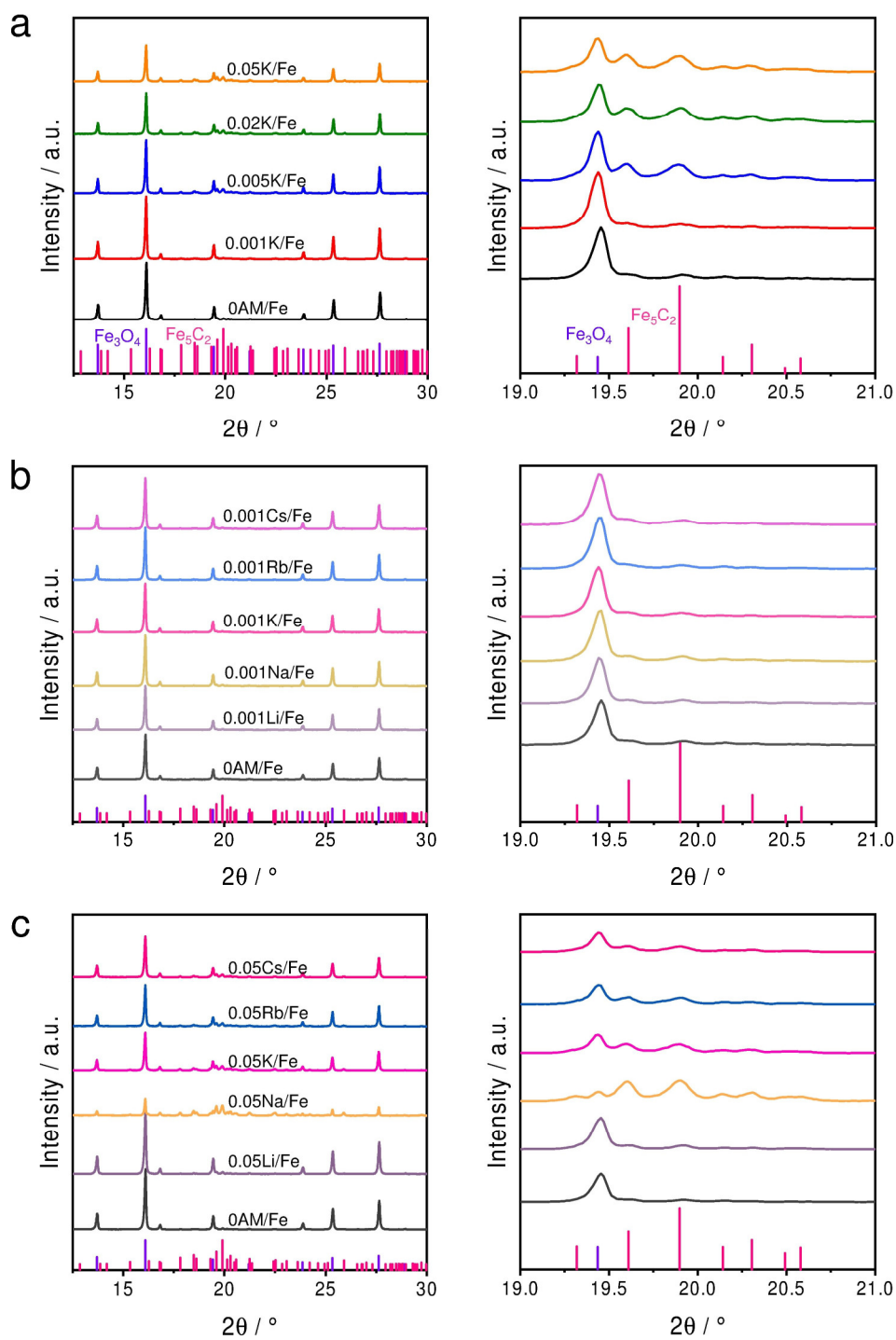
Figure A-15 X-ray diffraction (XRD) patterns of spent catalysts with (a) different loadings of K, or different alkali metal promoters in (b) 0.001AM/Fe or (c) 0.05AM/Fe.

a 0AM/Fe   b 0.001Li/Fe   c 0.001K/Fe   d 0.05K/Fe
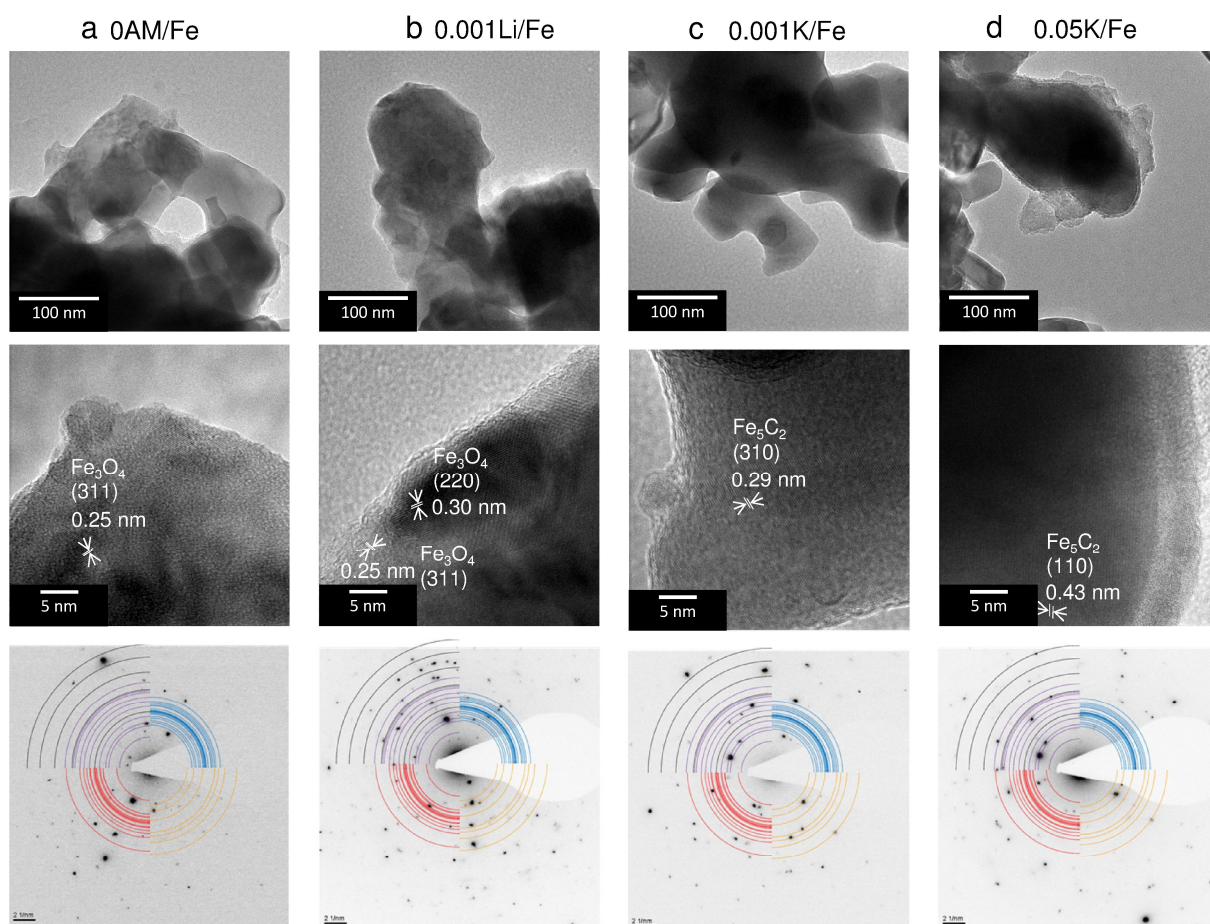
α-Fe$_2$O$_3$ (PDF-00-033-0664) Fe (PDF 00-006-0696) Fe$_3$C (PDF 03-065-2411)
Fe$_3$O$_4$ (PDF 00-019-0629) Fe$_5$C$_2$ (PDF 01-089-2544)

Figure A-16 TEM images selected area electron diffraction (SAED) of spent catalysts of (a) 0AM/Fe, (b) 0.001Li/Fe, (c) 0.001K/Fe and (d) 0.05K/Fe.
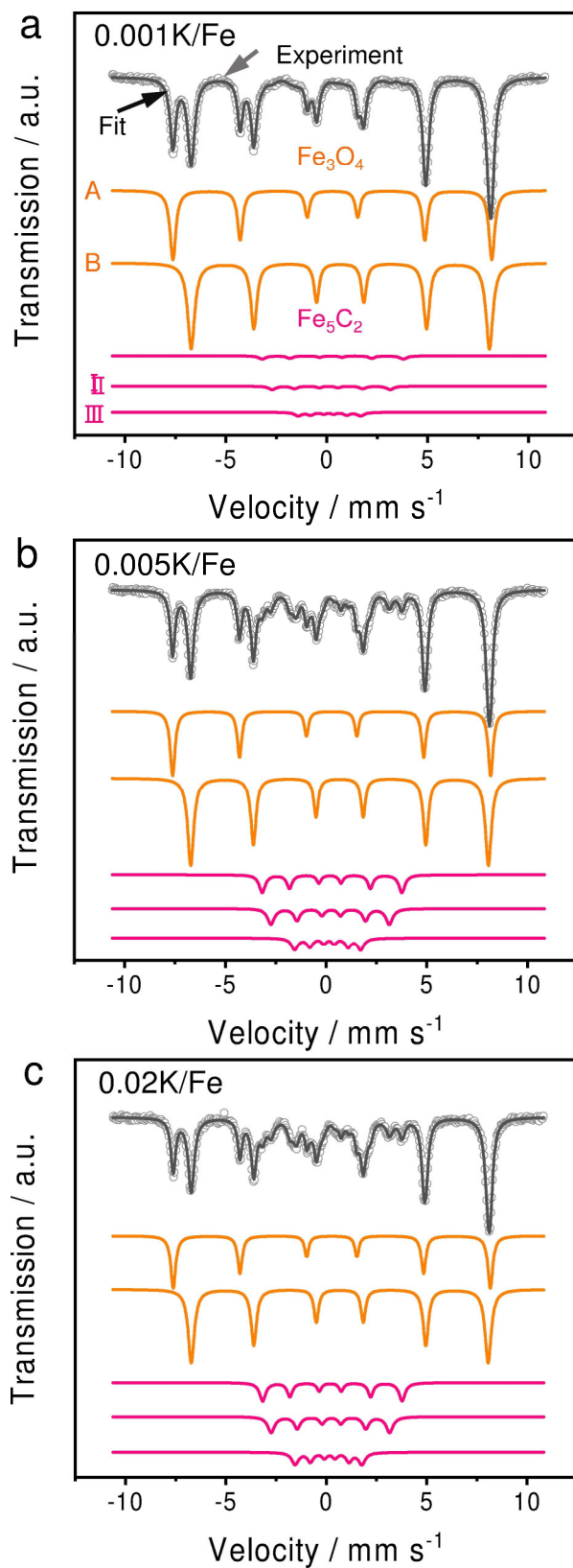
Figure A-17 Mössbauer spectra of (a) 0.001K/Fe, (b) 0.005K/Fe and (c) 0.02K/Fe spent catalysts.

131
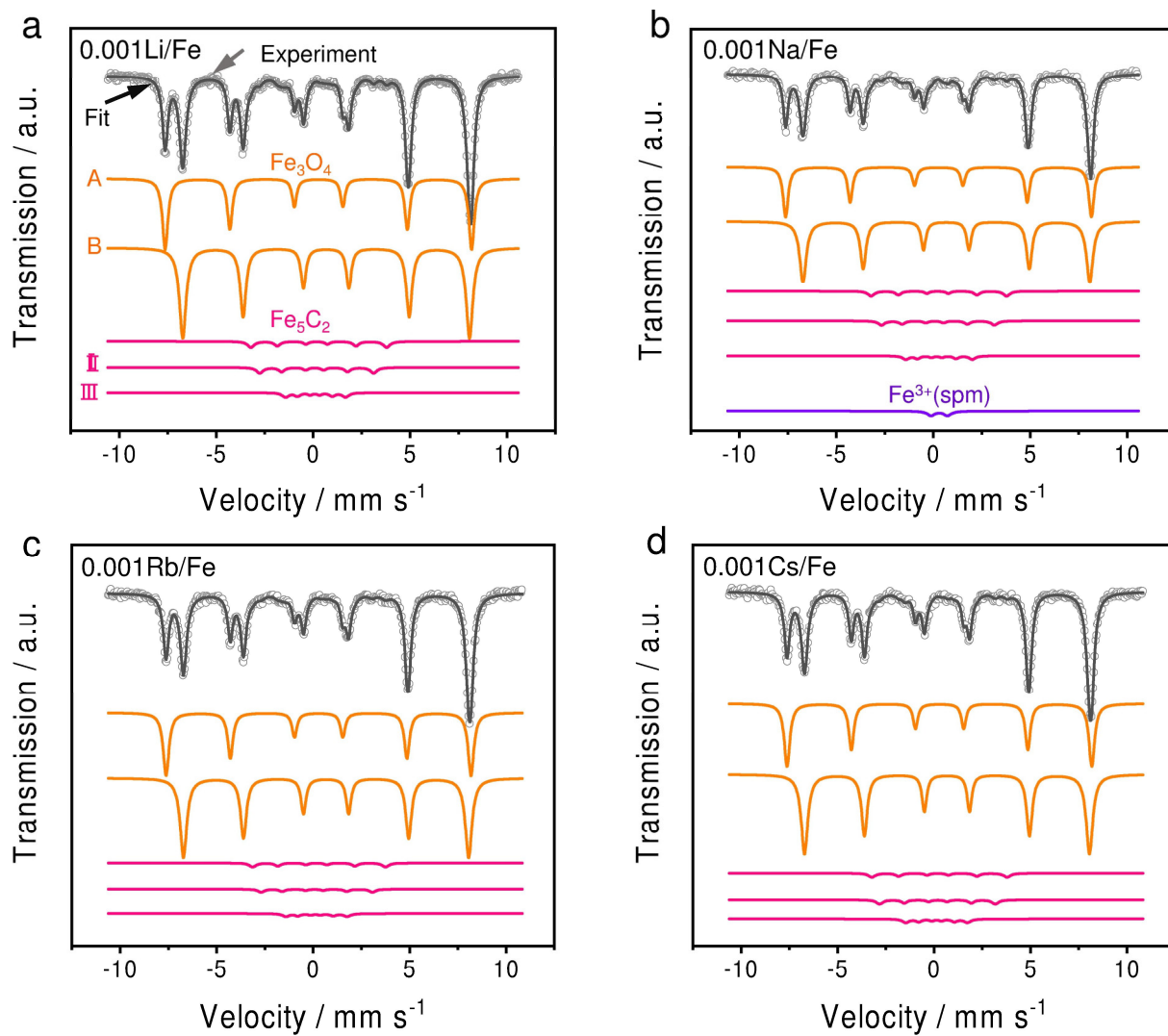
Figure A-18 Mössbauer spectra of (a) 0.001Li/Fe, (b) 0.001Na/Fe, (c) 0.001Rb/Fe and (d) 0.001Cs/Fe spent catalysts.
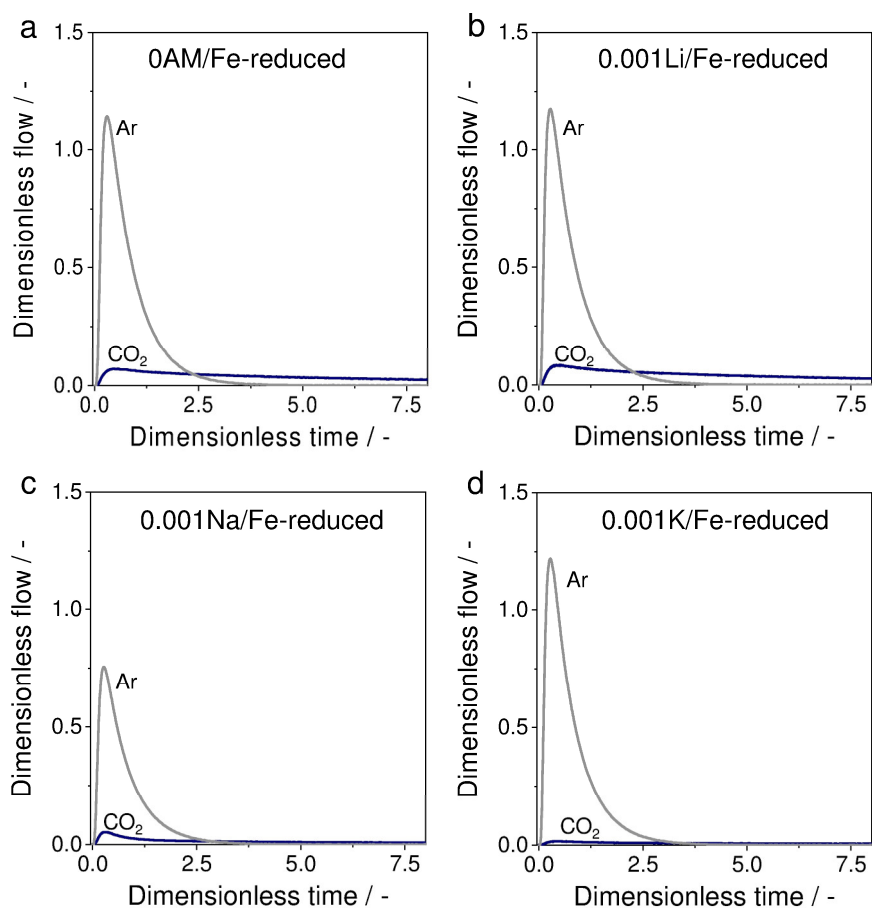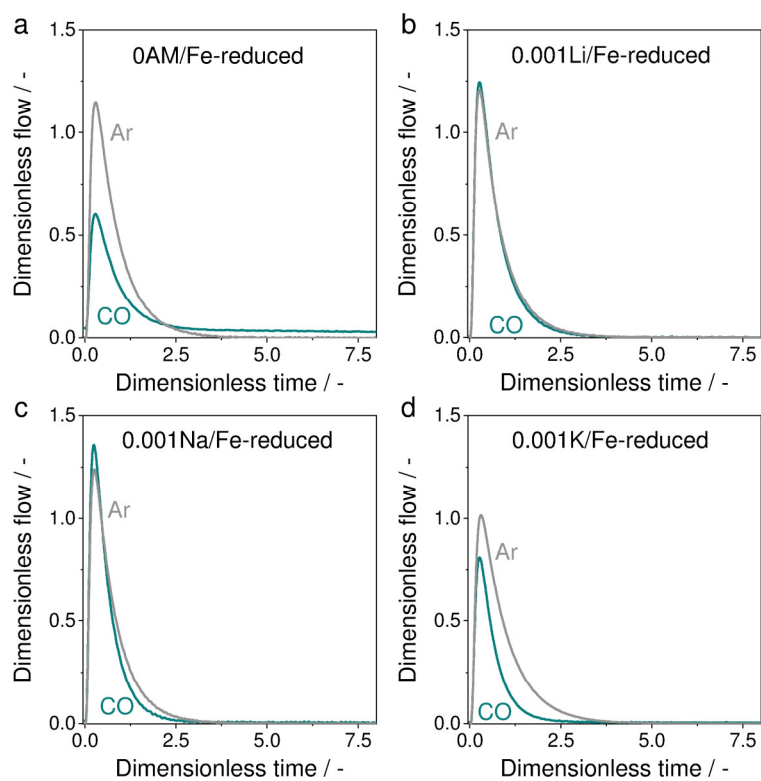
Figure A-19 Dimensionless responses of CO_2 and Ar after pulsing of a CO_2/Ar (1:1) mixture at 300°C over reduced catalysts of (a) 0AM/Fe, (b) 0.001Li/Fe, (c) 0.001Na/Fe and (d) 0.001K/Fe.
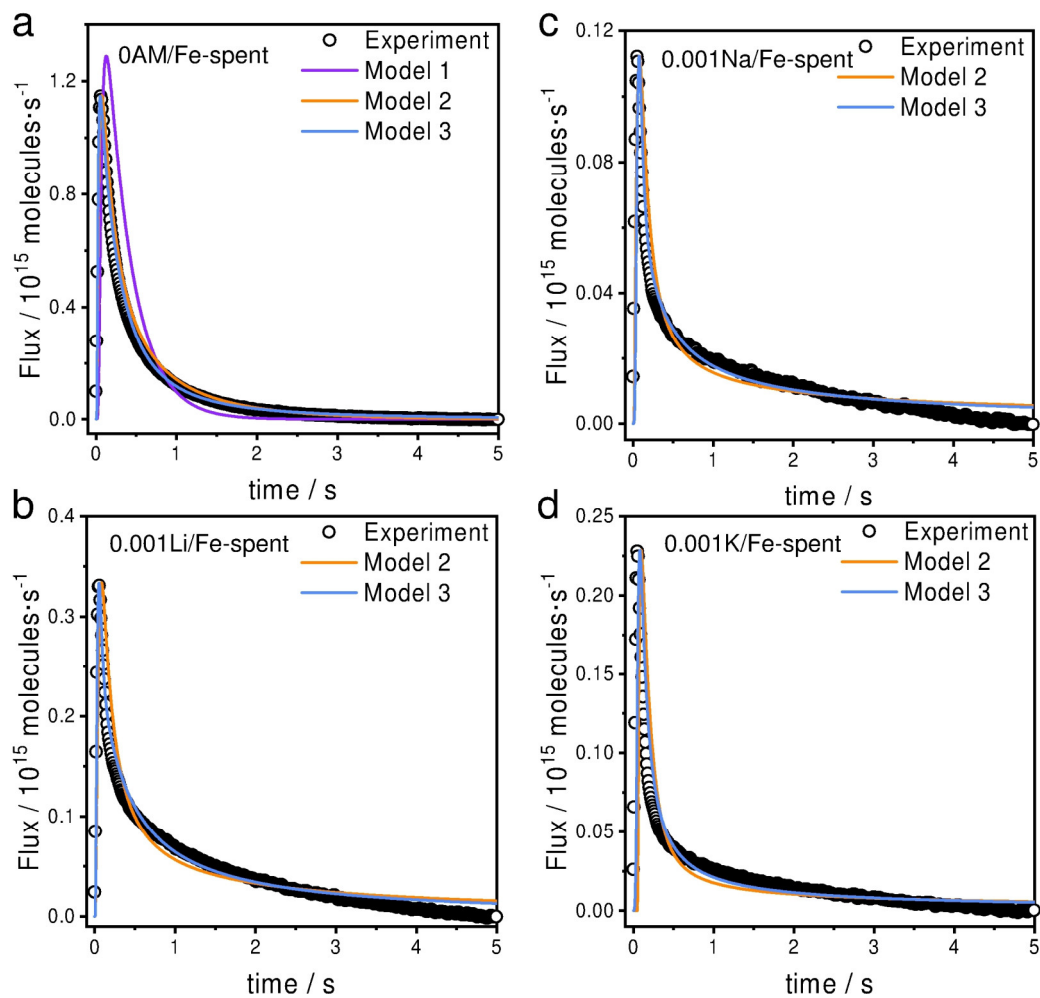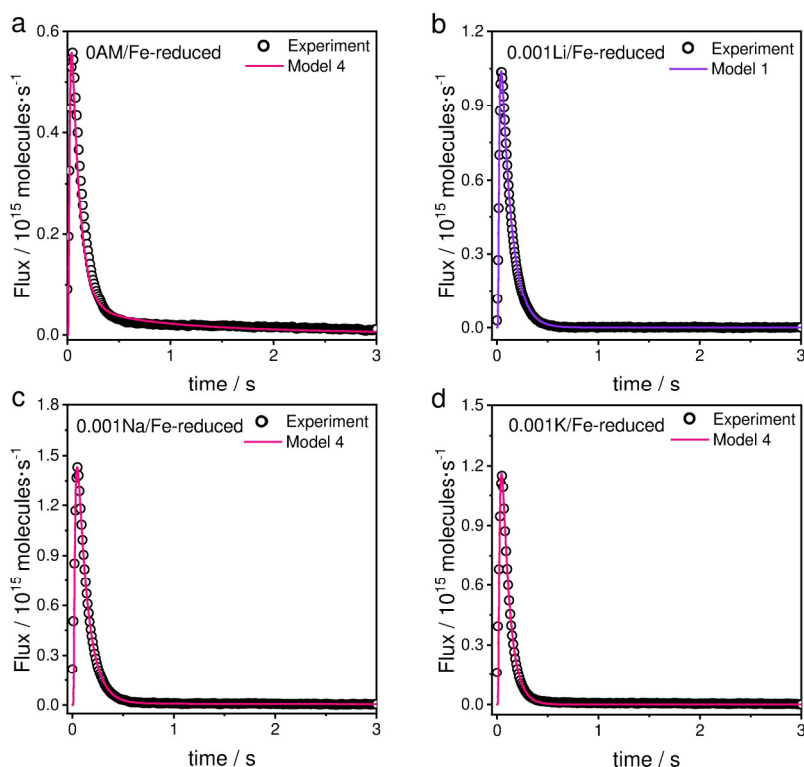
Figure A-20 Comparison of simulated responses obtained from Models 1–3 (see Table A-2) with the experimental CO_2 responses recorded after pulsing of a CO_2/Ar (1:1) mixture at 300°C over spent catalysts 0AM/Fe and 0.001AM/Fe (AM = Li, Na or K). For brevity, the simulated response obtained with Model 1 was omitted in b–d. None of these models correctly describes the experimental data.
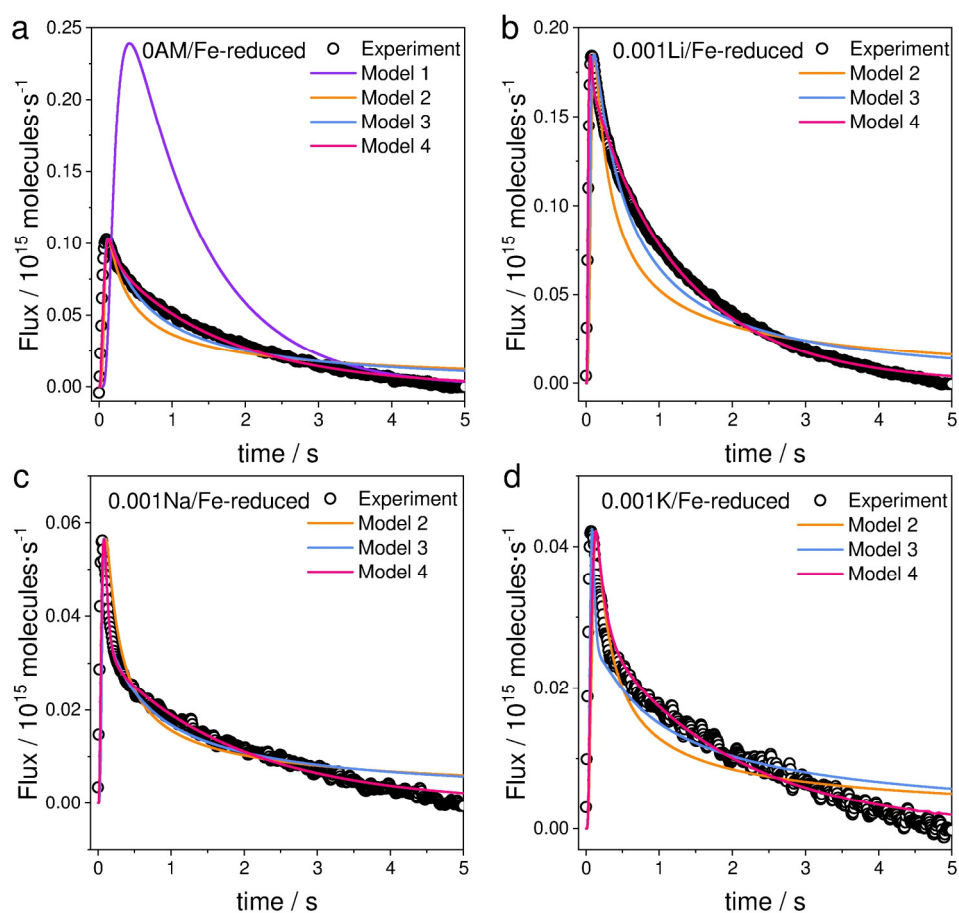
Figure A-21 Comparison of simulated responses obtained using the best model (Model 4 in Table A-2) with experimental CO_2 responses recorded after pulsing of a CO_2/Ar (1:1) mixture at 300°C over reduced catalysts 0AM/Fe and 0.001AM/Fe (AM = Li, Na or K). In this context, a simple diffusion model (Model 1, Table A-2) was also considered and proved to deviate from experimental response strongly for all the catalysts. For brevity, the simulated response obtained with Model 1 was omitted in b–d.
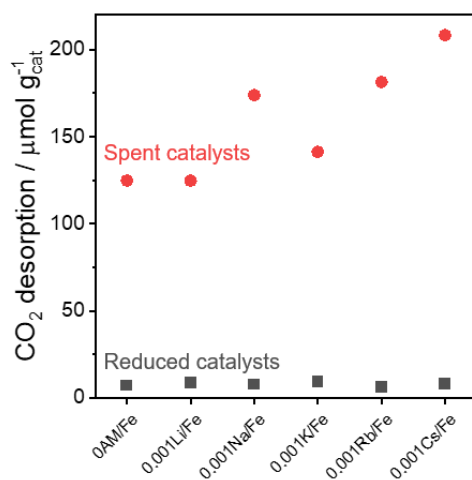
Figure A-22 The amount of CO_2 desorbed from reduced and spent catalysts.

Figure A-23 Dimensionless responses of CO and Ar after pulsing of a CO/Ar (1:1) mixture at 300°C over reduced catalysts of (a) 0AM/Fe, (b) 0.001Li/Fe, (c) 0.001Na/Fe and (d) 0.001K/Fe.
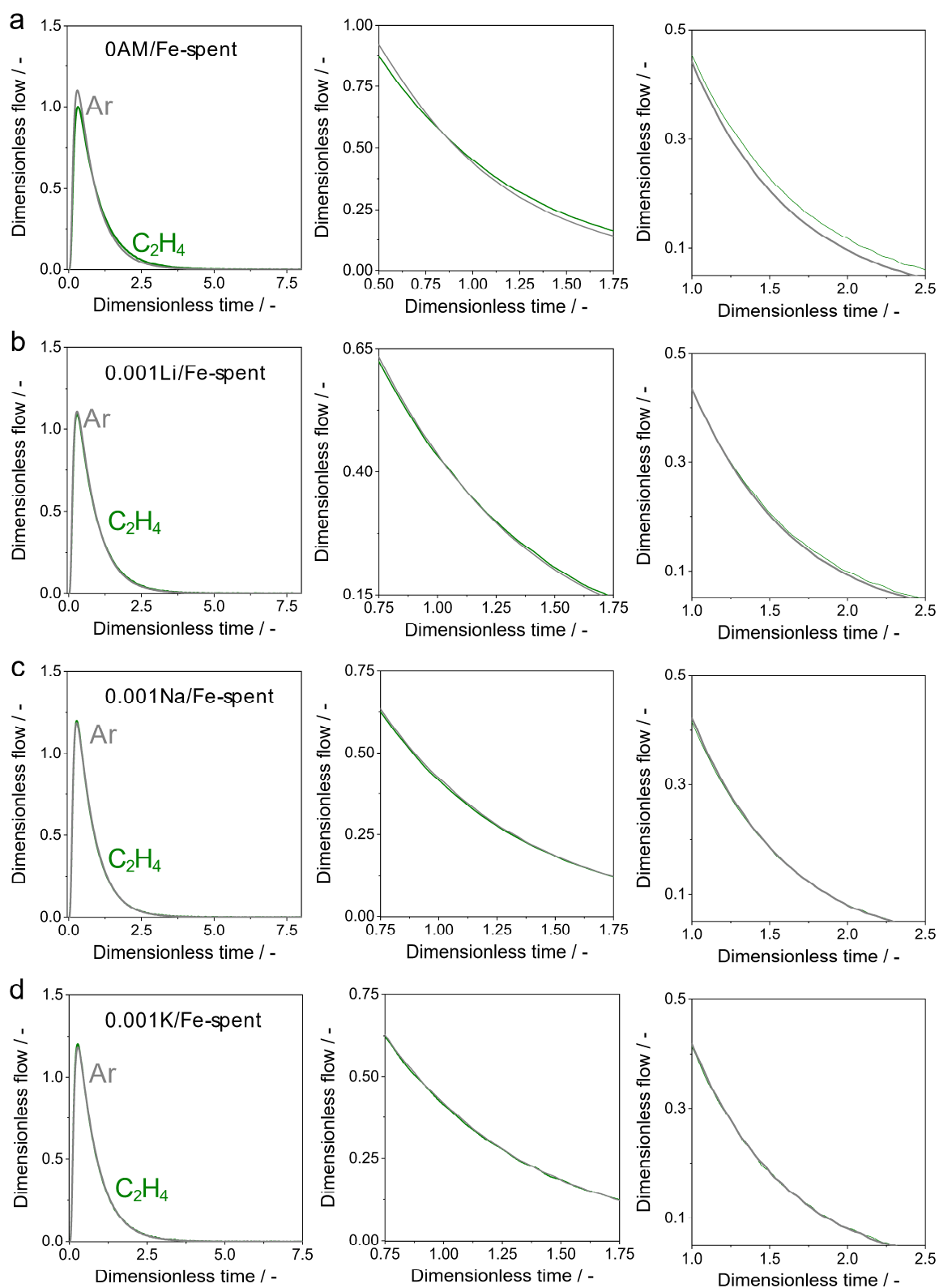

Figure A-24 Comparison of simulated responses obtained using the best model (Model 4 for 0AM/Fe, 0.001Na/Fe and 0.001K/Fe; Model 1 for 0.001Li/Fe) with the experimental CO responses recorded after pulsing of a CO/Ar (1:1) mixture at 300°C over reduced catalysts of (a) 0AM/Fe, (b) 0.001Li/Fe, (c) 0.001Na/Fe and (d) 0.001K/Fe.

Figure A-25 Dimensionless responses of C_2H_4 and Ar and zoomed-in view at low dimensionless time after pulsing of a C_2H_4/Ar (1:1) mixture at 300°C over spent catalysts of (a) 0AM/Fe, (b) 0.001Li/Fe, (c) 0.001Na/Fe and (d) 0.001K/Fe.
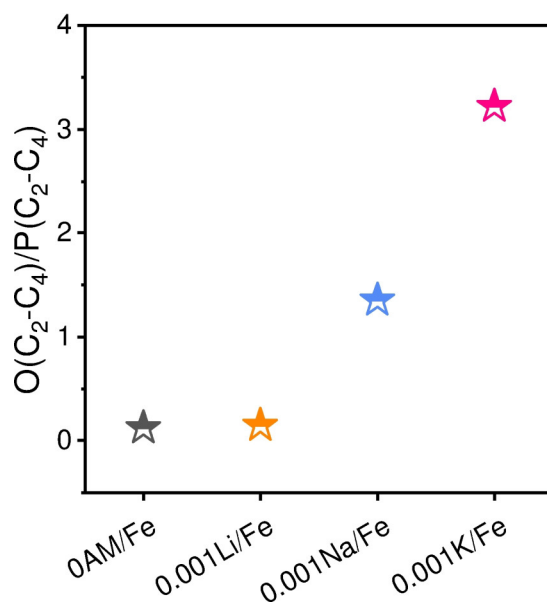
Figure A-26 The ratio of light olefins to light paraffins obtained in CO_2-FTS over 0AM/Fe and 0.001AM/Fe catalysts. Reaction conditions: 15 bar, 300 °C, $3H_2/CO_2/0.3N_2$ with a GHSV of 1160 mL g_{cat}^{-1} h^{-1}; the catalysts were initially reduced at 400 °C in $1H_2/1N_2$ for 2 h.
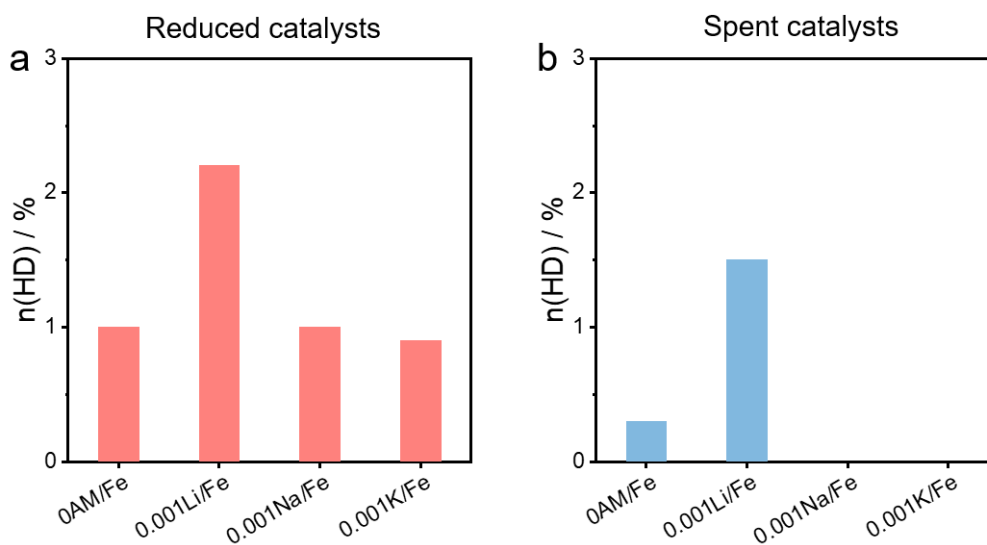

Figure A-27 Fraction of HD in H_2–D_2 exchange experiments on (a) reduced and (b) spent 0AM/Fe and 0.001AM/Fe catalysts.
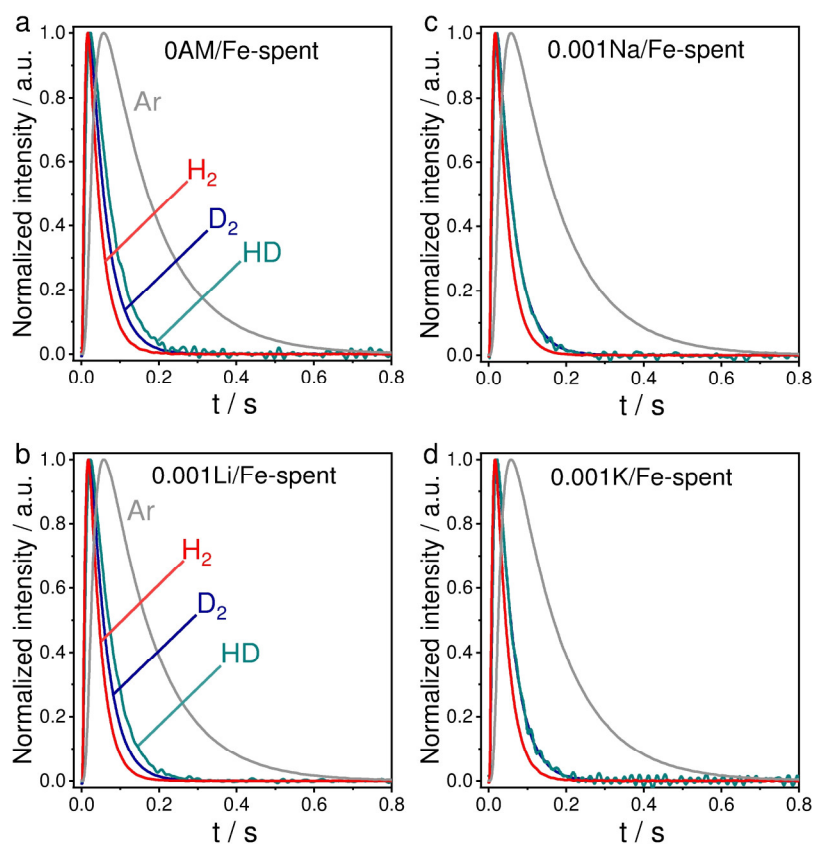
Figure A-28 Height-normalized responses of Ar, H_2, D_2 and HD obtained after pulsing of $H_2/D_2/Ar$ (1:1:1) at 300 °C over spent catalysts.
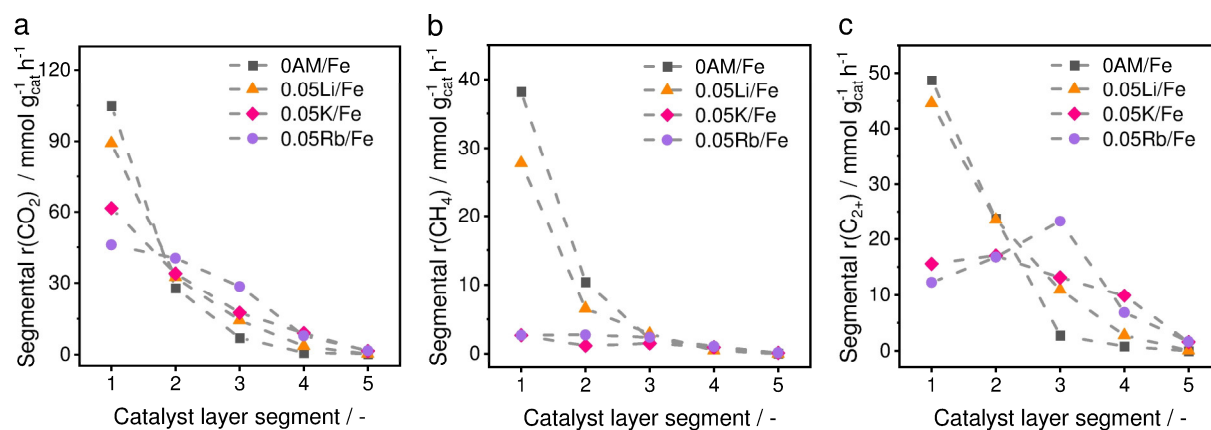

Figure A-29 The segmental rates of (a) overall CO_2 consumption ($r(CO_2)$), (b) CH_4 formation ($r(CH_4)$) and (c) C_{2+}-hydrocarbons formation ($r(C_{2+})$) over 0AM/Fe and 0.05AM/Fe catalysts in CO_2-FTS. Reaction conditions: $H_2/CO_2/N_2 = 3/1/0.3$, 15 bar and 300 °C.
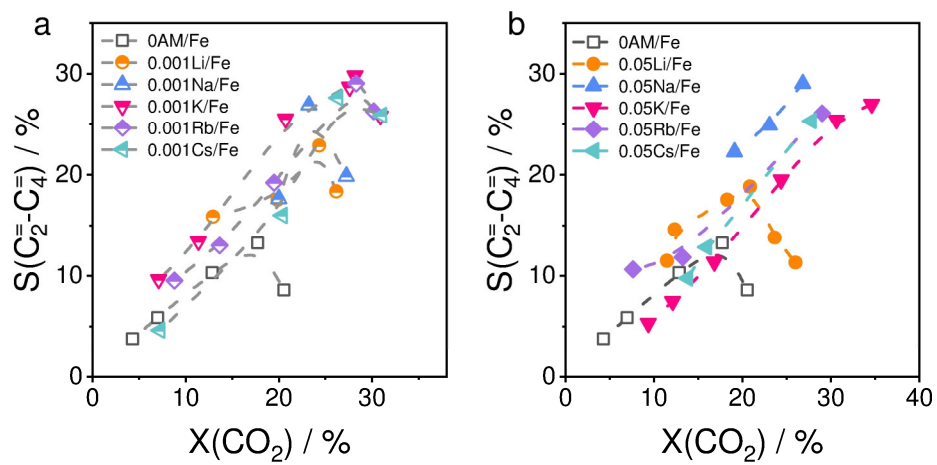
Figure A-30 The selectivity-conversion relationship for C_2-C_4 olefins as a function of CO_2 conversion over (a) 0.001AM/Fe and (b) 0.05AM/Fe catalysts (AM = Na, K, Rb, and Cs). Reaction conditions: 350°C, 15 bar, $3H_2/1CO_2/0.3N_2$, after 40 h on stream.
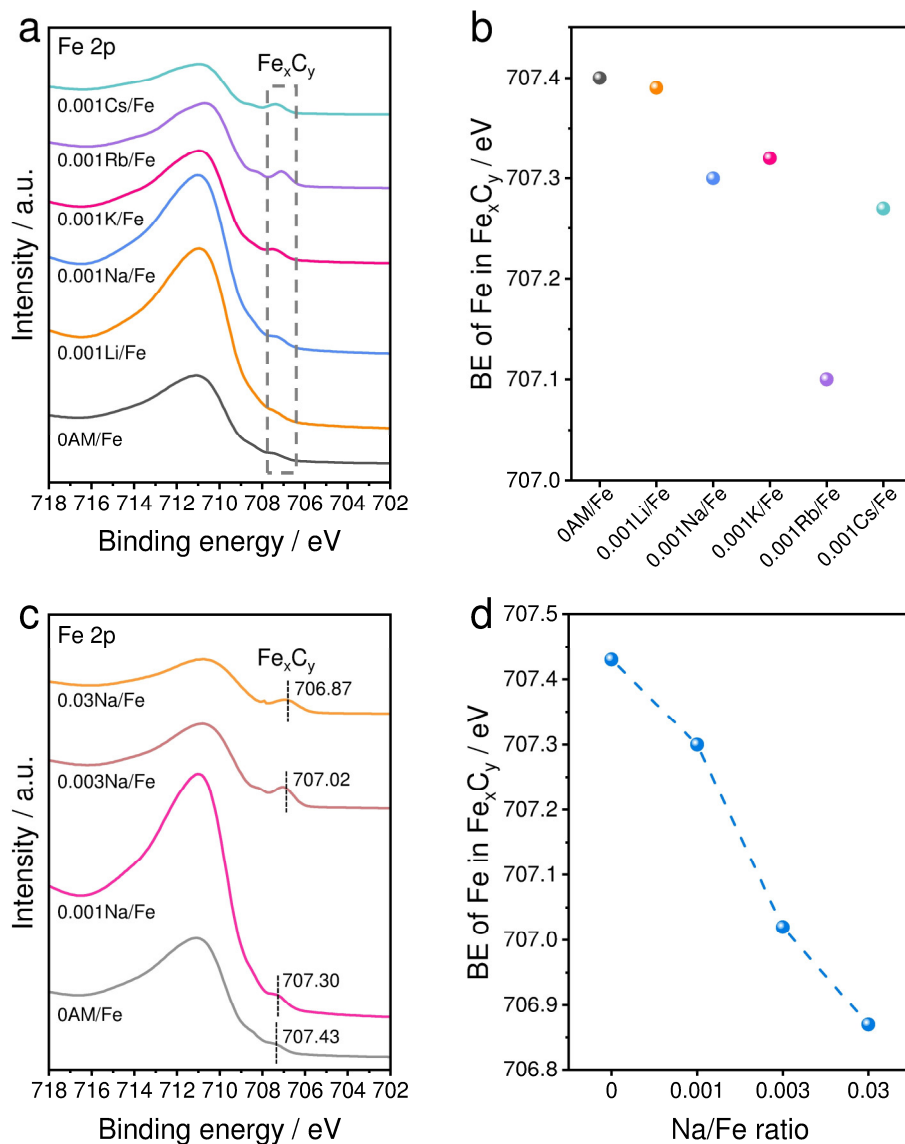
Figure A-31 (a) XPS spectra of Fe 2p of spent 0AM/Fe and 0.001AM/Fe catalysts and (b) the binding energy of Fe in Fe_xC_y species in these spent catalysts. (c) XPS spectra of Fe 2p of spent xNa/Fe catalysts with different loading of Na and (d) the binding energy of Fe in Fe_xC_y species in these spent catalysts. The spent catalysts were obtained after time-on-stream of 90 h in CO_2-FTS (300 °C, 15 bar with $CO_2/H_2/Ar$ = 1/3/0.3).
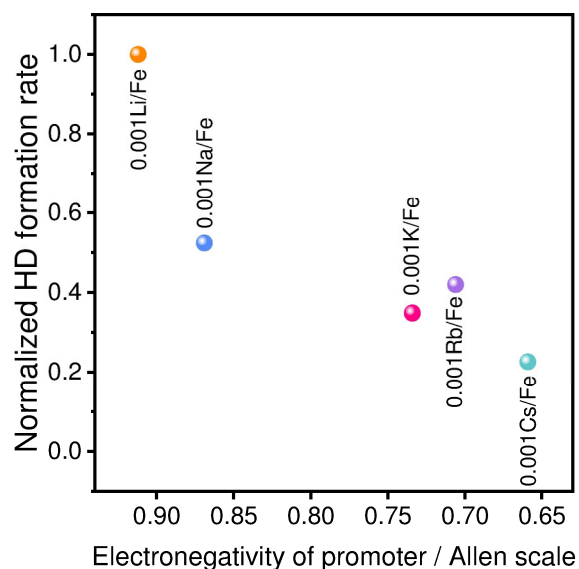
Figure A-32 Normalized HD formation rates in H_2–D_2 exchange experiments at 400 °C over spent catalysts.

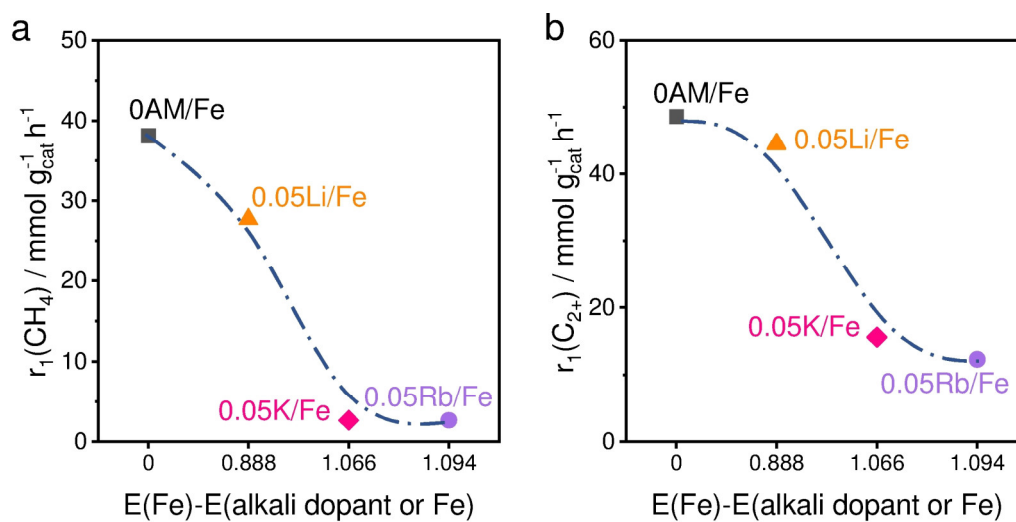

Figure A-33 The rates of (a) CH_4 ($r_1(CH_4)$) or (b) C_{2+}-hydrocarbons ($r_1(C_{2+})$) formation in the first segment of 0AM/Fe and 0.05AM/Fe catalysts versus the difference in the Allen scale electronegativity of iron and alkali metals.
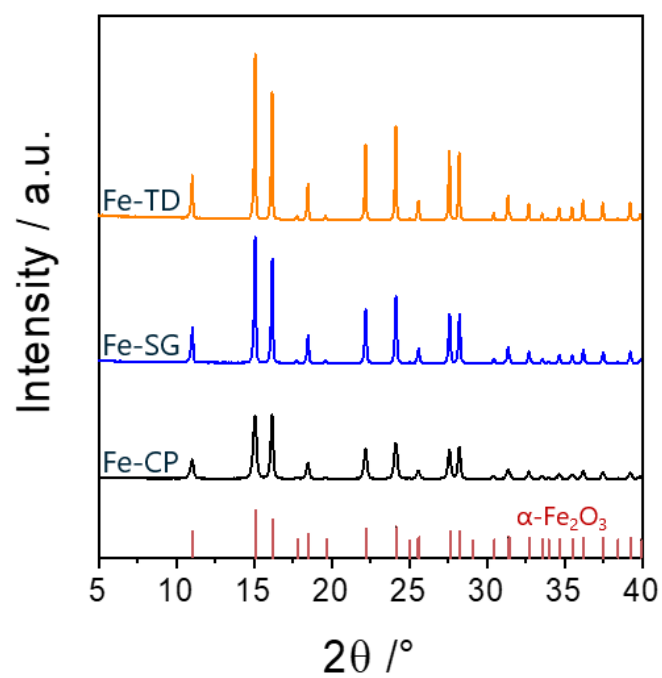
Figure A-34 XRD patterns of as-prepared catalysts and the reference pattern of α-Fe_2O_3 (ICDD 01-072-0469).
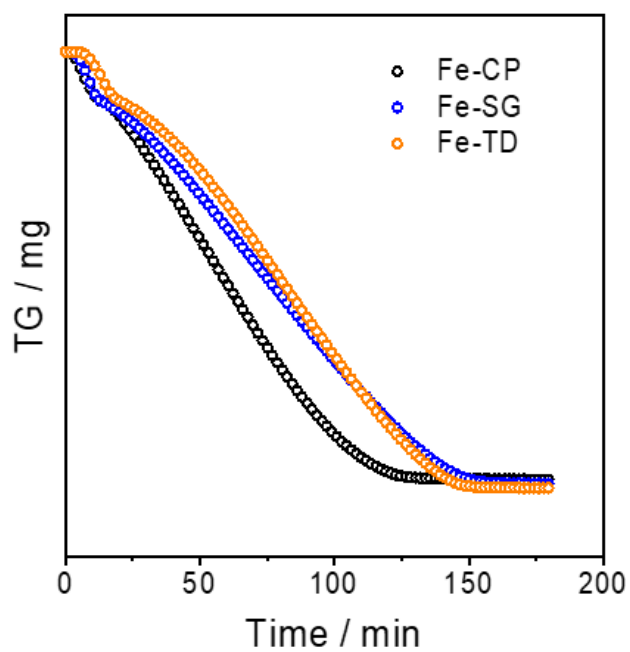

Figure A-35 TGA profiles obtained upon reduction of fresh α-Fe_2O_3 samples with H_2 (H_2:He = 1:1) at 300 °C .The plateau stage is characteristic for the complete reduction to metallic Fe.
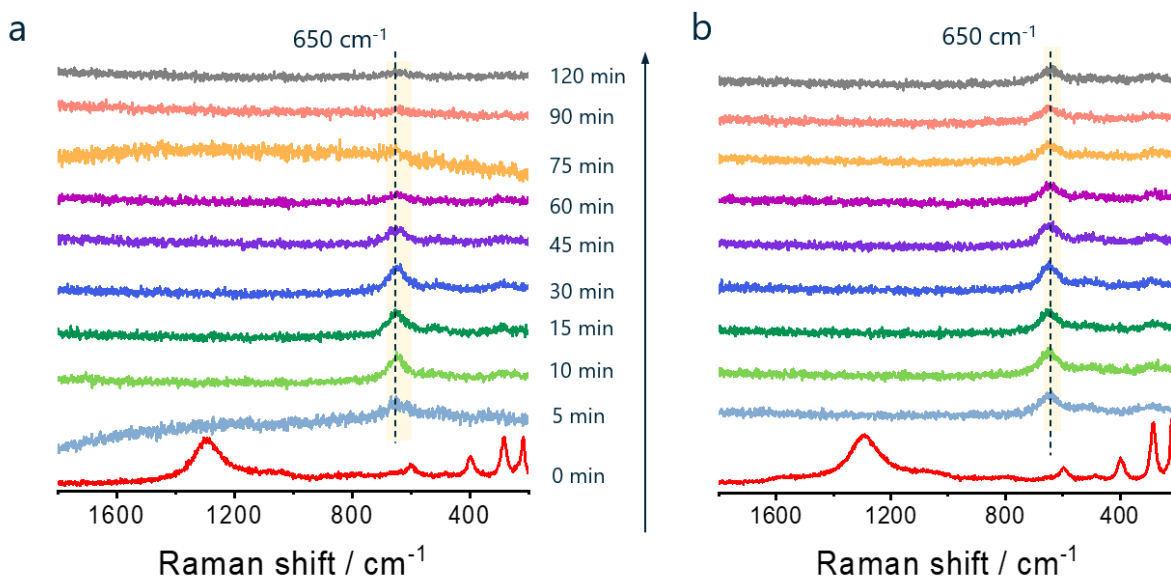
Figure A-36 *In situ* Raman spectra recorded upon reduction of (a) Fe-CP and (b) Fe-TD at 400 °C using a H_2/He feed (1/2, 15 mL min^{-1}). Before the introduction of the H_2-conating feed, Raman bands at 1297 cm^{-1}, 600 cm^{-1}, 400 cm^{-1}, 285 cm^{-1} and 221 cm^{-1}, characteristic for α-Fe$_2$O$_3$, are seen. When the samples are exposed to the H_2/He mixture, the band at 650 cm^{-1} appears, indicating the transformation of hematite (α-Fe$_2$O$_3$) to magnetite (Fe$_3$O$_4$).
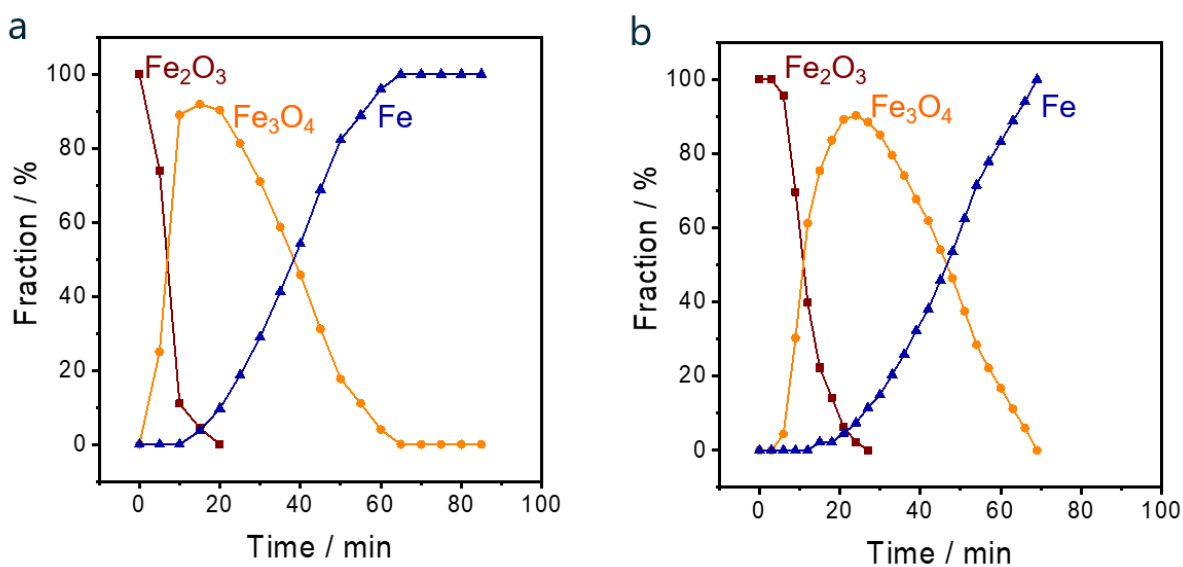
Figure A-37 Temporal profiles of phase composition obtained from *in situ* XRD patterns recorded upon reduction of (a) Fe-CP and (b) Fe-TD at 300 °C using a H_2/He (1:1, 10 mL min^{-1}) feed. The patterns were evaluated according to the Rietveld method. 100% metallic Fe was determined after 65 min reduction of Fe-CP, while about 70 min were needed for Fe-TD.
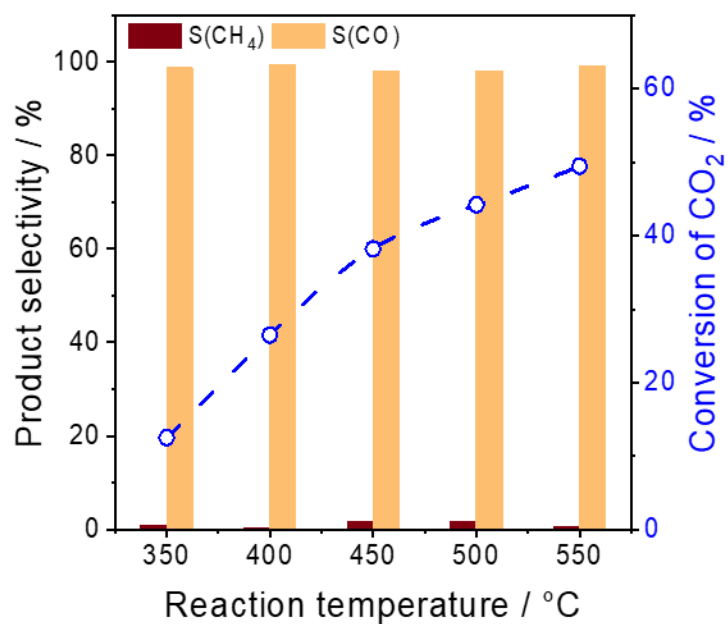
Figure A-38 Product selectivity and CO_2 conversion over Fe-TD as a function of reaction temperature at ambient pressure. Reaction conditions: T = 350–550 °C, P = 1 bar, CO_2:H_2:N_2 = 1:3:0.3, GHSV = 10,000 mL g_{cat}^{-1} h^{-1}; the catalyst was initially reduced at 300 °C for 2 h.
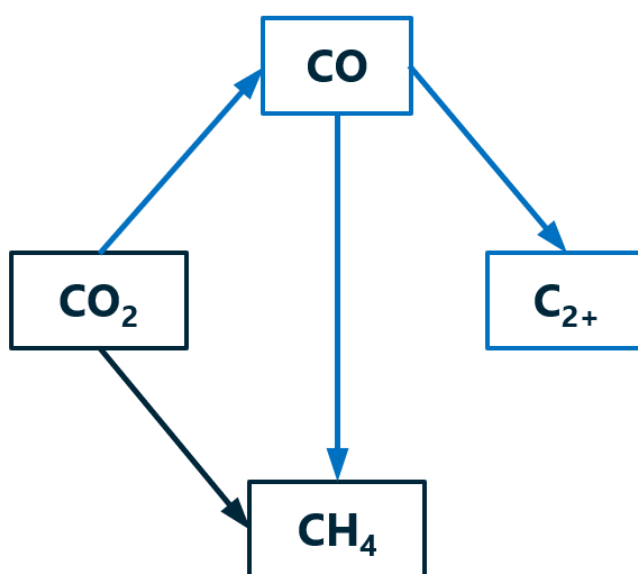
Figure A-39 The proposed reaction scheme of product formation in CO_2-FTS over Fe-based catalysts.
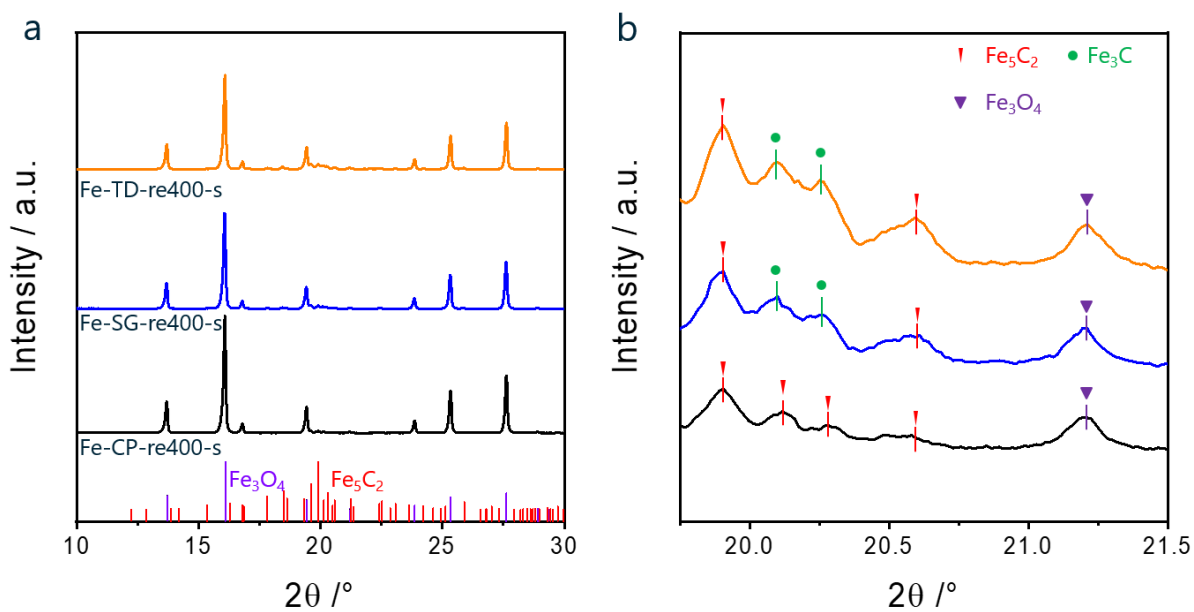
Figure A-40 (a) XRD patterns of spent Fe-CP (Fe-CP-re400-s), Fe-SG (Fe-SG-re400-s) and Fe-TD (Fe-TD-re400-s) catalysts initially reduced at 400 °C before starting CO_2 hydrogenation; (b) zoomed region between 19.75–21.5°.
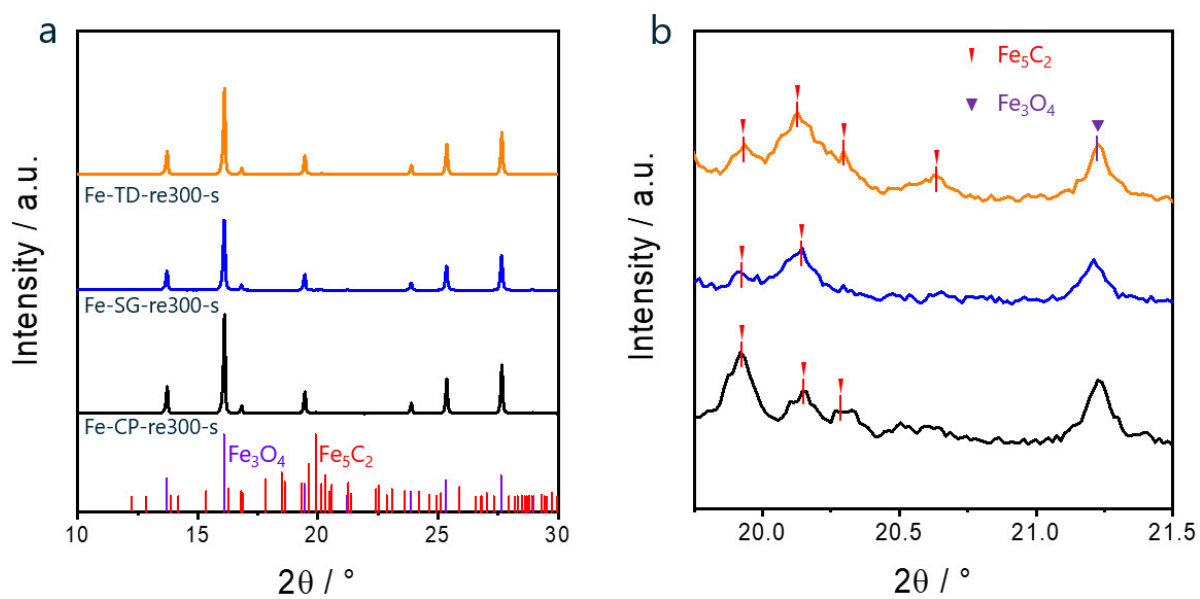
Figure A-41 (a) XRD patterns of spent Fe-CP (Fe-CP-re300-s), Fe-SG (Fe-SG-re300-s) and Fe-TD (Fe-TD-re300-s) catalysts initially reduced at 300 °C before starting CO_2 hydrogenation; (b) zoomed region between 19.75–21.5°.
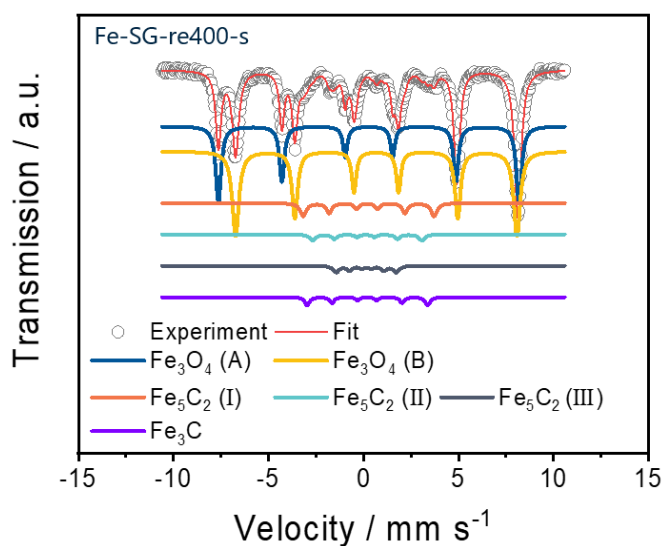
Figure A-42 Mössbauer spectrum (circles) of spent Fe-SG catalyst reduced at 400 °C before the CO_2-FTS reaction. The individual components obtained from the fit (thin red line) are presented as coloured thick lines.
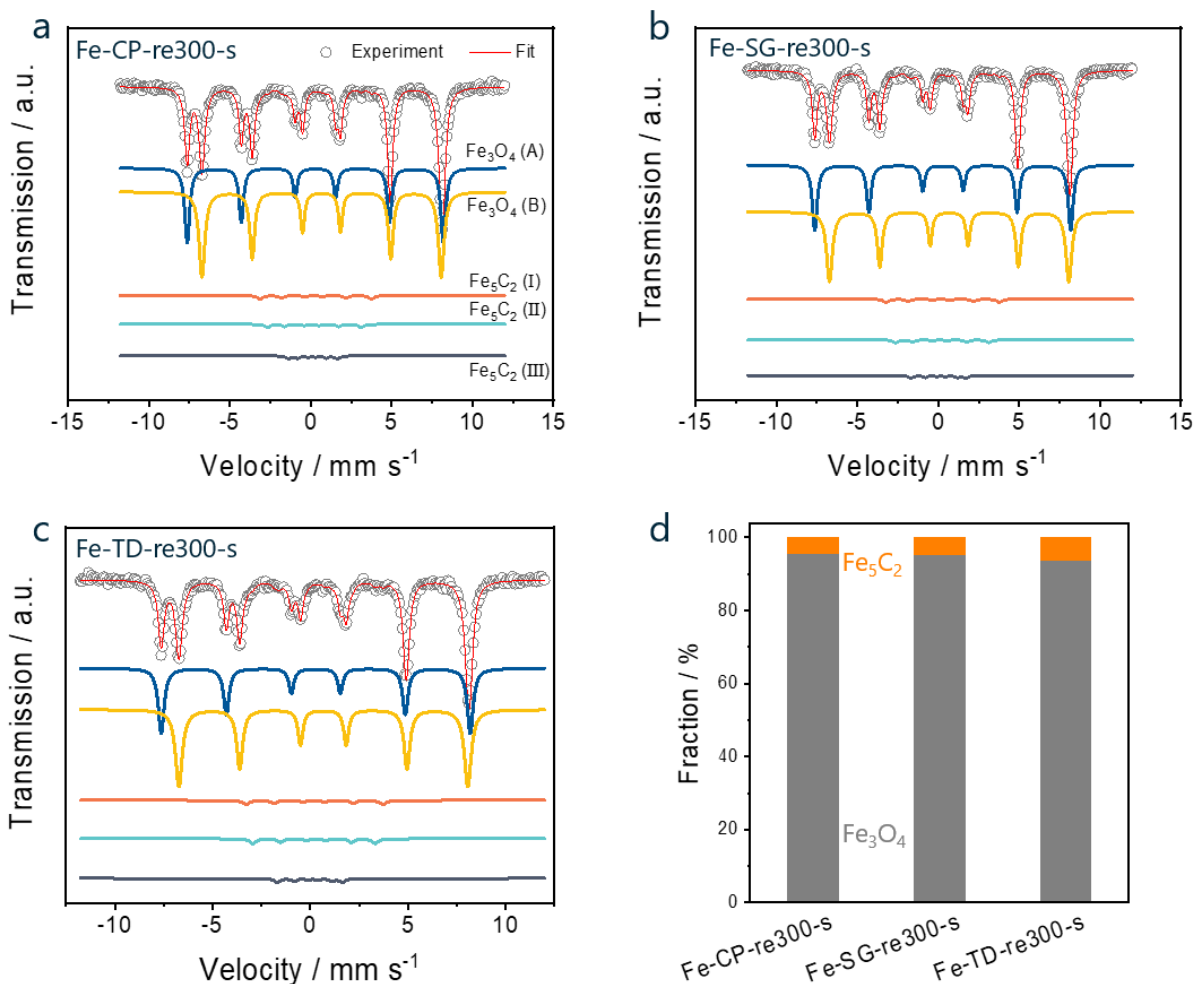
Figure A-43 (a–c) Mössbauer spectra (circles) of spent Fe-CP (a, Fe-CP-re300-s), Fe-SG (b, Fe-SG-re300-s) and Fe-TD (c, Fe-TD-re300-s) catalysts initially reduced at 300 °C before starting CO_2 hydrogenation. (d) The phase composition obtained from the Mössbauer spectra in a–c.

147
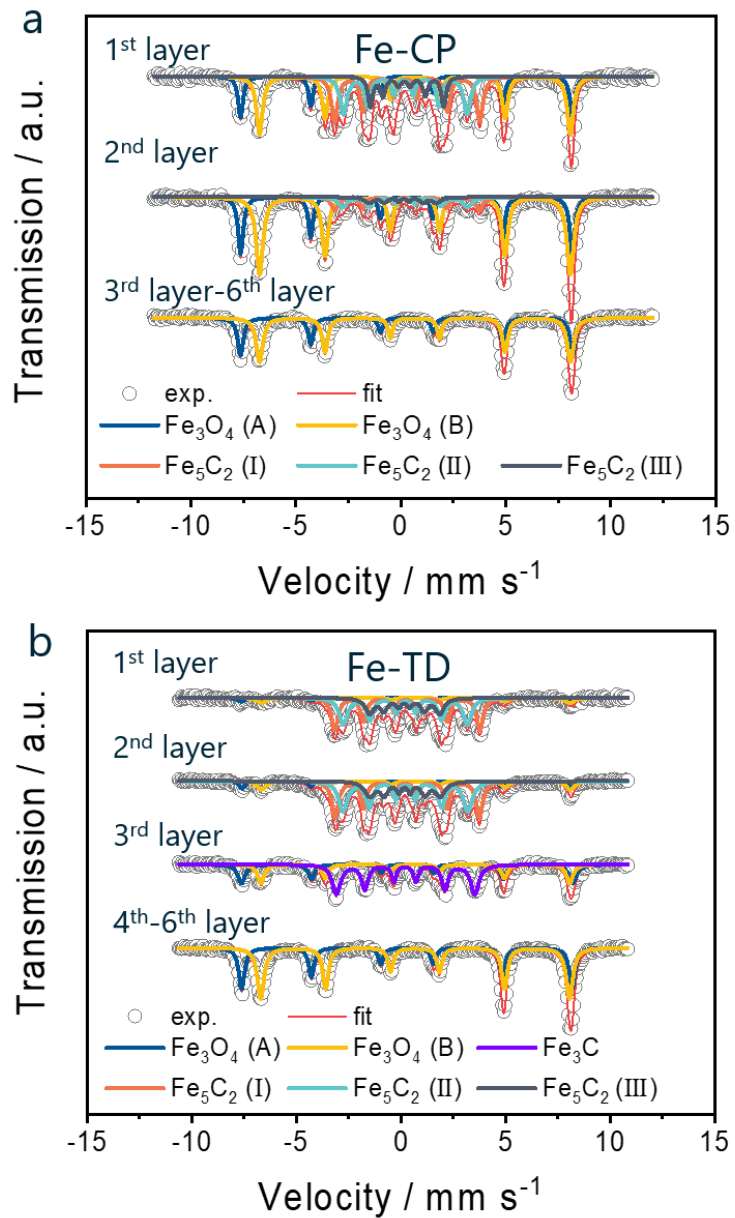
Figure A-44 Mössbauer spectra (circles) of (a) Fe-CP-re400-s and (b) Fe-TD-re400-s spent catalysts along the catalyst bed. The individual components obtained from the fit (thin red line) are presented as coloured thick lines.
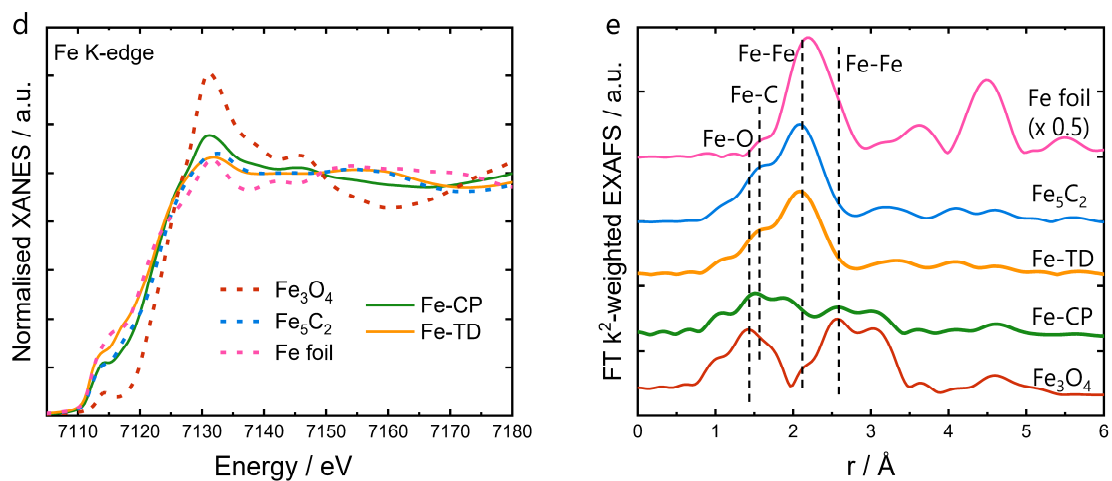
Figure A-45 Normalized XANES spectra at Fe K-edge and (b) k^2-weighted EXAFS Fourier-transform spectra of Fe-CP-re400-s and Fe-TD-re400-s located at the first upstream layer.
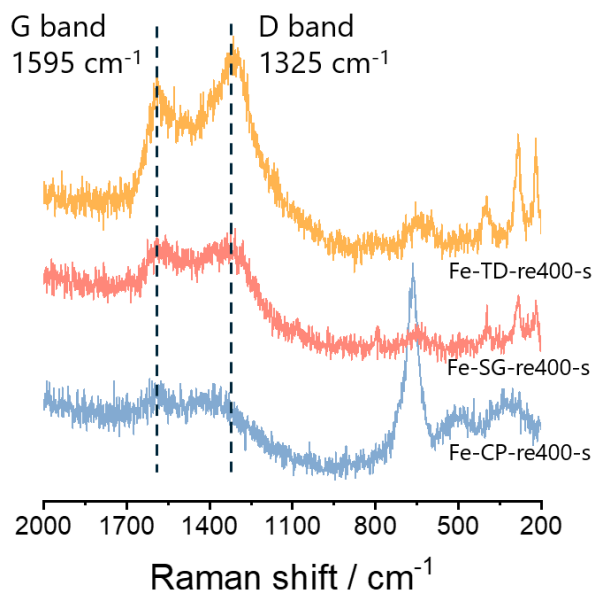
Figure A-46 Raman spectra of spent Fe-CP-re400-s, Fe-SG-re400-s and Fe-TD-re400-s catalysts.
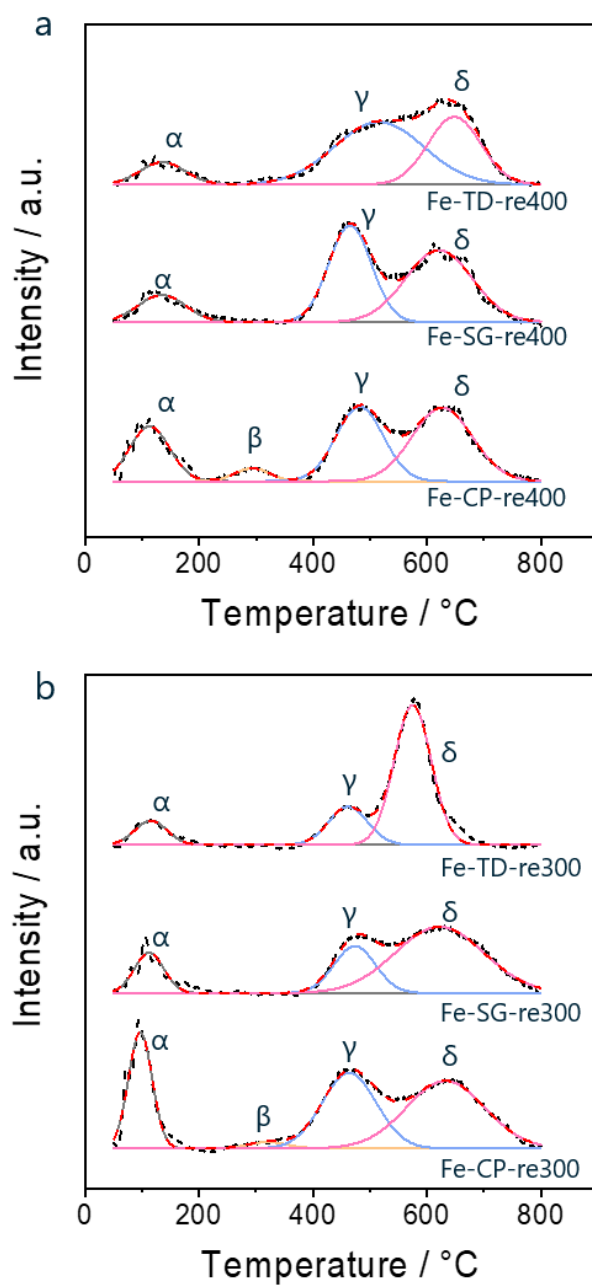
Figure A-47 CO$_2$-TPD profiles of catalysts reduced at (a) 400 °C (Fe-x-re400) or (b) 300 °C (Fe-x-re300).
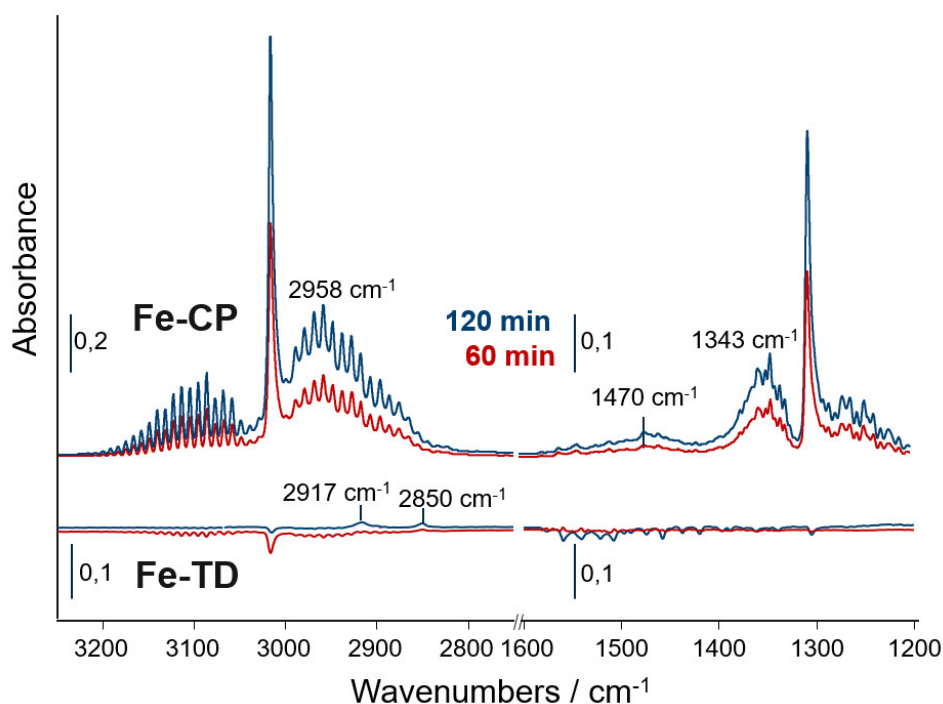
Figure A-48 *In situ* FTIR spectra recorded after 60 and 120 min on CO_2-FTS stream (15 bar and 250 °C) over Fe-CP and Fe-TD after subtracting the spectrum collected after 15 min on stream.
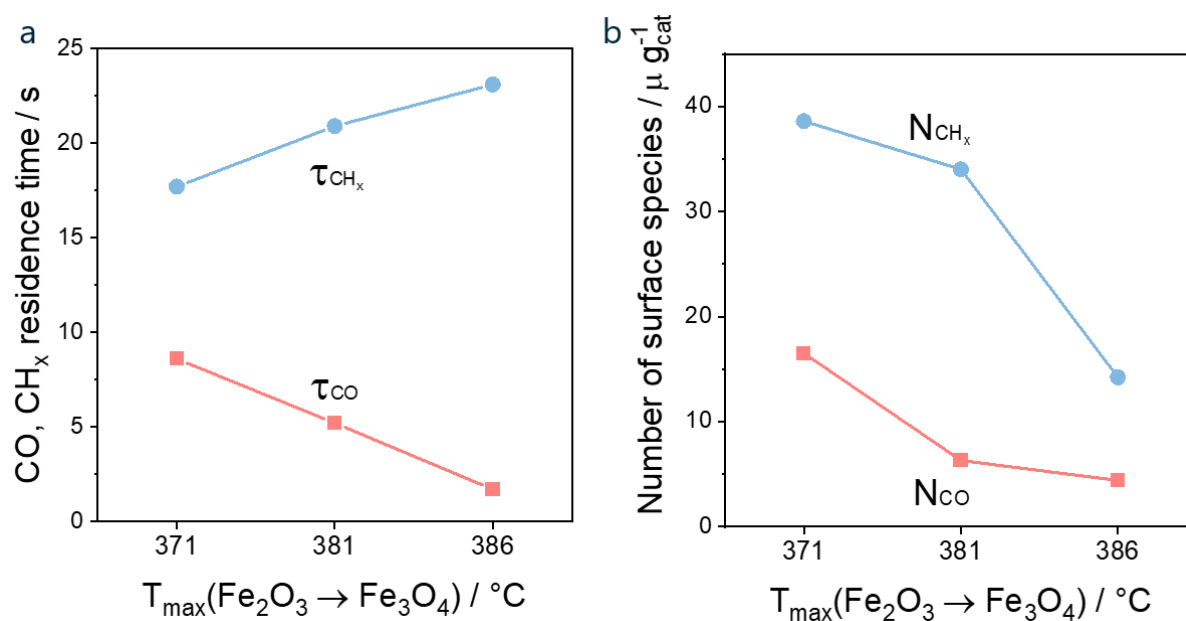
Figure A-49 (a) The lifetime and (b) the number of surface intermediates leading to CO or CH_4 over different catalysts determined from SSITKA tests in Figure 6a, b in the main article versus the temperature of the maximal reduction rate of Fe_2O_3 to Fe_3O_4.
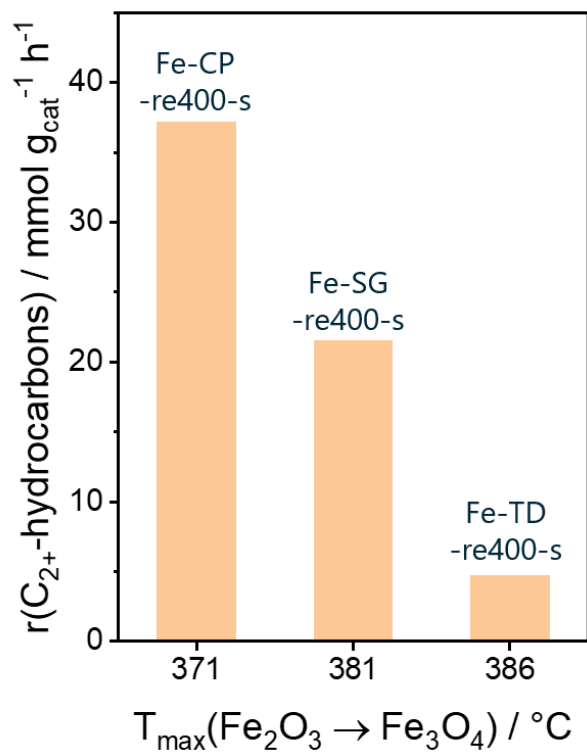
Figure A-50 The formation rate of C_{2+}-hydrocarbons versus versus the temperature of the maximal reduction rate of Fe_2O_3 to Fe_3O_4. The formation rate of C_{2+}-hydrocarbons was determined at 300 °C, 15 bar and about 10% CO_2 conversion using an $H_2/CO_2 = 3:1$ feed.

Table A-1 Weight contents of Fe and alkali metals as well as the atomic ratio of Fe to alkali metals for different as-prepared samples

Catalysts	Metal content / wt. %		AM/Fe atomic ratio [a]
	Fe	AM	
0AM/Fe	72.35	0	0.0
0.001K/Fe	72.12	0.056	0.001
0.005K/Fe	71.38	0.245	0.005
0.02K/Fe	71.36	0.931	0.018
0.05K/Fe	67.74	2.130	0.045
0.001Li/Fe	72.03	0.105	0.001
0.05Li/Fe	70.00	0.430	0.049
0.001Na/Fe	72.28	0.022	0.001
0.05Na/Fe	69.18	1.290	0.045
0.001Rb/Fe	73.32	0.067	0.001
0.05Rb/Fe	66.13	4.560	0.045
0.001Cs/Fe	--	--	0.001 [b]
0.05Cs/Fe	--	--	0.034 [b]

[a]. The atomic ratio of AM/Fe was determined by ICP-OES except xCs/Fe as the loadings of Cs cannot be measured by this method.

[b]. The loading of Cs for xCs/Fe was measured by atomic absorption spectroscopy (Flame AAS) method.

Table A-2 Micro-kinetic models applied for kinetic modeling of CO_2 adsorption and activation.

Model	Elementary step	Rate constants
1	Diffusion	D_{eff}
2	$CO_2 + * \rightarrow *-CO_2$	k_{ads}^{eff} [a]
	$*-CO_2 \rightarrow CO_2 + *$	k_{des}
3	$CO_2 + 2* \rightarrow *-CO + *-O$	k_{diss}^{eff} [a]
	$*-CO + *-O \rightarrow CO_2 + 2*$	k_{ass}^{eff}
4	$CO_2 + * \rightarrow *-CO_2$	k_{ads}^{eff} [a]
	$*-CO_2 \rightarrow * + CO_2$	k_{des}
	$*-CO_2 + * \rightarrow *-CO + *-O$	k_{diss}^{eff} [a]
	$*-CO + *-O \rightarrow *-CO_2 + *$	k_{ass}

[a]. Due to the correlation between total concentration of active sites (C_{total}) and the rate constants of adsorption $(k_{ads}(CO_2))$ or dissociation $(k_{diss}(CO_2))$, only their product could be calculated and denoted as k_{ads}^{eff} or k_{diss}^{eff}.

Table A-3 The best residual obtained from different kinetic models applied for CO_2 adsorption and activation over reduced and spent catalysts.

Catalysts	Model 1	Model 2	Model 3	Model 4
	Reduced materials			
0AM/Fe	$5.83 \cdot 10^{-2}$	$7.47 \cdot 10^{-2}$	$6.00 \cdot 10^{-2}$	$1.90 \cdot 10^{-2}$
0.001Li/Fe	$7.28 \cdot 10^{-2}$	$6.91 \cdot 10^{-2}$	$5.21 \cdot 10^{-2}$	$1.08 \cdot 10^{-2}$
0.001Na/Fe	$8.91 \cdot 10^{-2}$	$6.14 \cdot 10^{-2}$	$5.86 \cdot 10^{-2}$	$1.99 \cdot 10^{-2}$
0.001K/Fe	$8.06 \cdot 10^{-2}$	$6.71 \cdot 10^{-2}$	$7.22 \cdot 10^{-2}$	$2.29 \cdot 10^{-2}$
	Spent materials			
0AM/Fe	$2.58 \cdot 10^{-2}$	$8.86 \cdot 10^{-3}$	$2.93 \cdot 10^{-3}$	$9.67 \cdot 10^{-4}$
0.001Li/Fe	$7.28 \cdot 10^{-2}$	$3.96 \cdot 10^{-2}$	$3.48 \cdot 10^{-2}$	$4.82 \cdot 10^{-3}$
0.001Na/Fe	$7.97 \cdot 10^{-2}$	$3.79 \cdot 10^{-2}$	$3.39 \cdot 10^{-2}$	$5.88 \cdot 10^{-3}$
0.001K/Fe	$6.12 \cdot 10^{-2}$	$2.62 \cdot 10^{-2}$	$1.77 \cdot 10^{-2}$	$7.15 \cdot 10^{-3}$

Table A-4 Kinetic parameters of CO_2 activation (Model 4) over selected reduced and spent catalysts. The confidence interval for each parameter is listed in the parenthesis below the parameter.

Catalysts	$k_{ads}^{eff}(CO_2)$ / s^{-1}	$k_{des}(CO_2)$ / s^{-1}	$k_{ads}^{eff}(CO_2)$ / $k_{des}(CO_2)$	$k_{diss}^{eff}(CO_2)$ / s^{-1}
	Reduced materials			
0AM/Fe	$2.11 \cdot 10^4$ $(2.05 \cdot 10^4 – 2.18 \cdot 10^4)$	$1.27 \cdot 10^0$ $(1.21 \cdot 10^0 – 1.33 \cdot 10^0)$	$1.66 \cdot 10^4$	$2.48 \cdot 10^1$ $(2.44 \cdot 10^1 – 2.52 \cdot 10^1)$
0.001Li/Fe	$5.46 \cdot 10^3$ $(5.42 \cdot 10^3 – 5.50 \cdot 10^3)$	$1.17 \cdot 10^1$ $(1.15 \cdot 10^1 – 1.20 \cdot 10^1)$	$4.66 \cdot 10^2$	$7.39 \cdot 10^{-1}$ $(6.87 \cdot 10^{-1} – 7.97 \cdot 10^{-1})$
0.001Na/Fe	$2.93 \cdot 10^4$ $(2.90 \cdot 10^4 – 2.96 \cdot 10^4)$	$3.27 \cdot 10^{-1}$ $(2.96 \cdot 10^{-1} – 3.63 \cdot 10^{-1})$	$8.95 \cdot 10^4$	$3.60 \cdot 10^2$ $(3.54 \cdot 10^2 – 3.66 \cdot 10^2)$
0.001K/Fe	$7.22 \cdot 10^4$ $(7.15 \cdot 10^4 – 7.29 \cdot 10^4)$	$3.39 \cdot 10^{-1}$ $(3.16 \cdot 10^{-1} – 3.64 \cdot 10^{-1})$	$2.13 \cdot 10^5$	$7.72 \cdot 10^2$ $(7.67 \cdot 10^2 – 7.77 \cdot 10^2)$
	Spent materials			
0AM/Fe	$1.13 \cdot 10^3$ $(1.13 \cdot 10^3 – 1.13 \cdot 10^3)$	$8.71 \cdot 10^0$ $(8.66 \cdot 10^0 – 8.76 \cdot 10^0)$	$1.30 \cdot 10^2$	$5.60 \cdot 10^{-1}$ $(5.29 \cdot 10^{-1} – 5.93 \cdot 10^{-1})$
0.001Li/Fe	$3.44 \cdot 10^3$ $(3.43 \cdot 10^3 – 3.46 \cdot 10^3)$	$1.70 \cdot 10^0$ $(1.63 \cdot 10^0 – 1.76 \cdot 10^0)$	$2.03 \cdot 10^3$	$3.10 \cdot 10^0$ $(2.91 \cdot 10^0 – 3.29 \cdot 10^0)$
0.001Na/Fe	$7.84 \cdot 10^3$ $(7.80 \cdot 10^3 – 7.88 \cdot 10^3)$	$3.64 \cdot 10^{-1}$ $(3.49 \cdot 10^{-1} – 3.81 \cdot 10^{-1})$	$2.15 \cdot 10^4$	$1.01 \cdot 10^2$ $(9.96 \cdot 10^1 – 1.02 \cdot 10^2)$
0.001K/Fe	$1.58 \cdot 10^5$ $(1.56 \cdot 10^5 – 1.60 \cdot 10^5)$	$9.66 \cdot 10^{-1}$ $(8.85 \cdot 10^{-1} – 1.05 \cdot 10^0)$	$1.64 \cdot 10^5$	$1.04 \cdot 10^5$ $(1.03 \cdot 10^5 – 1.06 \cdot 10^5)$

Note: Using a sensitivity analysis, we also checked if all parameters are really required to correctly describe the experimental CO_2 responses. On this basis, the constant of recombination, i.e., $k_{ass}(CO_2)$, of adsorbed CO and O to adsorbed CO_2 over reduced catalyst can be omitted without worsening the fit. Thus, we do not report $k_{ass}(CO_2)$ values in this table.

Table A-5 Micro-kinetic models applied for fitting CO adsorption and activation using experimental transient response.

Model	Elementary step	Rate constants
1	Diffusion	D_{eff}
2	$CO + * \rightarrow *-CO$	k_{ads}^{eff} [a]
	$*-CO \rightarrow CO + *$	k_{des}
3	$CO + 2* \rightarrow *-C + *-O$	k_{diss}^{eff} [a]
	$*-C + *-O \rightarrow CO + 2*$	k_{ass}^{eff}
4	$CO + * \rightarrow *-CO$	k_{ads}^{eff} [a]
	$*-CO \rightarrow * + CO$	k_{des}
	$*-CO + * \rightarrow *-C + *-O$	k_{diss}^{eff} [a]
	$*-C + *-O \rightarrow *-CO + *$	k_{ass}

[a]. Due to the correlation between total concentration of active sites and the rate constants of adsorption or dissociation, only their product could be calculated and denoted as k_{ads}^{eff} or k_{diss}^{eff}.

Table A-6 The best residual obtained from different kinetic models applied for CO adsorption and activation over reduced and spent catalysts.

Catalysts	Model 1	Model 2	Model 3	Model 4
Reduced materials				
0AM/Fe	$4.43 \cdot 10^{-2}$	$5.16 \cdot 10^{-3}$	$7.63 \cdot 10^{-3}$	$4.87 \cdot 10^{-3}$
0.001Li/Fe	$1.48 \cdot 10^{-3}$	$3.94 \cdot 10^{-2}$	$3.94 \cdot 10^{-2}$	$3.94 \cdot 10^{-2}$
0.001Na/Fe	$1.21 \cdot 10^{-2}$	$1.27 \cdot 10^{-3}$	$1.09 \cdot 10^{-3}$	$9.99 \cdot 10^{-4}$
0.001K/Fe	$3.82 \cdot 10^{-2}$	$1.36 \cdot 10^{-3}$	$1.13 \cdot 10^{-3}$	$1.04 \cdot 10^{-3}$
Spent materials				
0AM/Fe	$9.48 \cdot 10^{-3}$	$1.86 \cdot 10^{-3}$	$1.90 \cdot 10^{-3}$	$1.26 \cdot 10^{-3}$
0.001Li/Fe	$2.63 \cdot 10^{-3}$	$1.17 \cdot 10^{-3}$	$1.09 \cdot 10^{-3}$	$1.00 \cdot 10^{-3}$
0.001Na/Fe	$3.09 \cdot 10^{-3}$	$1.27 \cdot 10^{-3}$	$1.22 \cdot 10^{-3}$	$1.05 \cdot 10^{-3}$
0.001K/Fe	$1.81 \cdot 10^{-3}$	$1.80 \cdot 10^{-3}$	$1.80 \cdot 10^{-3}$	$1.80 \cdot 10^{-3}$

Table A-7 Kinetic parameters of CO activation over selected reduced and spent catalysts.

Catalysts	$k_{ads}^{eff}(CO)$ / s^{-1}	$k_{des}(CO)$ / s^{-1}	$k_{diss}^{eff}(CO)$ / s^{-1}	$k_{ass}(CO)$ / m$_{cat}^3$ mol^{-1} s^{-1}
		Reduced materials		
0AM/Fe	$4.32 \cdot 10^2$ $(4.27 \cdot 10^2 - 4.36 \cdot 10^2)$	$3.31 \cdot 10^1$ $(3.22 \cdot 10^1 - 3.40 \cdot 10^1)$	$1.39 \cdot 10^1$ $(1.20 \cdot 10^1 - 1.60 \cdot 10^1)$	$2.52 \cdot 10^2$ $(2.18 \cdot 10^2 - 2.94 \cdot 10^2)$
0.001Li/Fe				
0.001Na/Fe	$5.29 \cdot 10^2$ $(5.27 \cdot 10^2 - 5.30 \cdot 10^2)$	$1.03 \cdot 10^2$ $(1.02 \cdot 10^2 - 1.03 \cdot 10^2)$	$1.42 \cdot 10^1$ $(1.39 \cdot 10^1 - 1.44 \cdot 10^1)$	$1.33 \cdot 10^1$ $(3.22 \cdot 10^0 - 2.28 \cdot 10^1)$
0.001K/Fe	$6.56 \cdot 10^2$ $(6.54 \cdot 10^2 - 6.57 \cdot 10^2)$	$4.64 \cdot 10^1$ $(4.62 \cdot 10^1 - 4.65 \cdot 10^1)$	$2.17 \cdot 10^1$ $(2.14 \cdot 10^1 - 2.20 \cdot 10^1)$	--[a]
		Spent materials		
0AM/Fe	$6.92 \cdot 10^2$ $(6.87 \cdot 10^2 - 6.96 \cdot 10^2)$	$3.25 \cdot 10^2$ $(3.23 \cdot 10^2 - 3.27 \cdot 10^2)$	$1.79 \cdot 10^1$ $(1.76 \cdot 10^1 - 1.82 \cdot 10^1)$	$2.43 \cdot 10^2$ $(2.23 \cdot 10^2 - 2.64 \cdot 10^2)$
0.001Li/Fe	$3.98 \cdot 10^2$ $(3.95 \cdot 10^2 - 4.00 \cdot 10^2)$	$2.38 \cdot 10^2$ $(2.36 \cdot 10^2 - 2.39 \cdot 10^2)$	$2.33 \cdot 10^1$ $(2.29 \cdot 10^1 - 2.36 \cdot 10^1)$	$1.86 \cdot 10^1$ $(2.89 \cdot 10^0 - 3.37 \cdot 10^1)$
0.001Na/Fe	$3.37 \cdot 10^2$ $(3.35 \cdot 10^2 - 3.38 \cdot 10^2)$	$1.58 \cdot 10^2$ $(1.57 \cdot 10^2 - 1.59 \cdot 10^2)$	$4.77 \cdot 10^1$ $(4.70 \cdot 10^1 - 4.83 \cdot 10^1)$	--[a]
0.001K/Fe	$1.64 \cdot 10^1$ $(1.56 \cdot 10^1 - 1.73 \cdot 10^1)$	--[a]	--[a]	--[a]

[a]. The rate constant determined in this model was insensitive to this step.

Table A-8 Textural and redox properties of as-prepared Fe$_2$O$_3$ catalysts.

Catalyst	Crystallite size [a] / nm	BET surface area / m^2 g^{-1}	$n_{H_2,I}$ [b] / mmol H$_2$ g^{-1}	$T_{max,I}$ [c] / °C	$T_{on,II}$ [d] / °C
Fe-CP	15	37	1.95	371	395
Fe-SG	25	30	1.94	381	406
Fe-TD	30	11	2.02	386	432

[a]. The crystallite size of Fe$_2$O$_3$ was determined according to the Scherrer equation using (012), (104), (110), (113), (024) and (116) reflexes and an average value was reported.

[b]. The amount of consumed H$_2$ for the reduction of Fe$_2$O$_3$ to Fe$_3$O$_4$ in H$_2$-TPR profiles.

[c]. The temperature for maximal reduction rate of Fe$_2$O$_3$ and Fe$_3$O$_4$ in H$_2$-TPR profiles.

[d]. The onset temperature of the reduction of Fe$_3$O$_4$ in H$_2$-TPR profiles.

Table A-9 Comparison of catalytic performance of the state-of-the-art RWGS catalysts and Fe-TD developed in this work.

Catalyst	Temp. / °C	Pressure / bar	GHSV / mL g_{cat}^{-1} h^{-1}	H_2:CO_2 ratio	CO_2 conversion / %	S(CO) / %	S (CH_4) / %	Ref.
Noble Metal-Based catalysts								
0.1Ru/Al_2O_3	480	1	72,000	3	~44	~51	~49%	101
K80-Pt/L	350	1	30,000	1	7.0	100	0	35
8-Pt/Au@Pdq@Co	400	20	12,000	3	18.2	96.1	--	33
5Ir/Ce	300	10	--	4	6.8	>99	trace	104
Rh@S-1	350	10	3600	3	11.9	91.5	8.5	103
Pd/BNCT	450	1	15,000	4	35	~90	~10	331
Non-Noble Metal-Based catalysts								
Fe-Cu/Al_2O_3	400	1	12,500	4	36.2	89.7	10.3	56
3 wt.% Ni/Ce-Zr-O	550	1	10,000	1	34.0	55.1	44.9	332
SCuCe-re	300	1	1.08 h^{-1}	3	~18	~100	0	333
7.4Ni/ZIF-8-C	420	1	15,000	4	43.8	97.5	2.5	334
Co_3O_4-2h	350	1	36,000	3	~10	~92	~8	40
$BaCe_{0.2}Zr_{0.6}Y_{0.16}Zn_{0.04}O_3$	600	1	2400	1	36.3	94	6	335
TiFe/C	375	30	12,000	3	23	96	4	336
P-K-Mo_2C/γ-Al_2O_3	600	21	13,320	3	59	98.3	1.6	111
Our results								
Fe-TD	350	15	1160	3	28.0	99.2	0.8	This work
	350	1	10,000	3	12.5	98.7	0.9	This work
	450	1	10,000	3	38.2	98.1	1.6	This work
	550	1	10,000	3	49.4	99.3	0.7	This work

Table A-10 The rate ratio of primary reactions (RWGS reaction and CO_2 methanation) when the conversion of CO_2 is zero.

Catalyst	$r_{RWGS,p} / r_{CH4,p}$ [a]
Fe-CP	1.4
Fe-SG	5.7
Fe-TD	11.5

[a]. $r_{RWGS,p}$ and $r_{CH4,p}$ are the reaction rates of reverse water gas shift and CO_2 methanation, respectively, when the conversion of CO_2 is zero. Their ratio is given by the following equation:

$$\frac{r_{RWGS,p}}{r_{CH4,p}} = \frac{S(CO)_p}{S(CH_4)_p}$$

where, $S(CH_4)_p$ and $S(CO)_p$ are the selectivity values to CH_4 and CO at zero CO_2 conversion, respectively.

Table A-11 Phase composition (wt.%) of the catalysts after reduction at different temperatures (Fe-x-re300 and Fe-x-re400) determined through Rietveld quantitative phase analysis (R-QPA) towards their XRD patterns.

Catalyst	300 °C		400 °C	
	Fe	Fe_3O_4	Fe	Fe_3O_4
Fe-CP	2.4	97.5	31.1	68.9
Fe-SG	2.1	97.9	25.1	74.9
Fe-TD	1	99.0	23.5	76.5

Table A-12 The temperatures of maximal CH_4 formation and the assignment to carbon species in H_2-TPH profiles of different spent catalysts.

Catalysts	Adsorbed, atomic carbon	Polymeric, amorphous aggregates		Iron carbides		Graphitic carbon
	$T(\alpha)$ / °C	$T(\beta_1)$ / °C	$T(\beta_2)$ / °C	$T(\gamma_1, Fe_5C_2)$ / °C	$T(\gamma_2, Fe_3C)$ / °C	$T(\delta)$ / °C
Fe-CP						
Fe-CP-re300-s	296	385		528		900
Fe-CP-re400-s		400		528		900
Fe-SG						
Fe-SG-re400-s		432		558	635	900
Fe-SG-re300-s		431		676		900
Fe-TD						
Fe-TD-re400-s		433	505	610	649	890
Fe-TD-re300-s		430		650		880

Table A-13 The temperatures of maximal CO_2 desorption rates in CO_2-TPD tests with different reduced catalysts (Fe-x-re y) and the amount of CO_2 desorbed.

Catalysts	Peak α		Peak β		Peak γ		Peak δ		
	T_α / °C	Area / %	T_β / °C	Area / %	T_γ / °C	Area / %	T_δ / °C	Area / %	CO_2 desorption / $\mu mol\ g_{cat}^{-1}$
Fe-CP-re400	112	20.1	293	4.22	482	33.5	627	42.2	7.64
Fe-SG-re400	134	12.5			465	40.4	621	47.2	7.39
Fe-TD-re400	136	9.77			515	55.1	648	35.1	7.33
Fe-CP-re300	97	22.0	321	1.96	464	33.2	633	42.8	11.2
Fe-SG-re300	112	13.1			473	21.7	622	65.1	8.19
Fe-TD-re300	115	10.4			462	20.0	575	69.6	6.77

Table A-14 The temperatures of maximal CO_2 desorption rates in CO_2-TPD tests with different spent catalysts (Fe-x-re y-s) and the amount of CO_2 desorbed.

Catalysts	Peak I		Peak II		Peak III		Peak IV		
	T / °C	Area / %	T / °C	Area / %	T / °C	Area / %	T / °C	Area / %	CO_2 desorption / $\mu mol\ g_{cat}^{-1}$
Fe-CP-re400-s	533	52.5	537	11.5	565	33.4	695	2.66	121.0
Fe-SG-re400-s	550	6.03	564	42.6	580	22.7	656	28.7	136.3
Fe-TD-re400-s	552	17.1			574	55.1	675	27.8	182.2
Fe-CP-re300-s			521	35.7	546	60.0	666	4.28	93.8
Fe-SG-re300-s	393	9.14	578	24.6	662	62.9	694	3.39	35.8
Fe-TD-re300-s	415	2.91			598	89.4	742	7.71	45.0

Table A-15 The temperatures of maximal CO desorption rates in CO-TPD tests with different spent catalysts (Fe-x-re y-s) and the amount of CO desorbed.

Catalysts	Peak I		Peak II		Peak III		Peak IV	
	T / °C	Area / %	T / °C	Area / %	T / °C	Area / %	T / °C	Area / %
Fe-CP-re400-s	530	33.2	547	40.9	576	19.3	727	6.65
Fe-SG-re400-s	568	29.5			629	66.9	842	3.62
Fe-TD-re400-s	583	11.5	602	35.4	693	47.2	832	5.99

Table A-16 CO_2 conversion and product selectivity as well as SSITKA-derived kinetic parameters determined at 1.5 bar and 300°C using a $H_2/CO_2=11$ feed for 1.5 h. The catalysts were initially reduced in 50% H_2/N_2 at 400°C for 2 h.

| Catalyst	$X(CO_2)$ / %	$S(CO)$ / %	$S(CH_4)$ / %	$S(C_{2+})$ / %	r_{CO} / $\mu mol\ g_{cat}^{-1}\ s^{-1}$	r_{CH4} / $\mu mol\ g_{cat}^{-1}\ s^{-1}$	τ_{CO} / s	τ_{CHx} / s	N_{CO} / $\mu mol\ g_{cat}^{-1}$	N_{CHx} / $\mu mol\ g_{cat}^{-1}$
Fe-CP	25.6	31.5	35.7	32.8	1.92	2.18	8.6	17.7	16.5	38.6
Fe-SG	14.9	35.1	47.2	17.7	1.21	1.63	5.2	20.9	6.3	34.0
Fe-TD	15.4	72.6	17.2	10.1	2.59	0.62	1.7	23.1	4.4	14.2

Table A-17 Parameters obtained through fitting Mössbauer spectra of iron carbides in spent catalysts Fe-x-re400-s and Fe-x-re300-s.

Catalyst	Phase	IS (mm s^{-1})	QS (mm s^{-1})	Hyperfine field (T)
Fe-CP-re400-s	Fe_5C_2 (I)	0.2311	0.0571	21.4396
	Fe_5C_2 (II)	0.1285	0.0474	18.4181
	Fe_5C_2 (III)	0.0810	-0.015	10.0133
Fe-CP-re300-s	Fe_5C_2 (I)	0.2479	0.0653	21.4820
	Fe_5C_2 (II)	0.1315	0.0895	18.0123
	Fe_5C_2 (III)	0.0989	0.0316	9.4072
Fe-SG-re400-s	Fe_5C_2 (I)	0.2245	0.0421	21.4586
	Fe_5C_2 (II)	0.1583	0.0393	17.8892
	Fe_5C_2 (III)	0.1516	-0.0115	9.8188
	Fe_3C	0.1943	0.0075	19.7738
Fe-SG-re300-s	Fe_5C_2 (I)	0.2194	0.0520	21.8120
	Fe_5C_2 (II)	0.1662	0.0767	18.0339
	Fe_5C_2 (III)	0.0933	-0.0858	10.6944
Fe-TD-re400-s	Fe_5C_2 (I)	0.2312	0.0489	21.5911
	Fe_5C_2 (II)	0.2081	0.00039	18.3881
	Fe_5C_2 (III)	0.1027	-0.0387	10.1067
	Fe_3C	0.199	0.0093	20.3291
Fe-TD-re300-s	Fe_5C_2 (I)	0.1979	0.0289	21.8120
	Fe_5C_2 (II)	0.2401	-0.0485	19.4853
	Fe_5C_2 (III)	0.0562	-0.0819	10.4043

Curriculum Vitae

Personal details:

Name	Qingxin Yang
Date of birth	19.07.1993
Place of birth	Shandong, China
Email:	Qingxin.Yang@catalysis.de
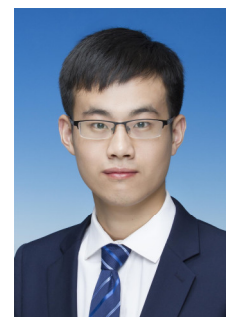
Education:

01/2019 – present

Doctoral Student

Leibniz-Institute for Catalysis (LIKAT, Rostock, Germany)

Topic: CO_2 hydrogenation over Fe-based catalysts

Supervisor: Prof. Dr. Evgenii V. Kondratenko

09/2015 – 06/2018

Master in Chemical Engineering

China University of Petroleum-Beijing (China)

Topic: *n*-Butane catalytic cracking into light olefins

Supervisor: Prof. Guiyuan Jiang

09/2011 – 06/2015

Bachelor of Chemical Engineering and Technology

Northeast Petroleum University (China)

Awards:

- Outstanding graduate student of China University of Petroleum (2018)
- The first-class scholarship of China University of Petroleum (2016, 2017)
- Scholarship for school post-graduate Academic Forum, 3rd Scholarship (2016)
- Level A scholarship of Northeast Petroleum University (2012, 2013, 2014)
- National Scholarship (2012)

List of Publications

1. **Q. Yang**, V.A. Kondratenko, S.A. Petrov, D.E. Doronkin, E. Saraçi, H. Lund, A. Arinchtein, R. Kraehnert, A. S. Skrypnik, A.A. Matvienko, E.V. Kondratenko, Identifying performance descriptors in CO_2 hydrogenation over iron-based catalysts promoted with alkali metals, *Angew. Chem. Int. Ed.* **2022**, e202116517 (Doi: 10.1002/anie.202116517)

2. **Q. Yang**, A. Skrypnik, A. Matvienko, H. Lund, M. Holena, E. V. Kondratenko, Revealing property-performance relationships for efficient CO_2 hydrogenation to higher hydrocarbons over Fe-based catalysts: Statistical analysis of literature data and its experimental validation, *Appl. Catal. B-Environ.* **2021**, 282, 119554 (Doi: 10.1016/j.apcatb.2020.119554)

3. **Q. Yang**#, Y. Li#, Z. Chen, L. Hu, Z. Li, Y. Wang, Z. Zhao, C. Xu, G. Jiang (# contributed equally), Core-shell structured HZSM-5@mesoSiO$_2$ catalysts with tunable shell thickness for efficient n-butane catalytic cracking, *AIChE J.* **2021**, 67, e17130 (Doi: 10.1002/aic.17130)

4. A. Arinchtein, M. Ye, **Q. Yang**, C. Kreyenschulte, A. Wagner, M. Frisch, A. Brückner, E. Kondratenko, R. Kraehnert, Dynamics of Reaction-Induced Changes of Model-Type Iron Oxide Phases in the CO_2-Fischer-Tropsch-Synthesis, *ChemCatChem* **2022**, e202200240 (Doi: 10.1002/cctc.202200240)

5. S. Weber, R.T. Zimmermann, J. Bremer, K.L. Abel, D. Poppitz, N. Prinz, J. Ilsemann, S. Wendholt, **Q. Yang**, R. Pashminehazar, F.Monaco, P. Cloetens, X. Huang, C. Kübel, E.V. Kondratenko, M. Bauer, M. Bäumer, M. Zobel, R. Gläser, K. Sundmacher, T. Sheppard, Digitization in Catalysis Research: Towards a Holistic Description of a Ni/Al$_2$O$_3$ Reference Catalyst for CO_2 Methanation, *ChemCatChem* **2022**, e202101878 (Doi: 10.1002/cctc. 202101878)

6. A. Skrypnik, **Q. Yang**, A.A. Matvienko, V.Y. Bychkov, Y.P. Tulenin, H. Lund, S.A. Petrov, R. Kraehnert, A. Arinchtein, J. Weiss, A., Brueckner, E.V. Kondratenko, Understanding reaction-induced restructuring of well-defined Fe$_x$O$_y$C$_z$ compositions and its effect on CO_2 hydrogenation, *Appl. Catal. B-Environ.* **2021**, 291, 120121 (Doi.: 10.1016/ j.apcatb.2021.120121)

7. J. Liu, Y. Li, Z. Chen, Z. Li, **Q. Yang**, L. Hu, G. Jiang, C. Xu, Y. Wang, Z. Zhao, Hierarchical ZSM-5 Zeolites with Tunable Sizes of Building Blocks for Efficient Catalytic Cracking of i-Butane, *Ind. Eng. Chem. Res.* **2018**, 57, 31, 10327–10335 (Doi.: 10.1021/acs.iecr.8b02421)

Conference Participations

Talks

1. **Q. Yang**, A. Arinchtein, J. Weiß, U. Bentrup, A. Brückner, R. Kraehnert and E.V. Kondratenko, Iron-based catalysts for CO_2 conversion into higher hydrocarbons under dynamic conditions, 1st PhD and PostDoc Workshop of SPP2080, Hamburg, Germany, 19.09-20.09 (2019)

Posters

1. **Q. Yang**, E.V. Kondratenko, *In situ* reaction-induced and externally forced dynamics of Fe-based catalysts in CO_2 hydrogenation, 758. WE-Heraeus-Seminar, Hanau, Germany, 10.01–13.01 (2022)

2. **Q. Yang**, V.A. Kondratenko, E.V. Kondratenko, Understanding the promotion effect of alkali metals on CO_2 hydrogenation to light olefins over Fe-based catalysts, 54. Germany catalysis meeting, Weimar-online event, Germany, 16.03–19.03 (2021)

3. **Q. Yang**, E.V. Kondratenko, Approaches for revealing property-performance relationships in CO_2 hydrogenation to higher hydrocarbons, SPP2080 Status Colloquium 2021, online event, Germany, 23.02–26.02 (2021)

4. **Q. Yang**, A. Skrypnik, A. Matvienko, H. Lund, S. Petrov, E.V. Kondratenko, Approaches for revealing property-performance relationships in CO_2 hydrogenation to higher hydrocarbons, Virtual Audit, Rostock, Germany, 30.11 (2020)

5. **Q. Yang**, M.J.G. Fait, M. Holena, E.V. Kondratenko, Revealing property-performance relationships through statistical analysis of literature data for efficient CO_2 hydrogenation to higher hydrocarbons, 17th International Congress on Catalysis, San Diego, USA, 14.06–19.06 (2020)

6. **Q. Yang**, M.J.G. Fait, M. Holena, E.V. Kondratenko, Property-performance relationships in CO_2 hydrogenation to higher hydrocarbons from statistical analysis of literature data, 53. Germany catalysis meeting, Weimar, Germany, 11.03–13.03 (2020)

7. **Q. Yang**, A. Skrypnik, E.V. Kondratenko, CO_2 conversion into higher hydrocarbons over Fe-based catalysts: Effect of preparation method and catalyst treatment, Status meeting of SPP 2080, Leipzig, Germany, 17.02–18.02 (2020)